République Algérienne Démocratique et Populaire
Ministère de l'Enseignement Supérieur et de la Recherche Scientifique

Ecole Nationale Polytechnique
Département d'Electronique
Laboratoire des Dispositifs de Communication
et de Conversion Photovoltaïque

Thèse de Doctorat

Présentée par **ABED Mansour**
Magistère en Génie Electrique, Université de l'Alexandrie, Egypte
Magistère en Communications, Université de Technologie, Bagdad, Irak

Thème

Time-Frequency Distributions : Compact Support Kernels, Performances and Implementations

Soutenue publiquement le **8 juin 2015** devant le jury :

Président :	HADDADI Mourad	(Prof, ENP)
Rapporteurs :	BELOUCHRANI Adel	(Prof, ENP)
	CHERIET Mohamed	(Prof, École de technologie supérieure, Québec, Canada)
Examinateurs:	GINI Fulvio	(Prof, University of Pisa , Italy)
	SERIR Amina	(Prof, USTHB)
	OULDALI Abdelaziz	(Docteur d'Etat, Université de Mostaganem)
Invité :	MERMOUL Atef	(Docteur/MRB, LDCCP/ENP)

2015

خلاصة

تعنى هذه الأطروحة ببناء توزيعات جديدة عالية التمييز من فئة كوهين تؤدي إلى توهين أفضل للتداخلات و تحافظ في نفس الوقت على أهم المعلومات المتعلقة بالقانون الترددي المتعلق بكل حدث زمني. تستخدم هذه التوزيعات عائلة جديدة من النوى تسمى نوى ذات سند محصور امتدادا للنواة الأساسية المقترحة لأول مرة من قبل شريط و بلوشراني لمعاجلة الإشارات في الزمن-التردد. بعد دراسة الخصائص الرياضية، تم تقييم التوزيعات المشتقة بشكل موضوعي و مقارنتها مع التمثيلات التربيعية الأكثر انتشارا باستعمال مقاييس كفاءة مختلفة تستند إلى معايير التركيز، التمييز و إخماد المركبات المتقاطعة. بعد إثبات فعالية التوزيعات الجديدة المقترحة، أدخلنا معيارا رابعا للتقييم الموضوعي للتوزيعات التربيعية و يتعلق الأمر بتحديد تكلفة حساب التوزيع. يعتبر هذا المعيار بالغ الأهمية عندما يتم التخطيط لتطبيقات الوقت الحقيقي. لأجل التمكن من ضبط مرن و تفاعلي للعناصر المتعلقة بكل توزيع و إتاحة عرض جذاب للرسومات و لنتائج، قمنا بتنظيم العمل المنجز في شكل صندوق أدوات بالاستعانة ب ماتلاب (Matlab) سمي TFDOP و الذي يعني بالإنجليزية 'Time-Frequency Distributions' OPtimazation'. تبقا لاحتياجات المستخدم، يمكن تطوير مجموعة البرامج المصممة و تحيينها لأجل احتواء إضافات و ميزات فعالة أخرى بكل يسر كأن تشمل توزيعات و مقاييس كفاءة جديدة.

الكلمات المفتاحية- فئة كوهين، كلفة الحساب، التوزيعات الزمن-التردد من الفئة التربيعية، توزيع شريط-بلوشراني، تقييم الكفاءة، مقياس الكفاءة لبوعشاش-سوسيك، نوى ذات سند محصور، نواة جذرية ذات سند محصور، نواة منفصلة ذات سند محصور، إشارات غير ثابتة

Résumé

Cette thèse s'occupe de la construction de nouvelles DTFs de haute résolution appartenant à la classe de Cohen qui résultent en meilleure atténuations des artéfacts et maintiennent en même temps l'information la plus importante sur la loi fréquentielle relative à chaque événement temporel. Ces distributions utilisent une nouvelle famille de noyaux appelés Noyaux à Support Compact comme une extension au noyau CB introduit la première fois dans l'analyse temps-fréquence par Cheriet et Belouchrani. Après l'étude des propriétés mathématiques, les distributions dérivées sont évaluées d'une manière objective et comparées aux représentations quadratiques les plus connues en utilisant des mesures de performance diverses basées sur les critères de concentration, de résolution et de suppression des termes croisés. Une fois l'efficacité des nouvelles distributions proposées est prouvée, nous avons introduit un quatrième critère d'évaluation objective des DTFs qui est le coût de calcul de la distribution. Ce dernier est particulièrement critique lorsqu'une implémentation en temps réel est planifiée. Pour permettre un réglage souple et interactif des paramètres de chaque DFT et fournir une visualisation agréable des tracés temps-fréquences et des résultats d'optimisation; nous avons organisé le travail sous la forme d'une boite à outils implémentée sous Matlab appelée TFDOP pour "Time-Frequency Distributions' OPtimization". Selon les besoins de l'utilisateur, le logiciel réalisé peut être personnalisé et amélioré afin d'inclure plus de distributions, de mesures de performance et de fonctions.

Mots-clés **—**Analyse temps-fréquence, classe de Cohen, coût de calcul, distributions temps-fréquence (DTF) de classe quadratique, DTF de Cheriet-Belouchrani, évaluation de performance, mesure instantanée normalisée de performance de résolution de Boashash-Sucic, noyau à support compact, noyau polynomial à support compact, noyau séparable à support compact, signal non-stationnaire.

Abstract

This thesis deals with the building of new high-resolution TFDs of Cohen's class that result on the best artifacts' mitigation and maintain at the same time the most important information about the frequency law related to each time event. These distributions employ a new family of kernels referred to as Kernels with Compact Support (KCS) as an extension to the CB kernel applied the first time to TFSA by Cheriet and Belouchrani. After analyzing their mathematical properties, the derived distributions are objectively evaluated and compared to the best known quadratic representations using several performance measures based on concentration, resolution and crossterm suppression criteria. Once the effectiveness of the new proposed distributions is proved, we have introduced a fourth criterion of objective assessment of TFDs which is the computational cost of the distribution. The later is particularly critical when real-time implementation is intended. In order to allow a flexible and interactive setting of each TFD's parameters and provide a fine display of the time-frequency diagrams and optimization results; we have organized the present work in the form of a toolbox implemented under Matlab environment referred to as TFDOP for "Time-Frequency Distributions' OPtimization". According to the user's needs, the realized software package can be customized and upgraded in order to include more distributions, performance measures and features.

Keywords — Boashash-Sucic normalized instantaneous resolution performance measure, Cheriet-Belouchrani (CB) TFD, Cohen's class, computational cost, kernels with compact support, nonstationary signal, performance evaluation, polynomial compact support kernel, quadratic time-frequency distributions (TFDs), separable compact support kernel, time-frequency analysis, time-frequency localization, uncertainty principle, Wigner-Ville distribution.

Acknowledgments

First of all, I thank almighty Allah our creator in helping me and accepting my prayers that made the accomplishment of this work more than a dream after all what happened during my years of postgraduate studies, then I would like to express my sincere gratitude and give my deepest thanks to my principal supervisor **Prof. Dr. Adel Belouchrani** for his helpful suggestions, scientific stimulation and encouragement. This work would not have been possible without his guidance throughout the entire course of my PhD research (from problem formulation to results and discussions!) and his extremely solid knowledge in signal processing area that made me greatly esteemed. I will be never able to thank him as it must be.

Also, I wish to express my deep gratitude to my associate supervisor **Prof. Dr. Mohamed Cheriet** for his supportive help, precious suggestions in the field of compact support kernels theory and his important scientific comments during the work review. Special thanks and gratitude to **Prof. Dr. Boualem Bouashash**, one of the most famous founders of the time-frequency analysis theory in the world, for his help in improving my work and for his precious support.

Next, I would like to thank my professors and colleagues at *Mostaganem University* and *Signaux et systèmes* laboratory especially **Prof. Dr. Malika Mimi**; the knowledge and experience I gained there were invaluable.

Special thanks must be given to **Prof. Dr. Abdelmalik Taleb-Ahmed** from *Université de Valenciennes et du Hainaut-Cambrésis (UVHC)* for his hospitality and support during my stays at Valenciennes. Many thanks to the teaching and administrative staff of *Ecole Nationale Polytechnique d'El-Harrach, Algiers*; it was a great pleasure and honor for me to accomplish my doctoral studies in this famous school.

Finally, I would like to thank my dear parents and wife for their love, support and prayers, which are the energy in my heart of hearts to do anything.

The author wishes to express his deep gratitude to F. Auger, O. Lemoine, P. Gonçalvès and P. Flandrin for their very helpful and valuable work in the development of many useful Matlab functions related to time-frequency signal analysis. Their toolbox was of great help since it permits to gain an enormous time in the comprehension and test of the most-known classical TFDs and also provides a fine and normalized display of the time-frequency diagrams.

The author would like to thank also Curtis Condon, Ken White, and Al Feng of the Beckman Institute of the University of Illinois for the bat data and for permission to use it in this thesis.

To ...
my parents,
my brothers and sisters,
my wife
my sons

Table of contents

List of figures

List of tables

List of abbreviations and symbols

Abbreviations

AF	Narrow-band ambiguity function
AWGN	Additive white Gaussian noise
BJD	Born-Jordan distribution
CB TFD	Cheriet-Belouchrani time-frequency distribution
CC	Computational cost
CF	Constant frequency
CWD	Choi-Willams distribution
FM	Frequency modulation
IF	Instantaneous frequency
KCS	Kernels with compact support
LFM (signal)	Linear frequency modulated (signal)
MBD	Modified B-distribution
PCB TFD	Polynomial Cheriet-Belouchrani time-frequency distribution
PWVD	Pseudo Wigner-Ville distribution
RID	Reduced interference distribution
SCB TFD	Separable Cheriet-Belouchrani time-frequency distribution
SPWVD	Smoothed pseudo Wigner-Ville distribution
STFT	Short-time Fourier transform
TFD	Time-frequency distribution
TFDOP	Toolbox for time-frequency distribution's optimization
TFSA	Time-frequency signal analysis
WVD	Wigner-Ville distribution
ZAMD	Zhao-Atlas-Marks distribution

Symbols

$t,\ \tau$	Time variables
$f,\ \eta$	Frequency variables
$x(t)$	Signal x in time
$X(f)$	Fourier transform of the signal $x(t)$
$STFT_x^h(t,f)$	Short-time Fourier transform of x with respect to the window h
E_x	Energy of the signal x
$W_x(t,f)$	Wigner-Ville distribution of x
$x_a(t)$	Analytic signal associated to the real signal x

$\hat{x}(t)$	Hilbert transform of the signal x
$a_x(t)$	Instantaneous amplitude of the signal x
$f_x(t)$	Instantaneous frequency of the signal x
$S_x^h(t,f)$	Spectrogram of x with respect to the window h
$PW_x(t,f)$	Pseudo-Wigner-Ville distribution of x
$SPW_x(t,f)$	Smoothed pseudo-Wigner-Ville distribution of x
$TFD_x(t,f)$	Time-frequency distribution of x
$J(s,\tau)$	Parametrization function of $TFD_x(t,f)$
$A_x(\eta,\tau)$	Ambiguity function of x
$\Pi(t,f)$	Time-frequency domain kernel
$G(t,\tau)$	Time-lag domain kernel
$\phi(\eta,\tau)$	Doppler-lag domain kernel
$\psi(\eta,f)$	Doppler-frequency domain kernel
$U_x(t,\tau)$	Instantaneous autocorrelation function of x
$G_{JB}(t,\tau)$	Born-Jordan time-lag kernel
$\phi_{JB}(\eta,\tau)$	Born-Jordan Doppler-lag kernel
$BJ_x(t,f)$	Born-Jordan distribution of x
$G_{CW}(t,\tau)$	Choi-Williams time-lag kernel
$\phi_{CW}(\eta,\tau)$	Choi-Williams Doppler-lag kernel
$CW_x(t,f)$	Choi-Williams distribution of x
$G_{ZAM}(t,\tau)$	Zhao-Atlas-Marks time-lag kernel
$\phi_{ZAM}(\eta,\tau)$	Zhao-Atlas-Marks Doppler-lag kernel
$ZAM_x(t,f)$	Zhao-Atlas-Marks distribution of x
$B(0,1)$	Unit ball support
$\varphi_\sigma(x)$	Mollifiers on $\Re^N$ with support $B(0,\sigma)$
$g_\sigma(x,y)$	2D one-parameter family of normalized symmetrical Gaussian
$\rho_\gamma(x,y)$	KCS kernel with control parameter γ
$\rho_{\sigma,\gamma}(x,y)$	Family of KCS kernels with control parameter γ and support $B(0,\sigma)$
$\phi_{CB}(\eta,\tau)$	Cheriet-Belouchrani (CB) kernel
$\phi_{SCB}(\eta,\tau)$	Separable CB kernel
$\phi_{PCB}(\eta,\tau)$	Polynomial CB kernel
C	Bandwidth controller of the CB and the SCB kernels
γ	Bandwidth controller of the PCB kernel
$CB_x(t,f)$	Cheriet-Belouchrani distribution of x
$SCB_x(t,)$	Separable Cheriet-Belouchrani distribution of x
$PCB_x(t,f)$	Polynomial Cheriet-Belouchrani distribution of x
R_α	Rényi entropy with order α
R_{NSE_α}	Rényi entropy normalized by signal energy with order α
R_{NDV_α}	Rényi entropy normalized by distribution volume with order α
RN	Ratio of norms concentration measure
S_β	Stankovic concentration measure with parameter β
A_M	Average amplitude of the main-lobes
A_S	Average amplitude of the side-lobes
A_X	Average amplitude of the crossterms

$f_i(t)$	The component instantaneous frequency
$V_i(t)$	The component instantaneous bandwidth
$D(t)$	The components' separation measure
P_i	The Boashash-Sucic's normalized instantaneous resolution performance measure
P	The Boashash-Sucic's overall performance measure

Summary

Signal processing is the discipline that develops and studies the techniques of processing, analysis and interpretation of signals. It calls upon to the results of information theory, statistics as well as various other domains of applied mathematics. This discipline becomes so wide that it presents itself as an independent field of research.

The processed signals can come from very different sources, but almost of them are electrical signals or became electrical using sensors and transducers such as microphones, thermal and optical sensors, pressure, position and velocity sensors, and in general all physical and chemical quantities that are convertible to currents and voltages.

In most cases, the acquired real-life signals are of nonstationary nature. In addition, they are often multicomponent, i.e. signals composed of many time-dependent frequency components. Among the nonstationary signals, we have speech signals, radar, sonar and telecommunications' signals, acoustics, seismics, biomedicals, just to name few.

In such situations, when the classical temporal and frequency representations are used separately, the desired perception and interpretation of the multiple oscillating components cannot be obtained since it is not possible to provide a simultaneous time and frequency localization. Hence, it is natural to move towards joint time-frequency representations if one wants to supply information about how the frequency of the signal varies during time. This particular field of signal processing is known in the literature as Time-Frequency Signal Analysis (TFSA).

If time-frequency distributions (TFDs) of quadratic class constitute a powerful tool for nonstationary signals' analysis, their readability, however, is severely affected by the presence of interference terms that are automatically generated due to the bilinear form of these representations. The introduction of a smoothing in time and/or frequency can reduce these undesirable terms but may introduce errors of localization due to the involved degradation in time-frequency resolution. Furthermore, the most efficient quadratic TFDs, that belong to the Cohen's class, require the specification of a kernel that defines the overall performance of the induced representation. However, an optimal universal kernel does not exist.

From this standpoint, we have focused our attention in this thesis on the building of new high-resolution TFDs of Cohen's class that result on the best artifacts' mitigation and maintain at the same time the most important information about the frequency law related to each time event. These distributions employ a new family of kernels referred to as Kernels with Compact Support (KCS) as an extension to the CB kernel applied the first time to TFSA by Cheriet and Belouchrani [44, 45]. After analyzing their mathematical properties, the derived distributions are objectively evaluated and compared to the best known quadratic representations using several performance measures based on concentration, resolution and crossterm suppression criteria.

Once the effectiveness of the new proposed distributions is proved, we have introduced a fourth criterion of objective assessment of TFDs which is the computational cost of the distribution. The later is particularly critical when real-time implementation is intended.

In order to allow a flexible and interactive setting of each TFD's parameters and provide a fine display of the time-frequency diagrams and optimization results ; we have organized the present work in the form of a toolbox implemented under Matlab environment referred to as TFDOP for "Time-Frequency Distributions' OPtimization". According to the user's needs, the realized software package can be customized and upgraded in order to include more distributions, performance measures and features. Extensive illustrative examples and precise arguments and interpretations are provided for each studied case according to the formulas and algorithms described through the theoretical part of the dissertation.

Keywords : Autoterms, Boashash-Sucic normalized instantaneous resolution performance measure, Cheriet-Belouchrani (CB) TFD, Cohen's class, comparison criteria, concentration, computational cost, crossterm suppression, Doppler-lag domain kernel, frequency modulated (FM) signal, instantaneous frequency, kernels with compact support, kernel design, kernel-based distributions, linear FM signal, multicomponent signal, nonlinear FM signal, nonstationary signal, optimal TFD, optimization, performance evaluation, polynomial compact support kernel, quadratic time-frequency distributions (TFDs), resolution, separable compact support kernel, spectrogram, time-frequency analysis, time-frequency localization, time-lag kernel, uncertainty principle, Wigner-Ville distribution.

Chapter 1

Introduction

In this first chapter, we show that the analysis of nonstationary signals requires necessarily a joint representation in time and in frequency. We then describe the problematic of the thesis and the motivation behind the research of new kernels and solutions in the field of time-frequency signal analysis and optimization. The original contributions are cited and the thesis organization is presented.

1.1 Problematic of the thesis - Motivation

In common practice, the analysis of a physical phenomenon passes through a signal acquisition process as a function of time. Hence, the temporal representation of a signal is the most natural, but it does not always contain the required information to perform a complete analysis. On the other hand, the frequency representation obtained by Fourier transform provides information about what frequencies are present in the signal and what their relative strengths are [1]. However, none of the two representations is capable of providing us with any sort of information about the nature of the signal components nor their behavior with respect to time or frequency [1]. Consequently, since almost of signals we encounter in our everyday life are nonstationary, and then characterized by time-dependent spectral contents, a simultaneous representation in time and frequency is necessary to allow a complete definition of such signals.

In order to clarify this concept, let us consider for example the signal $x(n)$ given by

$$x(n) = \begin{cases} e^{2\pi j 0.1n} & \text{for} \quad 1 \leq n \leq 500 \\ e^{2\pi j 0.3n} & \text{for} \quad 500 < n \leq 1024 \end{cases} \tag{1.1}$$

The signal $x(n)$ is composed of two constant frequency (CF) components of frequencies $f_1 = 0.1$ Hz and $f_2 = 0.3$ Hz, respectively. Fig. 1.1 shows how it is difficult to determine the instants of appearance and disappearance of the two sinusoids and their relative frequencies from temporal inspection while the frequency-domain representation includes only the spectral contents without any notion of time inside.

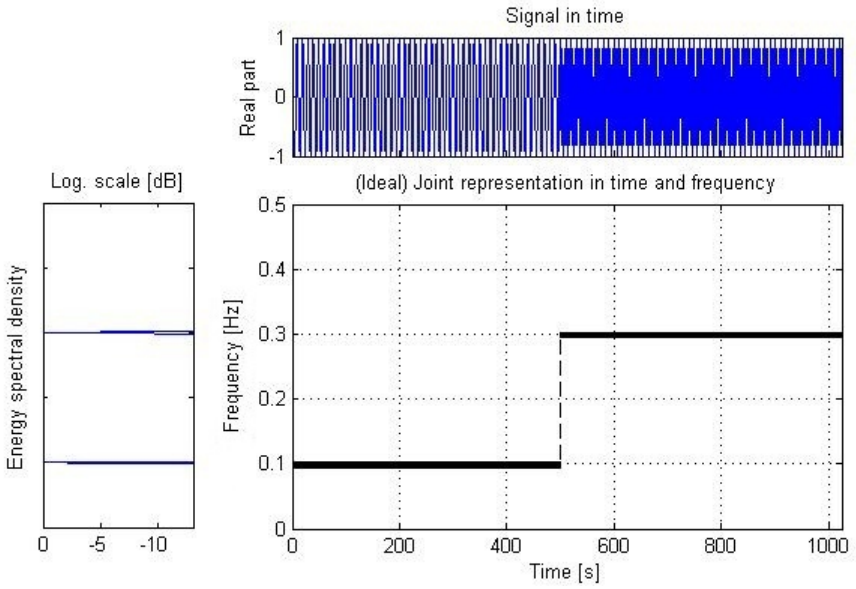

FIGURE 1.1 – Time, frequency and ideal time-frequency representations of the nonstationary signal defined by (1.1).

Hence, we imagine that a mixed approach combining simultaneously the two variables t and f will provide a full description of the signal's characteristics (Fig. 1.1). This includes the number of components present in the signal, the time durations and frequency bands

over which these components are defined, the components' relative amplitudes, phase information, and the instantaneous frequency (IF) laws that components follow in the time-frequency plane [2]. Although some of the methods used to show the time-dependent frequency variations may not result on a proper distribution, these techniques are generally known as time-frequency distributions (TFDs) [3, 4].

Among the distributions discussed in the literature, this dissertation deals with the signal-independent class of quadratic TFDs since it is the most frequently used in practical applications such as acoustics, speech processing, seismic signal interpretation, radar, sonar, telecommunications and biomedical engineering.

Before detailing in depth the problematic of the thesis, it is important to introduce first some useful historical notes. The original time-frequency signal analysis (TFSA) technique is the Wigner-Ville distribution (WVD) [5]. Its name comes from E. Wigner who proposed it in the field of quantum mechanics [6] and J. Ville [7], the first researcher who used it to explain the notion of instantaneous frequency for communications theory purposes [5]. Such transforms are known as bilinear or quadratic time-frequency distributions because the representation is formulated by the multiplicative comparison of the signal with itself, expanded in various directions around each point in time space.

The WVD and its variants like the Pseudo WVD (PWVD) have been the subject of many studies and were found to be optimal detectors for frequency modulated signals under some conditions [8, 9]. Because of the crossterms that the WVD produces [10], many researchers have investigated in the reduction of these undesirable effects in the early 1980s, for example the work of P. Flandrin [11] in 1984 and the introduction of Polynomial WVDs by B. Boashash [12, 13] in 1991.

The general theory of quadratic kernel-based transforms is due to L. Cohen [14]. He introduced the Cohen class of distributions for applications in quantum mechanics, an area that has driven many original contributions to time-frequency signal theory [5]. In this context, Claasen and Mecklenbrauker [15]-[17] made use of the similarities and differences of signal processing fundamentals with quantum mechanics and developed many ideas and procedures in the field of time-frequency analysis. However, B. Boashash [18] is believed to be the first researcher who used various TFDs for real world problems. He developed a number of new methods and particularly realized that a distribution may not behave properly in all aspects and interpretations, but it still be used if a particular property such as the instantaneous frequency (IF) is well defined [19]. Janse and Kaizer [20] developed innovative theoretical and practical techniques for the use of TFDs and introduced new methodologies.

The Gabor transform is the most easily accessible time-frequency transform, and this is due to the analytic tractability of the Gaussian window function [5]. Gabor's 1946 paper studied sets of signal atoms called the Gabor elementary functions with optimal joint resolution in the time and frequency domains [5]. Gabor applied the theory to acoustics [21] and communications theory [22]. Researchers in diverse areas such as speech recognition, image processing, communications and seismic signal interpretation investigated

with great interest in Gabor transform for many years.

The spectrogram [23]-[25], defined as the magnitude square of the short-time Fourier transform (STFT), has been the most widely used tool for the analysis of time-varying spectra. Even if it is irreversible, does not satisfy many desirable mathematical properties and results on unwanted smoothing of the signal components' energies around their IFs [3, 26] ; the spectrogram has found a great number of practical applications in signal and speech processing, phonetics, seismology, radar, sonar, RF and microwave systems (like the vector network analyzers), music and analysis of animal calls.

The research for the design of high-resolution distributions that overcome the presence of non-negligible crossterms induced by the WVD has opened the way for many derivations of quadratic representations ; the most popular among them belong to the class of reduced interference distributions [3]. One of the first ones was the Choi-Williams distribution (CWD)[27] in 1989, the Born-Jordan distribution (BJD) defined in [28] using an operational rule of Born and Jordan [29] and referred to as the sinc distribution in [30], the Zhao-Atlas-Marks distribution (ZAMD) [31] in 1990 and followed by numerous representations among the Cohen's class [32]-[36] having as a principal objective the improvement of the concentration and resolution performances. In [37], Moeness Amin introduced a class of recursive kernels for time-frequency signal representations and derived in [38] the minimum variance time-frequency distribution kernels for signals in additive noise. Then, Moeness Amin and Williams introduced in [39] a new class of TFD kernels providing high-frequency resolution. Barkat and Boashash proposed new powerful high-resolution bilinear distributions namely the B-Distribution (BD) [40] and the Modified B-Distribution (MBD) [41, 42] that was shown to be very effective in crossterms reduction and allows an efficient IF estimation [43]. More recently, Cheriet and Belouchrani enriched the TFSA literature by a new type of kernels of compact support [44]. The derived representation referred to as the CB TFD provides a very effective solution for energy estimation of nonstationary signals and permits significant crossterms suppression [45].

From applications point of view, time-frequency methods can be used in electroencephalogram (ECG) signal analysis, in particular for newborn babies ; while kernel-based time-frequency distributions have been used in new promising signal processing tasks like blind source separation [46]-[49], interference rejection in spread spectrum communications systems [50] and estimation of direction of arrival [51, 52].

Based on the historical review and bibliographic research, we conclude the following : 1) Kernels play the most important role in time-frequency analysis of signals and determine the overall performance of the related distribution. Various types of kernels have been introduced in this domain. Usually, different types of kernels (i.e., kernels in different function form) correspond to different types of TFDs [53] and 2) although many quadratic TFDs have been proposed in the literature, there is no specific "ideal" distribution that can be considered as the optimal choice for all possible cases and applications because every representation suffers from one or more drawbacks. This makes the building of new kernels for the analysis of time-varying spectra a promising and an open field of research.

The principal problematic of the thesis is then the derivation and use of new kernels to build new powerful quadratic time-frequency distributions that are as closest as possible to the ideal compromise between crossterm free, high component resolution and autoterm concentration as well as lowest required computational cost. How to objectively evaluate and compare the goodness and effectiveness of the proposed representations according to concentration, resolution and interference suppression criteria constitutes an important part of the present work.

1.2 Thesis objectives

The main objective of this dissertation is to enrich the time-frequency signal analysis field by new proposed high-resolution representations of Cohen's class based on kernels with compact support (KCS) in order to provide efficient tools for energy measurement of nonstationary signals. The performance of the KCS-TFDs is compared to the most used existing TFDs based on objective measures for quantifying the concentration and resolution performances. The selection of the best representation includes a new criterion related to the required computational cost of the kernel that must be considered especially when real-time energy estimation is intended.

On the other hand, we aim to provide signal analysts with a powerful and upgradeable software package by implementing a professional toolbox under Matlab environment referred to as TFDOP for "Time-frequency Distributions' Optimization". The toolbox serves to compute, display and test the performance of the best-known TFDs of quadratic class in addition to the new proposed KCS-based distributions and provides the numerical evaluation of the theoretical and practical objective performance measures discussed in the thesis. The best solution was then to organize the work in the form of Graphical User Interfaces (GUIs) in order to permit an extremely easy supervising of the input parameters, a flexible management of the investigated applications, a fine display of the obtained results and easy extensions for future development of this first version of the realized toolbox.

1.3 Principal contributions of the thesis

The work presented in this dissertation contains the following original contributions to the research field of time-frequency signal processing

1. Derived from the original Cheriet-Belouchrani distribution (CB TFD) based on the kernel with compact support (KCS) developed in [44], the first scientific contribution consists of designing a new high-resolution quadratic time-frequency distribution referred to as the SCB TFD for Separable Cheriet-Belouchrani TFD using a separable version of the compact support kernel referred to as SKCS (Chapter 3),

2. Building of a second new high-resolution quadratic time-frequency distribution referred to as the PCB TFD for Polynomial Cheriet-Belouchrani TFD implemented following the same procedure as for the CB TFD [45] and the SCB TFD using a

new kernel of compact support nature of polynomial form called PKCS (Chapter 3),

3. Derivation of the necessary conditions that must be verified by a given distribution in order to satisfy the classical mathematical properties in the $t - f$ plane with the attention focused on the KCS kernels and elaboration of a comparative study between the three investigated KCS-TFDs and the best-known quadratic distributions (Chapter 3),

4. Objective evaluation of the CB TFD, the SCB TFD and the PCB TFD performances together with the most used time-frequency representations using concentration-based theoretical measures (Chapter 4),

5. Optimization of the CB TFD, the SCB TFD and the PCB TFD based on the concentration criterion defined in (4) and comparison of their performance to the most known TFDs using several tests on real-life and multicomponent frequency modulated (FM) signals (Chapter 4),

6. Objective assessment of the KCS-based TFDs and the well-known TFDs based on the Boashash-Sucic normalized instantaneous resolution performance measure (Chapter 4),

7. Optimization and automatic selection of the optimal representation using the Boashash-Sucic methodology from a set of TFDs containing the CB TFD, the SCB TFD and the PCB TFD in addition to the classical best-known distributions and considering a large variety of test signals (Chapter 4),

8. Definition of a new quantitative criterion for objective assessment of kernel-based time-frequency distributions that consists of evaluating the numerical complexity of the kernel so that the selection of the best performing representation takes into consideration on one hand high resolution, concentration and interference rejection measured through the use of the Boashash-Sucic method and, on the other hand, the lowest required computational cost of the distribution (Chapter 5),

9. Implementation of the work presented in Chapters three, four and five through a Matlab toolbox referred to as TFDOP for "Time-Frequency Distributions' Optimization" that permits easy setting of the required parameters for TFD computing, display and optimization and also a fine visualization of the obtained results related to the different tests discussed in the thesis (Appendix A).

1.4 Scope of the thesis

The remainder of the thesis is organized as follows

Chapter 2 constitutes a theoretical review of the most important concepts related to time-frequency signal analysis such as short-time Fourier transform (STFT), window

functions, time-frequency localization, time-frequency resolution, analytic signal and instantaneous frequency (IF) with special attention to the Cohen's class of TFDs. In this chapter we analyze also the kernel effects on the whole performance of quadratic TFDs particularly the crossterms problem generated in the case of multicomponent signals.

Chapter 3 details the design procedure of the new proposed bilinear distributions based on compact support kernels that are derived from the Gaussian kernel. It also explains the building steps of the KCS kernel and its modified version referred to as the separable KCS (SKCS) as well as the polynomial KCS (PKCS). The chapter provides some illustrative examples presenting the time-frequency plots produced by the KCS-based distributions. Then, we discuss the suitable mathematical properties in the time-frequency domain and the relative condition that the kernel must verify in order to satisfy each property. This has led to perform a comparative study between the well known TFDs and the KCS-based ones and also to show the relationship between the interference suppression and the number of good classical properties. In addition, we present in this chapter the desirable characteristics of quadratic TFDs when practical time-frequency signal analysis is intended.

Chapter 4 describes the optimization criteria used to objectively assess the quadratic time-frequency distributions namely the autoterms' concentration, the components' resolution and the interference reduction. This had led to introduce several theoretical measures based on concentration criterion together with the recently developed Boashash-Sucic's normalized instantaneous resolution performance measure that allows to provide the optimal TFD using a specific methodology. Extensive illustrative tests on real-life and synthetic signals including the noise effects are presented and discussed in details. The performance of the KCS TFDs is compared to the best classical bilinear distributions and the obtained optimization results are recorded in tables and commented with determination of the main drawbacks of each objective measure.

Chapter 5 provides a new objective criterion for objective assessment of kernel-based quadratic TFDs that consists of evaluating the computational cost of the kernel whose parameters are optimized using the Boashash-Sucic performance measure. The TFDs based on compact support kernels are compared to the best known kernel-based distributions in the literature through several tests on real-life and synthetic multicomponent signals including noise and kernel length effects.

Finally, the thesis is concluded by **Chapter 6** that provides the main conclusions of this research and the recommendations and guidelines for future work.

Appendix A includes a detailed user help explaining the different operations and callback routines executed by each user interface control object contained in the TFDOP software package.

Chapter 2

Time-Frequency Analysis Basics

In this chapter, we review the most used analysis tools of nonstationary signals based on joint representations in time and in frequency. After presenting the general concepts, we identify the suitable properties for elaboration of a time-frequency analysis and its inevitable limitations. In particular, we study in depth the well-known time-frequency distributions of quadratic class. Illustrative examples are provided in order to check the effects of smoothing parameters, if they exist, on the energy estimation of multicomponent nonstationary signals as well as the drawbacks of each representation.

2.1 Introduction

We have seen in Chapter 1 that the classical signal analysis tools based on time domain and frequency domain representations cannot provide simultaneous time and frequency localization and hence they are not useful for analyzing time-variant, nonstationary signals. Consequently, the definition of the frequency variation with respect to time passes necessarily by a joint time-frequency representation. The latter has also many advantages compared to the classical methods such as the determination of the components that the signal contains, the identification of the time durations and the frequency bands and the extraction of the instantaneous frequency laws. The common basic principle of these representations is to combine traditional Fourier transform signal spectrum information with a time location variable. Such a signal operation constitutes an example of a mixed-domain signal transform [5].

2.2 Short-time Fourier transform (STFT)

A natural approach to the construction of a time-frequency representation is to multiply the signal, segmented into narrow time intervals so that it can be considered as stationary, by a window function $h(t)$ centered about the analysis time t and then applying the Fourier transform to each signal segment until the window reaches the end of the signal. This method is known as the short-time Fourier transform (STFT).

2.2.1 Definition

The STFT with respect to $h(t)$, also known as the windowed Fourier transform, is defined as the Fourier transform of the product $x(\tau)h(t-\tau)$ [3]-[5]

$$STFT_x^h(t,f) = \int_{-\infty}^{+\infty} x(\tau)h^*(t-\tau)e^{-j2\pi f\tau}d\tau \tag{2.1}$$

where the asterisk denotes complex conjugation.

Thus, the STFT can be viewed as simply a local spectrum of the signal $x(\tau)$ sliding over the entire signal duration thanks to the short time analysis window $h^*(t-\tau)$ that suppresses the signal outside a neighborhood around the analysis time point $\tau = t$.

If, in particular, the window $h(t)$ is Gaussian of the following general form

$$h(t) = \frac{1}{\sqrt{2\pi}\,\sigma}\, e^{(-t^2/(2\sigma^2))} \tag{2.2}$$

then, the STFT of $x(t)$ with respect to $h(t)$ is precisely the Gabor transform of $x(t)$ using the Gaussian $h(t)$ [5]. The positive parameter $A = 1/(\sqrt{2\pi}\,\sigma)$ is the peak of the Gaussian and $\sigma > 0$ controls the width of the bell curve.

The dual representation of the windowed Fourier transform is obtained by considering the signal and window spectra [4, 54]

$$STFT_x^h(t,f) = \int_{-\infty}^{+\infty} X(\eta)H^*(\eta-f)e^{j2\pi(\eta-f)t}d\eta \tag{2.3}$$

where X and H are respectively the Fourier transforms of x and h. This makes the STFT appears as a result of passing the signal through a continuous bank of band-pass filters with constant bandwidth [54, 55].

2.2.2 Time-frequency localization

The goodness of the time-frequency localization is directly related to the temporal resolution defined as the ability to distinguish between two successive events and the frequency resolution that expresses the ability to differentiate between two sinusoids with close frequencies [5].

Although the STFT provides some information about both when and at what frequencies a signal event occurs, we can only obtain this information with limited precision that is linked to the type and the size of the analysis window : The drawback is that once a specific window duration $\triangle t_h$ is chosen, it is fixed for all signal segments and hence for all frequencies.

Mathematically speaking, the time resolution of the STFT can be obtained by considering for x a Dirac impulse [55]

$$x(t) = \delta(t - t_0) \;\text{ then }\; STFT_x^h(t, f) = e^{-j2\pi t_0 f} h(t - t_0)$$

Thus, the time resolution of the STFT is proportional to the effective duration $\triangle t_h$ of the analysis window h. Similarly, by considering a Dirac impluse in the frequency domain (i.e. $x(t) = e^{j2\pi f_0 t}$), and referring to (2.3) ; the frequency resolution is obtained [55]

$$X(f) = \delta(f - f_0) \;\text{ then }\; STFT_x^h(t, f) = e^{-j2\pi t f_0} H(f - f_0)$$

The frequency resolution of the STFT is then proportional to the effective bandwidth $\triangle f_h$ of the window h. As a result, a tradoff always exists between time and frequency resolutions since we cannot design simultaneously a short window $h(t)$ and a narrow-band filter $H(f)$. This is known as the Heisenberg-Gabor uncertainty principle.

2.2.3 Uncertainty principle

The Heisenberg-Gabor uncertainty principle [22, 56], also known as the Heisenberg-Gabor inequality, states that the product of the time duration $\triangle t$ and the bandwidth $\triangle f$ is lower bounded [4]

$$\triangle t \triangle f \geq \frac{1}{4\pi} \tag{2.4}$$

This fundamental concept means that a waveform cannot simultaneously have an arbitrary small duration and an arbitrary small bandwidth : As a signal becomes more concentrated about its time-domain center, it becomes more dispersed about its frequency domain center [5]. For the STFT, the use of too short analysis window yields to perfect time localization/bad frequency localization and the converse is true (Table 2.1). This is in fact one of the fundamental practical arguments against the use of the STFT and its squared modulus, the spectrogram (see Sec. 2.3.2).

TABLE 2.1 – The two extreme cases of time and frequency localization for the STFT.

$h(t) = \delta(t) \rightarrow STFT_x^h(t,f) = x(t)e^{-j2\pi ft}$	$H(f) = \delta(f) \rightarrow STFT_x^h(t,f) = X(f)$
Perfect time localization	Perfect frequency localization
No frequency localization	No time localization

An illustrative example concerns a quadratic chirp signal (Fig. 2.1) whose name is a reference to chirping in analogy to the sound made by birds. Fig. 2.2 displays the modulus of the STFT of a wave containing four repetitions of this signal, each one starting from $f = 500$ Hz and ending by $f = 3500$ Hz during a time interval $\triangle t = 0.1$ sec. Different analysis windows are used with length $L = 64$ and 128, respectively.

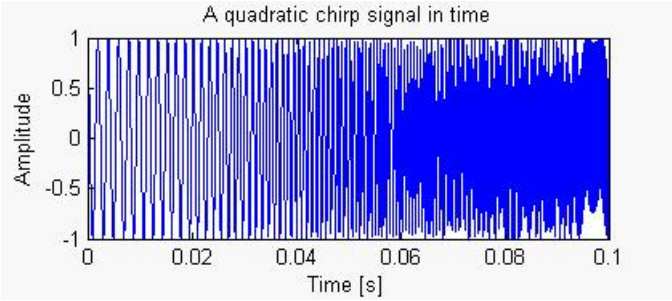

FIGURE 2.1 – The time-domain properties of a quadratic chirp with frequency range $f = 500 - 3500$ Hz and time extend $\triangle t = 0.1$ sec.

We see that for $L = 64$, a good time resolution is achieved since the STFT can localize the time separation between two different events (i.e. two different quadratic chirps) while the frequency resolution is bad. The opposite situation is seen when $L = 128$: The STFT localizes, as expected, the frequency start at around 500 Hz and the frequency end at 3500Hz of each chirp while the time localization is degraded. Moreover, the interference terms are best reduced using respectively the Blackman and Hanning windows compared to the Hamming window function that generates more important sidelobes in the frequency domain but still achieve in this case the best time-frequency resolution.

2.3 Quadratic time-frequency distributions

As seen in Sec. 2.2, the first intuitive solution to build a joint time and frequency representation is to enter the signal $x(t)$ to the transform integral as a linear input in dependence on some adaptive window function. To overcome the drawbacks of such transforms, it is natural to look for another type of solutions based on a joint time and frequency energy density $\rho_x(t,f)$ such that [55]

$$E_x = \int_{-\infty}^{+\infty} \int_{-\infty}^{+\infty} \rho_x(t,f) dt df \tag{2.5}$$

where E_x is the energy of the signal x. This class of solutions is known as energy distributions, bilinear distributions or more commonly quadratic time-frequency distributions

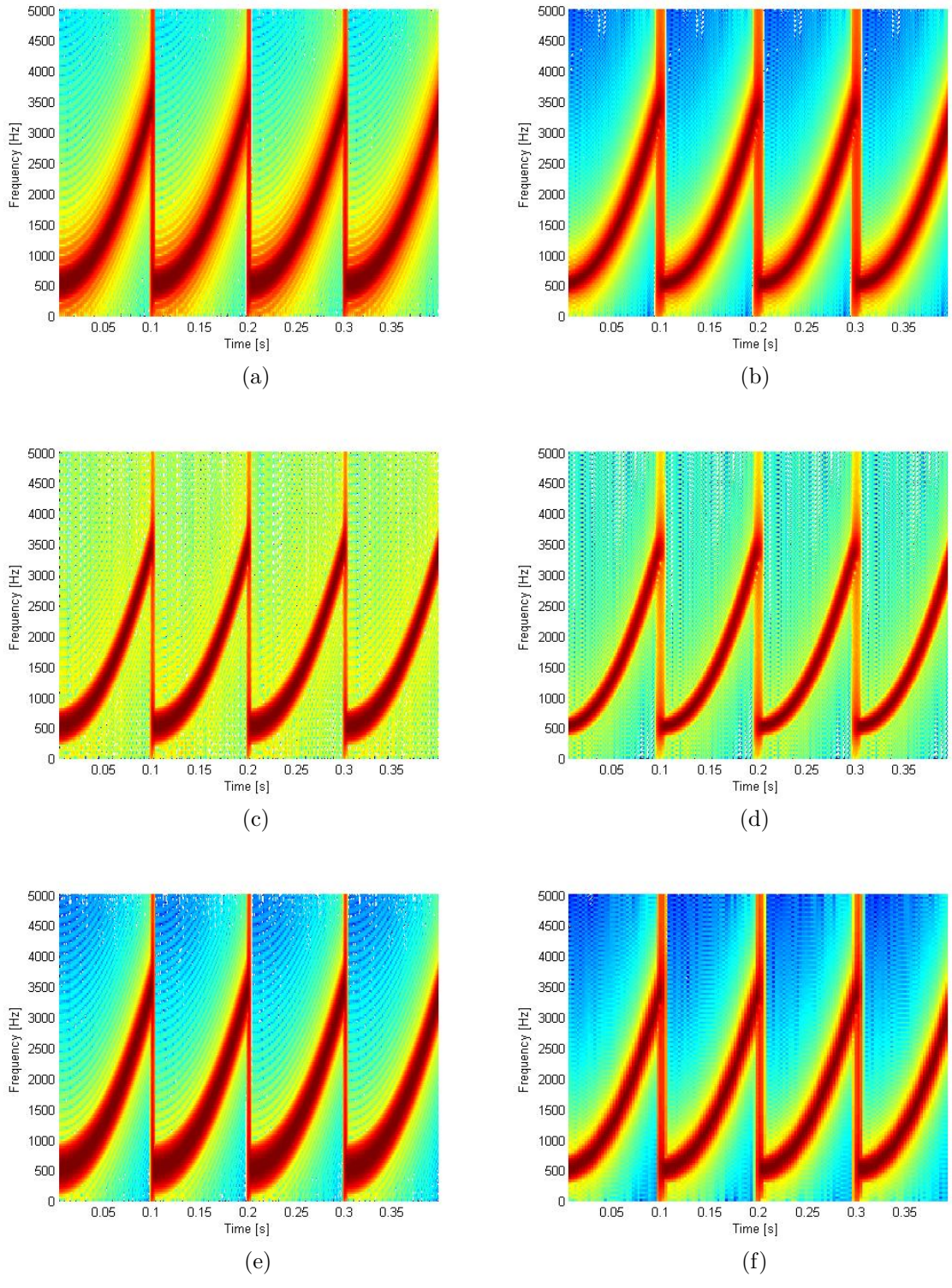

FIGURE 2.2 – The modulus of the STFT of a signal composed of four repetitions of a quadratic chirp varying from $f = 500$ Hz to $f = 3500$ Hz during 0.1 sec. (a) Hanning ($L = 64$), (b) Hanning ($L = 128$), (c) Hamming ($L = 64$), (d) Hamming ($L = 128$), (e) Blackman ($L = 64$)and (f) Blackman ($L = 128$).

[4, 54] since the signal $x(t)$ enters the representation integral as a quadratic rather than as a linear term. More precisely, the quadratic distribution is expressed as a function of the instantaneous autocorrelation $U_x(t,d) = x(t+d)x^*(t-d)$ of x expanded in various directions d around each point in the time domain. It results that, for any multicomponent signal $x(t)$ composed at least of two components $x_1(t)$ and $x_2(t)$, the induced distribution includes inevitably the cross product $x_1(t)x_2(t)$ that is considered as an interference term. This point constitutes the main disadvantage of time-frequency signal analysis using quadratic representations.

2.3.1 Wigner-Ville distribution (WVD)

2.3.1.1 Definition

The Wigner-Ville distribution (WVD) that dates to the early 1930s [6] is the oldest transform and the preeminent energy-based quadratic technique in the field of time-frequency signal analysis. It is defined as [3, 4, 54]

$$W_x(t,f) = \int_{-\infty}^{+\infty} x(t+\tau/2)x^*(t-\tau/2)e^{-j2\pi f\tau}d\tau \tag{2.6}$$

or equivalently as [4, 54]

$$W_x(t,f) = \int_{-\infty}^{+\infty} X(f+\eta/2)X^*(f-\eta/2)e^{j2\pi\eta t}d\eta \tag{2.7}$$

which corresponds to the Fourier transform of a product of the signal with its complex conjugate. This is similar to the power spectral density computation.

This distribution uses first a quadratic operation applied to the signal and then a linear transformation (Fourier transform) [54]. In its original form, the WVD does not introduce any windowing function for estimation of the instantaneous spectrum.

Fig. 2.3 shows the WVD plot of a linear chirp. We see that the distribution allows for this particular signal a perfect localization in both time and frequency which is one of a large number of desirable mathematical properties that makes the WVD a reference for the other quadratic distributions.

Here is a list of the main properties that the WVD satisfies

- Realness : $W_x(t,f) \in \Re, \quad \forall\, t, f$.
- Translation invariance : A time-shift (receptively a frequency shift) in the signal causes the same time shift (respectively the same frequency shift) in the WVD, i.e. $y(t) = x(t-t_0) \Rightarrow W_y(t,f) = W_x(t-t_0,f)$ and $y(t) = x(t)e^{j2\pi f_0 t} \Rightarrow W_y(t,f) = W_x(t,f-f_0)$.
- Dilations covariance : The WVD preserves dilations; i.e. for any $k > 0$, if $y(t) = \sqrt{k}\,x(kt)$ then $W_y(t,f) = W_x(kt, f/k)$.
- Energy conservation : By integrating the WVD over the entire time-frequency plane, the energy of x is obtained : $\int_{-\infty}^{+\infty}\int_{-\infty}^{+\infty} W_x(t,f)dtdf = E_x$.
- Marginal properties : Integration of the WVD over time (respectively over frequency) gives the energy spectral density (respectively the instantaneous power), i.e. $\int_{-\infty}^{+\infty} W_x(t,f)df = |x(t)|^2$ and $\int_{-\infty}^{+\infty} W_x(t,f)dt = |X(f)|^2$.

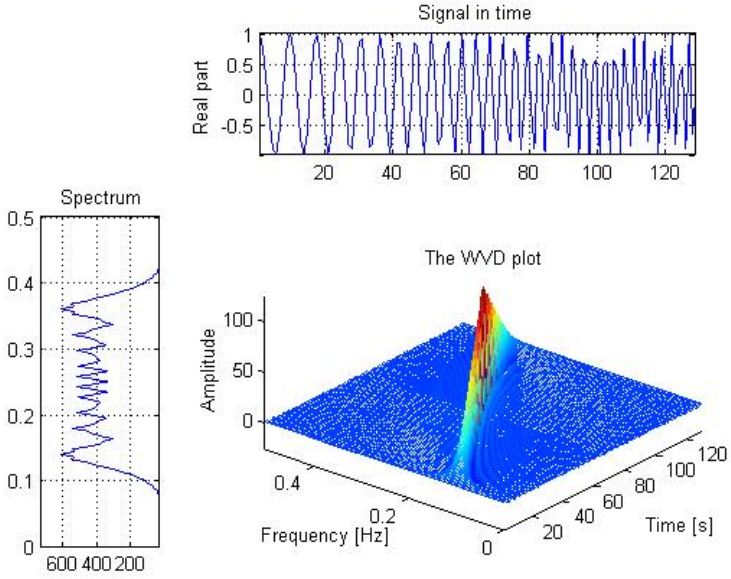

FIGURE 2.3 – Wigner-Ville distribution of a linear chirp.

- Wide-sense support conservation : The time support of W_x is limited by the duration of x and the frequency support of W_x is limited by the bandwidth of x ; that is, if $x(t) = 0$ for $|t| > T$ then $W_x(t, f) = 0$ for $|t| > T$ and if $X(f) = 0$ for $|f| > B$ then $W_x(t, f) = 0$ for $|f| > B$.
- Instantaneous frequency (IF) : The IF is given as the first moment of the WVD with respect to frequency : $\int_{-\infty}^{+\infty} f\ W_{x_a}(t, f)df / \int_{-\infty}^{+\infty} W_{x_a}(t, f)df = f_x(t)$, where x_a is the analytic signal associated to x (see Sec. 2.3.1.2).
- Group delay (GD) : The first moment of the WVD with respect to time is the GD, i.e. $\int_{-\infty}^{+\infty} t\, W_{x_a}(t, f)dt / \int_{-\infty}^{+\infty} W_{x_a}(t, f)\, dt = t_x(f)$.
- Compatibility with filterings : If y is the convolution of x and a filter h, then the WVD of y is the time-convolution between the WVD of h and the WVD of x : $y(t) = x(t) * h(t) = \int_{-\infty}^{+\infty} h(t-s)x(s)ds$ then $W_y(t, f) = \int_{-\infty}^{+\infty} W_h(t-s, f)W_x(s, f)ds$.
- Compatibility with modulations : In a dual manner, if y is the result of the modulation of x by a function m, the WVD of y is the frequency-convolution between the WVD of x and the WVD of m, i.e. $y(t) = m(t)\, x(t) \Rightarrow W_y(t, f) = \int_{-\infty}^{+\infty} W_m(t, f - \eta)W_x(t, \eta)d\eta$.
- Unitarity : This property means that the WVD preserves inner products $\int \int_{-\infty}^{+\infty} W_x(t, f)\, W_y^*(t, f)dtdf = \left| \int_{-\infty}^{+\infty} x(t)\, y^*(t)dt \right|^2$.
- Perfect localization on linear chirp signals (see Fig. 2.3).

However, due to its quadratic nature, the use of the Wigner-Ville representation is severely affected by the interference terms also called the crossterms or the artifacts.

2.3.1.2 Crossterm problem

Let $s(t) = s_1(t) + s_2(t)$ be a two-component nonstationary signal. Its WVD is thus given by

$$W_s(t,f) = W_{s_1}(t,f) + W_{s_2}(t,f) + W_{s_1,s_2}(t,f) \tag{2.8}$$

where

$$W_{s_1,s_2}(t,f) = \int_{-\infty}^{+\infty} s_1(t+\tau/2)s_2^*(t-\tau/2)e^{-j2\pi f\tau}d\tau + \int_{-\infty}^{+\infty} s_2(t+\tau/2)s_1^*(t-\tau/2)e^{-j2\pi f\tau}d\tau \tag{2.9}$$

is the term representing the interferences. The second integral in (2.9) can be rewritten as follows

$$\begin{aligned}\int_{-\infty}^{+\infty} s_2(t+\tau/2)s_1^*(t-\tau/2)e^{-j2\pi f\tau}d\tau &= -\int_{+\infty}^{-\infty} s_1^*(t+\tau'/2)s_2(t-\tau'/2)e^{+j2\pi f\tau'}d\tau' \\ &= \left(\int_{-\infty}^{+\infty} s_1(t+\tau/2)s_2^*(t-\tau/2)e^{-j2\pi f\tau}d\tau\right)^*\end{aligned}$$

Since for any complex number C we have $C + C^* = 2Re(C)$, then

$$W_s(t,f) = W_{s_1}(t,f) + W_{s_2}(t,f) + 2Re\left(\int_{-\infty}^{+\infty} s_1(t+\tau/2)s_2^*(t-\tau/2)e^{-j2\pi f\tau}d\tau\right). \tag{2.10}$$

The implied crossterms often scrambles the readability of a time-frequency diagram [54], especially if the components are numerous or close to each other, and the more so in the presence of noise [4]. Figs. 2.4-2.5 illustrate such situations that correspond to two multicomponent signals : The first one is composed of two non-parallel, non-intersecting linear chirps while the second signal contains two Gaussian atoms. We see that the interference terms lie between the two signal autoterms and take the form of oscillating contributions located at their geometrical midpoint. The crossterms oscillation takes place orthogonal to the line connecting the two signal terms with a frequency proportional to the distance between the two components [54]. Furthermore, in both figures, it seems to exist three components rather than two. This is because the extra crossterm components have large oscillating amplitudes that alternate in sign as we move parallel to the autoterms in the (t,f) domain. This is a characteristic feature of the crossterms [4]. It is important to note that, for a nonlinear frequency modulation, the WVD gives rise itself to an interference structure, called inner interference [54] which further complicates the use of the basic Wigner-Ville distribution in practical applications.

In the field of TFSA, it is befitting, in the most cases, to design representations that suppress the best the crossterms in order to provide the most accurate energy estimation of the time-varying spectra. For the WVD, the first solution was to consider an analytic signal in its definition. In fact, this form of signals is practically desirable for any time-frequency representation since the complex-valued analytic signal $x_a(t)$ has by definition no negative-frequency components. Consequently, the bandwidth is reduced to the half compared to the real signal $x(t)$ which means that the number of components in the time-frequency plane is also reduced to the half and then the spectral aliasing does not take place in the useful spectral domain of $x_a(t)$ [55]. This also allows a significant decrease of

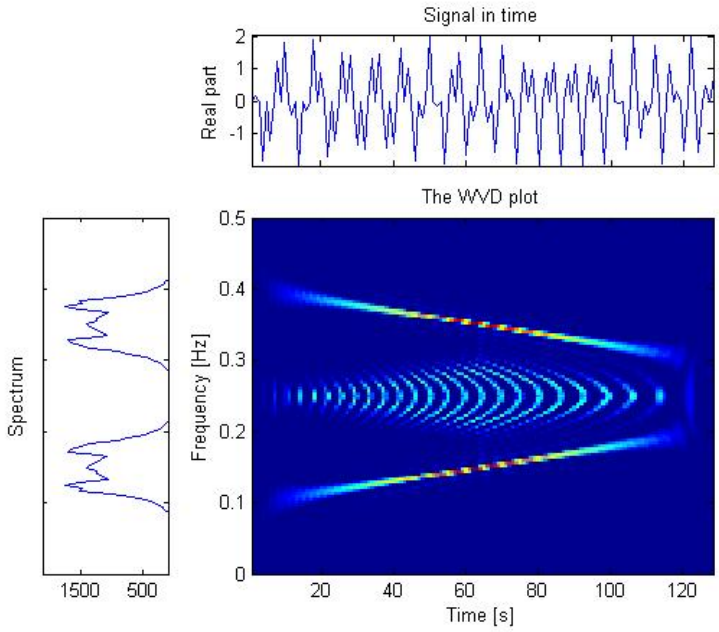

FIGURE 2.4 – The crossterms' structure of the Wigner-Ville distribution between two non-parallel, non-intersecting linear chirps occupying the frequency ranges $f = [0.1 - 0.2]$ Hz and $f = [0.4 - 0.3]$ Hz, respectively.

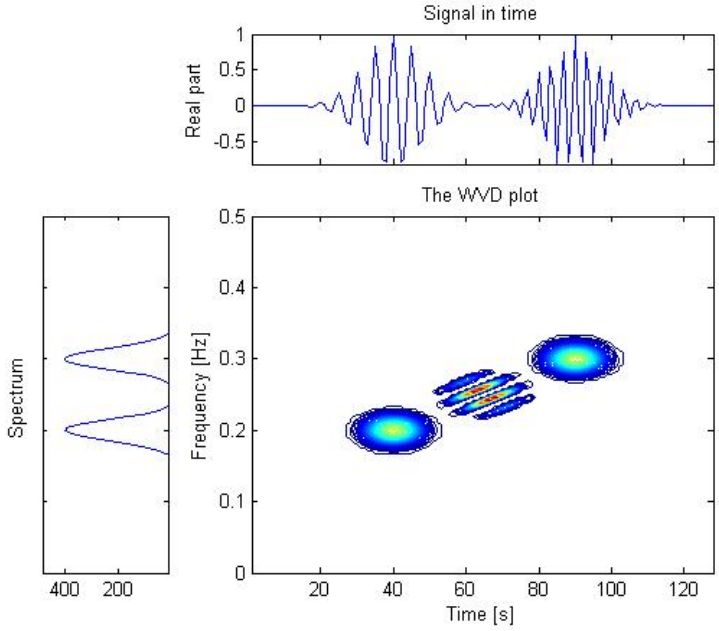

FIGURE 2.5 – The crossterms' structure of the Wigner-Ville distribution related to a signal composed of two Gaussian atoms.

the interference terms by suppressing the interacting terms between negative- and positive-frequency components.

The Fourier transform of the analytic signal $x_a(t)$ is defined as follows

$$\begin{aligned} X_a(f) &\stackrel{\triangle}{=} \begin{cases} 2X(f), & \text{for } f > 0 \\ X(f), & \text{for } f = 0 \\ 0, & \text{for } f < 0 \end{cases} \\ &= X(f)\, 2U(f) \end{aligned} \tag{2.11}$$

where $X(f)$ is the Fourier transform of the real-valued signal $x(t)$ and $U(f)$ is a unit step function. The operation is reversible due to the Hermitian property of the Fourier transform ($X(-f) = X^*(f)$). The complex analytic signal is expressed as

$$\begin{aligned} x_a(t) &= TF^{-1}\{X(f)\} * TF^{-1}\{2U(f)\} \\ &= x(t) * \left[\delta(t) + j\frac{1}{\pi t}\right] \\ &= x(t) + j\left[x(t) * \frac{1}{\pi t}\right] = x(t) + j\hat{x}(t) \end{aligned} \tag{2.12}$$

where $\hat{x}(t)$ is the Hilbert transform of $x(t)$.

Recall that based on the analytic signal $x_a(t)$, it is possible to define in a unique manner the concept of the instantaneous amplitude (or the signal's envelope) as

$$a_x(t) \stackrel{\triangle}{=} |x_a(t)| \tag{2.13}$$

and the instantaneous frequency as

$$f_x(t) \stackrel{\triangle}{=} \frac{1}{2\pi}\frac{d}{dt} arg(x_a(t)) \tag{2.14}$$

It is important to note that, from the definitions, the instantaneous frequency and its dual concept in the time domain, the group delay, are especially useful to represent mono-component nonstationary signals but are not sufficient to represent multicomponent signals.

2.3.2 Spectrogram

2.3.2.1 Definition

In contrast to the WVD, the spectrogram defined as the magnitude squared of the short-time Fourier transform [23]-[25]

$$S_x^h(t,f) = \left| \int_{-\infty}^{+\infty} x(\tau) h^*(t-\tau) e^{-j2\pi f\tau} d\tau \right|^2 \tag{2.15}$$

combines a linear operation (Fourier transform of the weighted signal) with a quadratic operation (modulus squared). In spite of these differences, we can still bring both representations closer together according to the Moyal's formula given by

$$\left| \int_{-\infty}^{+\infty} x(t)\, y^*(t) dt \right|^2 = \int_{-\infty}^{+\infty} \int_{-\infty}^{+\infty} W_x(t,f)\, W_y^*(t,f)\, dt\, df \tag{2.16}$$

The spectrogram can thus be expressed as follows [4, 54, 55]

$$S_x^h(t,f) = \int_{-\infty}^{+\infty} \int_{-\infty}^{+\infty} W_x(s,\eta)\, W_h(s-t,\eta-f)\, ds\, d\eta \tag{2.17}$$

2.3.2.2 Properties

The different view of the spectrogram given by (2.17) as a coupled smoothing of the WVD provides us with another interpretation of the tradeoff between the time and frequency resolutions of the spectrogram : If we choose a short window h, the smoothing function will be narrow in time and wide in frequency, leading to a good time resolution but bad frequency resolution ; and vice-versa [55] (Fig. 2.6).

As every quadratic distribution, the spectrogram presents interference terms as seen in the following equation

$$S_s^h(t,f) = S_{s_1}^h(t,f) + S_{s_2}^h(t,f) + 2Re\left(S_{s_1,s_2}^h(t,f)\right),\ s(t) = s_1(t) + s_2(t) \tag{2.18}$$

The third term describes the induced crossterms. It can be easily shown that

$$S_{s_1,s_2}^h(t,f) = STFT_{s_1}^h(t,f)\,(STFT_{s_2}^h(t,f))^* \tag{2.19}$$

However, one can show [58] that these interference terms are restricted to those regions of the time-frequency plane where the auto-spectrograms overlap : As the components s_1 and s_2 are sufficiently distant from each other, as the crossterms are considerably attenuated and approach zero. This principal advantage of the spectrogram is a consequence of its poor resolution. Fig. 2.7 shows an illustrative example. Here, the selection of a wide analysis window ($L = 145$) is justified by the fact that there is no time resolution while the frequency resolution is very important.

Note that if we multiply the WVD by the spectrogram, we obtain the so-called masked WVD [59]. This results on cleaner time-frequency diagrams that gather the advantages of the high resolution of the WVD and the better crossterm suppression of the spectrogram. However, the computational cost is considerably increased.

2.3.3 Smoothed-Pseudo Wigner-Ville distribution (SPWVD)

As we have seen in Sec. 2.3.2, since the spectrogram employs a unique analysis window ; its use as a coupled smoothing of the WVD faces a major drawback related to the Heisenberg-Gabor restrictions. Consequently, it is more intuitive to apply a separable, independent smoothing in time and frequency which yields an improvement over the spectrogram. The corresponding representation is called smoothed pseudo-Wigner-Ville distribution (SPWVD) [60] and has the form [54]

$$SPW_x(t,f) = \int_{-\infty}^{+\infty} h(\tau) \left[\int_{-\infty}^{+\infty} g(s-t)x(s+\tau/2)x^*(s-\tau/2)ds\right] e^{-j2\pi f\tau} d\tau \tag{2.20}$$

where the windows g and H (the Fourier transform of h) control the smoothing in time and in frequency, respectively.

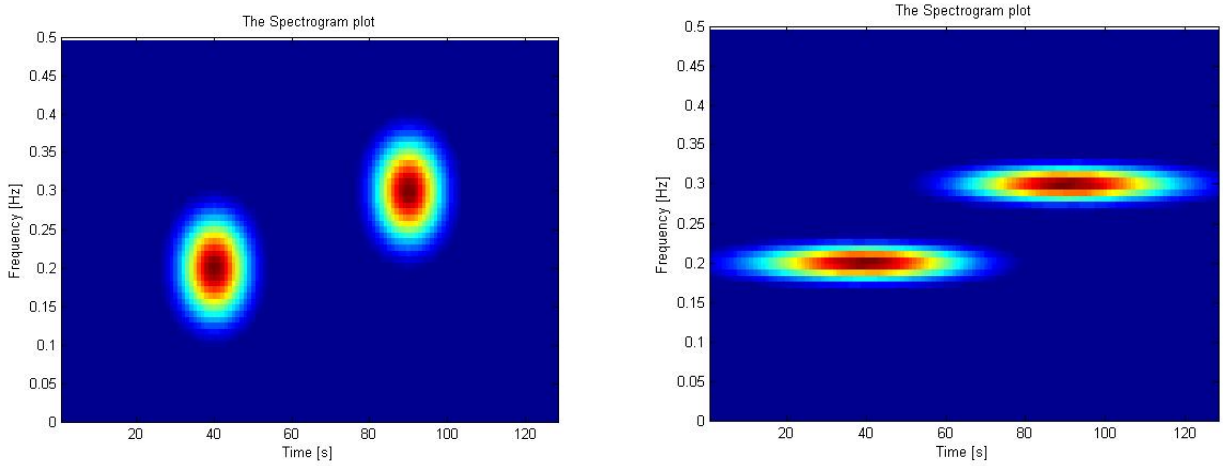

(a) (b)

FIGURE 2.6 – Spectrogram of two gaussian atoms using : (a) a short Hamming window of length L=15 (good time resolution/bad frequency resolution) and (b) a large Hamming window of length L=105 (good frequency resolution/bad time resolution).

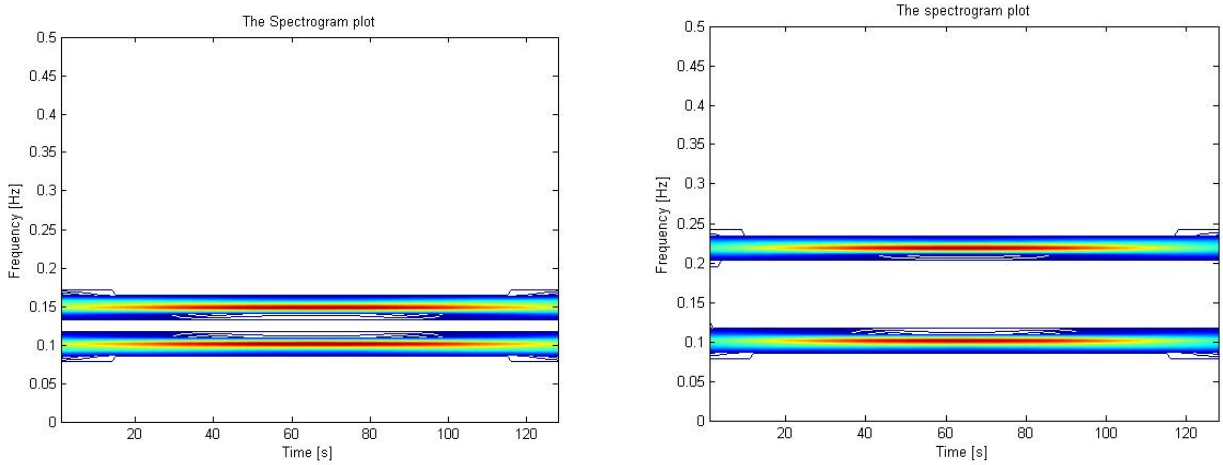

(a) (b)

FIGURE 2.7 – Relationship between the distance separating two pure frequencies and the structure of the crossterms generated by the spectrogram (Hanning, L=145) : (a) close components/high interference and (b) distant components/reduced interference.

Note that if we only consider a smoothing in frequency, i.e. $g(t) = \delta(t)$, the pseudo-WVD (PWVD) is obtained

$$PW_x(t,f) = \int_{-\infty}^{+\infty} h(\tau)x(t+\tau/2)x^*(t-\tau/2)e^{-j2\pi f\tau}d\tau \tag{2.21}$$

Let us check the effect of the separable smoothing on the signals considered in Figs. 2.4-2.5. For the two non-parallel, non-intersecting linear chirps ; it is obvious that the time resolution is not the most important here. Hence, an introduction of a frequency smoothing carried out by the analysis window h results on considerable suppression of the crossterms (Fig. 2.8). The same notable improvement in the time-frequency readability is provided by the SPWVD for the two Gaussian atoms (Fig. 2.9). We see that in both cases the smoothing done by the SPWVD almost completely suppress the crossterms, but the signal components localization becomes coarser. This is because the smoothing in time (respectively in frequency) degrades the time resolution (the frequency resolution, respectively). Another major drawback is the necessity to select carefully two analysis windows rather than a single one for the spectrogram, which complicates the research of the optimal setting.

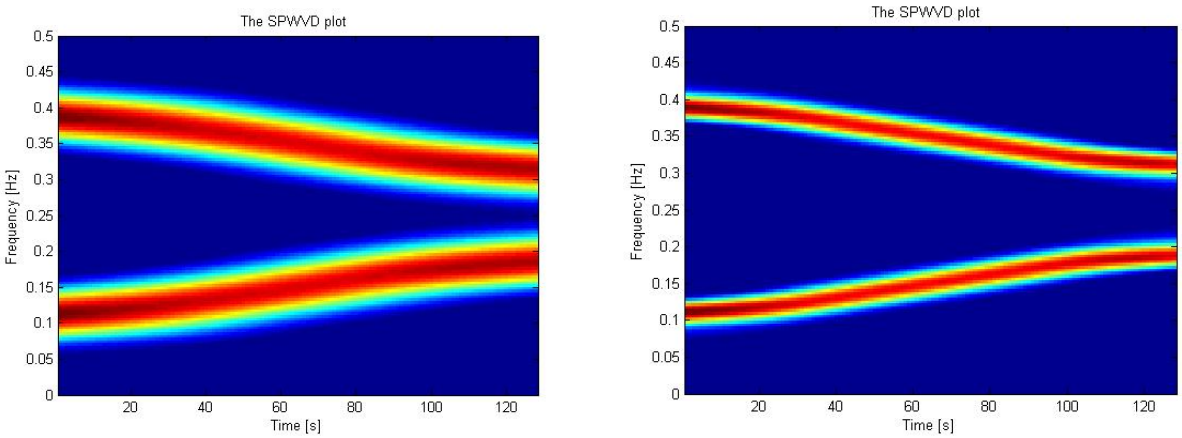

(a) (b)

FIGURE 2.8 – Effects of the separable smoothing performed by the SPWVD on interference suppression and time-frequency localization of the signal considered in Fig. 2.4 : (a) g (Hamming, L=95) ; h (Hamming, L=15)and (b) g (Hamming, L=55) ; h (Hamming, L=33).

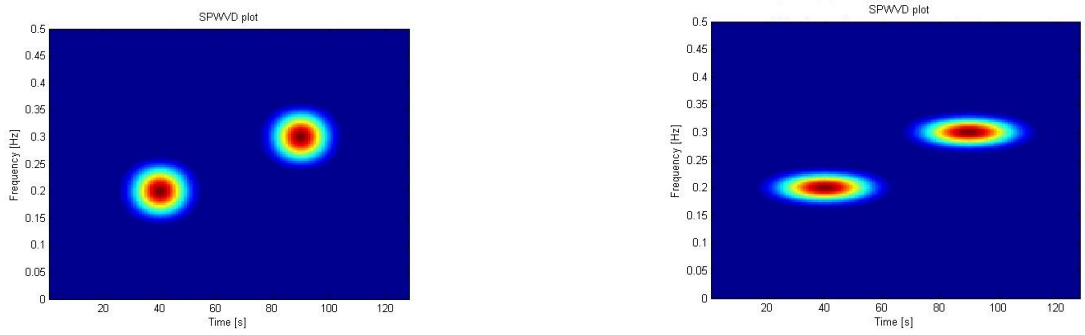

(a) (b)

FIGURE 2.9 – Effects of the separable smoothing performed by the SPWVD on interference suppression and time-frequency localization of two Gaussian atoms : (a) g, h (Hanning, L=15) and (b) g, h (Hanning, L=55).

2.3.4 Kernel-based distributions : The Cohen's class

2.3.4.1 Definition

The Cohen's class, also known in the literature as kernel-based transform, is defined as each class of energy time-frequency distributions verifying two important desirable properties namely time and frequency covariance and possesses the following general expression [4, 5, 10, 28, 54, 57]

$$TFD_x(t,f) = \int\int\int_{-\infty}^{+\infty} e^{j2\pi\eta(s-t)}\phi(\eta,\tau)x(s+\tau/2)x^*(s-\tau/2)e^{-j2\pi f\tau}d\eta ds d\tau \quad (2.22)$$

where $\phi(\eta,\tau)$ is a two dimensional function called the parameterization function or the TFD kernel that can be thought of as smoothing the interference; t and τ denote the time domain variables while f and η are the frequency domain variables. This class of distributions could also be written as follows

$$TFD_x(t,f) = \int_{-\infty}^{+\infty}\int_{-\infty}^{+\infty} J(s-t,\tau)x(s+\tau/2)x^*(s-\tau/2)e^{-j2\pi f\tau}ds d\tau \quad (2.23)$$

where

$$J(s',\tau) = \int_{-\infty}^{+\infty}\phi(\eta,\tau)e^{j2\pi\eta s'}d\eta \quad (2.24)$$

The advantage of expression (2.23) is to simplify the TFD computation and the proofs of the mathematical properties by reducing the number of integrals in particular when (2.24) has a known analytic form. Equivalently, one can use the time-lag kernel notation $G(t,\tau)$ expressed as the Fourier transform of the Doppler-lag kernel $\phi(\eta,\tau)$ with respect to η, i.e.

$$G(t,\tau) = J(-t,\tau) = \int_{-\infty}^{+\infty}\phi(\eta,\tau)e^{-j2\pi\eta t}d\eta; \quad (2.25)$$

so that the general class of quadratic TFDs can be defined in terms of the signal and the time-lag domain kernel as follows

$$TFD_x(t,f) = \int_{-\infty}^{+\infty}\int_{-\infty}^{+\infty} G(t-s,\tau)x(s+\tau/2)x^*(s-\tau/2)e^{-j2\pi f\tau}dsd\tau \tag{2.26}$$

Moreover, if we denote by $C_{Gx}(t,\tau)$ the convolution of the instantaneous autocorrelation function $U_x(t,\tau) = x(t+\tau/2)x^*(t-\tau/2)$ of x with the kernel $G(t,\tau)$, i.e.

$$C_{Gx}(t,\tau) = \int_{-\infty}^{+\infty} U_x(s,\tau)G(t-s,\tau)ds = \int_{-\infty}^{+\infty} x(s+\tau/2)x^*(s-\tau/2)G(t-s,\tau)ds \tag{2.27}$$

then any TFD of Cohen's class can be expressed as the Fourier transform of $C_{Gx}(t,\tau)$ with respect to τ.

2.3.4.2 Kernel effects

One interesting reformulation of (2.22) is given as follows [4, 5, 54, 55]

$$TFD_x(t,f) = \int_{-\infty}^{+\infty}\int_{-\infty}^{+\infty} \Pi(s-t,\eta-f)W_x(s,\eta)dsd\eta \tag{2.28}$$

where

$$\Pi(t,f) = \int_{-\infty}^{+\infty}\int_{-\infty}^{+\infty} \phi(\eta,\tau)e^{-j2\pi(f\tau+\eta t)}d\eta d\tau \tag{2.29}$$

is the time-frequency kernel [4] expressed as the two-dimensional Fourier transform of the Doppler-lag kernel $\phi(\eta,\tau)$ or equivalently as the Fourier transform of the time-lag kernel $G(t,\tau)$ with respect to τ. Thus, it appears that all TFDs of Cohen's class can be thought as simply smoothed versions of the WVD. Furthermore, since the kernel is a decreasing function, its principal effect is to considerably attenuate the artifacts generated by the WVD.

In fact, using Fourier transforms from lag to frequency and from time to Doppler (frequency shift), the quadratic TFDs and their kernels related by (2.22) can be formulated in four different but dependent two-dimensional domains namely the time-lag, the time-frequency, the Doppler-lag and the Doppler-frequency domains [4]. In particular, the Doppler-lag (η,τ) domain leads to the definition of the so-called narrow-band ambiguity function, noted AF, and clarifies the principal kernel effect as an arbitrary smoothing function performing a filtering. This gives [3, 4, 5, 10, 54, 55]

$$TFD_x(t,f) = \int_{-\infty}^{+\infty}\int_{-\infty}^{+\infty} \phi(\eta,\tau)A_x(\eta,\tau)e^{-j2\pi(f\tau+\eta t)}d\eta d\tau \tag{2.30}$$

where

$$A_x(\eta,\tau) = \int_{-\infty}^{+\infty} x(s+\tau/2)x^*(s-\tau/2)e^{-j2\pi\eta s}ds \tag{2.31}$$

is the symmetric ambiguity function that measures the correlation of a signal x with its translations in the time-frequency plane. The variables η and τ are relative coordinates or shifts called, respectively, Doppler and delay [3, 4]. Note that this function is of particular interest in the field of radar signal processing [55].

From (2.30)-(2.31), we conclude the following

1. The ambiguity function is also a quadratic time-frequency representation,
2. The AF is the dual of the WVD in the sense of the Fourier transform [4, 54]

$$A_x(\eta,\tau) = \int_{-\infty}^{+\infty}\int_{-\infty}^{+\infty} W_x(t,f)e^{j2\pi(f\tau-\eta t)}dtdf \tag{2.32}$$

   Consequently, it satisfies nearly all the mathematical properties of the WVD [55],
3. Since the AF's autoterms are located at the origin of the Doppler-delay plane while the AF's crossterms are located away from the origin (Fig. 2.10), the Doppler-lag kernel $\phi(\eta,\tau)$ is viewed as a weighting function or a 2D low-pass filter around the origin that tries to maintain the signal terms unchanged and reject the interference terms [55]. However, this smoothing operation results on a loss in the time-frequency resolution,
4. The WVD and the spectrogram are both distributions of Cohen's class corresponding, respectively, to the kernels $\phi_{WV}(\eta,\tau) = 1$ (or $G_{WV}(t,\tau) = \delta(t)$) and $\phi_S(\eta,\tau) = A_{\underset{h}{*}}(\eta,\tau)$; the ambiguity function of the window h.

Expressions (2.26), (2.28) and (2.30) show that the design of a Cohen's class quadratic TFD is reduced to the kernel design in different domains.

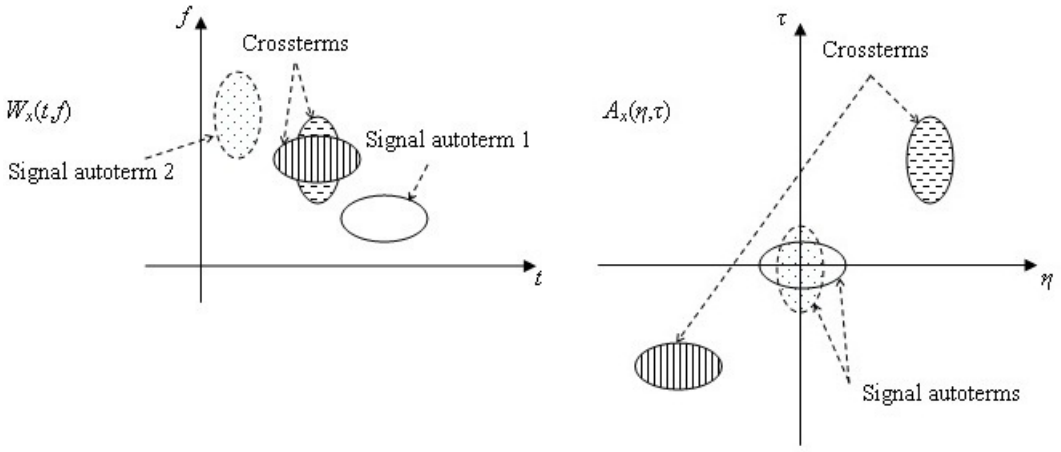

(a) (b)

FIGURE 2.10 – Signal autoterms and interference terms location : (a) the time-frequency domain (the WVD) and (b) the Doppler-lag domain (the ambiguity function).

Based on (2.28)-(2.29), many types of joint smoothing can be introduced so as to preserve some of the desirable mathematical properties satisfied by the WVD and reduce the interference terms as well. A simple way to achieve this double objective is to impose the following special form [4, 54]

$$\phi(\eta,\tau) = \varphi(\eta\tau) \tag{2.33}$$

where φ is a decreasing function such that $\varphi(0) = 1$. Consequently, ϕ acts as a low-pass filter, and according to (2.28), this form of kernels attenuates the artifacts generated by the Wigner-Ville distribution. That is why the corresponding time-frequency distributions are called Reduced Interference Distributions (RIDs) [61]. Note that the kernels in (2.33) satisfy the marginal properties and display a cross-like shape : The cross sections for $\eta = 0$ and $\tau = 0$ are constant, while the other contourlines ($\eta\tau = \text{const}$) form a set of hyperbolas [54]. The best-known distributions that belong to the RID category are presented below.

2.3.4.3 Born-Jordan distribution (BJD)

One of the first RIDs was the Born-Jordan distribution (BJD) [30]. Its kernel is given in the Doppler-lag domain by the cardinal sine function so that

$$\phi_{BJ}(\eta, \tau) = \frac{\sin(\pi\eta\tau)}{\pi\eta\tau} \tag{2.34}$$

which defines the BJD

$$BJ_x(t, f) = \int_{-\infty}^{+\infty} \frac{1}{|\tau|} \left[\int_{t-|\tau|/2}^{t+|\tau|/2} x(s + \tau/2)x^*(s - \tau/2)\, ds \right] e^{-j2\pi f\tau}\, d\tau \tag{2.35}$$

As the WVD, the Born-Jordan distribution does not contain any smoothing parameter and thus it cannot be optimized. Fig. 2.11 shows the performance of the BJD in estimating the energy of a signal composed of two distant Gaussian atoms and a second one defined as a sum of two non-parallel non-intersecting linear FMs. We see that, in Fig. 2.11.a, the distribution provides a good concentration of the signal autoterms and suppresses almost the entire interference terms generated by the WVD (Fig. 2.5) thanks to the successful low-pass filtering performed by the BJ kernel. Fig. 2.11.b shows, however, the generation of high oscillating positive and negative croosterms that occur in a region of the $t - f$ plane where we expect no energy at all and hence provide extra terms that scramble the readability of the induced distribution.

2.3.4.4 Choi-Willams distribution (CWD)

Choi and Williams [27] defined φ as a two-dimensional Gaussian function yielding to the following product kernel

$$\phi_{CW}(\eta, \tau) = e^{-\frac{(\pi\eta\tau)^2}{2\sigma^2}} \tag{2.36}$$

where σ is a free smoothing parameter that controls the spread of the Gaussian in the Doppler-lag domain and also the quantity of interference suppression in the $t - f$ plane. Fig. 2.12 shows the two-dimensional profile of the CW kernel in the ambiguity domain with parameter values : (a) $\sigma = 0.05$, (b) $\sigma = 1$ and (c) $\sigma = 50$. We see that as smaller values of σ are used as the reduction of the interference size is expected to be better. Inversely, when σ^2 tends to infinity, the WVD is obtained ($\phi_{CW}(\eta, \tau) \to 1$).

The Choi-Willams distribution, noted CWD, has the following form

$$CW_x(t, f) = \sqrt{\frac{2}{\pi}} \int_{-\infty}^{+\infty} \int_{-\infty}^{+\infty} \frac{\sigma}{|\tau|} e^{-2\sigma^2(s-t)^2/\tau^2} x(s + \tau/2)x^*(s - \tau/2)\, e^{-j2\pi f\tau}\, ds\, d\tau \tag{2.37}$$

where the quantity

$$G_{CW}(t,\tau) = \sqrt{\frac{2}{\pi}}\frac{\sigma}{|\tau|}e^{-2\sigma^2 t^2/\tau^2} \tag{2.38}$$

presents the CW time-lag kernel.

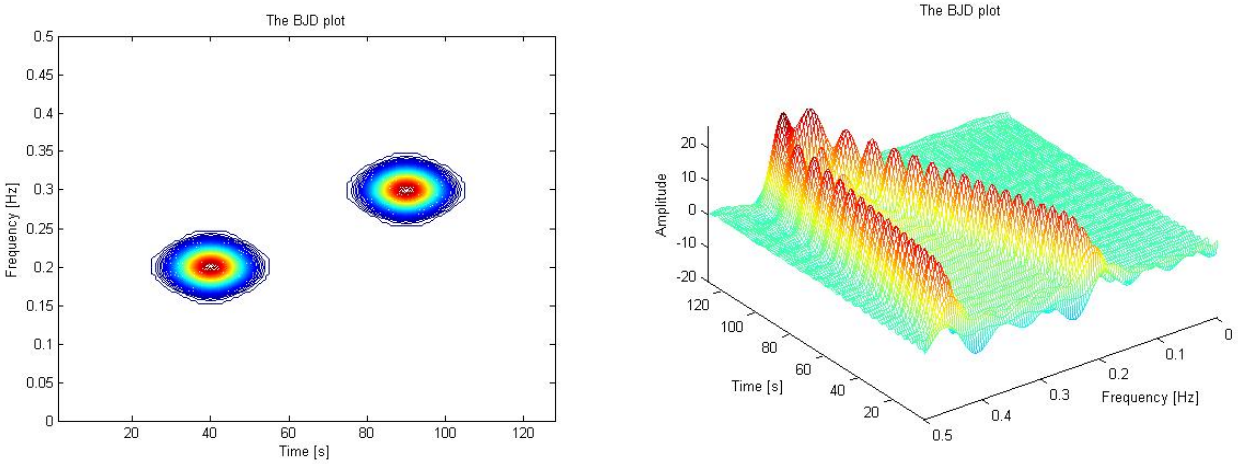

(a) (b)

FIGURE 2.11 – Effects of the nature of the analyzed signal on the performance of the Born-Jordan distribution : (a) Two distant atoms and (b) sum of two non-parallel non-intersecting linear FMs with frequency ranges $f = 0.2 - 0.35$ Hz and $f = 0.45 - 0.4$ Hz, respectively.

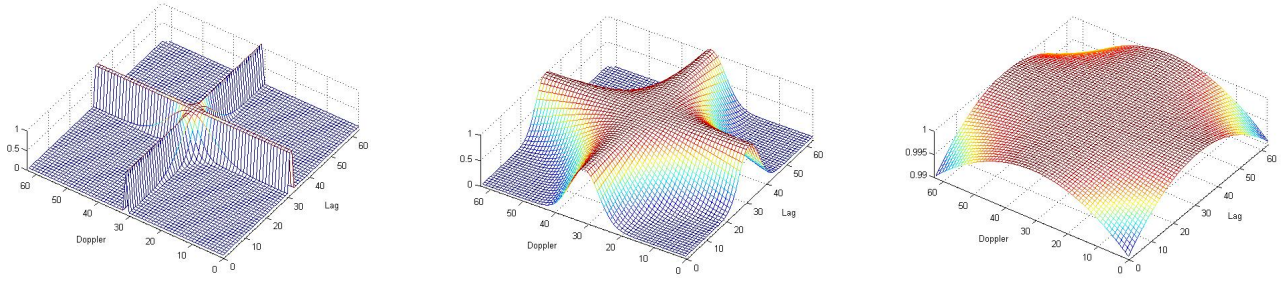

(a) (b) (c)

FIGURE 2.12 – The two-dimensional profile of the CW kernel in the Doppler-lag domain. (a) $\sigma = 0.05$, (b) $\sigma = 1$ and (c) $\sigma = 50$.

Fig. 2.13 shows the interference structure of a signal composed of a constant frequency component and a linear chirp using (a) $\sigma = 4$ and (b) $\sigma = 0.9$. We see that the crossterms oscillate in the time-direction, with registration of high oscillating interference terms over the entire frequency support around the time instant $t = 0$. Moreover, a better reduction of the interference terms is obtained using a smaller smoothing parameter ($\sigma = 0.9$).

A second crossterms' feature is shown in Fig. 2.14 that displays the CWD of a signal composed of two Gaussian atoms that have the same time or frequency support. We see

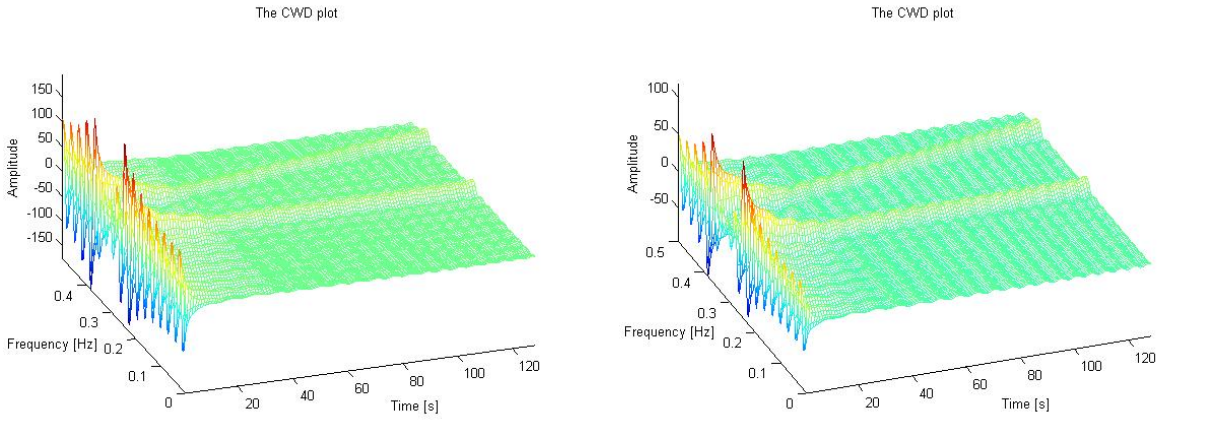

(a) (b)

FIGURE 2.13 – The CWD's interference structure between a constant frequency component ($f = 0.25$ Hz) and a linear chirp with frequency range $f = 0.35 - 0.45$ Hz using : (a) $\sigma = 4$ and (b) $\sigma = 0.9$.

that the CW TFD is enable to suppress the crossterms between two components that are synchronized in time (Fig. 2.14.a) or located at the same frequency band (Fig. 2.14.b). In this case, the interference terms can be even greater than the autoterms which results on providing wrong information about the time-frequency characteristics of the signal components.

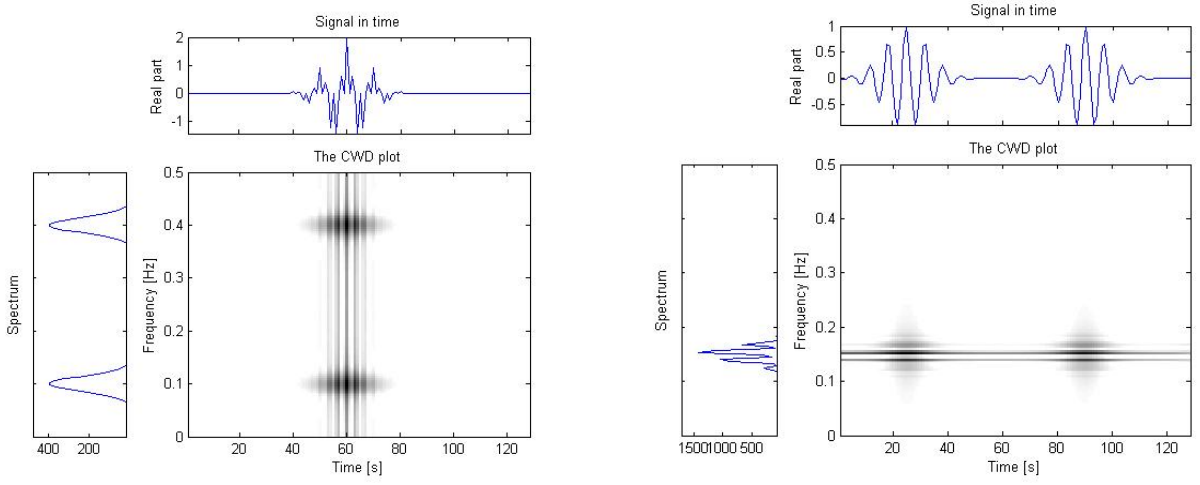

(a) (b)

FIGURE 2.14 – The interference terms generated by the CWD in the case of : (a) two Gaussian atoms synchronized in time ($\sigma = 0.7$) and (b) two Gaussian atoms that belong to the same frequency band ($\sigma = 2$).

2.3.4.5 Zhao-Atlas-Marks distribution (ZAMD)

Zhao, Atlas and Marks proposed in [31] a new cone-shaped time-frequency distribution referred to as the ZAMD. The ZAM kernel is defined in the time-lag domain as follows

$$G_{ZAM}(t,\tau) = \begin{cases} h(\tau) & \text{if } |\tau| \geq a|t| \\ 0 & \text{Otherwise} \end{cases} \tag{2.39}$$

where $h(\tau)$ is a window function and $a \geq 2$. The corresponding distribution is given by

$$ZAM_x(t,f) = \int_{-\infty}^{+\infty} h(\tau) \left[\int_{t-|\tau|/2}^{t+|\tau|/2} x(s+\tau/2)x^*(s-\tau/2)\, ds \right] e^{-j2\pi f\tau}\, d\tau \tag{2.40}$$

By comparing (2.35) to (2.40), we conclude that the ZAM TFD can be viewed as simply a generalized smoothed version of the BJD along the frequency axis. In fact, the Doppler-lag kernel filter of the ZAMD can be expressed as the inverse Fourier transform of $G_{ZAM}(t,\tau)$ with respect to time

$$\begin{aligned} \phi_{ZAM}(\eta,\tau) &= \int_t G_{ZAM}(t,\tau)e^{j2\pi\eta t}dt; \;\; |t| \leq |\tau|/a \\ &= h(\tau)\int_{-|\tau|/a}^{|\tau|/a} e^{j2\pi\eta t}dt = h(\tau)\frac{\sin\left(\frac{2\pi}{a}\eta|\tau|\right)}{\pi\eta} \end{aligned} \tag{2.41}$$

The sinc function in (2.41) generates sidelobes in the ambiguity domain which reduces the ability of the ZAM distribution in suppressing the interference terms. Furthermore, for $h(\tau) = 1/|\tau|$ and $a = 2$ we get

$$\phi_{ZAM}(\eta,\tau) = \text{sinc}(\pi\eta\tau). \tag{2.42}$$

the BJ kernel.

For example, if we take $h(\tau) = 1$ and $a = 2$; the expression of the ZAM kernel in the Doppler-lag domain is

$$\phi_{ZAM}(\eta,\tau) = \text{sinc}(\pi\eta\tau)\ \tau \tag{2.43}$$

The corresponding time-lag domain kernel is plotted in Fig. 2.15.

Fig. 2.16 shows the ZAMD plot of the same signal considered in Fig. 2.13 while Fig. 2.17 displays the ZAM TFD of a signal composed of two distant Gaussian atoms. The frequency smoothing is performed by a Gaussian analysis window $h(\tau) = e^{-\tau^2/2\sigma^2}$, the default window used for the ZAM kernel in the thesis, with a control parameter $\sigma = 0.07$ and $\sigma = 0.3$, respectively. Compared to the CW TFD, we see a better concentration of the autoterms. The interference terms, however, generate the biggest negative amplitudes in the close neighborhood of the autoterms; i.e. just outside the frequency bandwidth of each signal component.

As we move away from the interacting components, the crossterms' energy decreases considerably and can be further reduced through an appropriate tuning of the smoothing parameter σ. As for the CWD, the ZAM distribution depends strongly on the nature of the analyzed signal. On the other hand, the extra terms generated by this TFD can be more important than the signal true autoterms which results on wrong extraction of the time-frequency features of the analyzed signal (see Sec. 5.3.1).

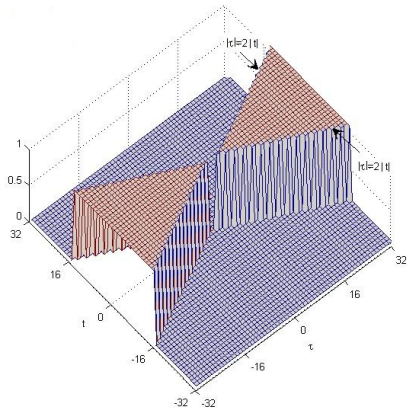

FIGURE 2.15 – The time-lag domain ZAM kernel with parameters $h(\tau) = 1$ and $a = 2$.

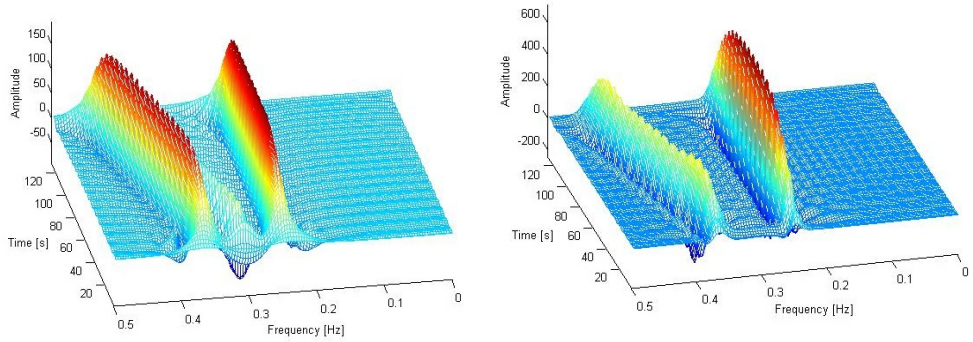

(a) (b)

FIGURE 2.16 – The ZAMD' interference structure of the signal considered in Fig. 2.13 using a Gaussian smoothing window : (a) $\sigma = 0.07$ and (b) $\sigma = 0.3$.

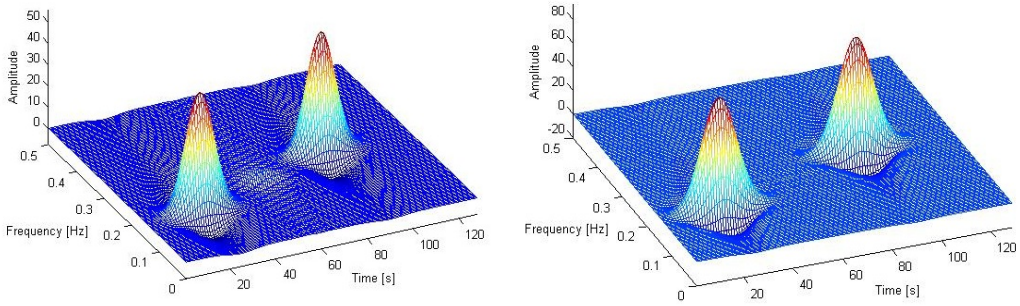

(a) (b)

FIGURE 2.17 – The interference terms generated by the ZAMD of a signal composed of two distant Gaussian atoms using a Gaussian smoothing window : (a) $\sigma = 0.07$ and (b) $\sigma = 0.3$.

2.4 Conclusion

Among the various representations that provide simultaneous information in both time and frequency domains, the quadratic time-frequency representations are recognized by their efficiency in analysis and interpretation of nonstationary signals. In particular, those distributions that belong to the Cohen's class ; i.e. all quadratic TFDs that are covariant by shifts in time and frequency, offer a wide set of powerful tools to extract the most important characteristics of multicomponent signals thanks to the various structures that the kernel can generate allowing interference mitigation by introducing a smoothing in time and/or frequency. However, two consequences are inevitable : 1) a decrease in time and frequency resolutions and 2) a loss of theoretical properties (see Sec. 3.7).

On the other hand, due to the various crossterm geometries that a quadratic distribution can induce, it is always suitable to have several kernels in our hand since each one is well adapted to a certain kind of signals. Moreover, the combination of different distributions offers in general complementary descriptions of the time-varying frequency components. Chapter 3 presents a new type of kernels with compact support (KCS) and details the design procedure of their respective quadratic distributions in addition to their mathematical properties.

Chapter 3

High-Resolution Time-Frequency Distributions based on Kernels with Compact Support : Building and Mathematical Properties

In this chapter, we explain how the new proposed KCS-based TFDs are built. This includes a review on the design and characteristics of the kernels with compact support as well as the general procedure used to generate their respective TFDs. Some examples related to nonstationary signal representation in the time-frequency domain are provided. Next, we review the classical mathematical properties suitable for quadratic TFDs. For each property, the relative condition that must be satisfied by the kernel is derived. The compact support kernels are analyzed and their mathematical properties are compared to the best-known kernels. Then, we present a set of desirable properties of quadratic time-frequency representations when practical applications are intended.

3.1 Introduction

It is known in the art that the use of a quadratic class of distributions permits the definition of kernels whose main property is to reduce the interference patterns induced by the distribution itself. The Gaussian kernel for example presents many desirable properties but it must be truncated to a finite window when implemented in a computer because of its infinite support. Regardless of the size of the window, a discontinuity will be introduced at its borders that could lead to serious errors in the derivatives [62]. As a result, the use of the Gaussian kernel presents two practical limitations : information loss and derivative border effects owing to diminished accuracy, and the prohibitive processing time due to the mask size [63].

In order to avoid these drawbacks, two approaches exist : approximating the Gaussian kernel by a finite support kernel, or defining new kernels with properties close to the Gaussian. In [44], it was shown that kernels with compact support (KCS), derived from the Gaussian kernel, allow a tradeoff between a good autoterm resolution and a high crossterm rejection. They are found to recover information loss and improve processing time and, at the same time, retain the most important properties of the Gaussian kernel [64]. These features are achieved thanks to the compact support analytical property of this type of kernels since they vanish themselves outside a given compact set.

Motivated by these interesting properties, we propose the use of two new time-lag domain kernels with compact support derived from the Gaussian for time-frequency analysis namely the separable KCS (SKCS) [65] and the polynomial KCS (PKCS) [63]. Similarly to the CB TFD [45], the induced TFDs referred to as SCB TFD and PCB TFD, respectively, are generated following the general form of kernel-based TFDs defined by (2.26). Then, the mathematical properties of these three TFDs are analyzed and compared to the best known quadratic distributions.

3.2 Construction of the KCS

Practically speaking, the convolution product with a Gaussian requires an approximation of the latter over a bounded set of $\Re^2$, commonly known as a mask [64]. The accuracy of the computation depends on the mask size. Wider masks provide more precise calculations, but increase the cost of processing time ; smaller masks sizes decrease the processing time, but the accuracy is sometimes severely diminished, which results on information loss. Among the solutions proposed to overcome these drawbacks, we note the approximation of the Gaussian by recursive filters [64, 66] or using truncated exponential functions instead of the Gaussian [66, 67]. The approximation solution, however, does not resolve the information loss problem.

The kernel with compact support was built from this standpoint so that there is no need to cut off the kernel while the processing time is controlled because the mask is the support of the kernel itself [64]. The new kernel is derived from the Gaussian kernel by transforming the $\Re^2$ space into a unit ball through a change of variables so that the Gaussian is defined on the unit ball and vanishes on the unit sphere. Then, the kernel is extended over all $\Re^2$ by taking zero values outside the unit ball to make the convolution

product possible [64].

Before detailing the KCS construction procedure, let us recall some necessary mathematical fundamentals about mollifiers and smooth functions theory.

3.2.1 Definition and construction of mollifiers

Mollifiers were first introduced by Kurt Otto Friedrichs [68]. They are smooth functions with special properties used for example in distribution theory to create smoothed functions approximating nonsmooth generalized functions via convolution. This operation is known as mollification [69].

Definition [69] : For each $\sigma > 0$, let $\varphi_\sigma \in C^\infty(\Re^N)$ [1] be given with the properties

1. $\varphi_\sigma \geq 0$,
2. supp $(\varphi_\sigma) \subset \{x \in \Re^N : |x| \leqslant \sigma\}$,
3. $\int\limits_{\Re^N} \varphi_\sigma(x)\, dx = 1$.

These functions are called mollifiers. Hence, the mollifier φ_σ is a test function, i.e. smooth function with compact support, nonnegative, infinitely differentiable, with a support decreasing as $\sigma \to 0$ but the volume under the graph is preserved [70]. As $\sigma \to 0$, these functions are concentrated at the origin. This is why mollifiers are also known as approximations of the delta function [69].

An interesting, simple and intuitive form of φ_σ is obtained by considering the function $\varphi(x)$ that vanishes on the unit ball, defined for any $x \in \Re^N$ as follows [70]

$$\varphi(x) = \begin{cases} c\, e^{-1/(1-|x|^2)} & \text{for } |x| < 1 \\ 0 & \text{Otherwise} \end{cases} \tag{3.1}$$

where c is chosen to ensure that the integral of φ is 1. $\varphi(x)$ is a test function on $\Re^N$, infinitely differentiable, positive and vanishes together with all its derivatives on $|x| \geq 1$ and can be used as the seeds from which an infinite variety of test functions φ_σ are constructed. The plot of $\varphi(x)$ for $N = 1$ is sketched in Fig. 3.1.

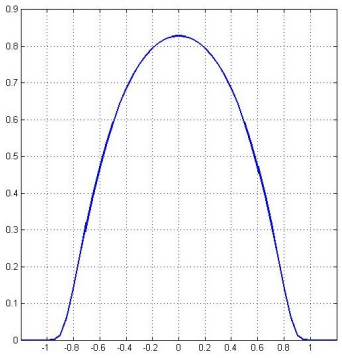

FIGURE 3.1 – The mollifier function.

1. The function f defined over $\Re^N$ is said to be of class C^k if the derivatives f', f'', ..., $f^{(k)}$ exist and are continuous (the continuity is implied by differentiability for all the derivatives except for $f^{(k)}$). The function f is said to be of class C^∞ over $\Re^N$, or smooth, if it has derivatives of all orders ; i.e. it is infinitely differentiable over $\Re^N$.

The family of smooth functions φ_σ based on φ is of the following form [70]

$$\varphi_\sigma(x) = \frac{1}{\sigma^N}\,\varphi_\sigma\left(\frac{x}{\sigma}\right),\ \sigma > 0 \tag{3.2}$$

verifying the properties [70]

1. $\varphi_\sigma \geq 0$, for all $x \in \Re^N$,
2. $\varphi_\sigma = 0$ for $|x| > \sigma \Rightarrow supp(\varphi_\sigma) \subset \left\{x \in \Re^N : |x| \leqslant \sigma\right\}$,
3. $\int\limits_{\Re^N} \varphi_\sigma(x)\,dx = 1$.

Hence, the functions φ_σ are mollifiers that become thinner and higher as σ tends to zero. However, the area under the graph is constantly equal to 1.

Since our kernel is defined in a plane (N=2), we have to consider a test function denoted by ρ satisfying the following requirements

- $\rho(x,y) \geq 0$, $\forall (x,y) \in \Re^2$,
- Its support is the unit ball in $\Re^2$, i.e. supp $(\rho) \subset \{(x,y) \in \Re^2 : x^2 + y^2 \leqslant 1\} = B(0,1)$ [2] ,
- $\int\limits_{\Re^2} \rho(x,y)\,dx\,dy = 1$.

from which we introduce for each $\sigma > 0$, the functions

$$\rho_\sigma(x,y) = \frac{1}{\sigma^2}\,\rho\left(\frac{x}{\sigma}, \frac{y}{\sigma}\right) \tag{3.3}$$

Then, from the development above, the family of functions ρ_σ is a mollifier verifying

- $\rho_\sigma(x,y) \geq 0$, for all $(x,y) \in \Re^2$,
- supp $(\rho_\sigma) \subset \{(x,y) \in \Re^2 : x^2 + y^2 \leqslant \sigma^2\} = B(0,\sigma)$,
- $\int\limits_{\Re^2} \rho_\sigma(x,y)\,dx\,dy = 1$.

3.2.2 Building the KCS using a mollifier-based approximation of the Gaussian

The building of kernels with compact support includes two main steps [64]
1) Formulation of a 2D one-parameter family of normalized symmetrical Gaussian [3] denoted by $g_\sigma(x,y)$ in the following manner :

In two dimensions, the power to which the exponential is raised in the Gaussian function is any negative-definite quadratic form. So, if we define $g(x,y)$ as

$$g(x,y) = \frac{1}{2\pi} e^{-(x^2+y^2)/2} \tag{3.4}$$

2. Let (M,d) be a metric space, namely a set M with a metric (distance function) d. The closed ball of radius $r > 0$ centered at a point p_0 in M, usually denoted by $B(p_0,r)$, is defined by $B(p_0,r) \triangleq \{p \in M : d(p,p_0) \leqslant r\}$. Considering the Euclidean distance over the Cartesian space $\Re^2$, the closed ball of radius r centered at $p_0(x_0,y_0)$ is the set $B(p_0,r) = \left\{p(x,y) \in \Re^2 : (x-x_0)^2 + (y-y_0)^2 \leqslant r^2\right\}$. The unit ball centered at the origin is a ball of radius 1 denoted by $B(0,1)$.

3. Symmetrical in order to be fully defined over $\Re^+$.

then

$$g_\sigma(x,y) = \frac{1}{\sigma^2} g\left(\frac{x}{\sigma}, \frac{y}{\sigma}\right) = \frac{1}{2\pi\sigma^2} e^{-(x^2+y^2)/2\sigma^2} \tag{3.5}$$

2) Application of a change of variables to g_σ so that it is approximated by a mollifier as defined in (3.3). Since the compact support of the mollifier ρ is limited to the unit ball, a polar change of coordinates is performed by the function

$$\Gamma(r,\theta) = (r\cos\theta, r\sin\theta),\ 0 \leq r < 1 \tag{3.6}$$

then, any approximation of the 2D normalized symmetrical Gaussian given by (3.5) must define a certain function $w(r)$ so that $\Gamma(w(r),\theta)$ transforms the unit ball $B(0,1)$ into an $\Re^2$ plane. The simplest way to transform the interval $[0,1[$ into $\Re^+$ is to consider the following function

$$f(z) = \frac{1}{1-z} - 1,\ 0 \leq z < 1 \tag{3.7}$$

so that when $z = 0$, $f(z) = 0$ and when $z \to 1^-$, $f(z) \to +\infty$. The f function values are only obtained after three operations. However, w should be in our case a function of r^2 in order to 1) obtain an expression comparable to that of the Gaussian and 2) facilitate the change of variables from polar to Cartesian coordinates and vice-versa. This justifies the following choice (even it is not unique) of the function w [64]

$$\begin{aligned} [0,1[&\longrightarrow \Re^+ \\ r &\longrightarrow w(r) = \sqrt{\frac{1}{1-r^2} - 1},\ 0 \leq r < 1 \end{aligned} \tag{3.8}$$

We see that for any $r \in [0,1[$ and $\theta \in \Re$ then

$$(x,y) = \Gamma(w(r),\theta) = (w(r)\cos\theta, w(r)\sin\theta) \in \Re^2 \tag{3.9}$$

so that

$$x^2 + y^2 = w^2(r) = \frac{1}{1-r^2} - 1 = -\left(\frac{1}{r^2-1} + 1\right),\ 0 \leq r < 1 \tag{3.10}$$

while the inverse of w transforms $\Re^+$ into $[0,1[$ in a continuous manner.

A final step is to exploit the parameter σ that controls the Gaussian's bandwidth to derive the KCS. Let $\gamma = 1/\sigma^2$ and then apply the change of variables given by (3.10) in the expression $(1/2\pi)\exp[-(\gamma/2)(x^2+y^2)]$ and extend it by zero outside the unit ball. After normalization [4], we obtained the desired KCS kernel [64]

$$\rho_\gamma(r,\theta) = \begin{cases} \dfrac{1}{C_\gamma} e^{\frac{1}{2}\left(\frac{\gamma}{r^2-1}+\gamma\right)} & \text{if } r^2 < 1 \\ 0 & \text{Elsewhere} \end{cases} \tag{3.11}$$

or, with the variables (x,y)

$$\rho_\gamma(x,y) = \begin{cases} \dfrac{1}{C_\gamma} e^{\frac{1}{2}\left(\frac{\gamma}{x^2+y^2-1}+\gamma\right)} & \text{if } x^2+y^2 < 1 \\ 0 & \text{Elsewhere} \end{cases} \tag{3.12}$$

4. In order to ensure that $\int_{\Re^2} \rho_\gamma(x,y)\,dx\,dy = 1$; the third property of a mollifier.

where

$$C_\gamma = \int_{-1}^{1}\int_{-1}^{1} e^{\frac{1}{2}\left(\frac{\gamma}{x^2+y^2-1}+\gamma\right)} 1_{B(0,1)}(x,y)\,dx\,dy \tag{3.13}$$

a normalization constant and

$$1_{B(0,1)}(x,y) = \begin{cases} 1 & \text{if } x^2+y^2<1 \\ 0 & \text{Elsewhere} \end{cases} \tag{3.14}$$

The function ρ_γ is infinitely differentiable, positive, vanishes outside the unit ball and verifies $\int\limits_{\Re^2} \rho_\gamma(x,y)\,dx\,dy = 1$.

Applied to time-frequency signal analysis, the compact support kernel has the following expression in the time-lag plane [44, 45]

$$G_{KCS}(t,\tau) = \begin{cases} e^{\frac{1}{2}\left(\frac{\gamma}{t^2+\tau^2-1}+\gamma\right)} & \text{if } t^2+\tau^2<1 \\ 0 & \text{Otherwise} \end{cases} \tag{3.15}$$

where γ is a parameter that controls the kernel's bandwidth as σ controls the width of the bell curve for the Gaussian kernel so that $\gamma = 1/\sigma^2$. Note that the KCS was found to keep the most important properties of the Gaussian function, in particular, when γ increases ; it was shown that the Heisenberg uncertainty product (H.u.p.) decreases very quickly and becomes close to $1/4\pi$ (Fig. 3.2), which is the optimal value reached by the Gaussian kernel [64].

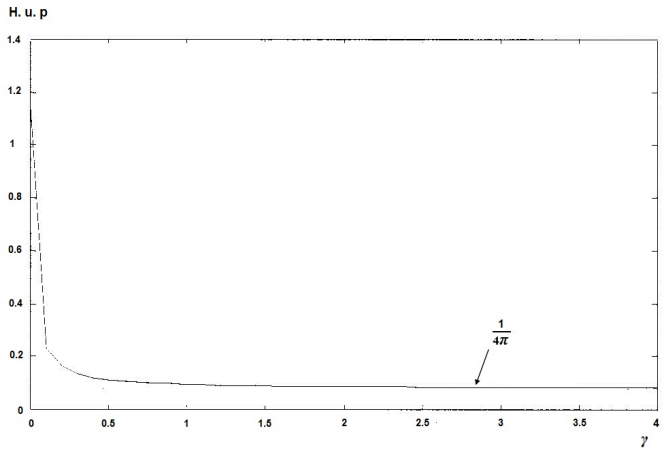

FIGURE 3.2 – Curve of the Heisenberg uncertainty product according to parameter γ [64].

Fig. 3.3 shows the plots of the KCS kernel in the time-lag domain for different values of the smoothing parameter γ while Fig. 3.4 displays the corresponding KCS profiles in the ambiguity domain. We see that the time-lag plot is a bell-shaped curve with respect to both time and delay whose spread in inversely related to γ. This is due to the fact that γ is set to $1/\sigma^2$ in the original approximation of the Gaussian function.

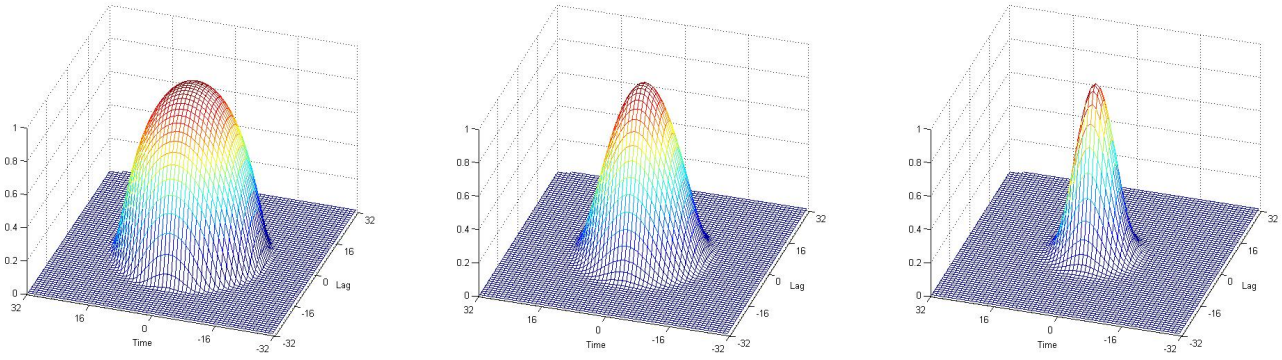

(a) (b) (c)

FIGURE 3.3 – The two-dimensional profile of the compact support kernel in the time-lag domain. (a) $\gamma = 0.8$, (b) $\gamma = 2.5$ and (c) $\gamma = 10$.

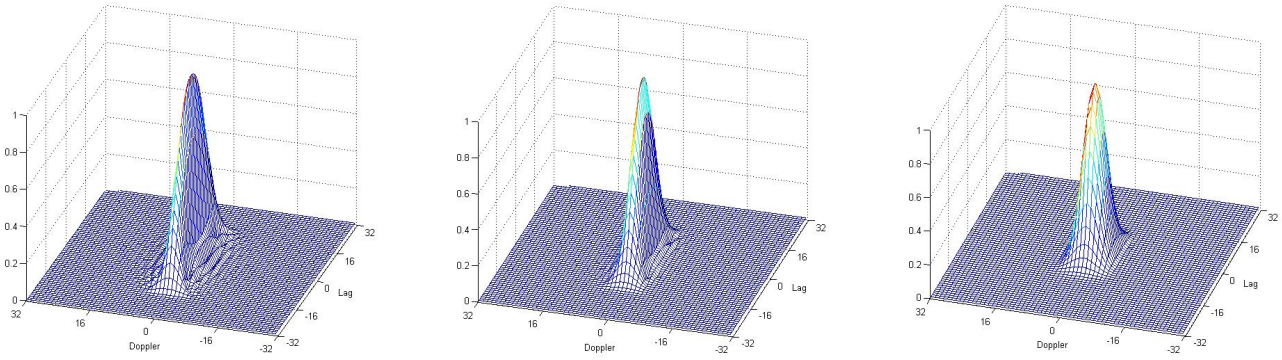

(a) (b) (c)

FIGURE 3.4 – The two-dimensional profile of the compact support kernel in the ambiguity domain normalized with respect to its peak located at the origin ($\eta = 0$, $\tau = 0$). (a) $\gamma = 0.8$, (b) $\gamma = 2.5$ and (c) $\gamma = 10$.

From time-frequency signal analysis point of view, the most important is that, thanks to the two-dimensional test function form of $G_{KCS}(t, \tau)$, no sidelobes are generated by its inverse Fourier transform with respect to t : The Doppler-lag kernel

$$\phi_{KCS}(\eta, \tau) = \int_{-\infty}^{+\infty} G_{KCS}(t, \tau) e^{j2\pi\eta t} dt \tag{3.16}$$

Consequently, due to its special compact support shape in both time-lag and ambiguity domains ; that is completely different from any previously proposed kernel form in the time-frequency analysis literature, the Doppler-lag KCS acts as a two-dimensional auto-windowed low-pass filter centered around the origin and, as a result, it shows a great ability of crossterms' suppression much better than the Gaussian kernel while preserving

the signal components yielding to a notable improvement of time-frequency resolution and energy concentration of the autoterms.

On the other hand, the Fourier transform of the time-lag compact support kernel with respect to τ is also sidelobe free and the corresponding time-frequency kernel defined by (2.29) acts as a 2D low-pass filter that smoothes the WVD in both time and frequency directions.

Another important point concerns the effect of increasing the kernel length L on the shape of the KCS in the ambiguity domain (Fig. 3.5). We see that as L increases, the Doppler-lag kernel becomes thinner and smoother and hence it is expected to improve the interference terms' elimination by suppressing the ripples about the IF laws and preserve much better the autoterms.

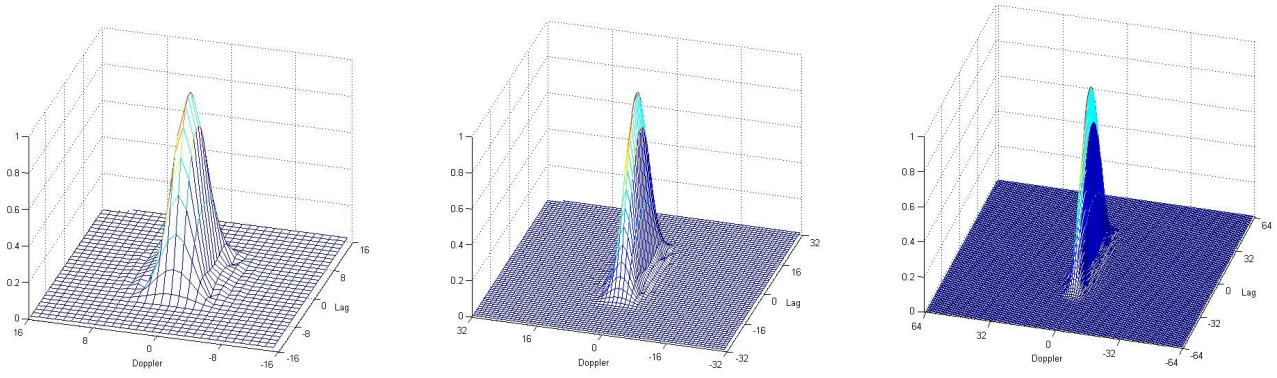

(a) (b) (c)

FIGURE 3.5 – The two-dimensional KCS profile in the ambiguity domain normalized with respect to its peak for a fixed bandwidth ($\gamma = 2.5$). (a) $L = 32$, (b) $L = 64$ and (c) $L = 128$.

3.3 Design procedure of the CB TFD

From the mollifier ρ_γ given by (3.12), we can define a family of KCS kernels $\rho_{\sigma,\gamma}$ so that [64]

$$\rho_{\sigma,\gamma}(x,y) = \frac{1}{\sigma^2}\,\rho_\gamma\left(\frac{x}{\sigma},\frac{y}{\sigma}\right) \tag{3.17}$$

which gives

$$\rho_{\sigma,\gamma}(x,y) = \begin{cases} \dfrac{1}{C_\gamma\,\sigma^2} e^{\frac{1}{2}\left(\frac{\gamma\,\sigma^2}{x^2+y^2-\sigma^2}+\gamma\right)} & \text{if } x^2+y^2<\sigma^2 \\ 0 & \text{elsewhere} \end{cases} \tag{3.18}$$

According to Sec. 3.2.2, $\rho_{\sigma,\gamma}$ is a family of mollifiers with support $B(0,\sigma)$. The Cheriet-Belouchrani (CB) kernel, also referred to as KCS, is then obtained by considering the time

and lag variables giving the following expression [45]

$$G_{CB}(t,\tau) = \begin{cases} e^{C\left(\frac{1}{\frac{t^2+\tau^2}{D^2}-1}+1\right)} & \text{if } \frac{t^2+\tau^2}{D^2} < 1 \\ 0 & \text{Otherwise} \end{cases} \tag{3.19}$$

where D is a predetermined parameter and C is a tuning positive real number that is inversely proportional to the kernel's bandwidth [5]. Note that, given the kernel length L, the range of variation of t and τ is within the interval $[0, D]$ with a step size $\triangle t = \triangle \tau = \frac{D}{(L/2)}$. Hence, the compact support kernels are evaluated at $(L/2)(L/2) = L^2/4$ points. The complete kernel form is simply obtained by symmetry.

The CB TFD is expressed as follows

$$CB_x(t,f) = \int_{-\infty}^{+\infty}\int_{-\infty}^{+\infty} G_{CB}(t-s,\tau)x(s+\tau/2)x^*(s-\tau/2)e^{-j2\pi f\tau}dsd\tau \tag{3.20}$$

By considering the compact support limits of the time-lag CB kernel we obtain

$$CB_z(t,f) = e^C \int_{-\infty}^{+\infty}\left[\int_{t-\sqrt{|D^2-\tau^2|}}^{t+\sqrt{|D^2-\tau^2|}} e^{\left\{\frac{C}{\frac{(t-s)^2+\tau^2}{D^2}-1}\right\}} z(s+\tau/2)z^*(s-\tau/2)ds\right] e^{-j2\pi f\tau}d\tau \tag{3.21}$$

where $z(t)$ denotes the analytic signal generated by applying the Hilbert transform to the real signal $x(t)$ for the reasons explained in Sec. 2.3.1.2. The convolutions of the compact support kernel $G_{CB}(t,\tau)$ and the instantaneous autocorrelation functions $U_z(t,\tau) = z(t+\tau/2)z^*(t-\tau/2)$ are computed and then a Fourier transform is applied to determine information related to the energy of the original signal with respect to time and frequency.

Fig. 3.6 displays the CB TFD plots of a Doppler signal while Fig. 3.7 shows the TF characteristics of a multicomponent signal composed of four closely spaced Gaussian atoms using a KCS of length 64 and different values of C with $D = 2.5$. We see that through a control of the kernel bandwidth, the obtained distribution allows a better localization of the signal components in the time-frequency plane, eliminates the energy of the interference terms due to the bilinearity of the distribution and hence results on high resolution in both time and frequency. Furthermore, compared to the plots of Fig. 2.14, the time-frequency diagrams of Fig. 3.7 show that, unlike the CWD that is defined from an exponential-based time-lag kernel ; the CB TFD is able to suppress the crossterms even if the Gaussian atoms are synchronized in time and/or located at the same frequency band.

3.4 Modification of the CB kernel : The separable CB (SCB) TFD

Recent results in the field of time-frequency signal analysis have shown that quadratic TFDs with separable kernels outperform many other popular TFDs in resolving closely

5. The bandwidth controller of the CB kernel is denoted here by C rather than γ so that it is not to be confused with the tuning parameter γ used to adjust the PCB kernel's bandwidth. The parameter D replaces σ that denotes the smoothing parameter of the Choi-Williams distribution.

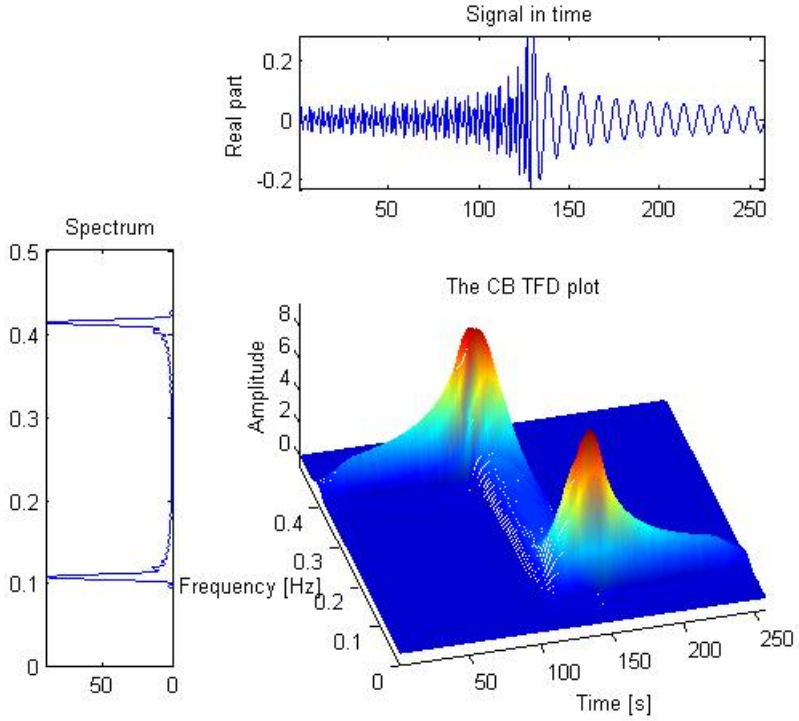

(a)

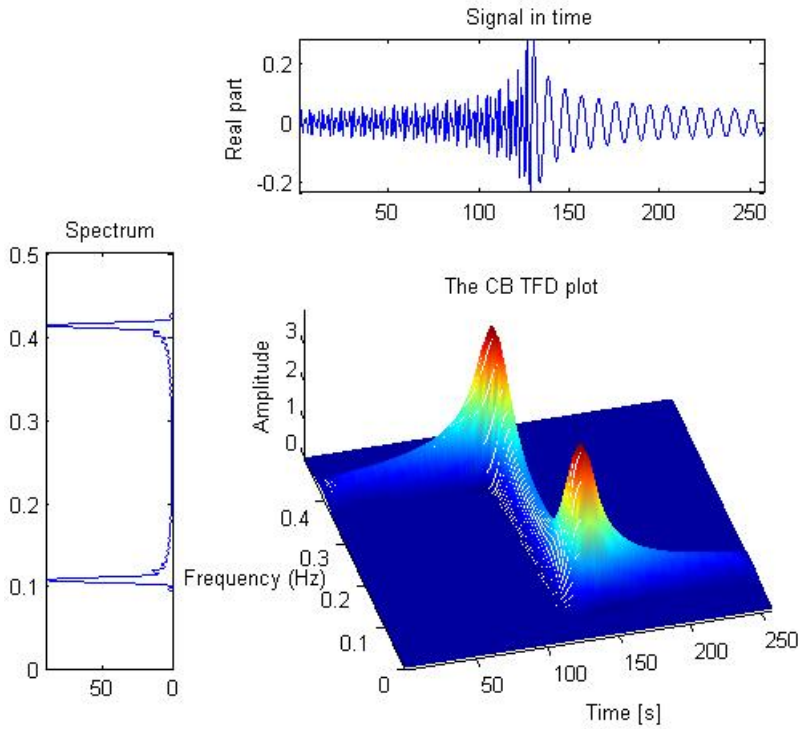

(b)

FIGURE 3.6 – CB TFD of a Doppler signal ($D = 2.5$). (a) $C = 0.5$ and (b) $C = 5$.

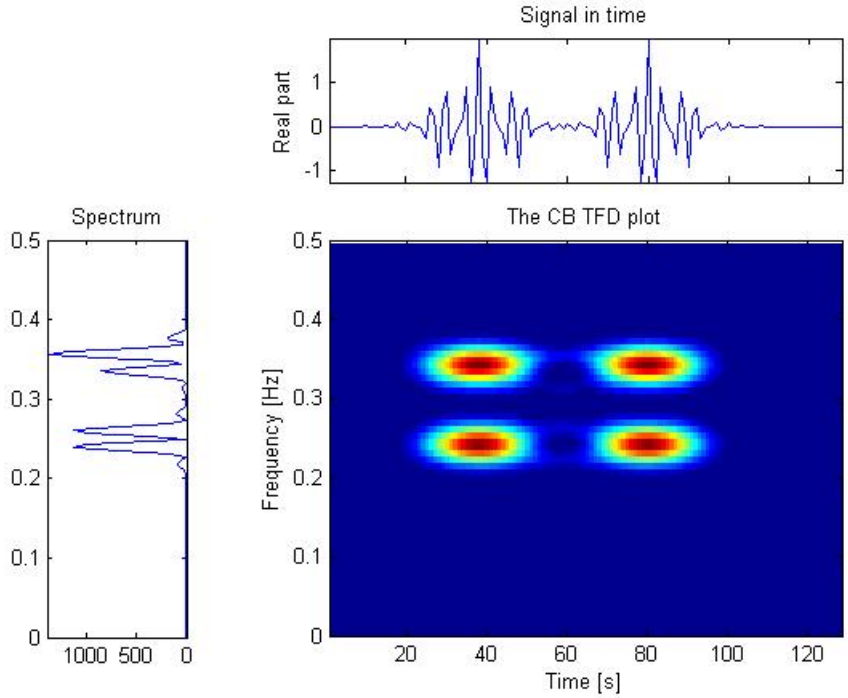
Signal in time
Real part
1
0
-1
Spectrum
0.5
0.4
0.3
0.2
0.1
0
1000 500 0
The CB TFD plot
Frequency [Hz]
20 40 60 80 100 120
Time [s]

(a)

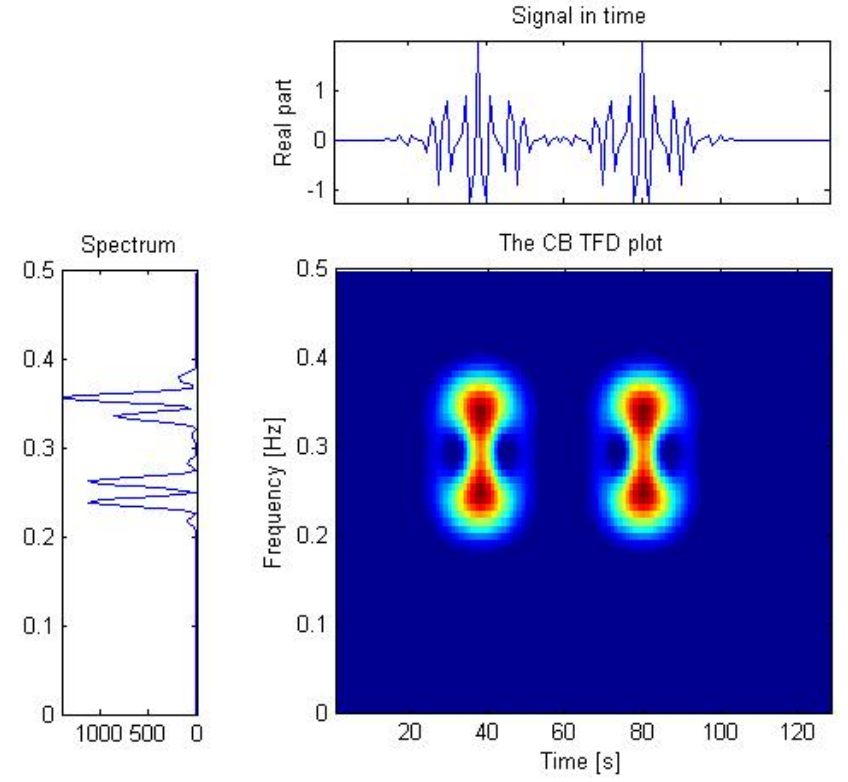
Signal in time
Real part
1
0
-1
Spectrum
0.5
0.4
0.3
0.2
0.1
0
1000 500 0
The CB TFD plot
Frequency [Hz]
20 40 60 80 100 120
Time [s]

(b)

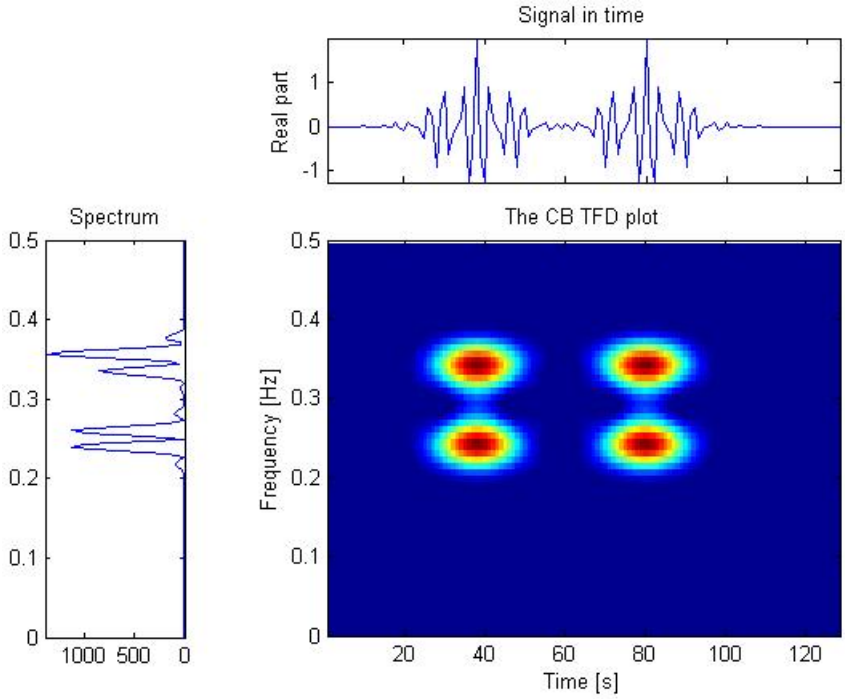

(c)

FIGURE 3.7 – CB TFD of a signal composed of four Gaussian atoms ($D = 2.5$). (a) $C = 2.5$, (b) $C = 18$ and (c) $C = 7$.

spaced components [71]-[73]. This type of kernels takes the following general form in the ambiguity domain

$$\phi(\eta, \tau) = G_1(\eta) g_2(\tau) \tag{3.22}$$

or equivalently in the time-lag domain

$$G(t, \tau) = \int_{-\infty}^{+\infty} G_1(\eta) g_2(\tau) e^{-j2\pi\eta t} d\eta = g_1(t) g_2(\tau) \tag{3.23}$$

where g_1 is the Fourier transform of G_1 with respect to η.

As seen in (2.28), any quadratic TFD can be expressed as a smoothed version of the WVD using the time-frequency kernel notation $\Pi(t, f) = \int_{-\infty}^{+\infty} \int_{-\infty}^{+\infty} \phi(\eta, \tau) e^{-j2\pi(f\tau+\eta t)} d\eta d\tau$. In the case of a separable kernel we get

$$\begin{aligned} \Pi(t, f) &= \int_{-\infty}^{+\infty} G_1(\eta) e^{-j2\pi\eta t} d\eta \int_{-\infty}^{+\infty} g_2(\tau) e^{-j2\pi f\tau} d\tau \\ &= g_1(t) G_2(f) \end{aligned} \tag{3.24}$$

where G_2 is the Fourier transform of g_2 with respect to τ. Substituting (3.24) in (2.28)

and using the convolution properties we get

$$\begin{aligned} TFD_x(t,f) &= \int_{-\infty}^{+\infty}\int_{-\infty}^{+\infty} g_1(s-t)G_2(\eta-f)W_x(s,\eta)dsd\eta \\ &= \int_{-\infty}^{+\infty}\left[\int_{-\infty}^{+\infty} g_1(s-t)W_x(s,\eta)ds\right]G_2(\eta-f)d\eta \\ &= g_1(t) \underset{t}{*} W_x(t,f) \underset{f}{*} G_2(f) \end{aligned} \tag{3.25}$$

Equivalently, in (3.25), the two convolutions can be evaluated in either order, indicating that the Doppler-dependent and lag-dependent factors in the separable kernel lead to separate convolutions in time and frequency, respectively [4, 10].

By putting

$$G_1(\eta) = 1 \Rightarrow g_1(t) = \delta(t) \tag{3.26}$$

the Doppler-independent (DI) kernel is obtained so that [4, 10]

$$TFD_x(t,f) = W_x(t,f) \underset{f}{*} G_2(f) \tag{3.27}$$

Hence, in this special case of the separable Doppler-lag kernel, the DI kernel causes smearing of the WVD in the frequency direction only, reducing the inner artifacts [4].

A second special case of the separable kernel, the lag-independent (LI) kernel [4, 10], is obtained by putting

$$g_2(\tau) = 1 \Rightarrow G_2(f) = \delta(f) \tag{3.28}$$

In the time-lag domain, the resulting separable kernel is in this case a function of time alone ; for this reason, such kernels have been called time-only kernels [41, 72] defining the T-class of time-frequency distributions. Making this substitution in (3.25), we obtain

$$TFD_x(t,f) = g_1(t) \underset{t}{*} W_x(t,f) \tag{3.29}$$

The last expression shows that an LI kernel causes smearing of the WVD in the time direction only, reducing the crossterms [4].

The separable-kernel allows to understand the improved behavior of the SPWVD compared to the WVD as seen in Sec. 2.3.3. It also enables the construction of high-resolution quadratic TFDs using the classical smoothing functions commonly encountered in digital signal processing and spectral analysis [10]. Our contribution is developed in this context.

In [65], a separable kernel family with compact support (SKCS) applied to image processing was introduced. The later is a separable version of the compact support kernel. Hence, in order to benefit from the separate control of the frequency-smoothing and time-smoothing of the WVD, the CB kernel also referred to as KCS can be modified to the separable form that we call Separable Cheriet-Belouchrani (SCB) kernel yielding to a new time-frequency distribution of quadratic class referred to as SCB TFD. The derived time-lag SCB kernel is given by

$$G_{SCB}(t,\tau) = \begin{cases} G_{CB}(t,0)G_{CB}(0,\tau) & \text{if } t^2 < D^2 \text{ and } \tau^2 < D^2 \\ 0 & \text{Otherwise} \end{cases} \tag{3.30}$$

Here $g_1(t) = G_{CB}(t,0)$ is the Fourier transform of the Doppler-dependent factor with respect to η and $g_2(\tau) = G_{CB}(0,\tau)$ is the lag-dependent factor of the SCB kernel. Thus

$$G_{SCB}(t,\tau) = \begin{cases} e^{2C} e^{\frac{CD^2}{t^2-D^2} + \frac{CD^2}{\tau^2-D^2}} & \text{if } t^2 < D^2 \text{ and } \tau^2 < D^2 \\ 0 & \text{Otherwise} \end{cases} \tag{3.31}$$

As for the CB, the SCB exhibits the same behavior of the Gaussian. The free positive real parameter C controls the kernel's bandwidth i.e. the distance between the zero-crossing of the kernel to the origin of the axis ; it does not affect the compact support nature of the kernel. In addition, when C increases, the Heisenberg uncertainty product was found to decrease rapidly and becomes close to the optimal value $(1/4\pi)$ reached by the Gaussian kernel [65]. Fig. 3.8 displays the two-dimensional profile of the time-lag SCB kernel for different values of C and $D = 2.5$ while Fig. 3.9 depicts the corresponding plots of the SCB kernel in the Doppler-lag domain.

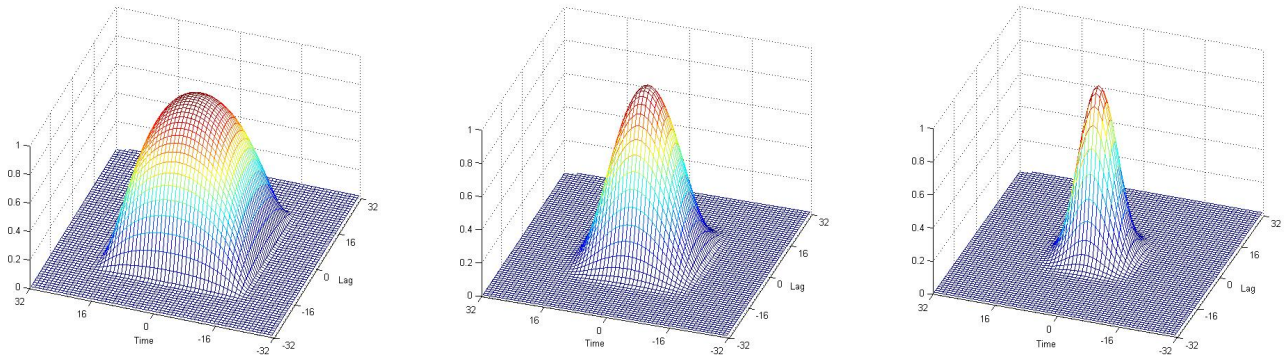

(a) (b) (c)

FIGURE 3.8 – The two-dimensional profile of the SCB kernel in the time-lag domain with $D = 2.5$. (a) $C = 0.8$, (b) $C = 2.5$ and (c) $C = 10$.

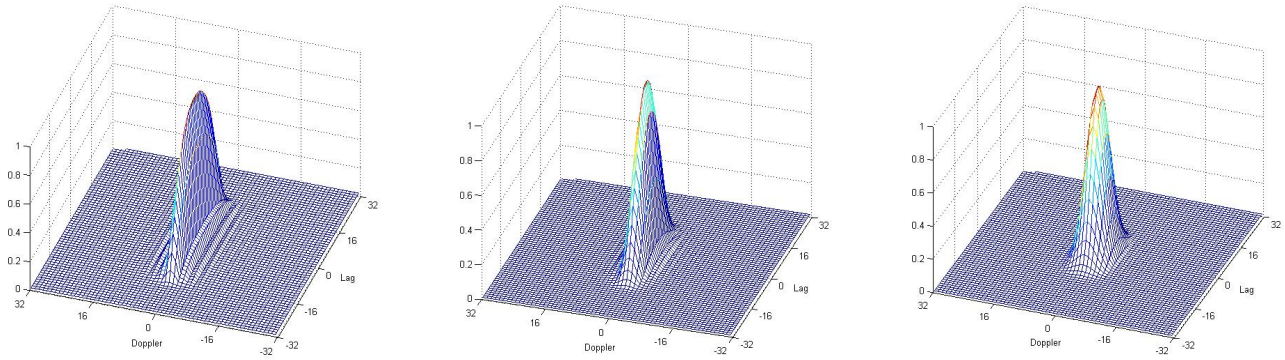

(a) (b) (c)

FIGURE 3.9 – The two-dimensional profile of the SCB kernel in the Doppler-lag domain normalized with respect to its peak located at the origin ($\eta = 0$, $\tau = 0$) with $D = 2.5$. (a) $C = 0.8$, (b) $C = 2.5$ and (c) $C = 10$.

Note that even the 1D KCS and SKCS kernels have nearly the same behavior ; the fact that the SCB is separable, its support over the time-lag plane takes a square form. The separable CB (SCB) TFD is expressed in the continuous form as follows

$$SCB_z(t,f) = \int_{-\infty}^{+\infty}\int_{-\infty}^{+\infty} G_{SCB}(t-s,\tau)z(s+\tau/2)z^*(s-\tau/2)e^{-j2\pi f\tau}dsd\tau \qquad (3.32)$$

where we recall that $z(t)$ is the complex analytic signal associated to the real analyzed signal $x(t)$. By substituting (3.31) in (3.32) we get

$$SCB_z(t,f) = e^{2C}\int_{-\infty}^{+\infty} e^{\frac{CD^2}{\tau^2-D^2}}\left[\int_{t-D}^{t+D} e^{\frac{CD^2}{(t-s)^2-D^2}} z(s+\tau/2)z^*(s-\tau/2)ds\right] e^{-j2\pi f\tau}d\tau \qquad (3.33)$$

Two examples showing the performance of the SCB TFD in representing two Doppler signals and a combination of a constant frequency component and two non-parallel chirps are depicted in Figs. 3.10-3.11 using $D = 7.5$ and different values of the compact support extent controller C. We observe that the tuning of the kernel bandwidth allows better reduction of the crossterms and improves largely the resolution and the concentration of the individual components. Note that the kernel length is set to 128 and as shown in Fig. 3.5, it may have an important effect on the overall performance of the induced distribution as it will be discussed in Chapter 5.

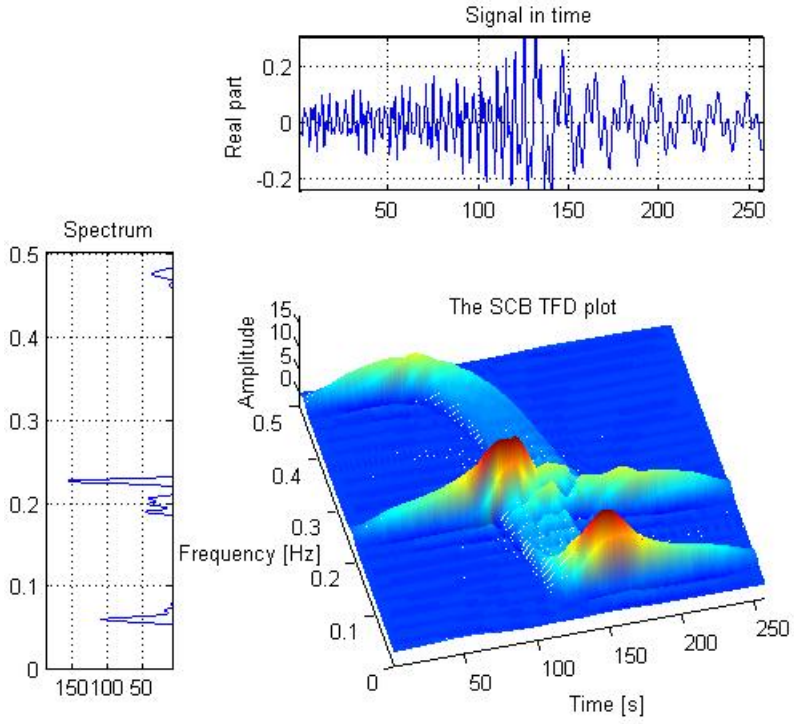

(a)

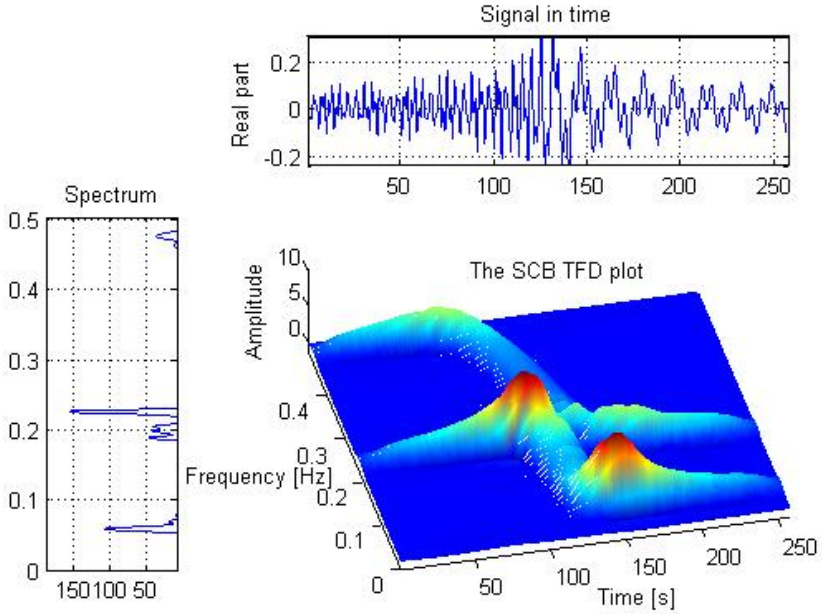

(b)

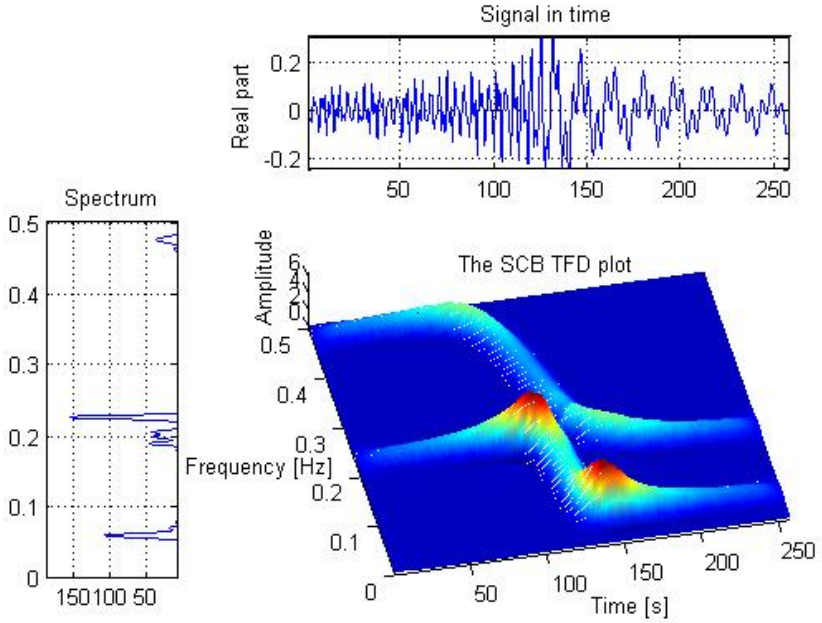

(c)

FIGURE 3.10 – SCB TFD of two Doppler signals ($D = 7.5$). (a) $C = 0.1$, (b) $C = 0.8$ and (c) $C = 2.8$.

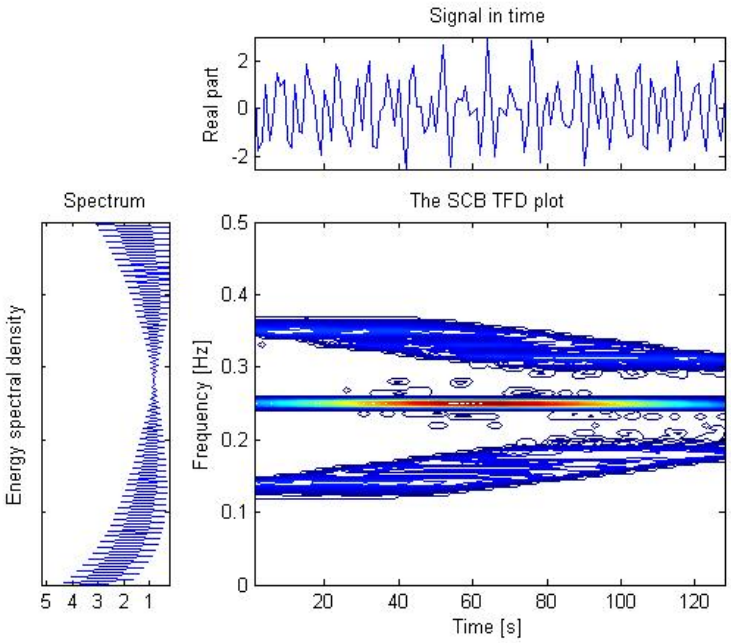
Signal in time
Real part
2
0
-2
Spectrum
The SCB TFD plot
Energy spectral density
5 4 3 2 1
Frequency [Hz]
0.5
0.4
0.3
0.2
0.1
0
20 40 60 80 100 120
Time [s]

(a)

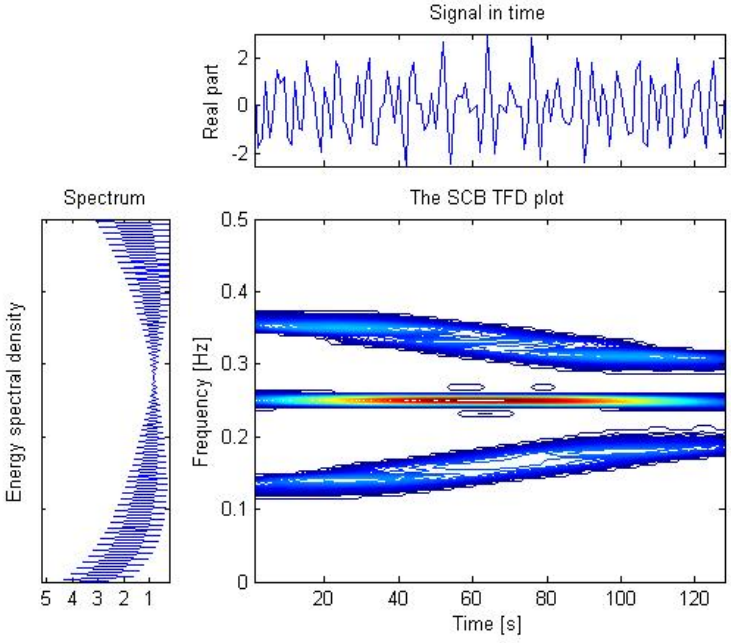
Signal in time
Real part
2
0
-2
Spectrum
The SCB TFD plot
Energy spectral density
5 4 3 2 1
Frequency [Hz]
0.5
0.4
0.3
0.2
0.1
0
20 40 60 80 100 120
Time [s]

(b)

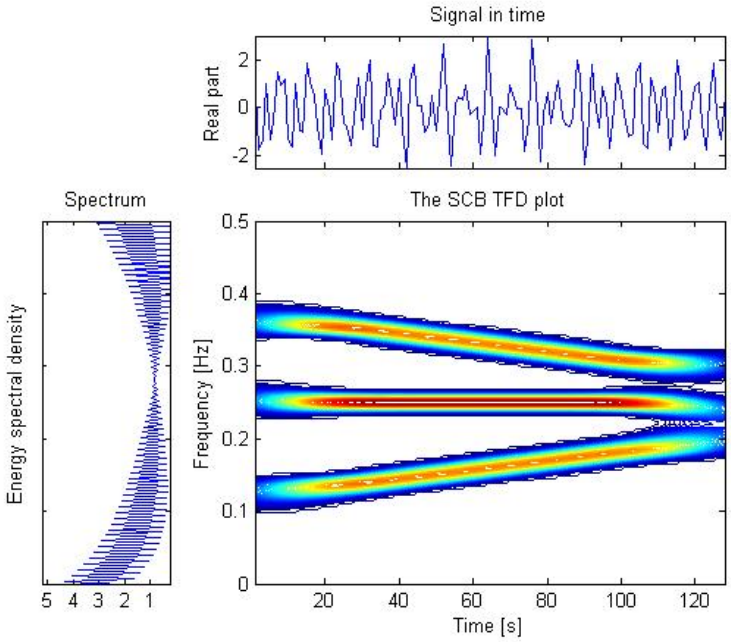

(c)

FIGURE 3.11 – SCB TFD of a signal composed of a pure frequency ($f = 0.25$ Hz) and two non-parallel chirps with frequency ranges $f = [0.37 - 0.29]$ Hz and $f = [0.12 - 0.2]$ Hz, respectively ($D = 7.5$). (a) $C = 0.05$, (b) $C = 0.5$ and (c) $C = 5.8$.

3.5 The polynomial KCS-based TFD (PCB TFD)

As shown in Sec. 3.2.2, in order to build the KCS kernel, a change of variables is applied to g_σ using a function w as defined for example by (3.8). This results in the deformation of the plane into a unit ball in order to permit the approximation of the Gaussian kernel by a mollifier. Unfortunately, there is no analytical expression for the corresponding normalization constant C_γ given by (3.13), and so it must be computed by a numerical method.

To avoid this drawback, and since the choice of w is not unique, the following effective and efficient transformation is proposed in [63]

$$\begin{aligned} [0,1[&\longrightarrow \Re^+ \\ r &\longrightarrow w(r) = \sqrt{-\ln(1-r^2)},\ 0 \leq r < 1 \end{aligned} \tag{3.34}$$

Following the same steps as for the KCS, the resulting normalization constant C_γ is now easily calculated as follows [63]

$$C_\gamma = \int_{-1}^{1}\int_{-1}^{1}(1-(x^2+y^2))^\gamma\,dx\,dy = 2\pi\int_0^1(1-r^2)^\gamma r\,dr = \frac{\pi}{\gamma+1} \tag{3.35}$$

The 2D family of the new compact support kernel, called PKCS, is defined as [63]

$$\rho_{\gamma,\lambda}(x,y) = \begin{cases} \frac{\gamma+1}{\pi\lambda^{2\gamma+2}}\left(\lambda^2 - (x^2+y^2)\right)^{\gamma} & \text{if } x^2+y^2 < \lambda^2 \\ 0 & \text{Otherwise} \end{cases} \tag{3.36}$$

where λ is the radius of the kernel support.

The compact support nature of the PKCS together with the possibility of controlling the kernel's window width led us to propose a new kernel for time-frequency analysis called Polynomial Cheriet-Belouchrani (PCB) kernel yielding to a new quadratic time-frequency distribution referred to as PCB TFD. The latter is implemented following the same procedure as for the CB TFD and the SCB TFD.

The PCB kernel is defined in the time-lag domain as

$$G_{PCB}(t,\tau) = \begin{cases} \frac{\gamma+1}{\pi\lambda^{2\gamma+2}}\left(\lambda^2 - (t^2+\tau^2)\right)^{\gamma} & \text{if } t^2+\tau^2 < \lambda^2 \\ 0 & \text{Otherwise} \end{cases} \tag{3.37}$$

where λ is a predetermined parameter and γ controls the bandwidth of the PCB and is considered to be a positive integer so that the resulting kernel has a polynomial form.

It is important to note that, physically speaking, the sum $(\lambda^2 - (t^2+\tau^2))$ is only possible if we suppose that the time parameter t, the lag parameter τ and λ are implicitly normalized by $t_0 = 1$, $\tau_0 = 1$ and $\lambda_0 = 1$, respectively so that the sum is unitless.

Fig. 3.12 shows the plots of the time-lag PCB kernel for different values of the smoothing parameter γ with $\lambda = 2.5$. Their corresponding ambiguity domain kernel plots are depicted in Fig. 3.13. We see that the PKCS exhibits more similar behavior to the Gaussian than KCS and as γ increases, the compact support is narrowed and consequently, the bandwidth of the kernel decreases.

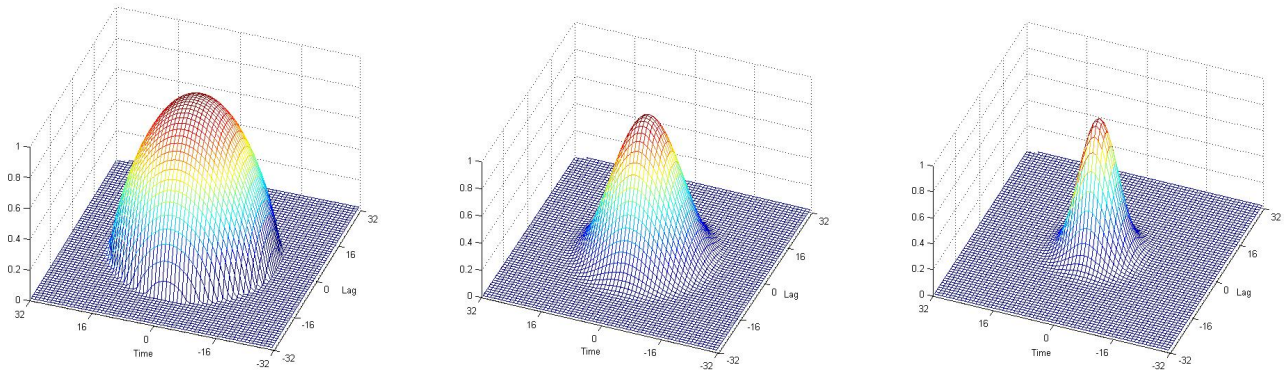

(a) (b) (c)

FIGURE 3.12 – The 2D profile of the PCB time-lag kernel normalized with respect to its peak located at the origin ($t = 0$, $\tau = 0$) with $\lambda = 2.5$. (a) $\gamma = 1$, (b) $\gamma = 3$ and (c) $\gamma = 10$.

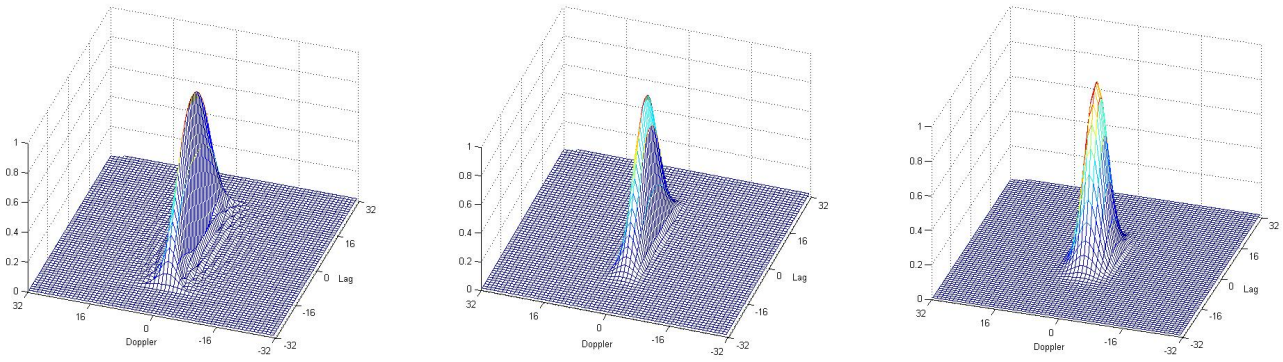

(a) (b) (c)

FIGURE 3.13 – The 2D profile of the PCB Doppler-lag kernel normalized with respect to its peak located at the origin ($\eta = 0$, $\tau = 0$) with $\lambda = 2.5$. (a) $\gamma = 1$, (b) $\gamma = 3$ and (c) $\gamma = 10$.

The polynomial CB (PCB) TFD is formulated as follows

$$PCB_z(t,f) = \frac{\gamma+1}{\pi\lambda^{2\gamma+2}} \int_{-\infty}^{+\infty} \left[\int_{t-\sqrt{|\lambda^2-\tau^2|}}^{t+\sqrt{|\lambda^2-\tau^2|}} \left(\lambda^2 - ((t-s)^2+\tau^2)\right)^{\gamma} U_z(s,\tau) ds \right] e^{-j2\pi f\tau} d\tau \tag{3.38}$$

where we recall that $U_z(s,\tau) = z(s+\tau/2)z^*(s-\tau/2)$ is the instantaneous autocorrelation function of the analytic signal $z(t)$. Figs. 3.14-3.15 show the PCB TFD plots of the signals considered in Sec. 3.4 using various values of γ with $\lambda = 4$. It turns out that through a control of the bandwidth of the kernel, the corresponding TFD allows a better elimination of crossterms while providing high resolution in both time and frequency.

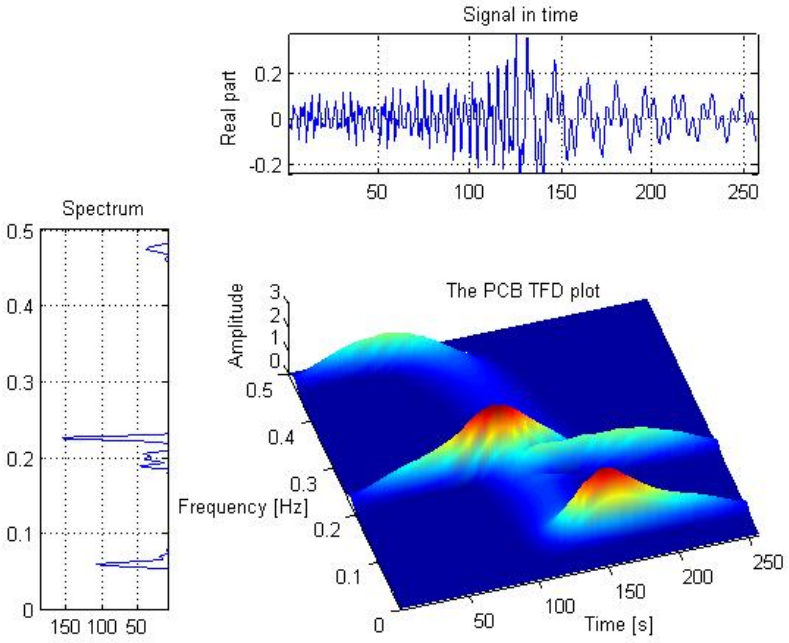

(a)

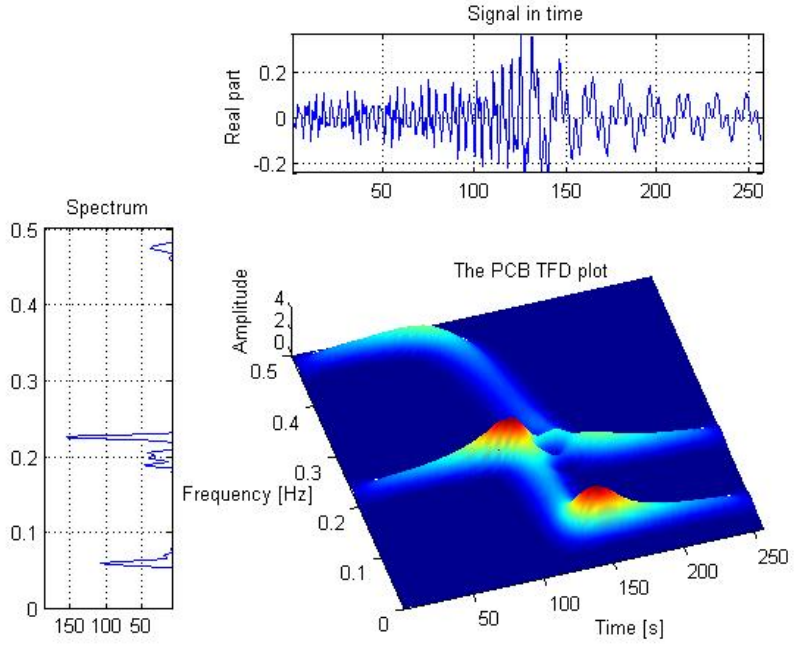

(b)

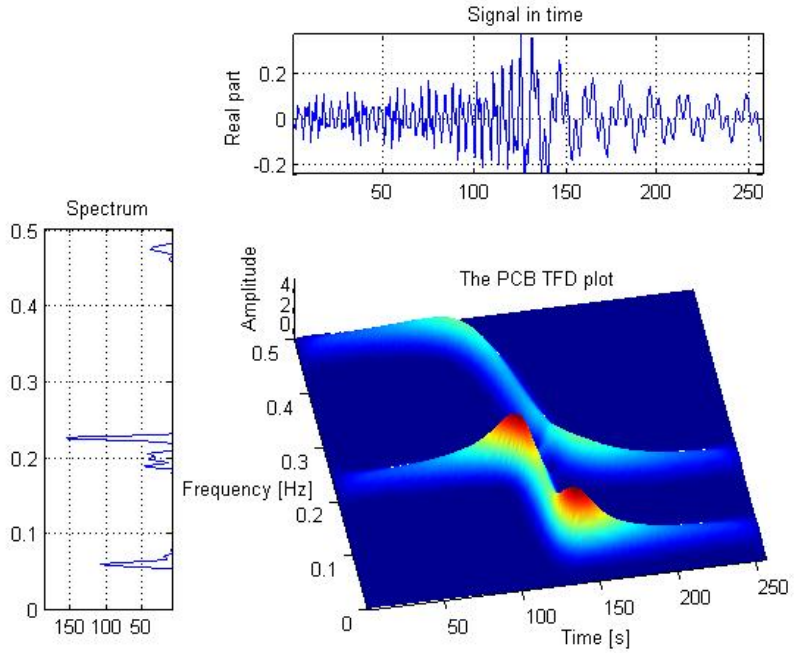

(c)

FIGURE 3.14 – PCB TFD of two Doppler signals ($\lambda = 4$). (a) $\gamma = 3$, (b) $\gamma = 9$ and (c) $\gamma = 23$.

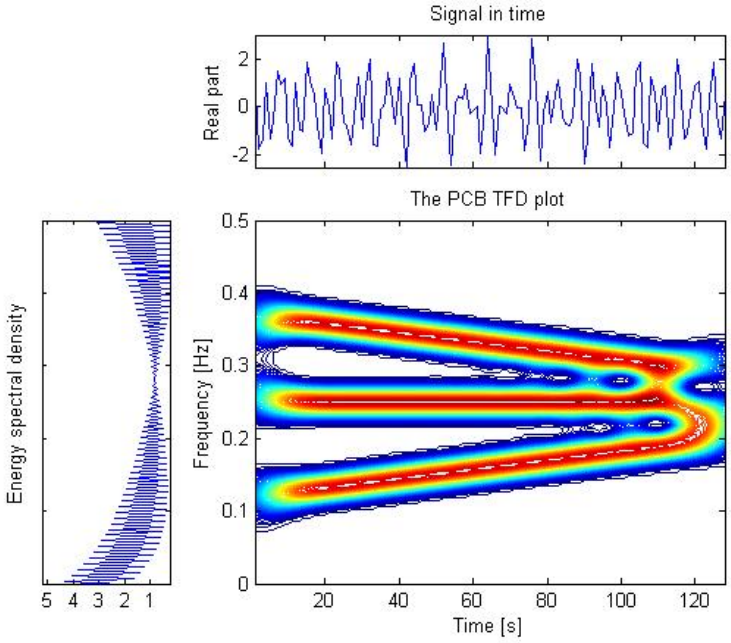
Signal in time
Real part
2
0
-2
The PCB TFD plot
Energy spectral density
5 4 3 2 1
Frequency [Hz]
0.5
0.4
0.3
0.2
0.1
0
20 40 60 80 100 120
Time [s]

(a)

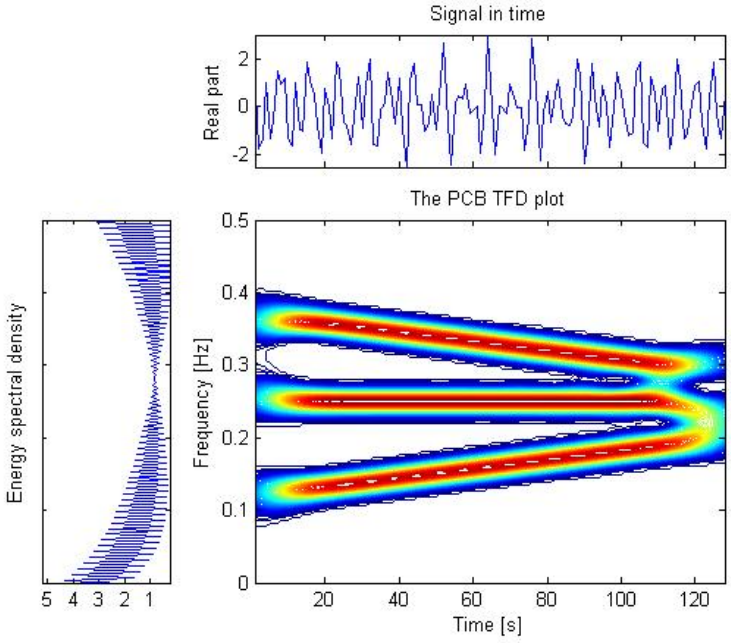
Signal in time
Real part
2
0
-2
The PCB TFD plot
Energy spectral density
5 4 3 2 1
Frequency [Hz]
0.5
0.4
0.3
0.2
0.1
0
20 40 60 80 100 120
Time [s]

(b)

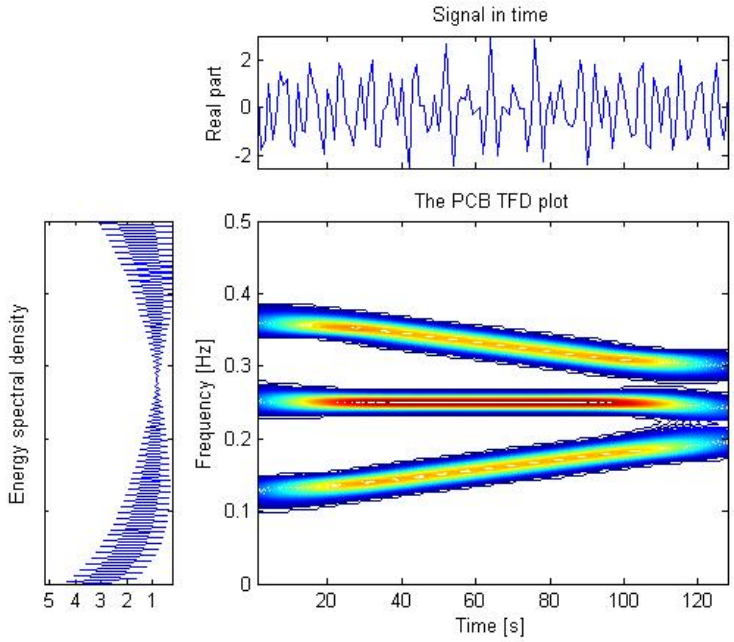

(c)

FIGURE 3.15 – PCB TFD of the signal considered in Fig. 3.11 ($\lambda = 4$). (a) $\gamma = 25$, (b) $\gamma = 17$ and (c) $\gamma = 5$.

3.6 Classical mathematical properties of quadratic TFDs

The choice of the two-dimensional kernel is critical in the definition of a quadratic TFD and it determines the properties of the generated distribution e.g. real-valued, marginal conditions, instantaneous frequency (IF) as well as its overall performance in terms of energy concentration and resolution. In general, the purpose of the kernel is to reduce the interference terms in the time-frequency distribution. However, (2.22) shows that the reduction of the interference patterns involves smoothing and thus results in a reduction of time-frequency resolution. Moreover, depending on the type of kernel, some of the desired properties of the time-frequency distribution are preserved while others are lost [74]. The crucial question that arises here is : For practical purposes, what mathematical properties would a quadratic TFD satisfy in order to ensure useful and efficient signal analysis and interpretation ? The answer to this question justifies our choice of the objective performance measure criteria adopted in Chapter 4.

The following is a list of the main desirable properties for TFDs of quadratic class [4, 54, 55]. We relate to each property the corresponding kernel constraints and provide the mathematical proofs as well.

3.6.1 Real-valued

A time-frequency distribution is real-valued if

$$TFD_x(t,f) = TFD_x^*(t,f) = \Re\{TFD_x(t,f)\} \quad \forall \ \ t,f \tag{3.39}$$

By calculating the complex conjugate of (2.22) using the instantaneous autocorrelation notation $U_x(t,\tau) = x(t+\tau/2)x^*(t-\tau/2)$ and making the change of integration variables $\tau' = -\tau$ and $\eta' = -\eta$ we get

$$\begin{aligned} TFD_x^*(t,f) &= \int\int\int_{-\infty}^{+\infty} e^{-j2\pi\eta(s-t)}\phi^*(\eta,\tau)U_x^*(s,\tau)e^{+j2\pi f\tau}d\eta ds d\tau \\ &= -\int_{+\infty}^{-\infty}\int\left(-\int_{+\infty}^{-\infty} e^{j2\pi\eta'(s-t)}\phi^*(-\eta',-\tau')U_x(s,\tau')e^{-j2\pi f\tau'}d\eta' ds d\tau'\right) \\ &= \int\int\int_{-\infty}^{+\infty} e^{j2\pi\eta(s-t)}\phi^*(-\eta,-\tau)U_x(s,\tau)e^{-j2\pi f\tau}d\eta ds d\tau \end{aligned}$$

Hence, a real quadratic distribution is obtained if the corresponding Doppler-lag kernel satisfies

$$\phi(\eta,\tau) = \phi^*(-\eta,-\tau), \ \forall \ \eta,\tau \ \in \Re. \tag{3.40}$$

When (3.40) holds, we get

$$\begin{aligned} G(t,\tau) = \int_{-\infty}^{+\infty}\phi(\eta,\tau)e^{-j2\pi\eta t}d\eta &= \int_{-\infty}^{+\infty}\phi^*(-\eta,-\tau)e^{-j2\pi\eta t}d\eta \\ &= \int_{-\infty}^{+\infty}\phi^*(\eta,-\tau)e^{+j2\pi\eta t}d\eta \\ &= \left(\int_{-\infty}^{+\infty}\phi^*(\eta,-\tau)e^{-j2\pi\eta t}d\eta\right)^* \end{aligned}$$

The realness requirement of a TFD in the time-lag domain is then

$$G(t,\tau) = G^*(t,-\tau), \ \forall \ t,\tau \ \in \Re. \tag{3.41}$$

3.6.2 Time marginal (conservation of spectral energy density)

A time-frequency distribution $TFD_x(t,f)$ of $x(t)$ obeys the time marginal property if

$$\int_{-\infty}^{+\infty} TFD_x(t,f)dt = |X(f)|^2 \tag{3.42}$$

where $|X(f)|^2$ is the energy spectral density.

By integrating (2.22) over t we obtain

$$\begin{aligned} I(f) &= \int_{-\infty}^{+\infty}\left(\int\int\int_{-\infty}^{+\infty} e^{-j2\pi\eta(s-t)}\phi(\eta,\tau)U_x(s,\tau)e^{-j2\pi f\tau}d\eta ds d\tau\right)dt \qquad (3.43) \\ &= \int\int\int_{-\infty}^{+\infty}\left[\int_{-\infty}^{+\infty} e^{+j2\pi\eta t}dt\right]e^{-j2\pi\eta s}\phi(\eta,\tau)U_x(s,\tau)e^{-j2\pi f\tau}d\eta ds d\tau \end{aligned}$$

Since $\int_{-\infty}^{+\infty} e^{+j2\pi\eta t}dt = \delta(\eta)$ and $\delta(\eta)e^{-j2\pi\eta s}\phi(\eta,\tau) = \phi(0,\tau)\delta(\eta)$ it yields

$$\begin{aligned} I(f) &= \int\int_{-\infty}^{+\infty} \underbrace{\left[\int_{-\infty}^{+\infty} \delta(\eta)d\eta\right]}_{1} \phi(0,\tau)U_x(s,\tau)e^{-j2\pi f\tau}dsd\tau \\ &= \int\int_{-\infty}^{+\infty} \phi(0,\tau)U_x(s,\tau)e^{-j2\pi f\tau}dsd\tau \end{aligned} \tag{3.44}$$

In the case of (the requirement for time marginal property in the Doppler-lag domain)

$$\phi(0,\tau) = 1,\ \forall\tau. \tag{3.45}$$

then

$$I(f) = \int\int_{-\infty}^{+\infty} x(s+\tau/2)x^*(s-\tau/2)e^{-j2\pi f\tau}dsd\tau \tag{3.46}$$

From the definition of the Wigner-Ville distribution, the integral (3.46) can be rewritten as follows

$$I(f) = \int_{-\infty}^{+\infty} W_x(s,f)ds = |X(f)|^2. \tag{3.47}$$

since the WVD verifies the marginal properties.

From the development above, we conclude that in order to a TFD of the quadratic class preserves the marginal property with respect to time, the kernel must satisfy (3.45).

3.6.3 Frequency marginal (conservation of instantaneous power)

A time-frequency distribution $TFD_x(t,f)$ obeys the frequency marginal property if it reduces to the instantaneous power by integrating over f, i.e.

$$\int_{-\infty}^{+\infty} TFD_x(t,f)df = |x(t)|^2 \tag{3.48}$$

By integrating (2.22) over f we obtain

$$\begin{aligned} I(t) &= \int_{-\infty}^{+\infty} \left(\int\int\int_{-\infty}^{+\infty} e^{-j2\pi\eta(s-t)}\phi(\eta,\tau)U_x(s,\tau)e^{-j2\pi f\tau}d\eta dsd\tau\right) df \\ &= \int\int\int_{-\infty}^{+\infty} \left[\int_{-\infty}^{+\infty} e^{-j2\pi f\tau}df\right] e^{-j2\pi\eta(s-t)}\phi(\eta,\tau)U_x(s,\tau)d\eta dsd\tau \end{aligned} \tag{3.49}$$

Since $\int_{-\infty}^{+\infty} e^{-j2\pi f\tau}\ df = \delta(\tau)$ and $\delta(\tau)\ \phi(\eta,\tau)\ U_x(s,\tau) = \delta(\tau)\ \phi(\eta,0)\ U_x(s,0) = \phi(\eta,0)\ x(s)\ x^*(s)\ \delta(\eta) = \phi(\eta,0)\ |x(s)|^2\ \delta(\tau)$ it yields

$$\begin{aligned} I(t) &= \int\int_{-\infty}^{+\infty} \underbrace{\left[\int_{-\infty}^{+\infty} \delta(\tau)d\tau\right]}_{1} e^{-j2\pi\eta(s-t)}\phi(\eta,0)|x(s)|^2dsd\eta \\ &= \int\int_{-\infty}^{+\infty} e^{-j2\pi\eta(s-t)}\phi(\eta,0)|x(s)|^2dsd\eta \end{aligned} \tag{3.50}$$

In the case of (the requirement for frequency marginal property in the ambiguity domain)

$$\phi(\eta, 0) = 1, \ \forall \eta. \tag{3.51}$$

it results

$$I(t) = \int_{-\infty}^{+\infty} \left[\int_{-\infty}^{+\infty} e^{-j2\pi\eta(s-t)} d\eta \right] |x(s)|^2 ds \tag{3.52}$$

From the delta function properties we have $\int_{-\infty}^{+\infty} e^{-j2\pi\eta(s-t)} d\eta = \delta(s-t)$. Thus, (3.52) can be rewritten as follows

$$\begin{aligned} I(t) &= \int_{-\infty}^{+\infty} \delta(s-t)|x(s)|^2 ds \\ &= \int_{-\infty}^{+\infty} \delta(s-t)|x(t)|^2 ds \\ &= |x(t)|^2 \underbrace{\left[\int_{-\infty}^{+\infty} \delta(s') ds' \right]}_{1} \quad (s' = s - t) \\ I(t) &= |x(t)|^2. \end{aligned} \tag{3.53}$$

We conclude that in order to a quadratic TFD preserves the marginal property with respect to frequency, the kernel must satisfy condition (3.51). Then, $G(t, \tau)$ verifies (the requirement for frequency marginal property in the time-lag domain)

$$G(t, 0) = \int_{-\infty}^{+\infty} \phi(\eta, 0) e^{-j2\pi\eta t} d\eta = \delta(t), \ \forall t. \tag{3.54}$$

3.6.4 Energy conservation

A given TFD of x conserves energy if, by integrating it over time and frequency, we obtain the energy of x

$$E_x = \int_{-\infty}^{+\infty} \int_{-\infty}^{+\infty} TFD_x(t, f) dt df = \int_{-\infty}^{+\infty} I(f) df. \tag{3.55}$$

where $I(f) = \int_{-\infty}^{+\infty} TFD_x(t, f) dt$. From (3.44), the right-hand side (RHS) integral in (3.55) is expressed as follows

$$\begin{aligned} \int_{-\infty}^{+\infty} I(f) df &= \int_{-\infty}^{+\infty} \left[\int_{-\infty}^{+\infty} \int_{-\infty}^{+\infty} \phi(0, \tau) U_x(s, \tau) e^{-j2\pi f\tau} ds d\tau \right] df \\ &= \int_{-\infty}^{+\infty} \int_{-\infty}^{+\infty} \underbrace{\left[\int_{-\infty}^{+\infty} e^{-j2\pi f\tau} df \right]}_{\delta(\tau)} \phi(0, \tau) U_x(s, \tau) ds d\tau \end{aligned}$$

Since $\delta(\tau)\phi(0,\tau)U_x(s,\tau) = \phi(0,0)U_x(s,0)\delta(\tau) = \phi(0,0)x(s)x^*(s)\delta(\tau) = \phi(0,0)|x(s)|^2\delta(\tau)$ it yields

$$\begin{aligned}\int_{-\infty}^{+\infty} I(f)df &= \phi(0,0)\underbrace{\int_{-\infty}^{+\infty}\delta(\tau)d\tau}_{1}\int_{-\infty}^{+\infty}|x(s)|^2ds \\ &= \phi(0,0)\int_{-\infty}^{+\infty}|x(s)|^2ds. \end{aligned} \tag{3.56}$$

Hence, if one wants to preserve the energy conservation characteristic, the kernel must satisfy (the requirement for energy conservation property)

$$\phi(0,0) = 1. \tag{3.57}$$

Note that since the peaks of the KCS kernels in the ambiguity domain are located at the point ($\eta = 0$,$\tau = 0$), they can always be normalized so that $\phi_{KCS}(0,0) = 1$. Hence, their respective distributions satisfy the energy conservation property.

3.6.5 Translation covariance

A bilinear TFD is time and frequency covariant if

$$y(t) = x(t-t_0) \;\Rightarrow\; TFD_y(t,f) = TFD_x(t-t_0,f) \tag{3.58}$$

$$y(t) = x(t)e^{j2\pi f_0 t} \;\Rightarrow\; TFD_y(t,f) = TFD_x(t,f-f_0) \tag{3.59}$$

Conditions (3.58) and (3.59) hold for any quadratic TFD that belongs to the Cohen's class since the Doppler-lag kernel $\phi(\eta,\tau)$ is independent of t and f. In fact, for any time-shift t_0 so that $y(t) = x(t-t_0)$ we have

$$\begin{aligned} TFD_y(t,f) &= \int_{-\infty}^{+\infty}\int_{-\infty}^{+\infty} J(s-t,\tau)y(s+\tau/2)y^*(s-\tau/2)e^{-j2\pi f\tau}dsd\tau \\ &= \int_{-\infty}^{+\infty}\int_{-\infty}^{+\infty} J(s-t,\tau)x(s-t_0+\tau/2)x^*(s-t_0-\tau/2)e^{-j2\pi f\tau}dsd\tau \\ &= \int_{-\infty}^{+\infty}\int_{-\infty}^{+\infty} J(s'-(t-t_0),\tau)x(s'+\tau/2)x^*(s'-\tau/2)e^{-j2\pi f\tau}ds'd\tau \\ &= TFD_x(t-t_0,f). \end{aligned} \tag{3.60}$$

On the other hand, for any frequency-shifted signal $y(t) = x(t)e^{j2\pi f_0 t}$ we have

$$\begin{aligned} TFD_y(t,f) &= \int_{-\infty}^{+\infty}\int_{-\infty}^{+\infty} J(s-t,\tau)y(s+\tau/2)y^*(s-\tau/2)e^{-j2\pi f\tau}dsd\tau \\ &= \int_{-\infty}^{+\infty}\int_{-\infty}^{+\infty} J(s-t,\tau)x(s+\tau/2)e^{j2\pi f_0(s+\tau/2)}x^*(s-\tau/2)e^{-j2\pi f_0(s-\tau/2)} \\ &\qquad \times e^{-j2\pi f\tau}dsd\tau \end{aligned}$$

$$= \int_{-\infty}^{+\infty}\int_{-\infty}^{+\infty} J(s-t,\tau)x(s+\tau/2)x^*(s-\tau/2)e^{-j2\pi(f-f_0)\tau}dsd\tau$$

$$= \quad TFD_x(t,f-f_0). \tag{3.61}$$

Similarly, a simultaneous time shift and modulation lead to a shift in both time and frequency of the TFDs of Cohen's class

$$y(t) = x(t-t_0)e^{j2\pi f_0 t} \Rightarrow TFD_y(t,f) = TFD_x(t-t_0, f-f_0). \tag{3.62}$$

3.6.6 Dilations covariance

A given TFD preserves dilations if

$$y(t) = \sqrt{k}\,x(kt),\ k>0 \ \Rightarrow\ TFD_y(t,f) = TFD_x\left(kt, \frac{f}{k}\right) \tag{3.63}$$

From (2.23), the TFD of y is given by

$$\begin{aligned} TFD_y(t,f) &= \int_{-\infty}^{+\infty}\int_{-\infty}^{+\infty} J(s-t,\tau)y(s+\tau/2)y^*(s-\tau/2)e^{-j2\pi f\tau}dsd\tau \\ &= k\int\int_{-\infty}^{+\infty} J(s-t,\tau)x(ks+k\tau/2)x^*(ks-k\tau/2)e^{-j2\pi f\tau}dsd\tau \end{aligned} \tag{3.64}$$

Let : $s' = ks$ and $\tau' = k\tau$. Then

$$TFD_y(t,f) = \frac{1}{k}\int_{-\infty}^{+\infty}\int_{-\infty}^{+\infty} J\left(\frac{s'}{k}-t, \frac{\tau'}{k}\right)x(s'+\tau'/2)x^*(s'-\tau'/2)e^{-j2\pi\frac{f}{k}\tau'}ds'd\tau' \tag{3.65}$$

On the other hand

$$TFD_x\left(kt, \frac{f}{k}\right) = \int_{-\infty}^{+\infty}\int_{-\infty}^{+\infty} J(s-kt,\tau)x(s+\tau/2)x^*(s-\tau/2)e^{-j2\pi\frac{f}{k}\tau}dsd\tau \tag{3.66}$$

Hence, the dilations are preserved if

$$J\left(\frac{s}{k}-t, \frac{\tau}{k}\right) = \ k\,J(s-kt,\tau). \tag{3.67}$$

or equivalently (the requirement for dilation covariance property in the time-lag domain)

$$G\left(t-\frac{s}{k}, \frac{\tau}{k}\right) = \ k\,G(kt-s,\tau). \tag{3.68}$$

According to (2.24), the left-hand side (LHS) of (3.67) is expressed as follows

$$J\left(\frac{s}{k}-t, \frac{\tau}{k}\right) = \int_{-\infty}^{+\infty}\phi\left(\eta, \frac{\tau}{k}\right)e^{j2\pi\eta\left(\frac{s-kt}{k}\right)}\,d\eta \tag{3.69}$$

By making $\eta' = \eta/k$ we get

$$J\left(\frac{s}{k} - t, \frac{\tau}{k}\right) = k \int_{-\infty}^{+\infty} \phi\left(\eta' k, \frac{\tau}{k}\right) e^{j2\pi\eta'(s-kt)}\, d\eta' \tag{3.70}$$

The RHS of (3.67) is given by

$$k\, J(s - kt, \tau) = k \int_{-\infty}^{+\infty} \phi(\eta, \tau) e^{j2\pi\eta(s-kt)}\, d\eta \tag{3.71}$$

From (3.70) and (3.71), for $k \neq 1$; condition (3.67) holds only for product kernels verifying (the requirement for dilation covariance property in the ambiguity domain)

$$\phi(\eta, \tau) = \varphi(\eta\tau). \tag{3.72}$$

3.6.7 Wide-sense time support conservation

This property is satisfied if the quadratic TFD of a signal that has a compact support in time possesses also the same compact support in time

$$x(t) = 0 \text{ for } |t| > T \Rightarrow TFD_x(t, f) = 0 \text{ for } |t| > T \tag{3.73}$$

From (2.23), condition (3.73) implies that the following equality holds

$$\int_{-\infty}^{+\infty} J(s - t, \tau) x(s + \tau/2) x^*(s - \tau/2) ds = 0 \text{ for } |t| > T \tag{3.74}$$

or equivalently

$$\int_{-\infty}^{+\infty} J(s, \tau) x(s + t + \tau/2) x^*(s + t - \tau/2) ds = 0 \text{ for } |t| > T \tag{3.75}$$

The integral above is different from zero if

$$-T \leq s + t + \tau/2 \leq T \text{ and } -T \leq s + t - \tau/2 \leq T \tag{3.76}$$

which corresponds to the values of s verifying

$$-T - t - \tau/2 \leq s \leq T - t - \tau/2 \text{ and } -T - t + \tau/2 \leq s \leq T - t + \tau/2 \tag{3.77}$$

Hence, the integration boundaries in (3.75) are limited to the interval

$$-T - t + |\tau|/2 \leq s \leq T - t - |\tau|/2. \tag{3.78}$$

For $t > |T|$, we distinguish two ranges of variation for the variable s

$$t > T \Rightarrow T - t < 0 \quad \Rightarrow \quad s < -|\tau|/2 \tag{3.79}$$

$$t < -T \Rightarrow -T - t > 0 \quad \Rightarrow \quad s > |\tau|/2 \tag{3.80}$$

From (3.79) and (3.80), we conclude that the nullity of (3.75) is guaranteed if

$$\forall \tau,\ J(s, \tau) = 0 \text{ for } |s| > |\tau|/2\,. \tag{3.81}$$

Using the time-lag domain notation we get (the kernel requirement for wide-sense time support conservation property)

$$\forall \tau,\ G(t, \tau) = 0 \text{ for } |t| > |\tau|/2\,. \tag{3.82}$$

3.6.8 Wide-sense frequency support conservation

This property is verified if the TFD of a signal that possesses a compact support in frequency has also the same compact support in frequency

$$X(f) = 0 \text{ for } |f| > B \Rightarrow TFD_x(t,f) = 0 \text{ for } |f| > B \tag{3.83}$$

Similarly to the development of Sec. 3.6.7, the requirement for frequency support conservation in the wide sense includes the following condition [54]

$$\forall \eta,\, \psi(\eta, f) = 0 \text{ for } |f| > |\eta|/2\,. \tag{3.84}$$

where

$$\psi(\eta, f) = \int_{-\infty}^{+\infty} \phi(\eta,\tau) e^{j2\pi f\tau} d\tau \tag{3.85}$$

denotes the Doppler-frequency kernel.

3.6.9 Instantaneous frequency conservation

This property is satisfied if the instantaneous frequency of a signal x can be recovered from the TFD as its first order moment in frequency, that is

$$f_x(t) = \frac{\int_{-\infty}^{+\infty} f\; TFD_{x_a}(t,f) df}{\int_{-\infty}^{+\infty} TFD_{x_a}(t,f) df} \triangleq \frac{1}{2\pi}\frac{d}{dt} arg(x_a(t)) = \frac{1}{2\pi}\theta'(t) \tag{3.86}$$

where $x_a(t) = a(t)e^{j\theta(t)}$ is the analytic signal associated to x.

The importance of this property is more apparent in case of a monocomponent signal with frequency modulation : A time-frequency representation that satisfies (3.86) should live near the curve of the instantaneous frequency [57], which results on good estimation of the IF laws.

To prove the instantaneous frequency conservation, we use the derivative with respect to τ of the inverse Fourier transform of $TFD_{x_a}(t,f)$

$$\begin{aligned} \frac{\partial}{\partial\tau} TF^{-1}(TFD_{x_a}(t,f)) &= \frac{\partial}{\partial\tau}\int_{-\infty}^{+\infty} TFD_{x_a}(t,f) e^{j2\pi f\tau} df \\ &= j2\pi \int_{-\infty}^{+\infty} f\, TFD_{x_a}(t,f) e^{j2\pi f\tau} df \end{aligned} \tag{3.87}$$

On the other hand, we have seen in Sec. 2.3.4 that $TFD_{x_a}(t,f)$ can be viewed as the Fourier transform of $C_{Jx_a}(t,\tau)$ with respect to τ. Hence

$$\begin{aligned} \frac{\partial}{\partial\tau} TF^{-1}(TFD_{x_a}(t,f)) &= \frac{\partial}{\partial\tau} C_{Jx_a}(t,\tau) \\ &= \frac{\partial}{\partial\tau}\int_{-\infty}^{+\infty} x_a(s+\tau/2) x_a^*(s-\tau/2) J(s-t,\tau) ds \\ &= I_1(t,\tau) + I_2(t,\tau) \end{aligned} \tag{3.88}$$

where

$$I_1(t,\tau) = \int_{-\infty}^{+\infty} \frac{\partial}{\partial\tau} J(s-t,\tau)\,(x_a(s+\tau/2)x_a^*(s-\tau/2))\,ds \tag{3.89}$$

and

$$I_2(t,\tau) = \frac{1}{2}\int_{-\infty}^{+\infty} \left(x_a^{'}(s+\tau/2)x_a^*(s-\tau/2) - x_a(s+\tau/2)x_a^{*'}(s-\tau/2)\right) J(s-t,\tau)ds \tag{3.90}$$

At $\tau = 0$ it results in

$$I_1(t,0) = \int_{-\infty}^{+\infty} \frac{\partial}{\partial\tau} J(s-t,\tau)|_{\tau=0}|x_a(s)|^2 ds \tag{3.91}$$

and

$$I_2(t,0) = \frac{1}{2}\int_{-\infty}^{+\infty} \left(x_a^{'}(s)x_a^*(s) - x_a(s)x_a^{*'}(s)\right) J(s-t,0)ds \tag{3.92}$$

with

$$\begin{aligned} x_a^{'}(s)\,x_a^*(s) \;-\; x_a(s)\,x_a^{*'}(s) \;&=\; \left(a^{'}(s)\,e^{j\theta(s)} + j\,\theta^{'}(s)\,a(s)\,e^{j\theta(s)}\right)\,a(s)\,e^{-j\theta(s)} - \\ &\quad \left(a^{'}(s)\,e^{-j\theta(s)} - j\,\theta^{'}(s)\,a(s)\,e^{-j\theta(s)}\right)\,a(s)\,e^{j\theta(s)} \\ &=\; 2j\,\theta^{'}(s)\,|x_a(s)|^2 \end{aligned} \tag{3.93}$$

In the case of $\phi(\eta,0) = 1,\ \forall\eta$; then

$$\begin{aligned} I_2(t,0) \;&=\; j\int_{-\infty}^{+\infty} \theta^{'}(s)|x_a(s)|^2\delta(s-t,0)ds \\ &=\; j\theta^{'}(t)|x_a(t)|^2\int_{-\infty}^{+\infty}\delta(s-t,0)ds = j\theta^{'}(t)|x_a(t)|^2 \end{aligned} \tag{3.94}$$

On the other hand, we have $\int_{-\infty}^{+\infty} TFD_{x_a}(t,f) = |x_a(t)|^2$ since the time marginal constraint is satisfied. From (3.87) and (3.88) we get

$$\frac{\int_{-\infty}^{+\infty} f\ TFD_{x_a}(t,f)df}{\int_{-\infty}^{+\infty} TFD_{x_a}(t,f)df} = \frac{1}{2\pi}\theta^{'}(t) + \frac{1}{j2\pi|x_a(t)|^2}\int_{-\infty}^{+\infty}\frac{\partial}{\partial\tau}J(s-t,\tau)|_{\tau=0}|x_a(s)|^2 ds \tag{3.95}$$

If the following additional condition holds

$$\frac{\partial}{\partial\tau}J(s-t,\tau)|_{\tau=0} = 0 \Longrightarrow \int_{-\infty}^{+\infty}\frac{\partial}{\partial\tau}\phi(\eta,\tau)|_{\tau=0}e^{j2\pi\eta(s-t)}d\eta = 0,\ \forall\eta \tag{3.96}$$

then (3.86) follows.

In conclusion, the instantaneous frequency is conserved if the following two conditions hold

$$\forall\eta,\ \phi(\eta,0) = 1 \ \text{ and } \ \frac{\partial}{\partial\tau}\phi(\eta,\tau)|_{\tau=0} = 0. \tag{3.97}$$

Using the time-lag kernel notation, the required conditions are

$$\forall t,\ G(t,0) = \delta(t) \ \text{ and } \ \frac{\partial}{\partial\tau}G(t,\tau)|_{\tau=0} = 0. \tag{3.98}$$

3.6.10 Group delay conservation

In a dual way, this property is verified if the group delay of x can be obtained as the first order moment in time of its TFD

$$t_x(f) = \frac{\int_{-\infty}^{+\infty} t\ TFD_{x_a}(t,f)dt}{\int_{-\infty}^{+\infty} TFD_{x_a}(t,f)\,dt} \triangleq -\frac{1}{2\pi}\frac{d}{df}arg(X_a(f)) = -\frac{1}{2\pi}\Phi'(f) \tag{3.99}$$

where $X_a(f) = |X_a(f)|e^{j\Phi(f)}$ is the Fourier transform of the analytic signal $x_a(t)$.

Similarly to the instantaneous frequency case but using the frequency domain relations ; we find that the requirement for group delay property includes the following two conditions

$$\forall\tau,\ \phi(0,\tau) = 1 \ \text{ and } \ \frac{\partial}{\partial\eta}\phi(\eta,\tau)|_{\eta=0} = 0. \tag{3.100}$$

3.6.11 Unitarity

The unitarity property expresses the conservation of the scalar product from the time-domain to the time-frequency domain (apart from the squared modulus)

$$\left|\int_{-\infty}^{+\infty} x(t)\,y^*(t)dt\right|^2 = \int_{-\infty}^{+\infty}\int_{-\infty}^{+\infty} TFD_x(t,f)\,TFD_y^*(t,f)\,dt\,df \tag{3.101}$$

The identity above is usually called Moyal's formula [54].

From the definition (3.101), it is clear that the unitarity cannot be satisfied by any smoothed version of the WVD : It can be easily proved that the following requirement must follow

$$|\phi(\eta,\tau)| = 1,\ \forall\eta,\tau. \tag{3.102}$$

3.6.12 Perfect localization on linear chirp signals

This property is achieved if the following condition holds

$$x(t) = e^{j2\pi(f_0+2\beta t)t} \Rightarrow TFD_x(t,f) = \delta(f-(f_0+\beta t)) \tag{3.103}$$

It is obvious that condition (3.103) only holds for the Wigner-Ville distribution since it is the only case where we get a sum of complex exponentials (the kernel $\phi_{WV}(\eta,\tau) = 1, \forall\,\eta,\tau$)

$$\begin{aligned} W_x(t,f) &= \int_{-\infty}^{+\infty} e^{j2\pi[f_0+2\beta(t+\tau/2)](t+\tau/2)}e^{-j2\pi f\tau}e^{-j2\pi[f_0+2\beta(t-\tau/2)]\,(t-\tau/2)}d\tau \\ &= \int_{-\infty}^{+\infty} e^{-j2\pi[f-(f_0+\beta t)]\tau}d\tau \\ &= \delta(f-(f_0+\beta t)). \end{aligned} \tag{3.104}$$

3.7 Comparative study of mathematical properties

Table 3.1 gives comparison between the most known quadratic kernel-based transforms and the KCS TFDs in terms of mathematical properties. It is important to note that there is a tradeoff between the quantity of interferences and the number of good properties. In fact, many popular and valuable TFDs (e.g., the spectrogram) do satisfy neither the time and frequency marginals nor the IF moment condition. Another example is the pseudo-WVD : Its improved readability and considerable interference attenuation compared to the basic WVD induces the loss of the marginal properties, the unitarity, and also the frequency-support conservation [55].

What is more important in most practical applications is to maximize the energy concentration about the IF for monocomponent signals and improve the resolution for multicomponent signals [2]. A detailed study of components concentration preservation versus crossterm suppression tradeoff was performed by Hlawatsch et al. [75]. The authors show that while the separable kernel TFD did not satisfy the mathematical desirable properties of the WVD, it resulted in the best artifacts suppression/components concentration preservation compromise for all of the considered signals [26]. They also argued that the classical mathematical properties are secondary or even not important when practical time-frequency signal analysis is considered. Concerning KCS-based TFDs, the powerful point is that they have by definition a limited bandwidth extent since they have a compact support. The kernel bandwidth is controlled through the parameter C for both the CB and the SCB kernels and γ for the PCB allowing a tradeoff between a good autoterm resolution and sufficient crossterm suppression.

Table 3.1 – Mathematical properties verified by WVD, CWD, BJD, ZAMD, Spectrogram, CB TFD, SCB TFD and PCB TFD.

	WVD	CWD	BJD	ZAMD	Spectrogram	CB TFD	SCB TFD	PCB TFD
Real-valued	×	×	×	×	×	×	×	×
Time marginal	×	×	×					
Frequency marginal	×	×	×					
Energy conservation	×	×	×		×	×	×	×
Translation covariance	×	×	×	×	×	×	×	×
Dilations covariance	×	×	×					
Wide-sense time support conservation	×	×	×	×				
Wide-sense frequency support conservation	×	×		×				
Instantaneous frequency	×	×	×					
Group delay	×	×	×					
Perfect localization on linear chirp signals	×							
Unitarity	×							

3.8 Suitable properties of TFDs for practical uses

The practical efficiency of a time-frequency representation is directly related to the following properties [4, 26]

1. Energy distribution property

The TFD should be real, and the signal energy in a certain region R in the $t-f$ plane, E_{x_R}, should be given by the following integral over R

$$\int_{\triangle t}\int_{\triangle f} TFD_x(t,f)df\,dt = E_{x_R} \tag{3.105}$$

where E_{x_R} is a portion of signal energy in the time interval $\triangle t$ and the frequency band $\triangle f$.

2. IF peak property

The dominant peak of the constant-time cross-section of the TFD of a monocomponent FM signal should provide the IF law which describes the signal FM law

$$\max_f TFD_x(t,f) = f_i(t) \tag{3.106}$$

For multicomponent FM signals, the same property should apply to each of the signal's components.

3. Concentration and resolution property

The TFD of a multicomponent FM signal should provide a good time-frequency resolution of the individual components. This requires a good energy concentration for each of the components and a good elimination of the inner and outer interference terms relative to the signal components. The practical experience shows also that the TFD's robustness against noise is directly related to the goodness of this property.

Note that a TFD has best energy concentration for a given multicomponent signal if for each signal component, it yields a) the smallest instantaneous bandwidth relative to the component IF, and b) the minimum sidelobe magnitude relative to mainlobe magnitude [2]. More details are provided in Sec. 4.3. The frequency resolution in a power spectrum density (PSD) of two single tones of frequencies f_1 and f_2, respectively is defined as the minimum difference $f_1 - f_2$ for which the following inequality holds [2]

$$f_1 + \frac{V_1}{2} < f_2 - \frac{V_2}{2},\ f_1 < f_2 \tag{3.107}$$

where the $V_i, i = 1, 2$ are the respective bandwidths of the two sinusoids as shown in Fig. 3.16. We say in such situations that the signal components are resolved in contrast to the case of Fig. 3.17 where the TFD's two components and the crossterm or probably the TFD's two crossing autoterms have merged in a single lobe. The components are said to be unresolved.

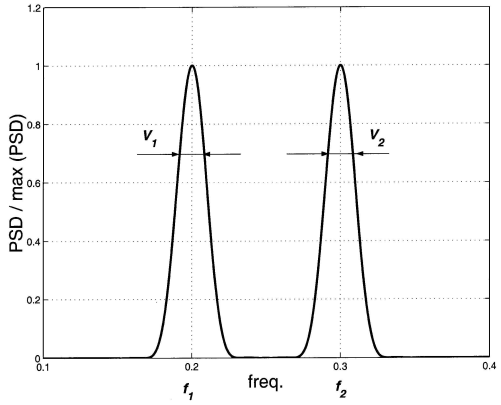

FIGURE 3.16 – Resolution in a PSD of a signal consisting of two sinusoids f_1 and f_2, with the corresponding bandwidths V_1 and V_2. The two lobes are clearly distinguishable from each other ; the components are said to be resolved [2].

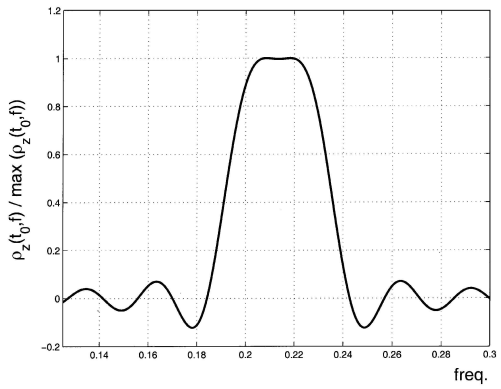

FIGURE 3.17 – Slice of a TFD $\rho_z(t, f)$ of a two-component FM signal $z(t)$ taken at the time instant $t = t_0$. In this case, the components are said to be unresolved [2].

3.9 Conclusion

The building of the KCS TFDs is based on two fundamental concepts : 1) Approximation of the Gaussian kernel based on the theory of mollifiers in order to benefit from its most important features and 2) extension of the kernels over a time-lag compact support in order to overcome the information loss and prohibitive processing time due to the truncation of the Gaussian function and the mask size, respectively, and provide at the same time impressive reduced-interference and higher resolution in both time and frequency by simply tuning the kernel's bandwidth.

After examination of the satisfied mathematical properties, we evaluate in the next chapter the performance of the KCS TFDs by referring to a specific set of objective criteria. Then, by taking into consideration different types of nonstationary multicomponent signals ; we optimize a selection of TFDs including the most known quadratic distributions and the KCS-based representations using several theoretical measures related to signal concentration and the recently developed Boashash-Sucic's normalized instantaneous resolution performance measure [1, 26].

Chapter 4

Objective Assessment and Optimization Criteria of TFDs

Observation and analysis of signal energy distributions over the $t - f$ plane permits to provide information about the number of components present in the signal with their respective time supports and frequency bandwidths, their related amplitudes and instantaneous frequency laws. However, the choice of the right TFD to analyze the given signal is not straightforward, even for monocomponent signals and the task becomes more complex when one deals with multicomponent signals [2].

According to the common practice, determination of the best representing TFD is based on visual inspection of the TFD plots so that the most appealing one is chosen [2]. In this chapter, the performance of the KCS-based TFDs is compared to the best classical quadratic TFDs using several tests on multicomponent signals with linear and nonlinear frequency modulation (FM) components including the noise effects. Instead of relying solely on visual inspection of the time-frequency domain plots, comparisons are based on practical parameters' computation that requires a deep analysis of each time slice plot and include the evaluation of the recently developed Boashash-Sucic's normalized instantaneous resolution performance measure that permits to provide the optimized TFD using a specific methodology. The latter is described in detail after presenting a review on some theoretical measures that deal essentially with signal concentration. In all presented examples, the KCS TFDs show a significant interference rejection, with the component energy concentration around their respective instantaneous frequency laws yielding to high resolution measure values.

4.1 Introduction

Just like some spectral estimates are better than others, some time-frequency distributions outperform others when used to analyze certain classes of signals [3, 39, 76, 77]. For example, the Wigner-Ville distribution (WVD) is known to be optimal for linear frequency modulated monocomponent signals since it achieves the best energy concentration around the signal IF law. The spectrogram, on the other hand, results in an undesirable smoothing of the signal energy around its IF [3]. Consequently, the choice of the right TFD to analyze a given signal is not straightforward. An illustration example is the bat echolocation signal [78] whose time and frequency variations are depicted in Fig. 4.1. This signal is represented in the $t-f$ plane using the WVD, the spectrogram, the Born-Jordan distribution, the Choi-Williams distribution, the Zhao-Atlas-Marks distribution, the CB TFD, the SCB TFD and the PCB TFD (Fig. 4.2). The KCS length is set to 64 while $D = \lambda = 3$.

According to the common practice, one would visually inspect the eight images then compare the different TFD plots and choose the most appealing one, i.e. the plot that corresponds to less interference and better components' concentration [2]. For our example, we can see that the KCS-based TFDs and the spectrogram have cleaner plots (better componenents' concentration and reduced interference) than the other distributions. However, the visual inspection is difficult and very subjective which justifies the need for an objective informational performance measure for TFDs.

Note that the plots and the numerical results are obtained from our realized toolbox (TFDOP) that uses some functions and graphical user interfaces of F. Auger et al. toolbox [79] in order to generate some synthetic signals and distributions and display the TFDs.

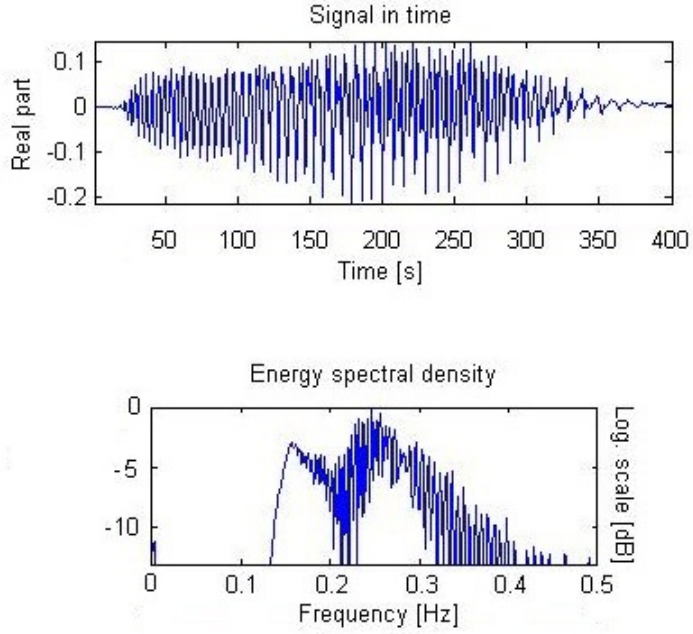

FIGURE 4.1 – Time and frequency representations of the bat echolocation signal.

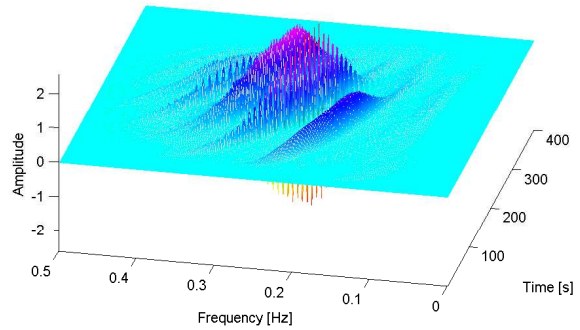
Amplitude
Frequency [Hz]
Time [s]

(a)

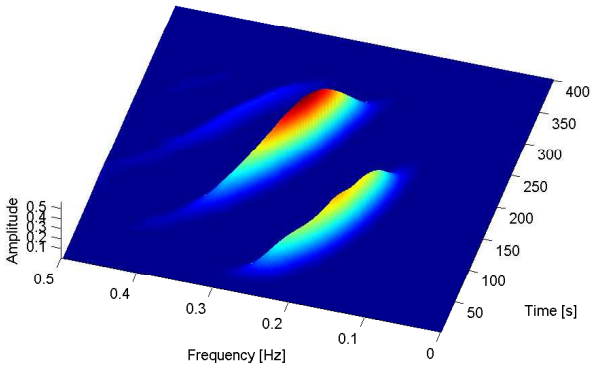
Amplitude
Frequency [Hz]
Time [s]

(b)

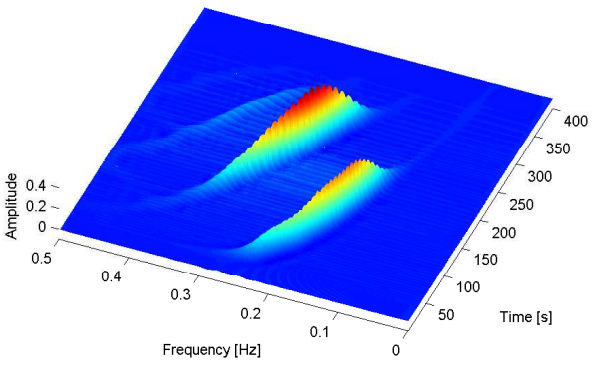
Amplitude
Frequency [Hz]
Time [s]

(c)

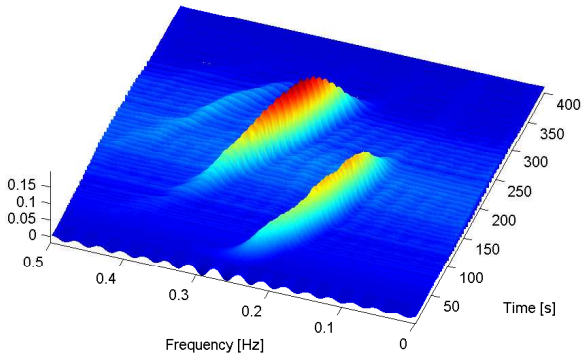
Frequency [Hz]
Time [s]

(d)

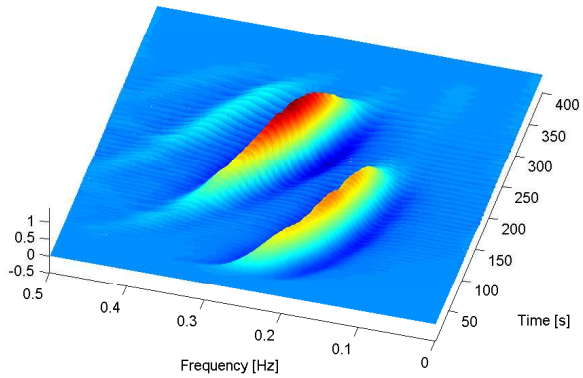
Frequency [Hz]
Time [s]

(e)

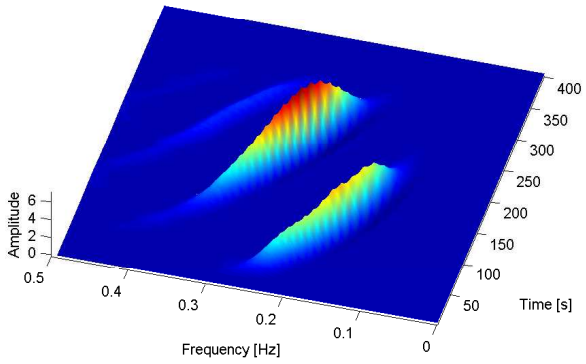
Amplitude
Frequency [Hz]
Time [s]

(f)

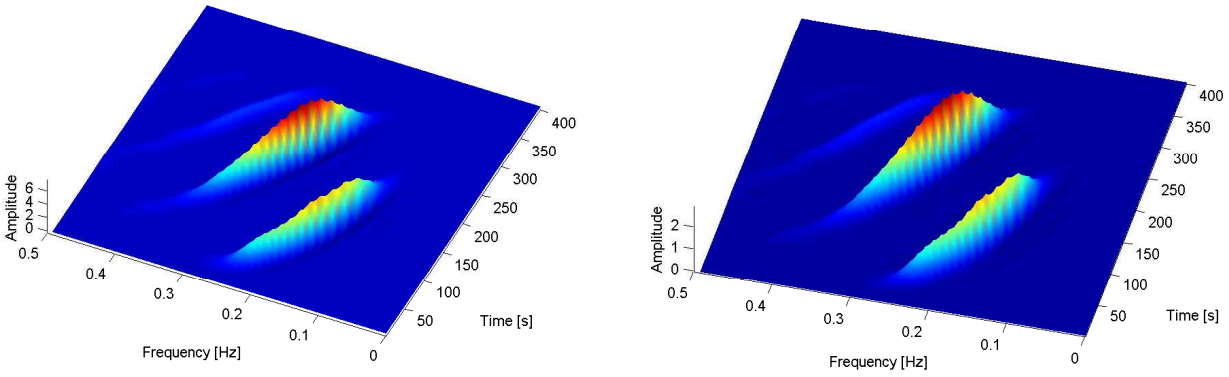

(g) (h)

FIGURE 4.2 – A selection of TFDs of the bat echolocation signal. (a) WVD, (b) Spectrogram (Hanning, $L = 55$), (c) BJD, (d) CWD ($\sigma = 0.6$), (e) ZAMD ($\alpha = 0.8$), (f) CB TFD ($C = 1.4$), (g) SCB TFD ($C = 1.4$) and (h) PCB TFD ($\gamma = 2$).

4.2 Concentration-based performance measures of TFDs

The performance of a given time-frequency representation of a multicomponent signal is usually measured through the inspection of three important criteria

- Concentration of the autoterms around the IF laws,
- Resolution of the individual nonstationary signal's components,
- Suppression of the crossterms of the TFD.

Among the quantitative performance measures that exist in the time-frequency signal analysis literature, few of them are based on an objective numerical evaluation of the goodness of a TFD. In this section, a selection of measurement methods based on concentration criterion are viewed and applied to different quadratic TFDs.

4.2.1 Rényi entropy

In [80], the entropy measure, originally used in probability, information theory and quantification of the diversity and uncertainty of a system ; was introduced in the field of time-frequency signal analysis in order to quantify the information by measuring the signal's complexity. By the probabilistic analogy, minimizing the complexity or information in a particular TFD is equivalent to maximizing its concentration, peakiness, and, therefore, resolution [81].

The continuous form of the Rényi entropy, introduced as a TFD measure by Sang and Williams [82], is given by

$$R_\alpha = \frac{1}{1-\alpha}\log_2 \int_{-\infty}^{+\infty}\int_{-\infty}^{+\infty} TFD_x^\alpha(t,f)dtdf \tag{4.1}$$

where α is the order of Rényi entropy and it is recommended to be greater than or equal to 2 for time-frequency applications [83]. The discrete form of this entropy is formulated as follows

$$R_\alpha = \frac{1}{1-\alpha}\log_2\left(\sum_n\sum_k TFD_x^\alpha(n,k)\right) \tag{4.2}$$

Such a measure of entropy is employed for estimating the concentration of a TFD according to the following rule : Small values of entropy correspond to low complexity/high concentration TFDs.

4.2.2 Rényi entropy normalized by signal energy

A normalized version of the Rényi entropy by the signal energy is defined as [82]

$$R_{NSE_\alpha} = \frac{1}{1-\alpha}\log_2\left(\frac{\int_{-\infty}^{+\infty}\int_{-\infty}^{+\infty} TFD_x^\alpha(t,f)dtdf}{\int_{-\infty}^{+\infty}\int_{-\infty}^{+\infty} TFD_x(t,f)dtdf}\right) \tag{4.3}$$

with $\alpha \geq 2$. Its discrete form is

$$R_{NSE_\alpha} = \frac{1}{1-\alpha}\log_2\left(\frac{\sum_n\sum_k TFD_x^\alpha(n,k)}{\sum_n\sum_k TFD_x(n,k)}\right) \tag{4.4}$$

4.2.3 Rényi entropy normalized by distribution volume

A normalized version of the Rényi entropy by the distribution volume is expressed as follows [82]

$$R_{NDV_\alpha} = \frac{1}{1-\alpha}\log_2\left(\frac{\int_{-\infty}^{+\infty}\int_{-\infty}^{+\infty} TFD_x^\alpha(t,f)dtdf}{\int_{-\infty}^{+\infty}\int_{-\infty}^{+\infty} |TFD_x(t,f)|dtdf}\right);\ \alpha \geq 2 \tag{4.5}$$

or equivalently, in the discrete form

$$R_{NDV_\alpha} = \frac{1}{1-\alpha}\log_2\left(\frac{\sum_n\sum_k TFD_x^\alpha(n,k)}{\sum_n\sum_k |TFD_x(n,k)|}\right) \tag{4.6}$$

4.2.4 Ratio of norms concentration measure

This measure was proposed by Jones and Parks [84]. It is defined as the ratio of the fourth power norm of $TFD_x(t,f)$ and its second power norm

$$RN = \frac{\int_{-\infty}^{+\infty}\int_{-\infty}^{+\infty} TFD_x^4(t,f)dtdf}{\left(\int_{-\infty}^{+\infty}\int_{-\infty}^{+\infty} TFD_x^2(t,f)dtdf\right)^2} \tag{4.7}$$

RN is given in the discrete case as follows

$$RN = \frac{\sum_n\sum_k TFD_x^4(n,k)}{\left(\sum_n\sum_k TFD_x^2(n,k)\right)^2} \tag{4.8}$$

The optimal distribution from concentration point of view is the one that maximizes the measure RN.

4.2.5 Stankovic concentration measure

Stankovic has developed a new optimization criterion for objective assessment of TFD's concentration. The proposed measure is defined in the continuous form as [85]

$$S_\beta = \left(\int_{-\infty}^{+\infty} \int_{-\infty}^{+\infty} |TFD_x(t,f)|^{(1/\beta)} dtdf \right)^\beta ; \ \beta \geq 2 \tag{4.9}$$

Its discrete expression is given by

$$S_\beta = \left(\sum_n \sum_k |TFD_x(n,k)|^{(1/\beta)} \right)^\beta \tag{4.10}$$

This concentration measure was used for the optimal window selection in the spectrogram [4]. The optimized distribution results on high concentration of the autoterms. This corresponds to the smallest value of S_β.

4.2.6 Comparative study of concentration-based performance measures

The first comparative example concerns the bat echolocation real-life signal whose time-frequency characteristics are depicted in Fig. 4.2. Table 4.1 provides comparisons between several popular concentration-based performance measures of TFDs in representing the investigated signal.

Table 4.1 – Concentration-based performance measures for a selection of TFDs of the bat echolocation signal.

TFD	Optimal kernel parameters	R_{NSE_3}	R_{NDV_3}	$RN(\times 10^4)$	$S_4(\times 10^{-8})$
WVD	N/A	4.1652	5.2922	3.84	5.4639
Spectrogram	Hanning, $L = 55$	4.4409	4.4409	3.38	0.3511
BJD	N/A	4.4429	4.7582	2.73	1.6843
CWD	$\sigma = 0.6$	5.0425	5.1125	1.2	1.6500
ZAMD	$\alpha = 0.8$	4.0625	5.6043	1.08	11.644
CB TFD	$C = 1.4$	4.7542	4.7788	11.46	0.3959
SCB TFD	$C = 1.4$	4.7436	4.7921	12.12	0.4143
PCB TFD	$\gamma = 2$	3.8948	3.9015	11.63	0.0539

We observe that the energy normalized Rényi entropy measure R_{NSE_3} defines the ZAMD and the WVD as the best-performing TFDs after the PCB TFD. On the other hand, the SCB TFD and the CB TFD are identified as the worst-performing representations together with the CWD while the BJD performs as well as the spectrogram.

The volume normalized Rényi entropy measure R_{NDV_3} classifies the PCB TFD as the best TFD in representing the bat echolocation signal followed by the spectrogram and the BJD whose concentration performance is better than the CB TFD and the SCB TFD.

The ratio of norms measure RN is optimized using the KCS-based TFDs, as expected from the plots of Fig. 4.2. However, the WVD is classified as the signal fourth best TFD, better than the spectrogram, the BJD, the CWD and the ZAMD TFDs.

It is obvious that neither R_{NSE_3}, R_{NDV_3} nor RN can exactly match the expected results of TFDs' performances in accordance to the visual inspection of the $t-f$ plots. We deduce that minimizing the Rényi entropy or maximizing the ratio of norms does not imply necessarily good resolution measure and better crossterms' suppression.

The measure S_4 identifies the KCS-based TFDs as the signal best representations followed by the spectrogram. This approaches from the visual inspection results and then the Stankovic measure is, in this case, the best informative one in terms of accurate concentration/resolution performances and crossterms reduction indications.

The second example deals with a two-component synthetic signal of duration $T = 128$ that contains two crossing quadratic FMs such that ($f(t = 1) = f(t = 128) = 0.1$ Hz; $f(t = 64) = 0.35$ Hz) for the concave component and ($f(t = 1) = f(t = 128) = 0.3$ Hz; $f(t = 64) = 0.15$ Hz) for the convex one. We inspect again the coherence between a selection of quadratic time-frequency plots of Fig. 4.3 and the numerical values depicted in Table 4.2 presenting a set of concentration-based performance measures.

TABLE 4.2 – Concentration-based performance measures for a selection of TFDs of a signal consisting of two crossing quadratic FMs.

TFD	Optimal kernel parameters	R_{NSE_3}	R_{NDV_3}	$RN(\times 10^4)$	$S_4(\times 10^{-17})$
WVD	N/A	5.7202	6.8062	6.14	3.5967
Spectrogram	Bartlett, $L = 27$	5.7752	5.7752	13.45	0.0902
BJD	N/A	5.7862	6.0471	6.89	0.6711
CWD	$\sigma = 0.85$	5.8153	6.1853	20.75	1.5265
ZAMD	$\alpha = 0.16$	5.6468	6.9282	7.57	5.7092
CB TFD	$D = 3$, $C = 7$	6.8675	6.8703	12.23	0.1413
SCB TFD	$D = 3$, $C = 10.2$	6.7742	6.7775	13.39	0.1225
PCB TFD	$\lambda = 3$, $\gamma = 11$	6.4623	6.4627	13.44	0.0719

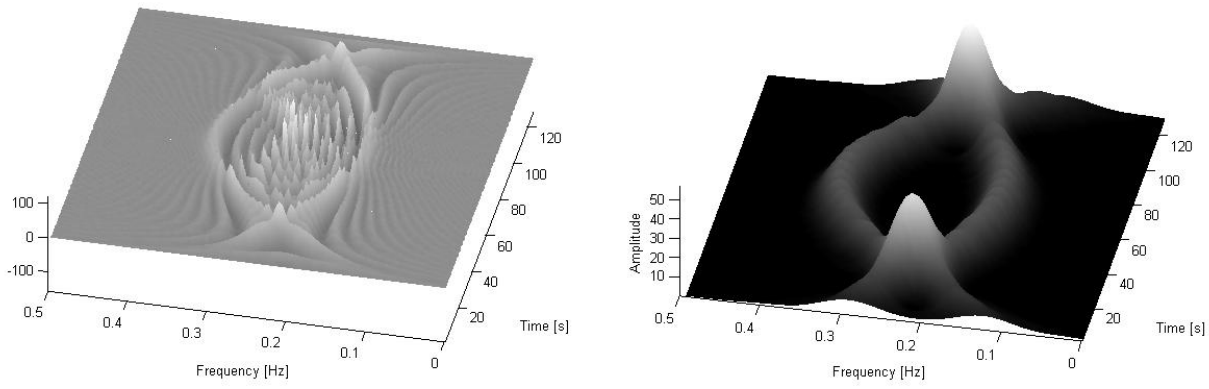

(a) (b)

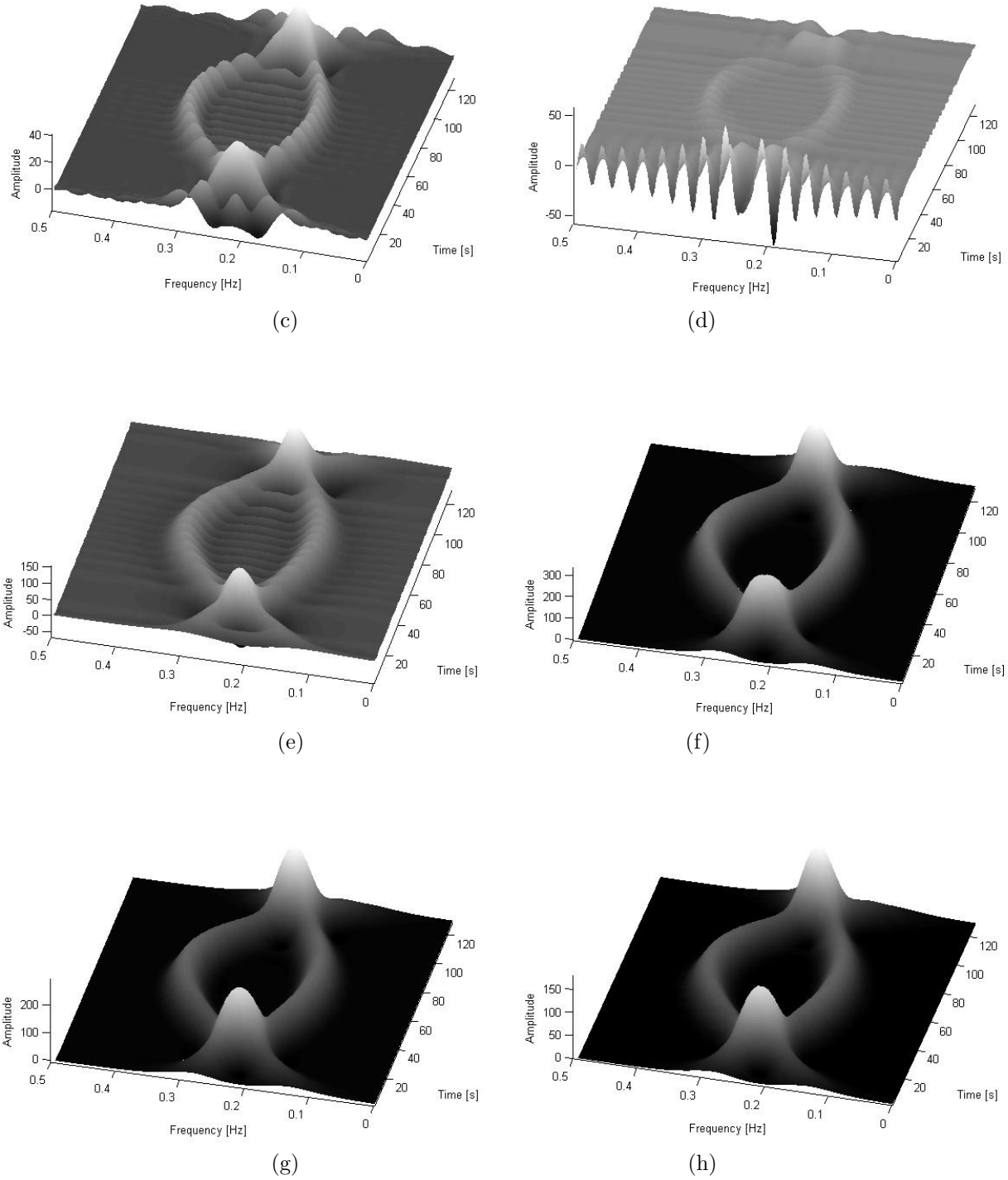

FIGURE 4.3 – A selection of TFDs of a signal composed of two crossing quadratic FMs. (a) WVD, (b) Spectrogram (Bartlett, $L = 27$), (c) BJD,(d) CWD ($\sigma = 0.85$), (e) ZAMD ($\alpha = 0.16$), (f) CB TFD ($D = 3$, $C = 7$), (g) SCB TFD ($D = 3$, $C = 10.2$) and (h) PCB TFD ($\lambda = 3$, $\gamma = 11$).

From theoretical point of view, the energy normalized Rényi entropy measure of order 3 classifies the ZAMD and the WVD as the optimal representations whereas the KCS-based TFDs are defined as the worst ones. Furthermore, the spectrogram, the BJD and the CWD perform almost the same.

The volume normalized Rényi entropy measure R_{NDV_3} identifies the spectrogram, the BJD, the CWD and the PCB TFD as the fourth best performing TFDs while the WVD is found to outperform the CB TFD and the ZAMD.

The RN measure is maximized by the CWD that performs better than the spectrogram and the KCS-based TFDs. On the other hand, the ZAMD, the BJD and the WVD are classified as the signal three worst TFDs.

The Stankovic measure S_4 is minimized using the PCB TFD followed by the spectrogram, the SCB TFD and the CB TFD. The BJD performs better than the CWD. The signal two worst representations are the WVD and the ZAMD.

From Fig. 4.3, we see clearly that the TFDs derived from the KCS kernels and the spectrogram provide the most appealing plots and hence are the best representations of the nonlinear nonstationary signal in terms of energy concentration, components' resolution and crossterms' suppression. However, the investigated theoretical measures fail to identify the optimal TFDs in the right order of increasing performance. We conclude that the consideration of concentration as a unique optimization criterion is not sufficient for objective assessment of time-frequency representations.

4.3 Boashash-Sucic performance measure

From Sec. 4.2, we have concluded that efficient TFD concentration and resolution measurement can provide a quantitative criterion to evaluate performances of different distributions and can be used for adaptive and automatic parameters selection in $t-f$ analysis [4]. Signal parameters important to be considered for this purpose are shown in Fig. 4.4, which represents a time slice (t=t_0) of a typical quadratic TFD of a two-component signal. The two dominant peaks are the signal resolved components with the corresponding magnitudes A_{M_1} and A_{M_2} and the instantaneous bandwidths V_{i_1} and V_{i_2}, centered about the components' IFs $f_{i_1}(t)$ and $f_{i_2}(t)$. The middle peak is the crossterm of magnitude A_X, whereas other smaller peaks are the two components' sidelobes with magnitudes A_{S_1} and A_{S_2} [2, 26].

From Fig. 4.4, it is seen that the frequency resolution can be quantified by the minimum difference $f_{i_2}(t)-f_{i_1}(t)$ for which a separation measure D between the components' mainlobes, centered about their respective IFs $f_{i_1}(t)$ and $f_{i_2}(t)$ is positive. The components' separation measure D is defined as [2, 4]

$$D(t)=\frac{\left(f_{i_2}(t)-\frac{V_{i_2}(t)}{2}\right)-\left(f_{i_1}(t)+\frac{V_{i_1}(t)}{2}\right)}{f_{i_2}(t)-f_{i_1}(t)}=1-\frac{V_i(t)}{\triangle f_i(t)} \tag{4.11}$$

where $V_i(t)=(V_{i_1}(t)+V_{i_2}(t))/2$ is the components' mainlobes average instantaneous bandwidth, and $\triangle f_i(t)=f_{i_2}(t)-f_{i_1}(t)$ is the difference between the components' IFs. By combining these parameters, the Boashash-Sucic's normalized instantaneous resolution

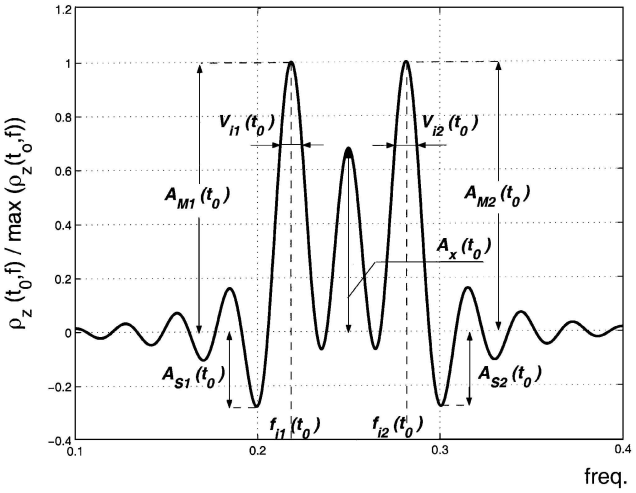

FIGURE 4.4 – Slice of a TDF $\rho_z(t, f)$ of a two-component FM signal $z(t)$ taken at the time instant $t = t_0$ (adopted from Boashash [2].)

performance measure P_i is defined as [2, 4, 86]

$$P_i(t) = 1 - \frac{1}{3}\left[\frac{A_S(t)}{A_M(t)} + \frac{1}{2}\frac{A_X(t)}{A_M(t)} + (1 - D(t))\right], \quad 0 < P_i(t) < 1 \tag{4.12}$$

A_M, A_S, A_X are respectively the average amplitudes of the main-lobes, side-lobes and crossterms of two consecutive signal components. P_i is close to 1 for well-performing TFDs and 0 for poorly-performing ones. An overall measure P is taken to be the median of the instantaneous measures P_i corresponding to different time slices in the relevant sections of the signals.

The parameters in (4.12) can be computed automatically for a two-component signal's TFD using the methodology described in [1, 26]. This includes the following steps :

1. Calculate $TFD_s(t, f)$, the TFD of the signal $s(t)$. The kernel parameters are initially set to a value close to their lower bounds,
2. Take a time slice of $TFD_s(t, f)$ at the instant $t = t_0$,
3. Normalize $TFD_s(t_0, f)$ so that its global maximum is 1,
4. Determine the three largest peaks of $TFD_s(t_0, f)$ (in our implementation we have considered $|TFD_s(t_0, f)|$ so that the largest peak correspond always to a positive maximum),
5. The middle peak is initially considered to be the crossterm,
6. Verify that the ratio between the remaining two peaks is close to one, and that the peak selected as the crossterm is located close to the mid-point between the centers (f_{i_1} and f_{i_2}) of the other two peaks. Otherwise, select the two largest peaks as the autoterms located at frequencies f_{i_1} and f_{i_2}, respectively, and the maximum located half-way between the autoterms IFs as the crossterm,

7. The average of the autoterms amplitudes presents the parameter A_M in (4.12), whereas the magnitude of the crossterm presents the parameter A_X,

8. Measure the components bandwidths at -3 dB of the autoterms' amplitudes and check whether the components are resolved by referring to condition (3.107). For the resolved components, calculate the parameter D in (4.11). Note that if most of the components are not resolved for some region of interest of time instants, the TFDOP toolbox displays a warning message indicating to the user to change the parameters' setting of the considered TFD and then repeat the optimization procedure again,

9. Define the components' sidelobes corresponding to the largest peaks located at the left side of the first component and the right side from the second component as shown in Fig. 4.4. Their average presents the parameter A_S in (4.12),

10. Compute the Boashash-Sucic's normalized instantaneous resolution performance measure P_i defined by (4.12) and evaluated at $t = t_0$,

11. Repeat the steps 1-10 for a defined time interval $[t_{start}, t_{end}]$ that can be set by the user through the TFDOP toolbox (see Appendix A). The average of the P_i values is defined as the overall performance measure $P_{overall}$ of the considered TFD given its specific kernel parameters. The entire procedure must be repeated for different values of the kernel's parameters so that the optimal ones (relatively to the given TFD and given signal) correspond to those resulting into the largest $P_{overall}$,

12. After optimizing different TFDs in this way, the optimized TFD which possesses the largest value of $P_{overall}$ among the whole set of the considered TFDs is selected as the best-performing one in representing the signal $s(t)$ in the $t - f$ plane.

Note that the algorithm above can be generalized to optimize nonstationary signals with more than two components as illustrated for example in Sec. 4.4.4. In all tests presented in the remainder of this thesis, the incremental step size of the kernel parameter is 2 for the spectrogram window size and as small as 0.01 for the other smoothing parameters of the kernels. The purpose is to define with high precision the desired global optimum of $P_{overall}$. Unless indicated, a default length $L = 64$ is used for the three time-lag compact support kernels while D and λ are set to 5.

4.4 TFDs' optimization using Boashash-Sucic performance measure : Experimental results

The performance of the KCS-based TFDs is compared to the classical best known time-frequency distributions. Four examples are considered and discussed in detail in order to evaluate each TFD and determine the best one in terms of concentration and resolution. The TFDs with smoothing parameters are first optimized and their relative overall performance measure P values are recorded in tables where

$$P = \frac{1}{N} \sum_{j=1}^{N} P_i(t_0 = j); \tag{4.13}$$

and N is the full range of time instants. Then, the maximum value among them is selected and it corresponds to the best performing TFD in representing the multicomponent test signal.

4.4.1 Example 1 : Sum of two crossing linear FM signals

Here, we deal with a multicomponent signal $s_1(t)$ of duration $T = 128$ composed of two noiseless crossing chirps of frequency ranges $f = [0.1 - 0.2]$ Hz and $f = [0.2 - 0.1]$ Hz, respectively. The time-frequency representations of the signal $s_1(t)$ are given in Fig. 4.5 using several popular TFDs together with the CB TFD, the SCB TFD and the PCB TFD. It can be seen that the KCS-based TFDs and the spectrogram have the greatest ability to remove the cross terms and present all clear curves in contrast to the other representations. Let us examine in depth the performance of each distribution. For this purpose, the considered TFDs are optimized with respect to the Boashash-Sucic's criterion over the time interval $[1, T]$ except for the WVD and the BJD that have no smoothing parameters and then they cannot be optimized.

The resulting P's values are recorded in Table 4.3 and they clearly reveal that the KCS-based TFDs produce the best performance compared with the other time-frequency representations. Moreover, the CB TFD with control parameter $C = 1.44$ gives the largest value of P and hence is selected as the best performing TFD of the signal $s_1(t)$ [87].

4.4.2 Example 2 : Sum of two parallel FM signals

As a second illustration test, we consider a multicomponent signal $s_2(t)$ of length $N = 128$ that consists of two closely spaced parallel linear FMs with frequencies increasing from 0.15 to 0.25 Hz and from 0.2 to 0.3 Hz, respectively. The signal $s_2(t)$ is analyzed in the $t - f$ domain using the same selection of TFDs as in example 1. The time-frequency plots of the optimized TFDs according to Boashash-Sucic's performance measure are shown in Fig. 4.6, where we can see that the CB TFD, the SCB TFD and the PCB TFD have all clear plots since the two time-varying components of the signal $s_2(t)$ are well concentrated in their respective frequency ranges and the interferences between them are largely attenuated by the effects of the compact support nature of the three investigated kernels.

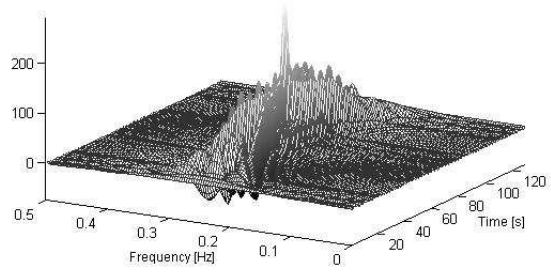
200
100
0
0.5
0.4
0.3
0.2
0.1
0
Frequency [Hz]
20
40
60
80
100
120
Time [s]

(a)

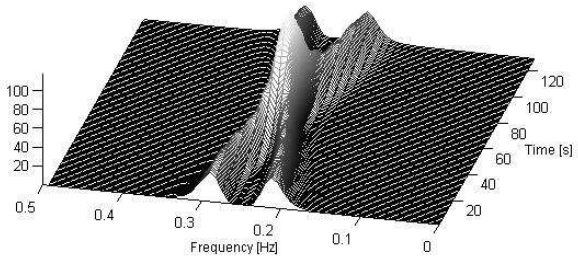
100
80
60
40
20
0.5
0.4
0.3
0.2
0.1
0
Frequency [Hz]
120
100
80
60
40
20
Time [s]

(b)

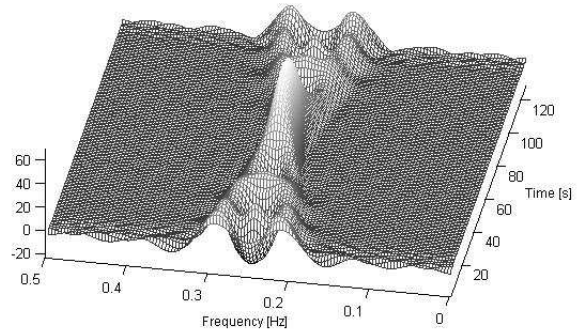
60
40
20
0
-20
0.5
0.4
0.3
0.2
0.1
0
Frequency [Hz]
120
100
80
60
40
20
Time [s]

(c)

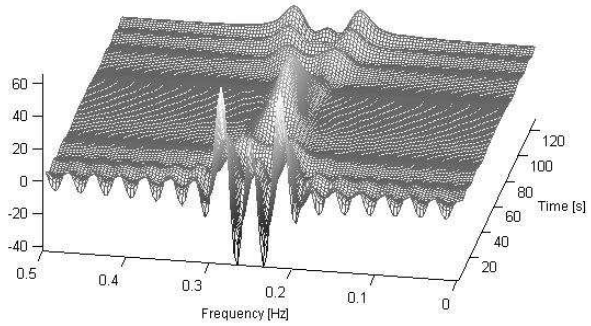
60
40
20
0
-20
-40
0.5
0.4
0.3
0.2
0.1
0
Frequency [Hz]
120
100
80
60
40
20
Time [s]

(d)

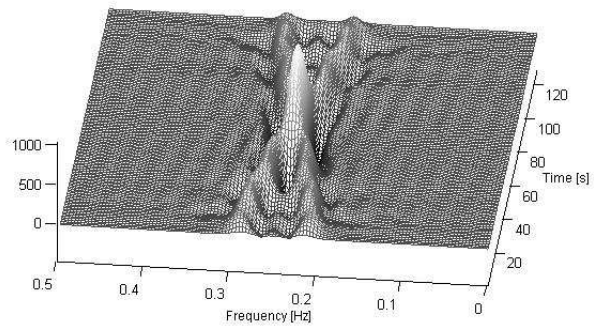
1000
500
0
0.5
0.4
0.3
0.2
0.1
0
Frequency [Hz]
120
100
80
60
40
20
Time [s]

(e)

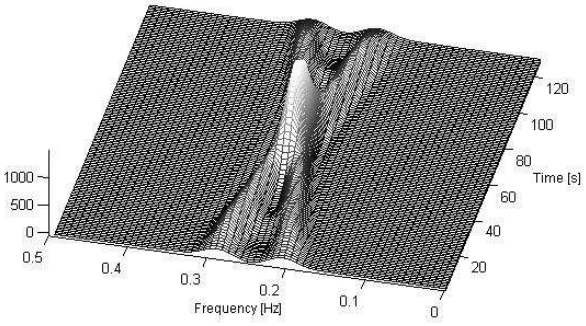
1000
500
0
0.5
0.4
0.3
0.2
0.1
0
Frequency [Hz]
120
100
80
60
40
20
Time [s]

(f)

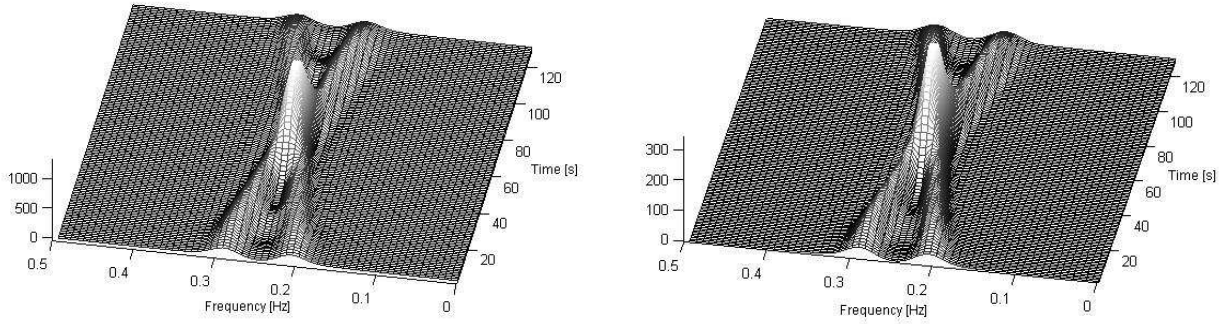

(g) (h)

FIGURE 4.5 – Optimized TFDs over the entire time interval $[1, 128]$ of the signal of example 1 composed of two crossing chirps with frequency ranges $f = 0.1-0.2$ Hz and $f = 0.2-0.1$ Hz, respectively. (a) WVD, (b) Spectrogram (Hanning, L=85), (c) BJD, (d) CWD (σ =0.45), (e) ZAMD (α=0.8), (f) CB TFD (C=1.44), (g) SCB TFD (C=2.1) and (h) PCB TFD (γ=2).

TABLE 4.3 – Optimization results for a selection of TFDs of the signal of example 1 (two crossing chirps test).

TFD	Optimal kernel Parameters	P
WVD	N/A	0.6581
Spectrogram	Hanning, $L = 85$	0.8588
BJD	N/A	0.7072
CWD	$\sigma = 0.45$	0.7269
ZAMD	$\alpha = 0.8$	0.6822
CB TFD	$C = 1.44$	0.8708
SCB TFD	$C = 2.1$	0.8678
PCB TFD	$\gamma = 2$	0.8626

In this example, we first compare the TFDs' resolution performance at time instant $t_0 = 64$; the middle of the signal duration, including the Modified B-distribution (MBD) [41, 42] as well. Table 4.4 reports the related performed measurements by referring to the Boashash-Sucic's methodology that is used to compute the parameters of (4.12), whereas Fig. 4.7 shows the slices of a selection of TFDs at $t_0 = 64$. It indicates that the SCB TFD with smoothing parameter $C = 0.13$ is the optimal TFD of the signal $s_2(t)$ at this time instant giving the largest value of P_i. Let us then search for the TFD that best resolves the two chirp components of the signal $s_2(t)$ over the entire time interval [1,128]. Table 4.5 contains the optimization process and indicates that the KCS-based TFDs outperform the other quadratic time-frequency distributions. Furthermore, it shows that the signal $s_2(t)$ is best presented in the $t - f$ plane using the CB TFD with parameter $C = 0.11$

since it has the largest value of P.

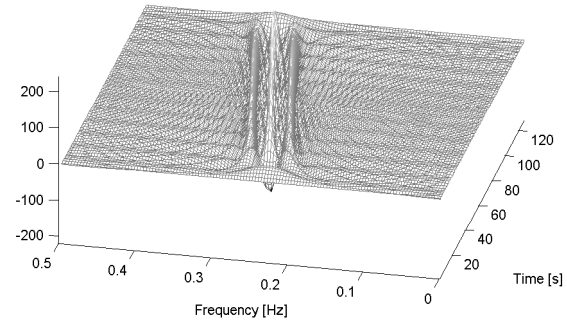

(a)

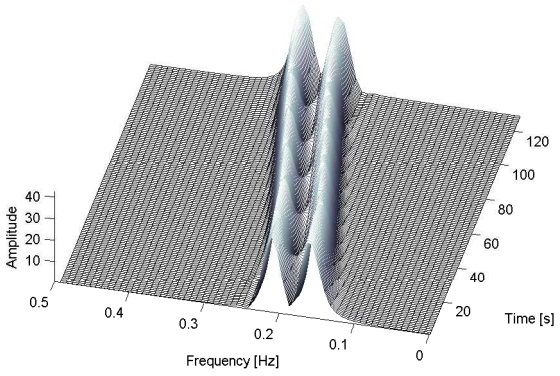

(b)

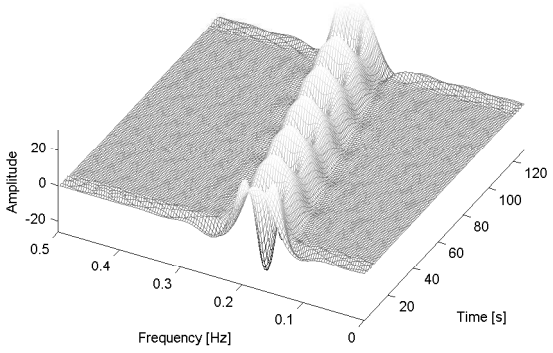

(c)

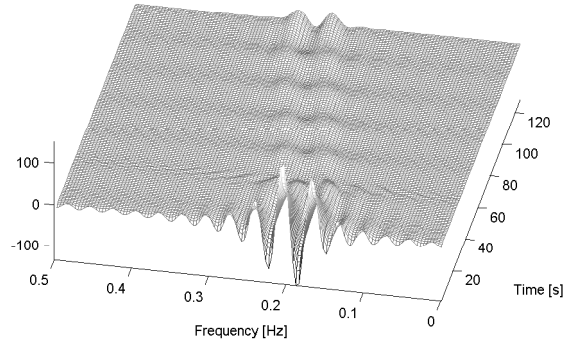

(d)

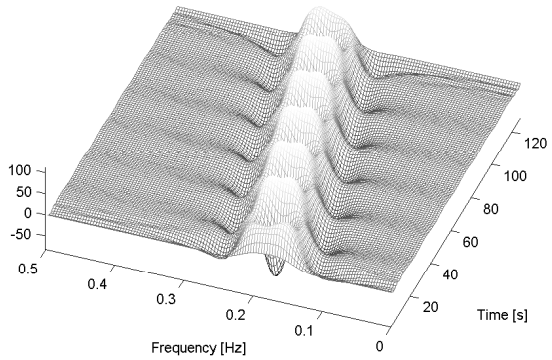

(e)

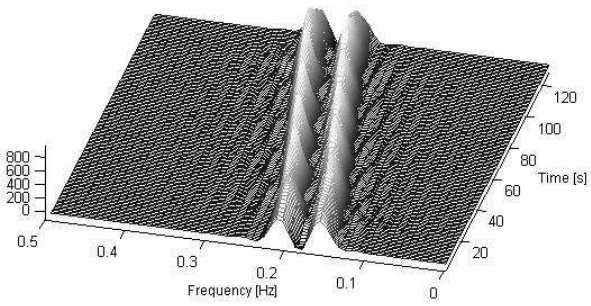

(f)

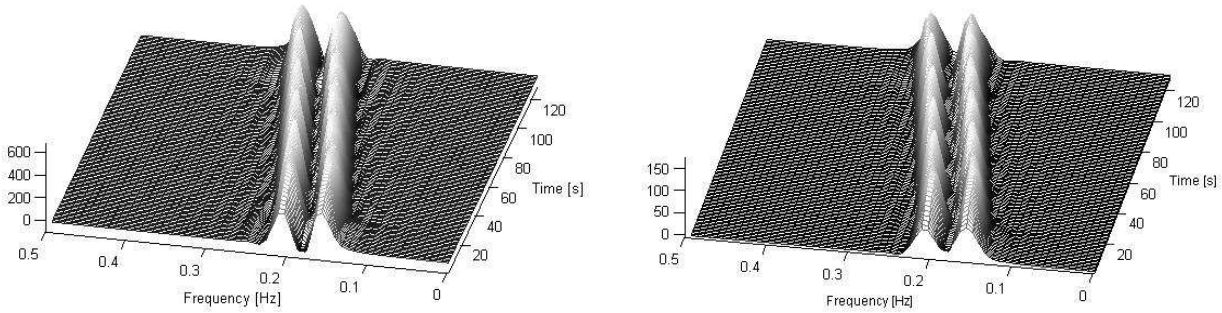

(g) (h)

FIGURE 4.6 – Optimized TFDs over the entire time interval $[1, 128]$ of the signal of example 2 composed of two parallel LFMs with frequency ranges spreading from 0.15 to 0.25 Hz and 0.2 to 0.3 Hz, respectively. (a) WVD, (b) Spectrogram (Hanning, $L = 73$), (c) BJD,(d) CWD ($\sigma = 1.2$), (e) ZAMD ($\alpha = 0.8$), (f) CB TFD ($C = 0.11$), (g) SCB TFD ($C = 0.487$) and (h) PCB TFD ($\gamma = 1$).

TABLE 4.4 – Parameters and the normalized instantaneous resolution performance measure P_i of different TFDs for the time instant $t_0 = 64$ related to example 2. The first six measurements are adopted from [2].

TFD (optimal parameter)	$A_M(64)$	$A_S(64)$	$A_X(64)$	$V_i(64)$	$\Delta f_i(64)$	$D(64)$	$P_i(64)$
WVD	0.9153	0.3365	1	0.0130	0.0574	0.7735	0.6199
Spectrogram (Hanning, $L = 35$)	0.9119	0.0087	0.5527	0.0266	0.0501	0.4691	0.7188
BJD	0.9320	0.1222	0.3798	0.0219	0.0488	0.5512	0.7388
CWD ($\sigma = 2$)	0.9355	0.0178	0.4415	0.0238	0.0493	0.5172	0.7541
ZAMD ($\alpha = 2$)	0.9146	0.4847	0.4796	0.0214	0.0420	0.4905	0.5661
Modified B ($\beta = 0.01$)	0.9676	0.0099	0.0983	0.0185	0.0526	0.5957	0.8449
CB TFD ($C = 0.48$)	0.9941	0.0314	0.0179	0.0159	0.0556	0.7143	0.8912
SCB TFD ($C = 0.13$)	0.9868	0.0183	0.0323	0.0159	0.0556	0.7143	0.8931

TABLE 4.5 – Optimization results for a selection of TFDs of the signal $s_2(t)$ using Boashash-Sucic methodology.

TFD	Optimal kernel Parameters	P
WVD	N/A	0.6449
Spectrogram	Hanning, $L = 73$	0.8232
BJD	N/A	0.6860
CWD	$\sigma = 1.2$	0.7228
ZAMD	$\alpha = 0.8$	0.6856
CB TFD	$C = 0.11$	0.8449
SCB TFD	$C = 0.487$	0.8442
PCB TFD	$\gamma = 1$	0.8409

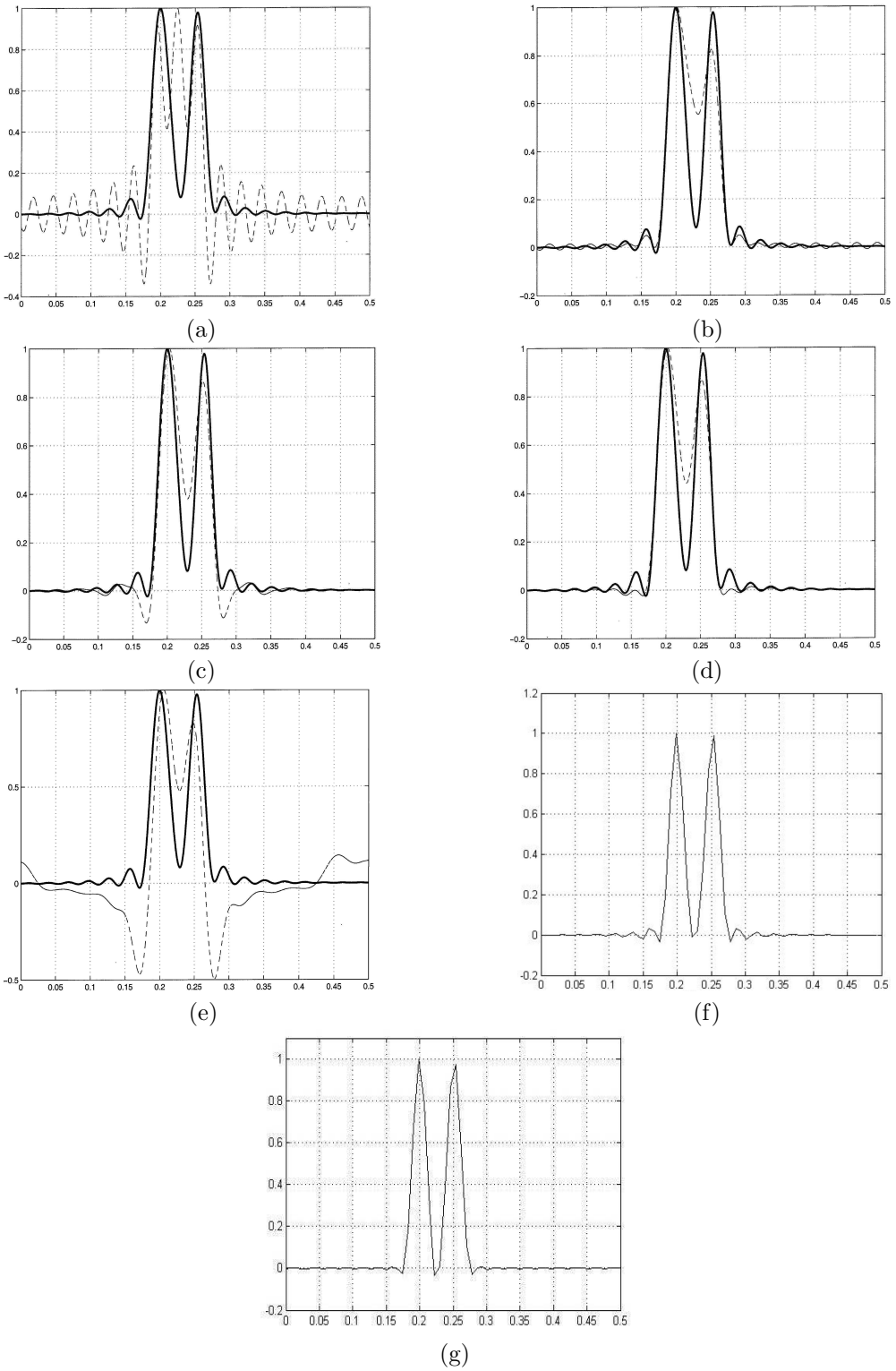

FIGURE 4.7 – Normalized slices of TFDs at t_0=64 of the signal $s_2(t)$. (a) WVD, (b) Spectrogram (Hanning, $L = 35$), (c) BJD,(d) CWD ($\sigma = 2$), (e) ZAMD ($\alpha = 2$), (f) CB TFD ($C = 0.48$) and (g) SCB TFD ($C = 0.13$). The first five plots are adopted from [2] and compare the TFDs (dashed) against the Modified B-distribution ($\beta = 0.01$) (solid).

Given the optimal kernel parameters of Table 4.5, we compare next the same TFDs using a selection of concentration measures described in Sec. 4.2. The obtained results are recorded in Table 4.6 together with the P values in order to permit quantitative analysis and comparison.

TABLE 4.6 – Optimization results for a selection of TFDs of the signal $s_2(t)$ using several performance measures.

TFD	Optimal kernel Parameters	R_{NSE_4}	R_{NDV_4}	$RN(\times 10^3)$	$S_4(\times 10^{-16})$	P
WVD	N/A	3.8318	4.3738	2.5380	19.6868	0.6449
Spectrogram	Hanning, $L = 73$	3.9116	3.9116	1.1380	0.2260	0.8232
BJD	N/A	3.9394	4.0901	0.5860	3.2865	0.6860
CWD	$\sigma = 1.2$	3.8795	4.0975	4.6640	11.5398	0.7228
ZAMD	$\alpha = 0.8$	3.8289	4.7735	0.4710	50.9235	0.6856
CB TFD	$C = 0.11$	5.0370	5.0672	1.5300	5.6429	0.8449
SCB TFD	$C = 0.487$	4.9554	4.9831	1.3230	2.6746	0.8442
PCB TFD	$\gamma = 1$	4.0003	4.0069	1.3160	0.2484	0.8409

We see that the R_{NSE_4} measure identifies the ZAMD and the WVD as the best TFDs, the BJD is performing as well as the spectrogram while the KCS-based TFDs are classified as the signal worst representations. On the other hand, R_{NDV_4} defines the spectrogram and the PCB TFD as the best distributions followed by the BJD, the CWD, the WVD and the ZAMD TFDs whose concentration measures are higher than the SCB TFD and the CB TFD.

The ratio of norms concentration measure is maximized using the CWD followed by the WVD and the CB TFD. The SCB TFD and the PCB TFD outperform the spectrogram while the BJD and the ZAMD are classified as the worst representations.

The Stankovic measure of order $\beta = 4$ favors the spectrogram, the PCB TFD and the SCB TFD and classifies the CWD, the WVD and the ZAMD as the worst performing TFDs of the signal $s_2(t)$. Moreover, the BJD is judged to perform better than the CB TFD which does not correspond to the plots of Fig. 4.6.

Comparing these results to the P values indicates clearly that the Boashash-Sucic performance measure is the most objective and coherent one in optimizing the different quadratic TFDs and guides the analyst to the best choice of the representation that reveals the most important information about the time-frequency variations and characteristics of the considered signal. The most notable drawback of the Boashash-Sucic methodology is that it requires to be repeated $(M + 1)/2$ times for a signal containing an odd number M of distinct components and $M/2$ times for M even. This is because each inspected time slice corresponds to a unique pair of components unless we identify and optimize only the two overall closest components present in the signal as illustrated in Sec. 5.3. The second drawback is the high processing time needed to get the optimal TFD depending on the signal length, the numerical complexity of the TFD, the optimization region of interest of time instants and frequencies and the incremental step size of the kernel parameters. This is due to the fact that the Boashash-Sucic performance measure parameters defined by (4.11) and (4.12) are computationally expensive because they need many calculations for each time instant.

4.4.3 Example 3 : Effect of additive noise

In order to check the behavior of TFDs in the case of noisy multicomponent signals, let us search for the optimal TFD of the two-component signal $s_2(t)$ considered in example 2, embedded in additive white Gaussian noise, with a signal-to-noise ratio of 10 dB. The test signal, denoted by $s_3(t)$, is analyzed in the $t-f$ domain using a selection of quadratic TFDs.

The time-frequency plots of the optimized TFDs under the constraints of Boashash-Sucic's criterion are shown in Fig. 4.8. Here again, from visual inspection, we can see that the KCS-based TFDs and the spectrogram perform much better than the other considered TFDs since they generate the most appealing plots.

Fig. 4.9 presents the time slice plots of a selection of TFDs at $t_0 = 67$. The parameters recorded in Table 4.7 are computed using the Boashash-Sucic's procedure and they reflect the high concentration and resolution performances of the KCS-based representations [88].

Table 4.8 records the final numerical results of the optimization process over the entire time interval [1,128] and reveals that the optimal TFD of the noisy signal $s_3(t)$ is the CB TFD with smoothing parameter $C = 0.11$ since it possesses the largest value of P followed by the SCB TFD then the PCB TFD [88].

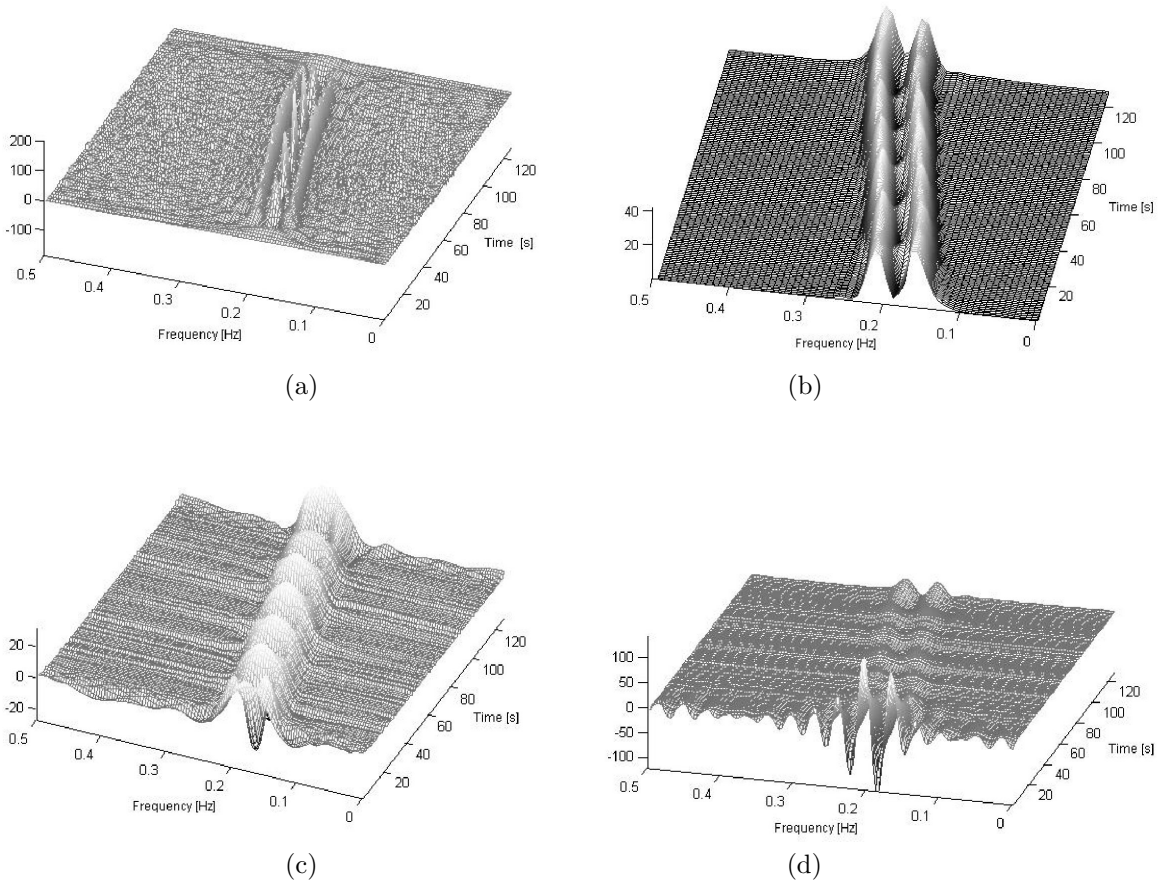

(a) (b)

(c) (d)

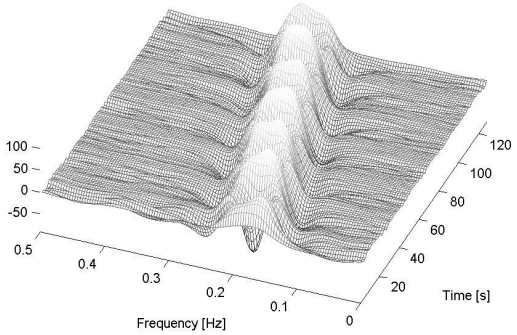

(e)

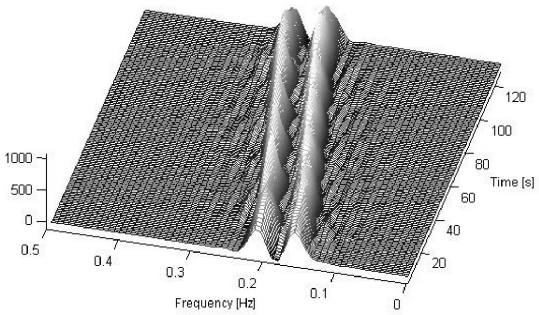

(f)

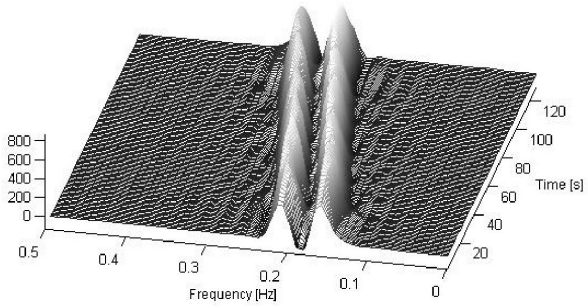

(g)

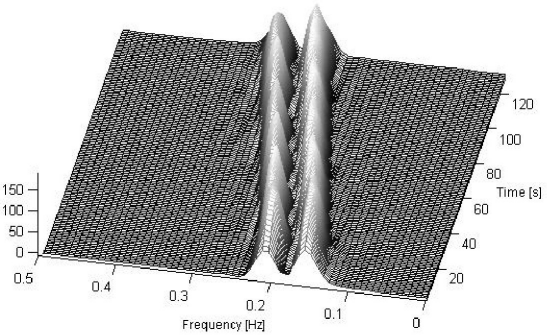

(h)

FIGURE 4.8 – Optimized TFDs over the full duration $T = 128$ of the signal of example 3 composed of two parallel LFMs with frequency ranges spreading from 0.15 to 0.25 Hz and 0.2 to 0.3 Hz, respectively ; embedded in 10 dB AWGN. (a) WVD, (b) Spectrogram (Bartlett, $L = 71$), (c) BJD,(d) CWD ($\sigma = 0.9$), (e) ZAMD ($\alpha = 0.56$), (f) CB TFD ($C = 0.11$), (g) SCB TFD ($C = 0.28$) and (h) PCB TFD ($\gamma = 1$).

A last important point concerns the instantaneous frequency estimation. As noted in Sec. 3.8, obtaining the IF laws information from the peaks of the TFD is an important property that should be satisfied for any practical time-frequency analysis. Table 4.7 and Fig. 4.9 show that the KCS TFDs provide accurate IF estimates for both components calculated from the peaks of the TFDs' dominant ridges (A_{M_1} and A_{M_2}).

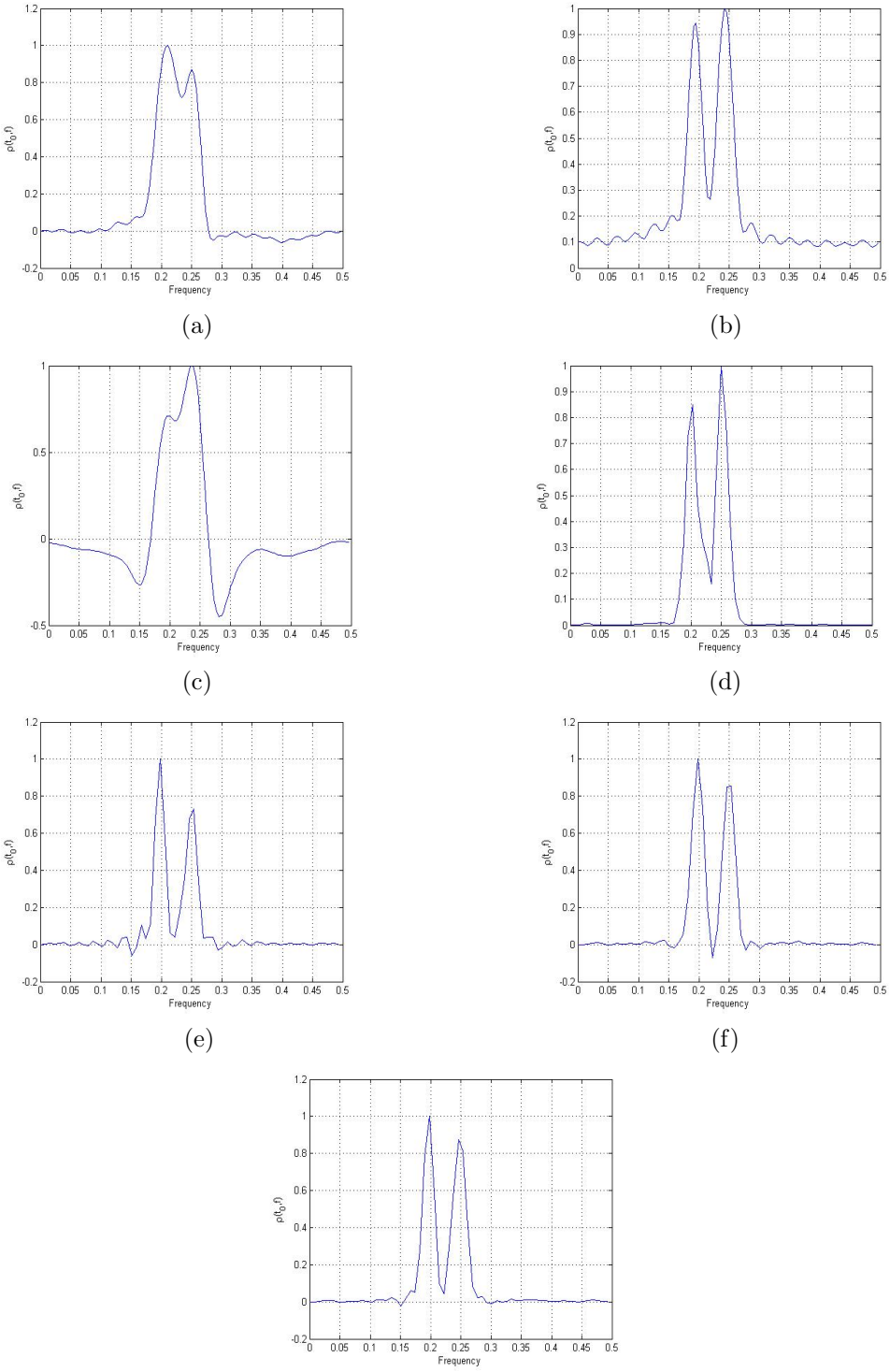

FIGURE 4.9 – Normalized slices of TFDs at t_0=67 of the signal $s_3(t)$. (a) BJD, (b) CWD ($\sigma = 0.9$), (c) ZAMD ($\alpha = 0.56$), (d) Spectrogram (Bartlett, $L = 71$), (e) CB TFD ($C = 0.11$), (f) SCB TFD ($C = 0.28$) and (g) PCB TFD ($\gamma = 1$).

TABLE 4.7 – Parameters and P_i values of different TFDs of example 3 computed at the time instant $t_0 = 67$.

TFD (optimal parameters)	A_M	A_S	A_X	f_{i_1}	f_{i_2}	V_{i_1}	V_{i_2}	V_i	Δf_i	D	P_i
BJD	0.9632	0.4210	0.7670	0.2578	0.3008	0.0234	0.0234	0.0234	0.0430	0.4545	0.5398
CWD ($\sigma = 0.9$)	0.9565	0.1903	0.2498	0.2031	0.2539	0.0313	0.0156	0.0234	0.0508	0.5385	0.7363
ZAMD ($\alpha = 0.56$)	0.8921	0.5292	0.7602	0.2070	0.2461	0.0234	0.0313	0.0273	0.0391	0.3000	0.4269
Spectrogram (Bartlett, $L = 71$)	0.8153	0.0087	0.1605	0.2031	0.2578	0.0203	0.0101	0.0152	0.0547	0.7219	0.8709
CB TFD ($C = 0.11$)	0.8658	0.0483	0.1751	0.1984	0.2540	0.0159	0.0094	0.0127	0.0556	0.7723	0.8718
SCB TFD ($C = 0.28$)	0.9269	0.0268	0.0817	0.1984	0.2540	0.0159	0.0099	0.0129	0.0556	0.7677	0.8982
PCB TFD ($\gamma = 1$)	0.9364	0.0553	0.0447	0.1984	0.2460	0.0159	0.0243	0.0201	0.0476	0.5777	0.8316

TABLE 4.8 – Optimization results for a selection of TFDs of the signal of example 3 (robustness to noise test).

TFD	Optimal kernel Parameters	P
WVD	N/A	0.6442
Spectrogram	Bartlett, $L = 71$	0.8222
BJD	N/A	0.6764
CWD	$\sigma = 0.9$	0.7173
ZAMD	$\alpha = 0.56$	0.6422
CB TFD	$C = 0.11$	0.8443
SCB TFD	$C = 0.28$	0.8439
PCB TFD	$\gamma = 1$	0.8363

4.4.4 Example 4 : Sum of two sinusoidal FM signals and two chirp signals

In this example, we consider a synthetic signal $s_4(t)$ consisting of two intersecting sinusoidal FMs and two non-parallel, non-intersecting chirps. The nonlinear components consist of an increasing and decreasing sinusoidal frequency modulated signals at $t = 1, f(t) = 0.35$ Hz, having both a period $T = 128$ sec with smallest and highest frequencies equal to 0.25 Hz and 0.45 Hz respectively. The two chirps occupy the frequency ranges $f = [0.16{-}0.19]$ Hz and $f = [0.07{-}0.1]$ Hz, respectively. The smallest frequency separation between the linear and nonlinear components is within the range $0.18 - 0.25$ Hz near 97 sec and it is low enough and is just avoiding intersection. The purpose here is to confirm again the effectiveness of the KCS-based kernels in detecting closely spaced components in the case of mixtures of linear and nonlinear nonstationary signals.

Fig. 4.10 shows the superiority of the KCS TFDs and the spectrogram over the other quadratic time-frequency distributions in resolving the four closely spaced components as well as in reducing the crossterms.

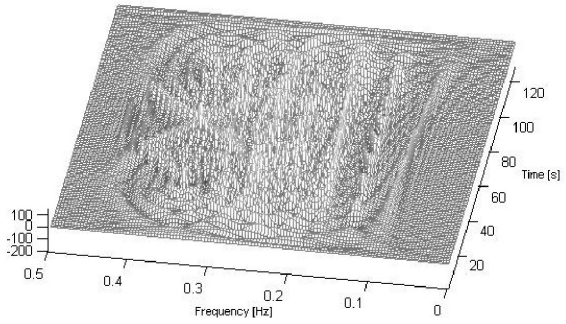
100
0
-100
-200
0.5
0.4
0.3
0.2
0.1
0
Frequency [Hz]
120
100
80
60
40
20
Time [s]

(a)

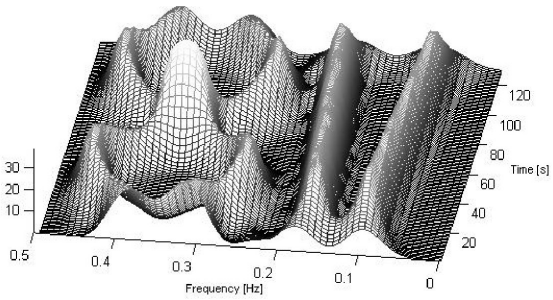
30
20
10
0.5
0.4
0.3
0.2
0.1
0
Frequency [Hz]
120
100
80
60
40
20
Time [s]

(b)

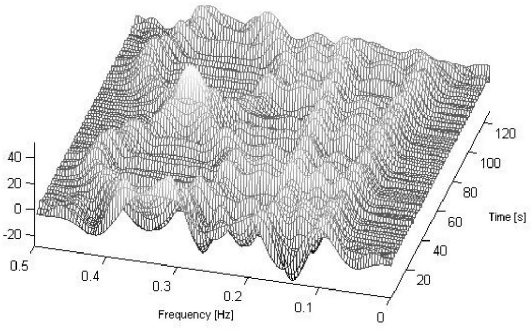
40
20
0
-20
0.5
0.4
0.3
0.2
0.1
0
Frequency [Hz]
120
100
80
60
40
20
Time [s]

(c)

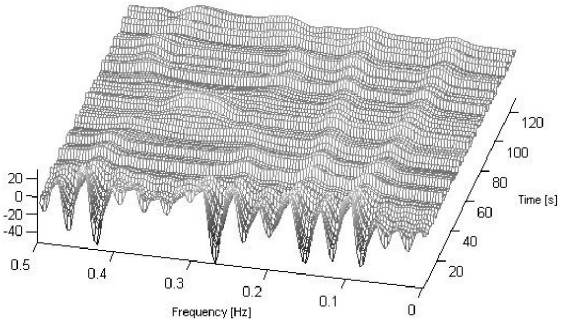
20
0
-20
-40
0.5
0.4
0.3
0.2
0.1
0
Frequency [Hz]
120
100
80
60
40
20
Time [s]

(d)

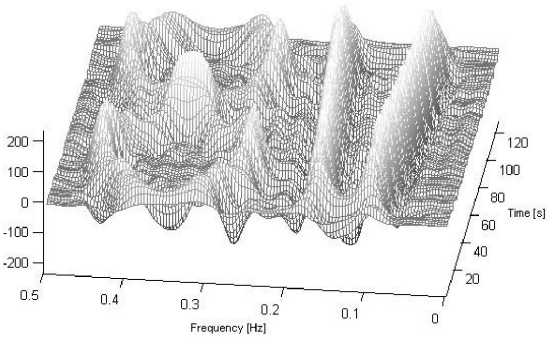
200
100
0
-100
-200
0.5
0.4
0.3
0.2
0.1
0
Frequency [Hz]
120
100
80
60
40
20
Time [s]

(e)

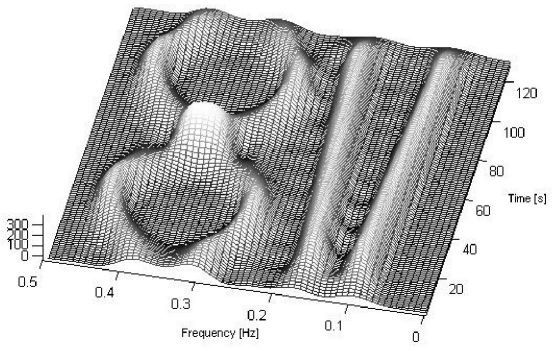
300
200
100
0
0.5
0.4
0.3
0.2
0.1
0
Frequency [Hz]
120
100
80
60
40
20
Time [s]

(f)

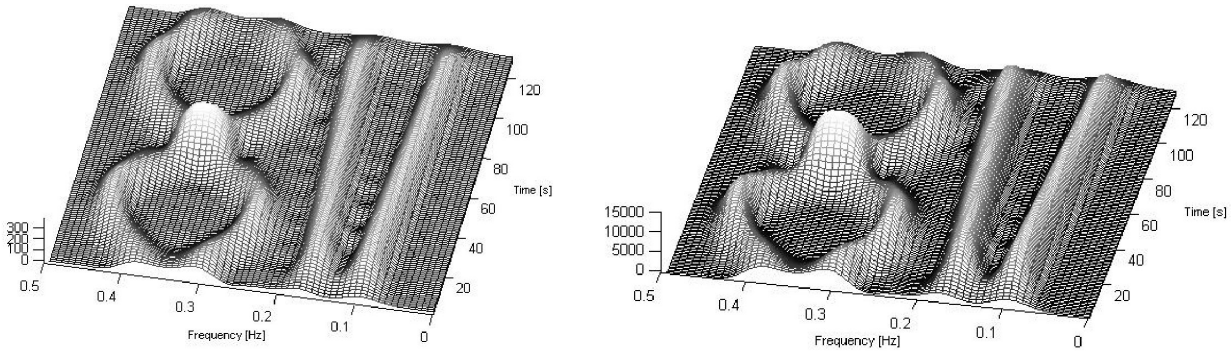

(g) (h)

FIGURE 4.10 – Optimized TFDs over the time duration $[1, 128]$ of the signal $s_4(t)$ composed of two non-parallel, non-intersecting chirps and two intersecting sinusoidal FMs. (a) WVD, (b) Spectrogram (Hanning, $L = 45$), (c) BJD,(d) CWD ($\sigma = 0.45$), (e) ZAMD ($\alpha = 0.5$), (f) CB TFD ($C = 3$), (g) SCB TFD ($C = 4$) and (h) PCB TFD ($\gamma = 4$).

The inspection of the time-depending spectrum at $t = 50$ sec plotted in Fig. 4.11 shows that the KCS TFDs and the spectrogram result on the best IF laws estimation, the artifacts suppression and the resolution of the individual components at this time instant.

In this example, the Boashash-Sucic's procedure is applied twice in order to measure the parameters for each of the pairs of consecutive components with equal amplitudes of each TFD time slice. The optimizing TFD's parameters are chosen so that they produce the greatest value of the Boashash-Sucic's overall performance measure for both the two linear chirps ($P^{(1)}$) and the two sinusoidal FMs ($P^{(2)}$) ; the resulting P to maximize is equal to $(P^{(1)} + P^{(2)})/2$ [87, 88]. Table 4.9 presents the numerical results of the optimization procedure and indicates that the CB TFD with parameter $C = 3$ is the optimal TFD for representing $s_4(t)$ since it produces the largest value of P whereas the SCB TFD with parameter $C = 4$ is the second best performing TFD [87, 88].

TABLE 4.9 – Optimization results of example 4.

TFD	Optimal kernel Parameters	$P^{(1)}$	$P^{(2)}$	P
WVD	N/A	0.6428	0.6089	0.6258
Spectrogram	Hanning, $L = 45$	0.8741	0.8644	0.8692
BJD	N/A	0.6869	0.7623	0.7246
CWD	$\sigma = 0.45$	0.7602	0.7687	0.7644
ZAMD	$\alpha = 0.5$	0.7352	0.7381	0.7366
CB TFD	$C = 3$	0.8780	0.8786	0.8783
SCB TFD	$C = 4$	0.8701	0.8802	0.8751
PCB TFD	$\gamma = 4$	0.8813	0.8701	0.8757

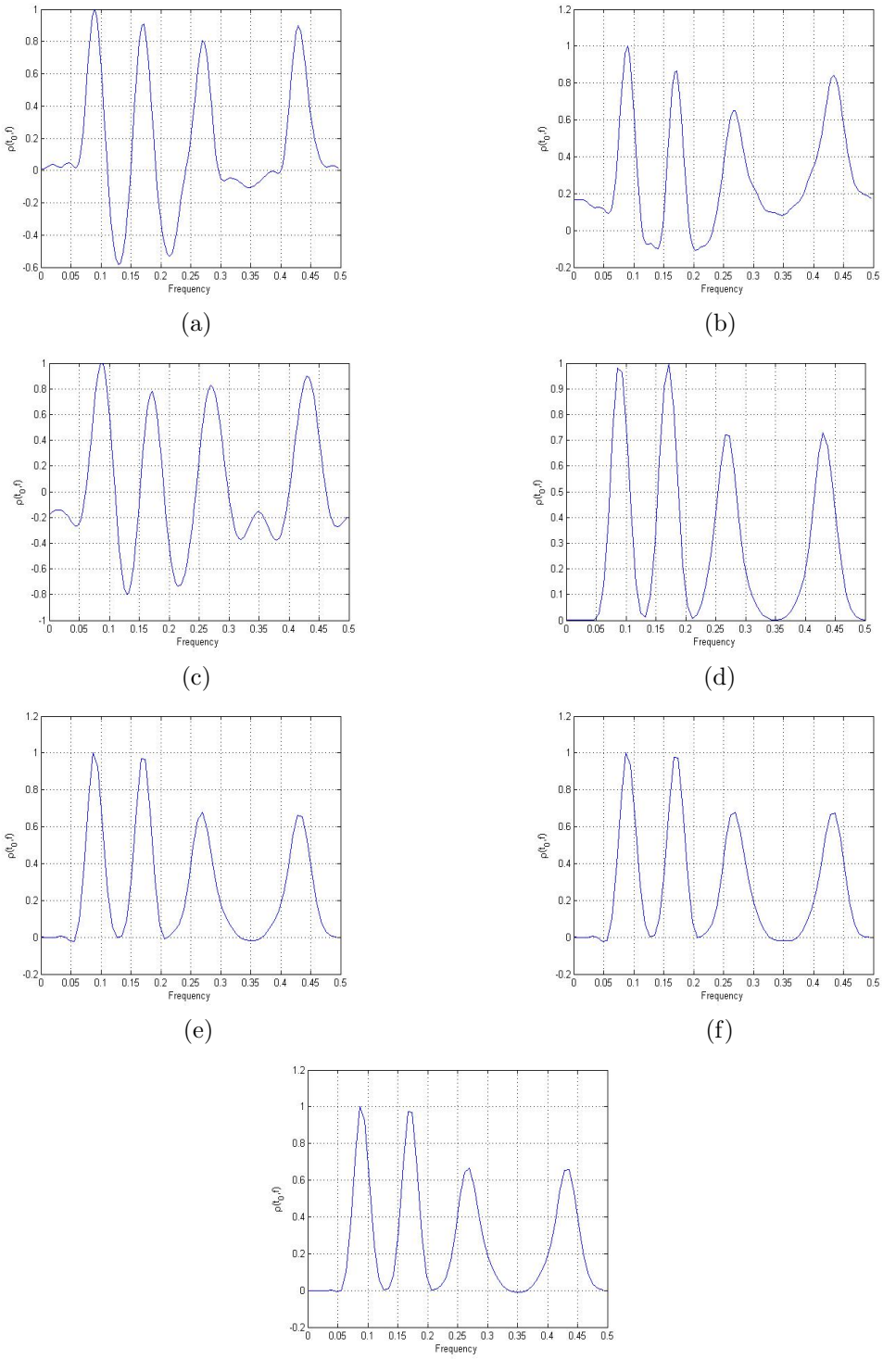

(a) (b) (c) (d) (e) (f) (g)

FIGURE 4.11 – Normalized slices of TFDs at the time instant $t = 50$ sec of the signal $s_4(t)$. (a) BJD, (b) CWD ($\sigma = 0.45$), (c) ZAMD ($\alpha = 0.5$), (d) Spectrogram (Hanning, $L = 45$), (e) CB TFD ($C = 3$), (f) SCB TFD ($C = 4$) and (g) PCB TFD ($\gamma = 4$).

One interesting practical property of TFDs is to provide the instantaneous frequency laws that describe the signal's component FM laws. Figs. 4.12 compares the measured IF laws obtained by the use of the Boashash-Sucic method to the exact nonlinear IF laws over the time interval $t \in [80, 115]$ sec. We see that the optimized KCS-based TFDs followed by the spectrogram provide the most accurate approximations of the components' actual IFs clearly much better than the other distributions. The IF estimation of very closely spaced linear FM components embedded in noise is examined in Chapter 5.

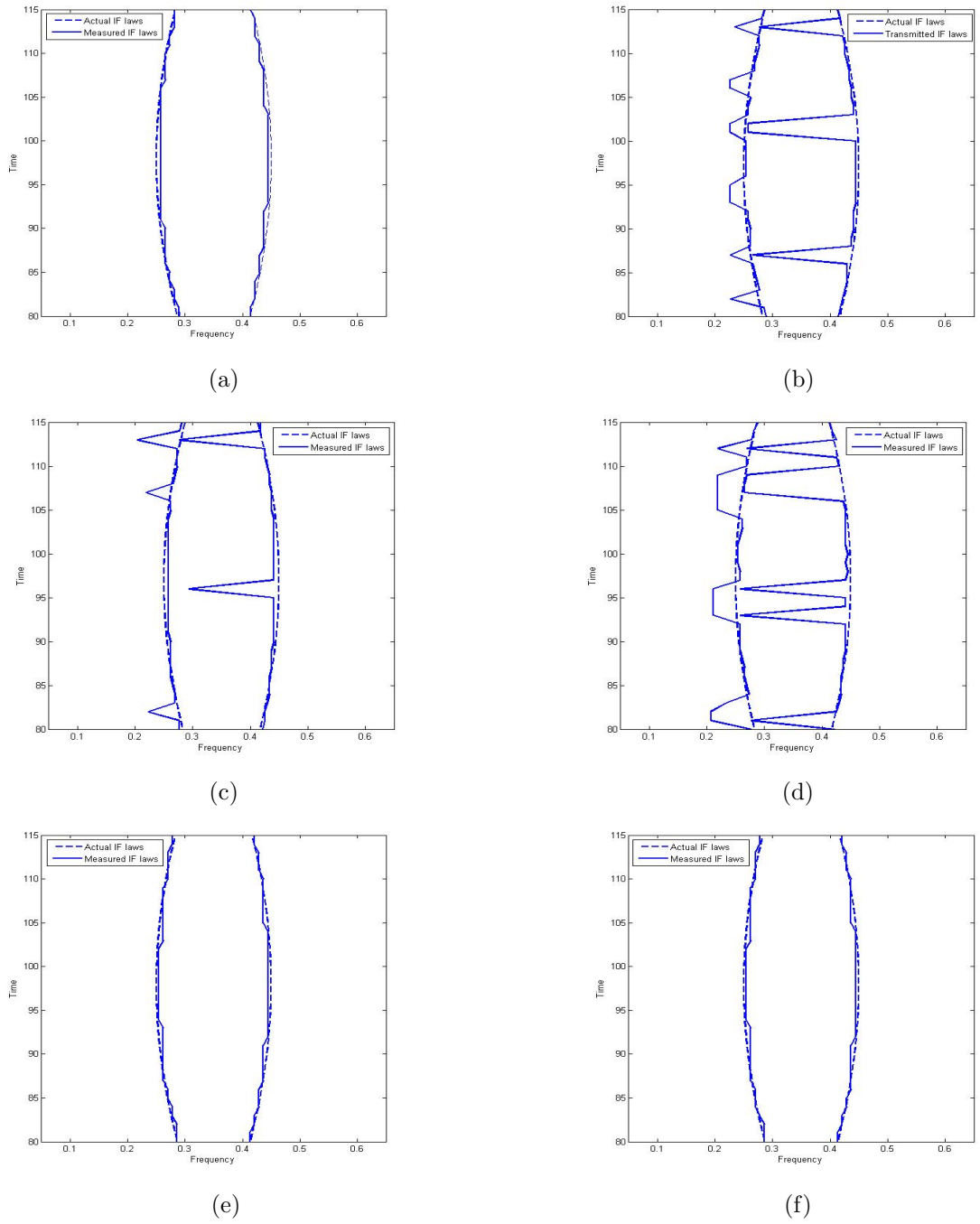

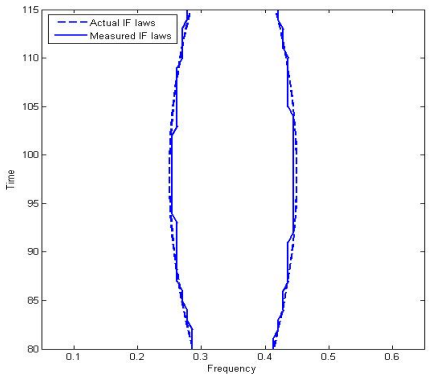

(g)

FIGURE 4.12 – Comparison of the measured and actual IF laws of the two nonlinear components of the signal $s_4(t)$. (a) Spectrogram (Hanning, $L = 45$), (b) BJD, (c) CWD ($\sigma = 0.45$), (d) ZAMD ($\alpha = 0.5$), (e) CB TFD ($C = 3$), (f) SCB TFD ($C = 4$) and (g) PCB TFD ($\gamma = 4$).

4.5 Conclusion

Several time-frequency experimental tests were made to analyze linear and nonlinear FM laws with very closely spaced multicomponent signals and noise effects. These tests showed that the KCS-based TFDs outperform other well-known classical TFDs in terms of crossterms reduction while still achieving the best time-frequency resolution and then preserving high energy concentration around the components' instantaneous frequencies.

The comparisons made are not based only on visual measure of goodness of TFD plots by looking for the most appealing one but are quantified using the Boashash-Sucic's objective methodology that implies a deep inspection of each time slice, together with some comparisons using the most popular concentration-based theoretical measures. The KCS TFDs give in all studied cases the largest performance measure value compared to the most known and powerful time-frequency representations. In addition, they reveal the most information about the time-varying test signals in the $t-f$ plane in terms of detection of the components' number, extraction of the IF laws from the TFD's peaks, estimation of signal components' bandwidths and evaluation of sidelobe and crossterm amplitudes. The later are the best eliminated using the KCS kernels thanks to their compact support nature and the flexibility in tuning the kernel's bandwidth through a single parameter until reaching their optimization.

Note that controlling the kernel shape is more flexible using the CB and SCB kernels compared with the PCB kernel that uses, by definition, an integer tuning parameter. The later, however, is quickly optimized compared to the other kernels thanks to this specific feature. The combining of these results opens the way for further promising development in high-performing DSP systems for practical measurement of nonstationary signals' energy.

Since the embedded systems are limited in terms of built-in hardware and software resources, the numerical complexity of the implemented methods is very important especially for real-time applications. The next chapter discusses the computational cost of the

kernel-based TFDs and introduces it as a fourth evaluation criterion of the investigated representations in addition to concentration, resolution and interference mitigation.

Chapter 5

Numerical Complexity of Kernel-Based Time-Frequency Distributions

This chapter presents a new objective criterion that serves to evaluate the performance of kernel-based time-frequency distributions together with the Boashash-Sucic's measure. Our contribution consists of evaluating the numerical complexity of each optimized TFD so that the final decision takes into account not only high resolution, concentration and significant crossterm suppression but the lowest required computational cost as well. The performance of TFDs based on kernels with compact support namely the CB TFD, the SCB TFD and the PCB TFD is compared to the well-known kernel-based TFDs using several tests on real-life and multicomponent signals with linear and nonlinear frequency modulation components including the noise effects and the influence of the kernel length.

5.1 Introduction

For any analytic signal $x_a(t)$ associated to the real signal $x(t)$, the time-lag-based formulation given by (2.26) shows that implementing a kernel-based TFD involves common operations of Hilbert transform, autocorrelation function and FFT. Hence, the computational cost required to implement a given time-frequency representation is directly related to the kernel's order of complexity. In this context, we propose in this contribution a new criterion for objective assessment and selection of the most efficient TFD by evaluating the numerical complexity of its time-lag kernel together with the Boashash-Sucic performance measure P. The best performing representation is thus the one that has, in the average, the greatest achieved P over some value that ensures sufficient time and frequency resolutions, and the lowest computational cost CC. It is shown through several tests that the compact support kernels outperform the other ones even for the hard case of closely spaced noisy multicomponent signals in the $t-f$ domain.

5.2 Computational cost evaluation of the kernels

We denote by M_r and A_r the computational cost in terms of real multiplications and real additions, respectively. Each time-lag kernel is computed using a window of length L. By taking advantage of the symmetry of the investigated kernels, the calculations are reduced to the half of the window size (i.e. the quarter of the kernel corresponding to positive values of t and τ).

Let N_G be the number of the evaluation points for each time-lag kernel given by $N_G = (L/2)(L/2) = L^2/4$, except for the Modified B-distribution (MBD) kernel [41, 42] where $N_G = L/2$ since it is lag-independent. The number of directly affected values, e.g. $e^0 = 1$, $\cosh(0) = 1$, is denoted by N_{da}. Hence, the number of points that require computation for a given kernel is $N_{rc} = N_G - N_{da}$.

5.2.1 BJ kernel computational cost

The time-lag BJ kernel (Fig. 5.1) is obtained by substituting $h(\tau) = 1/|\tau|$ and $a = 2$ in (2.39) yielding to

$$G_{BJ}(t,\tau) = \begin{cases} 1/|\tau| & \text{if } |\tau| \geq 2|t| \\ 0 & \text{Otherwise} \end{cases} \tag{5.1}$$

The ratio $1/|\tau|$ can be evaluated using the Newton-Raphson division algorithm. The problem consists of finding the root of a function *f(X)* by constructing the series X_n defined as

$$X_{i+1} = X_i - \frac{f(X_i)}{f'(X_i)} \tag{5.2}$$

To compute the quotient $q = a/b$, this method is used to find the reciprocal of b starting from an initial estimate X_0 obtained from a lookup table. By taking $f(X) = 1/X - b$, the

Newton-Raphson recursive solution is given by

$$X_{i+1} = X_i - \frac{1/X_i - b}{-1/X_i^2} = X_i(2 - bX_i) \tag{5.3}$$

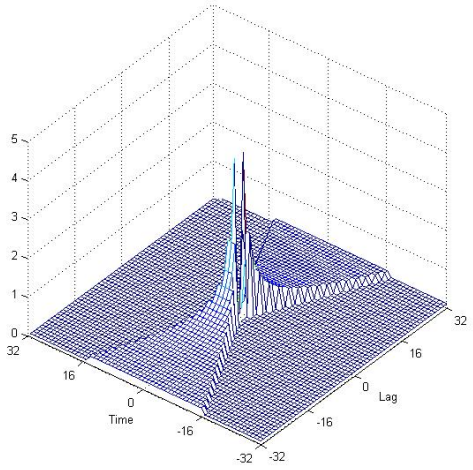

FIGURE 5.1 – The two-dimensional profile of the BJ kernel in the time-lag domain.

The convergence is quadratic and needs only four steps if the initial approximation is well chosen. The quotient is obtained by multiplying a by the reciprocal found in (5.3). Since the quantity $(2 - bX_i)$ is the two's complement of bX_i, the Newton-Raphson division algorithm needs nine multiplications only for $a \neq 1$. The order of complexity of the BJ kernel in terms of real multiplications m_r and real additions a_r at a given positive coordinate (t, τ) verifying $|\tau| \geq 2|t|$ is reported in Table 5.1.

TABLE 5.1 – Computational cost of the BJ time-lag kernel for a given $t > 0$ and $\tau > 0$ verifying $|\tau| \geq 2|t|$.

Operation	m_r	a_r
$O_1 = 2\,t$	1	0
$O_2 = 1/\tau$	8	0
Computational cost	9	0

If we denote by N_{nz}^{BJ} the number of nonzero elements of the time-lag BJ kernel, the resulting computational load is then

$$M_r = 9\,N_{nz}^{BJ} \tag{5.4}$$

$$A_r = 0 \tag{5.5}$$

5.2.2 CW kernel computational cost

Referring to Sec. 2.3.4.4, the CW kernel is adjusted in the time-lag plane through a control parameter σ such that

$$G_{CW}(t,\tau) = \sqrt{\frac{2}{\pi}}\frac{\sigma}{|\tau|}e^{-2\sigma^2 t^2/\tau^2} = 0.798\,\sigma\,\frac{e^{-2\sigma^2 t^2/\tau^2}}{|\tau|} \tag{5.6}$$

where $G_{CW}(t,\tau) \to 0$ when $\tau \to 0$. Fig. 5.2 displays the shape of the CW time-lag kernel for a) $\sigma = 0.5$ and b) $\sigma = 2.5$.

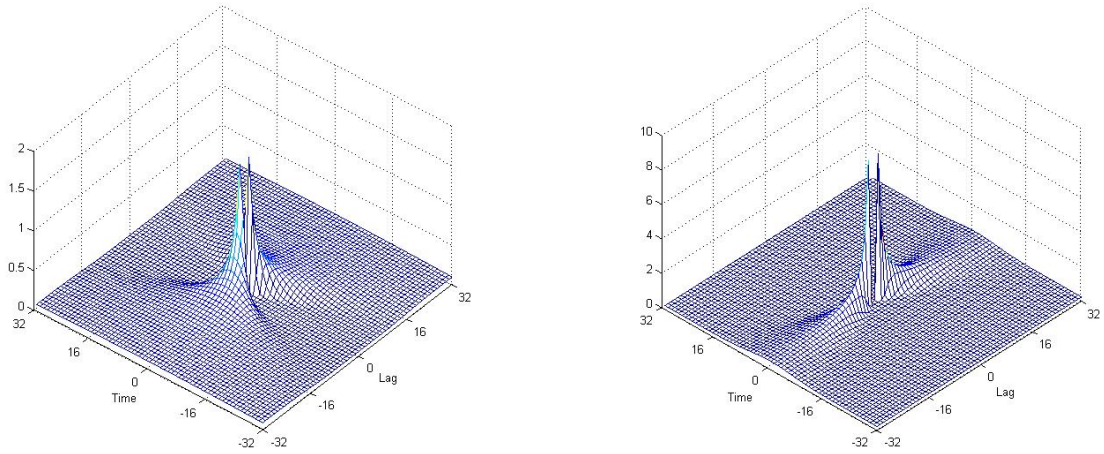

(a) (b)

FIGURE 5.2 – The two-dimensional profile of the CW kernel in the time-lag domain. (a) $\sigma = 0.5$ and (b) $\sigma = 2.5$.

The Taylor series representation of the exponential function e^x, $x > 0$, is given by

$$e^x = \sum_{n=0}^{+\infty} \frac{x^n}{n!} \tag{5.7}$$

For negative exponents, it is recommended to use the relationship $e^{-x} = 1/e^x$ in order to avoid divergence.

In practice, the sum in (5.7) is approximated using N_e terms and the inverse factorial constants $1/n!$ are precomputed and stored to a lookup table u. Moreover, if we save the previously computed powers of x in a table y, the implementation becomes so fast and the problem of approximating the exponential function is reduced to the following

$$\begin{aligned} u &= [1/(2!), 1/(3!), ..., 1/(N_e!)] \\ y &= [y_1, ..., y_{N_e}]; y_1 = x, y_2 = y_1 x, y_3 = y_2 x, ..., y_{N_e} = y_{N_e-1} x \end{aligned}$$

$$e^x \simeq 1 + y_1 + u_1 y_2 + u_2 y_3 + ... + u_{N_e-1} y_{N_e} \tag{5.8}$$

Table 5.2 gives the computational cost required to evaluate the CW kernel for each point (t,τ) verifying $t > 0$ and $\tau > 0$.

TABLE 5.2 – Computational cost of the CW kernel for a given $t > 0$ and $\tau > 0$.

Operation	m_r	a_r
$O_1 = 2\sigma^2 t^2$	4	0
$O_2 = O_1/\tau^2$	10	0
$O_3 = e^{O_2}$	$2(N_e - 1)$	N_e
$O_4 = 1/O_3$	8	0
$O_5 = 0.798\,\sigma\,O_4/\tau$	11	0
Computational cost	$2N_e + 31$	N_e

Since there are $L/2 - 1$ points directly affected to 0 ($G_{CW}(t,\tau) = 0$ when $\tau = 0$, $\forall\, t \neq 0$), and $G_{CW}(0,\tau) = \dfrac{0.798\,\sigma}{\tau}$ requires 10 multiplications for any $\tau \neq 0$ corresponding to $L/2 - 1$ distinct points ; the computational cost of the CW kernel for the full range of t and τ needs

$$M_r = \left(\frac{L}{2} - 1\right)\left(\frac{L}{2} - 1\right)(2N_e{+}31){+}10\left(\frac{L}{2} - 1\right) = \left(\frac{L}{2} - 1\right)^2(2N_e{+}31){+}10\left(\frac{L}{2} - 1\right) \tag{5.9}$$

$$A_r = \left(\frac{L}{2} - 1\right)\left(\frac{L}{2} - 1\right) N_e = \left(\frac{L}{2} - 1\right)^2 N_e \tag{5.10}$$

5.2.3 ZAM kernel computational cost

By taking $h(\tau) = e^{-\alpha\tau^2}(\alpha = 1/(2\sigma^2))$ and $a = 2$; the expression of the ZAM kernel in the time-lag domain is obtained from (2.39) as follows

$$G_{ZAM}(t,\tau) = \begin{cases} e^{-\alpha\tau^2} & \text{if } |\tau| \geq 2|t| \\ 0 & \text{Otherwise} \end{cases} \tag{5.11}$$

Fig. 5.3 displays the graph of the ZAM kernel in the time-lag plane for a) $\alpha = 0.02$ and b) $\alpha = 0.5$.

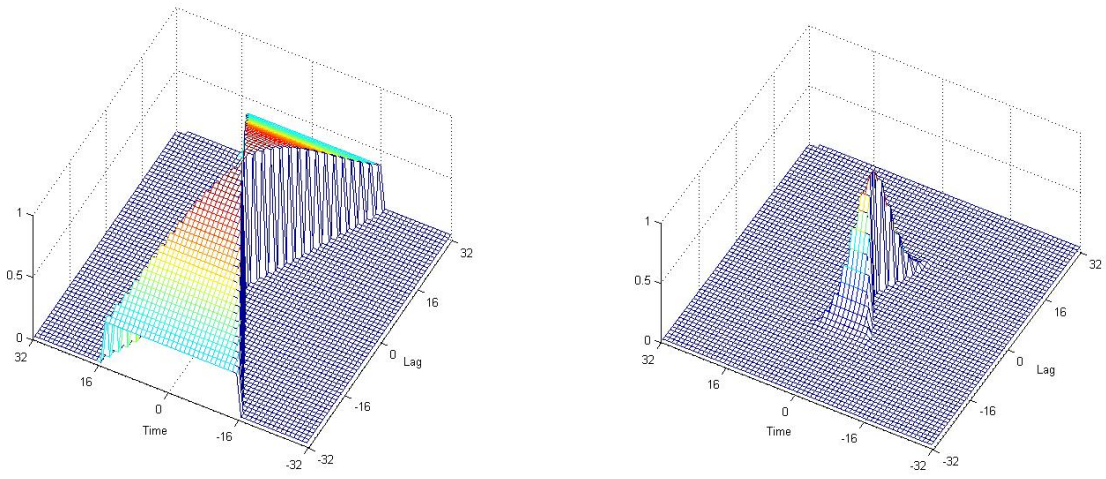

(a) (b)

FIGURE 5.3 – The two-dimensional profile of the ZAM kernel in the time-lag domain. (a) $\alpha = 0.02$ and (b) $\alpha = 0.5$.

Table 5.3 gives the computational cost required to evaluate the ZAM kernel at a given positive coordinates (t, τ) verifying $|\tau| \geq 2|t|$.

TABLE 5.3 – Computational cost of the ZAM kernel at a point $(t,\tau) \in \Re^{+^2}$ satisfying $|\tau| \geq 2|t|$.

Operation	m_r	a_r
$O_1 = \alpha\tau^2$	2	0
$O_2 = e^{O_1}$	$2(N_e - 1)$	N_e
$O_3 = 1/O_2$	8	0
Computational cost	$2N_e + 8$	N_e

Let N_{nz}^{ZAM} be the number of nonzero elements of the ZAM time-lag kernel. Since $G_{ZAM}(0,0) = 1$, the computational cost of this kernel is of the following order

$$M_r = \left(N_{nz}^{ZAM} - 1\right)(2N_e + 8) \tag{5.12}$$

$$A_r = \left(N_{nz}^{ZAM} - 1\right) N_e \tag{5.13}$$

5.2.4 Modified B-distribution (MBD) kernel computational cost

The expression of the lag-independent (LI) Modified B-distribution kernel in the time-lag domain is given by [4, 41, 42]

$$G_{MB}(t,\tau) = g_\beta(t) = \frac{\cosh^{-2\beta} t}{\int_{-\infty}^{+\infty} \cosh^{-2\beta} \varepsilon \; d\varepsilon} \tag{5.14}$$

where β is a positive real parameter and the denominator is for normalization. The corresponding ambiguity domain kernel is expressed as follows [4, 41, 42]

$$\phi_{MB}(\eta,\tau) = \frac{|\Gamma(\beta + j\pi\tau)|^2}{\Gamma^2(\beta)} \tag{5.15}$$

For discrete time n and discrete lag m, the MBD kernel becomes [4, 42]

$$G_{MB}(n,m) = g_\beta(n) = \frac{\cosh^{-2\beta} n}{\sum_{i=-M}^{M} \cosh^{-2\beta} i} \tag{5.16}$$

The graph of the MBD kernel in the time-lag plane is a bell-shaped curve vs. time whose spread is inversely related to β (Fig. 5.4). The induced Modified B-distribution is real, verifies the frequency marginal property and conserves energy, frequency support and group delay.

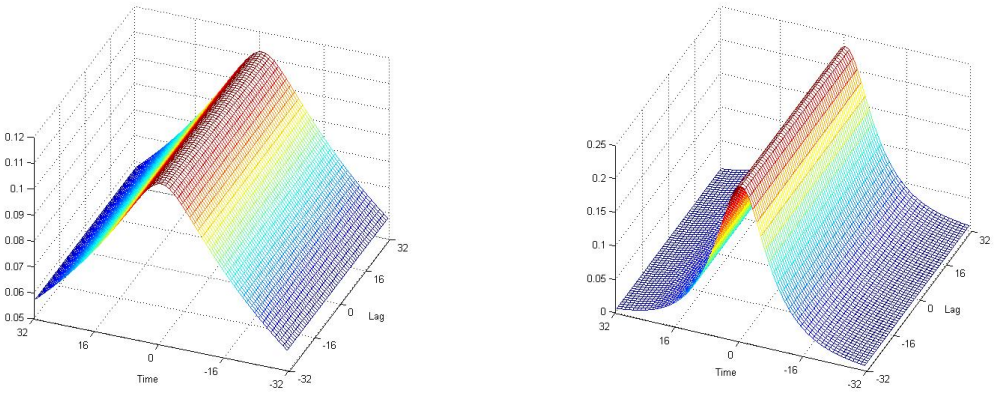

(a) (b)

FIGURE 5.4 – The two-dimensional profile of the MBD kernel in the time-lag domain. (a) $\beta = 0.05$ and (b) $\beta = 0.3$.

Since the hyperbolic cosine function is defined as

$$\cosh(x) = \frac{e^x + e^{-x}}{2} \tag{5.17}$$

then its power series expansion is expressed as follows

$$\cosh(x) = \sum_{n=0}^{+\infty} \frac{x^{2n}}{(2n)!} > 0,\ \forall\, x \in \Re \tag{5.18}$$

with $\cosh(0) = 1$. The notation $\mathrm{ch}(x)$ is sometimes also used.

Proceeding with the same manner as for the exponential function, the approximated hyperbolic cosine value of x using N_{hc} terms is given by

$$\begin{aligned} u &= [1/(2!), 1/(4!), .., 1/((2N_{hc})!)] \\ y &= [y_1, .., y_{N_{hc}}]; y_1 = x^2, y_2 = y_1 y_1, y_3 = y_2 y_1, .., y_{N_{hc}} = y_{N_{hc}-1} y_1 \end{aligned}$$

$$\begin{aligned}\cosh(x) &\simeq 1+\sum_{n=1}^{N_{hc}}\frac{x^{2n}}{(2n)!}\\ &= 1+u_1y_1+u_2y_2+u_3y_3+...+u_{N_{hc}}y_{N_{hc}}\end{aligned} \tag{5.19}$$

Hence, the evaluation of the cosh function for any $x \in \Re^*$ needs $2N_{hc}$ multiplications and N_{hc} additions.

On the other hand, the MBD kernel requires the computation of the following quantity

$$w^{-2\beta} = e^{\ln(w^{-2\beta})} = e^{-2\beta\ln(w)},\ w = \cosh(t) \tag{5.20}$$

From Table 5.2, the exponential in (5.20) needs $2N_e+6$ multiplications and N_e additions at most.

In order to evaluate the logarithm for any $x > 0$, we can exploit the following definition of the inverse hyperbolic tangent function

$$\operatorname{artanh}(z) = \frac{1}{2}\ln\left(\frac{1+z}{1-z}\right) \tag{5.21}$$

which can be also expressed as an infinite power series of the form

$$\operatorname{artanh}(z) = \sum_{n=0}^{+\infty}\frac{z^{2n+1}}{2n+1},\quad |z|<1 \tag{5.22}$$

For any real $x > 0$, the variable $z = (1-x)/(1+x)$ satisfies the condition $|z| < 1$. From (5.21) and (5.22) we get the following approximation of the logarithm function

$$\ln(x) = 2\operatorname{artanh}\left(\frac{1-x}{1+x}\right) \simeq \sum_{n=0}^{N_l}\frac{1}{2n+1}\left(\frac{1-x}{1+x}\right)^{2n+1} \tag{5.23}$$

or equivalently

$$\begin{aligned}u &= [1/3, 1/5, ..., 1/(2N_l+1)]\\ y_0 &= (1-x)/(1+x), z_0 = y_0^2, z_1 = y_0z_0, z_2 = z_1z_0, ..., z_{N_l} = z_{N_l-1}z_0\\ &\ln(x) \simeq y_0+u_1z_1+u_2z_2+u_3z_3+...+u_{N_l}z_{N_l}\end{aligned} \tag{5.24}$$

It follows that, using N_l terms, the computation of the logarithm function for any $x \in \Re^+$ requires $2N_l+10$ multiplications and N_l+2 additions.

Due to the fact that the hyperbolic cosine function is even, the denominator in (5.16) is evaluated for positive values of i only. Tables 5.4-5.5 detail the numerical complexity of the numerator and denominator of the MBD kernel for any $t \in \Re^+$.

TABLE 5.4 – Computational cost of the numerator of the MBD kernel for a given value of $t \in \Re^+$.

Operation	m_{r_1}	a_{r_1}
$O_1 = \cosh(t)$	$2N_{hc}$	N_{hc}
$O_2 = -2\beta$	1	0
$O_3 = O_2\ln O_1$	$2N_l+11$	N_l+2
$O_4 = e^{O_3}$	$2N_e+6$	N_e
Computational cost	$2(N_{hc}+N_l+N_e)+18$	$N_{hc}+N_l+N_e+2$

TABLE 5.5 – Computational cost of the denominator of the MBD kernel.

Operation	m_{r_2}	a_{r_2}
$O_1 = \cosh(i),\ 1 \leq i \leq M$	$2M\,N_{hc}$	$M\,N_{hc}$
$O_2 = -2\beta \ln O_1,\ 1 \leq i \leq M$	$M(2N_l + 11)$	$M(N_l + 2)$
$O_3 = e^{O_2},\ 1 \leq i \leq M$	$M(2N_e + 6)$	$M\,N_e$
$O_4 = \sum_{i=1}^{M} O_3$	0	$M - 1$
Computational cost	$2M(N_{hc}+N_l+N_e)+17M$	$M(N_{hc}+N_l+N_e)+3M-1$

By adding the cost of the division in (5.16), the numerical complexity of the MBD kernel for the full range of t is then of the following order

$$M_r = \left(\frac{L}{2} - 1\right) m_{r_1} + m_{r_2} + 9\left(\frac{L}{2} - 1\right) + 8 = \left(\frac{L}{2} - 1\right)(m_{r_1} + 9) + m_{r_2} + 8 \tag{5.25}$$

$$A_r = \left(\frac{L}{2} - 1\right) a_{r_1} + a_{r_2} \tag{5.26}$$

5.2.5 CB kernel computational cost

The CB time-lag kernel defined by (3.19) can be rewritten as follows

$$G_{CB}(t,\tau) = \begin{cases} e^{e_{CB}} & \text{if } \frac{t^2+\tau^2}{D^2} < 1 \\ 0 & \text{Otherwise} \end{cases} \tag{5.27}$$

where

$$e_{CB} = C + \frac{CD^2}{(t^2 + \tau^2) - D^2} \tag{5.28}$$

is the exponent of the kernel ; C is a parameter that controls the kernel's bandwidth. Table 5.6 gives the computational cost required to evaluate the CB kernel given t and τ such that $(t^2 + \tau^2) < D^2$.

TABLE 5.6 – Computational cost of the CB kernel at a point (t,τ) verifying $(t^2 + \tau^2) < D^2$.

Operation	m_r	a_r
$O_1 = CD^2$	2	0
$O_2 = t^2 + \tau^2 - D^2$	3	2
$O_3 = O_1/O_2$	9	0
$O_4 = C + O_3$	0	1
$O_5 = e^{O_4}$	$2(N_e - 1)$	N_e
Computational cost	$2N_e + 12$	N_e+3

Denoting by N_{nz}^{CB} the number of nonzero elements of the CB kernel, and since $G_{CB}(0,0)$=1, the evaluation of this compact support kernel results in the following computational load

$$M_r = \left(N_{nz}^{CB} - 1\right)(2N_e + 12) \tag{5.29}$$

$$A_r = \left(N_{nz}^{CB} - 1\right)(N_e + 3) \tag{5.30}$$

5.2.6 SCB kernel computational cost

According to (3.30), the SCB time-lag kernel can be rewritten under the following form

$$G_{SCB}(t,\tau) = \begin{cases} e^{e_{SCB}(t,0)} e^{e_{SCB}(0,\tau)} & \text{if } \begin{cases} t^2 < D^2 \\ \text{and} \\ \tau^2 < D^2 \end{cases} \\ 0 & \text{Otherwise} \end{cases} \tag{5.31}$$

where

$$e_{SCB}(t,0) = C + \frac{CD^2}{t^2 - D^2} \tag{5.32}$$

$$e_{SCB}(0,\tau) = C + \frac{CD^2}{\tau^2 - D^2} \tag{5.33}$$

are the exponents of the separable kernel as function of t and τ, respectively. The values in (5.32) are computed and stored in a table ; hence, the exponent in (5.33) does not need calculation. Table 5.7 gives the computational cost required to evaluate the SCB kernel for a given value of t and τ verifying the conditions $t^2 < D^2$ and $\tau^2 < D^2$.

TABLE 5.7 – Computational cost of the SCB kernel at a point (t,τ) verifying $t^2 < D^2$ and $\tau^2 < D^2$.

Operation	m_r	a_r
$O_1 = CD^2$	2	0
$O_2 = t^2 - D^2$	2	1
$O_3 = O_1/O_2$	9	0
$O_4 = e_{SCB}(t,0) = C + O_3$	0	1
$O_5 = e^{O_4}$	$2(N_e - 1)$	N_e
$O_6 = e_{SCB}(0,\tau)$	0	0
$O_7 = O_5 O_6$	1	0
Computational cost	$2N_e + 12$	N_e+2

The SCB kernel vanishes to zero outside a given set. If we denote by N_{nz}^{SCB} the number of nonzero elements of the kernel, and since $G_{SCB}(0,0) = 1$, the computations require

$$\left(N_{nz}^{SCB} - 1\right)(2N_e + 12) \quad \text{muliplications} \tag{5.34}$$

$$\text{and} \quad \left(N_{nz}^{SCB} - 1\right)(N_e + 2) \quad \text{additions} \tag{5.35}$$

5.2.7 PCB kernel computational cost

The PCB kernel has also a compact support nature in the time-lag domain following a polynomial law. From optimization point of view, the integer tuning parameter γ that adjusts the kernel's bandwidth makes the procedure very fast and hence the processing time needed to evaluate the Boashash-Sucic performance measure is considerably reduced. Consequently, the PCB can be used first to select the optimal kernel window length before optimizing the KCS-based TFDs.

Table 5.8 gives the computational cost required to evaluate the PCB kernel for a given value of t and τ in the range $(t^2 + \tau^2) < \lambda^2$.

TABLE 5.8 – Computational cost of the PCB kernel for any t and τ satisfying $(t^2 + \tau^2) < \lambda^2$.

Operation	m_r	a_r
$O_1 = \gamma + 1$	0	1
$O_2 = \lambda^2 - (t^2 + \tau^2)$	3	2
$O_3 = O_2^{\gamma}$	$\gamma - 1$	0
$O_4 = \pi\lambda^{2\gamma+2}$	$2\gamma + 2$	0
$O_5 = O_1/O_4$	9	0
$O_6 = O_3 O_5$	1	0
Computational cost	$3\gamma + 14$	3

The PCB kernel is computed for N_{nz}^{PCB} nonzero points yielding to the following order of complexity

$$M_r = (3\gamma + 14)\ N_{nz}^{PCB} \tag{5.36}$$

$$A_r = 3\, N_{nz}^{PCB} \tag{5.37}$$

5.3 Experimental results

The performance of the KCS-based TFDs is compared to the best known kernel-based time-frequency distributions. A real-life signal and three synthetic examples are considered and discussed in detail in order to evaluate each TFD and determine the best one in terms of concentration, resolution and numerical complexity. The kernel's window size is fixed to L. Following the same procedure explained in Sec. 4.3, and given the optimized kernel parameters for each TFD, the computational cost is then evaluated. The multicomponent signal is thus best represented by the TFD that shows the best compromise between largest P value and smallest required computational cost. Note that the integral in the MBD kernel denominator is approximated using $M = 40$ terms. The hyperbolic cosine, the exponential and the logarithm functions need only 10 terms to be very close to the exact values. The KCS parameters D and γ are both set to 7.5.

5.3.1 Example 1 : The bat echolocation signal

The first illustrative example concerns the bat echolocation real-life signal $s_1(t)$, represented in the $t-f$ plane using a selection of kernel-based time-frequency distributions namely the BJD, the CWD, the ZAMD, the Modified B-distribution (MBD), the CB TFD, the SCB TFD and the PCB TFD (Fig. 5.5). The window size of the kernel in the time-lag domain is set to 64. The number of KCS points that require computation was found to be equal to $N_{nz}^{CB} = 359$, $N_{nz}^{SCB} = 441$ and $N_{nz}^{PCB} = 359$, respectively while $N_{nz}^{BJ} = N_{nz}^{ZAM} = 272$. As we have mentioned in Sec. 4.3, the application of the Boashash-Sucic methodology is computationally expensive so, in this example ; the optimization region of interest, containing the two overall closest components, is limited to the rectangle shown in Fig. 5.5-(a) defined by $0.2 \leq f \leq 0.4$ Hz and $210 \leq t \leq 320$ sec. The drawback of the methodology in such situation is that the optimization region cannot be selected only after visual inspection of the TFDs' plots.

The smoothing parameters related to each TFD are the optimum values that correspond to the maximum achieved performance measure P as reported in Table 5.9 together with the computational cost CC of each kernel.

Table 5.9 – Optimization results for a selection of TFDs of the signal of example 1 over the region of interest delimited by the frequency and time intervals [0.2,0.4] Hz and [210,320] sec, respectively.

TFD	Optimal kernel parameters	P	CC
BJD	N/A	0.8195	$M_r = 2448;\ A_r = 0$
CWD	$\sigma = 0.62$	0.8243	$M_r = 49321;\ A_r = 9610$
ZAMD	$\alpha = 0.01$	0.8387	$M_r = 7588;\ A_r = 2710$
MBD	$\beta = 0.067$	0.8958	$M_r = 5785;\ A_r = 2311$
CB TFD	$C = 0.683$	0.8908	$M_r = 11456;\ A_r = 4654$
SCB TFD	$C = 0.575$	0.8771	$M_r = 14080;\ A_r = 5280$
PCB TFD	$\gamma = 2$	0.8881	$M_r = 7180;\ A_r = 1077$

The P values reflect the superiority of the MBD and the KCS kernels in presenting the signal $s_1(t)$ even when the ratio of the two successive autoterms is not close to one. This performance is achieved thanks to the high concentration of the signal components using the MBD kernel and the compact support nature of the KCS kernels that reduces considerably the energy of the crossterms. However, the most particular and notable advantage of the KCS TFDs is that they do not require any external smoothing neither in time nor frequency since the window is the kernel itself unlike the lag-independent MBD kernel that smoothes the WVD in the time direction only, and hence needs in general an additional smoothing over f in order to improve the frequency resolution (unless indicated, a 127-point Hamming window $h(\tau)$ is used and it is not included in the MBD kernel numerical complexity).

Table 5.10 shows the parameters and the instantaneous performance measure P_i of the different TFDs, while Fig. 5.6 displays the time slices at $t_0 = 286$ sec. Two important observations must be noted : First, from visual inspection of the ZAMD TFD, we see that the amplitude of some crossterms is more important than the amplitude of the autoterms.

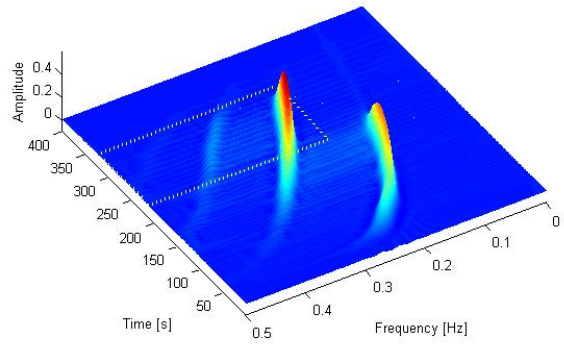
Amplitude
Time [s]
Frequency [Hz]

(a)

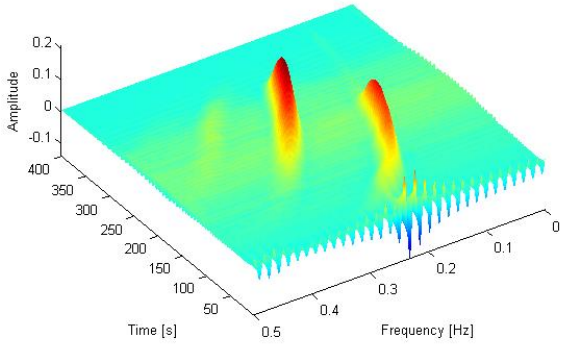
Amplitude
Time [s]
Frequency [Hz]

(b)

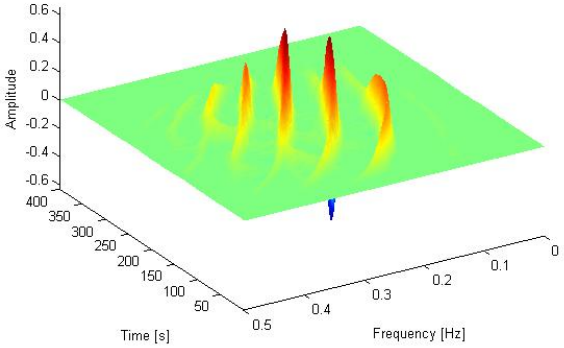
Amplitude
Time [s]
Frequency [Hz]

(c)

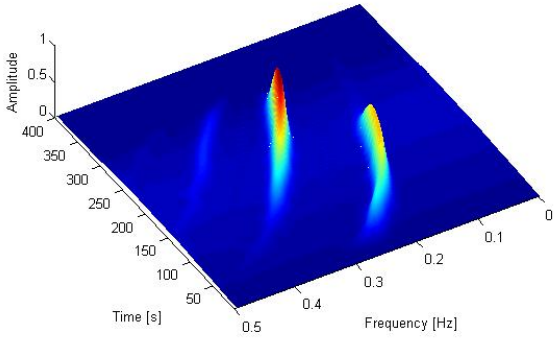
Amplitude
Time [s]
Frequency [Hz]

(d)

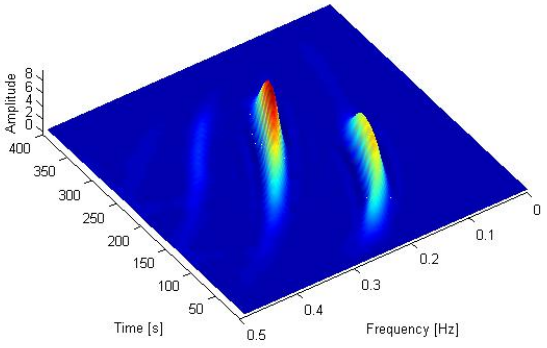
Amplitude
Time [s]
Frequency [Hz]

(e)

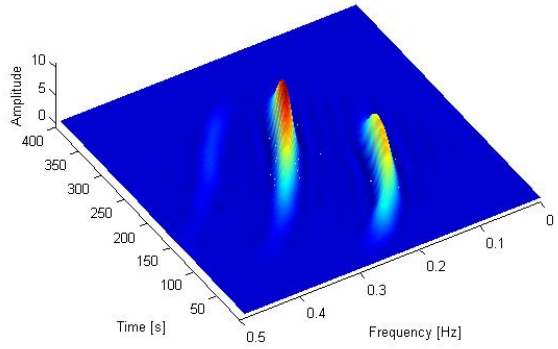
Amplitude
Time [s]
Frequency [Hz]

(f)

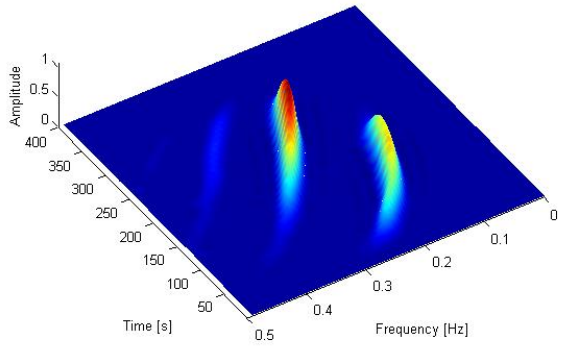

(g)

FIGURE 5.5 – Optimized TFDs over the region of interest delimited by the frequency range [0.2,0.4] Hz and the time duration [210,320] sec of the bat echolocation signal $s_1(t)$. (a) BJD, (b) CWD ($\sigma = 0.62$), (c) ZAMD ($\alpha = 0.01$), (d) MBD ($\beta = 0.067$), (e) CB TFD ($C = 0.683$), (f) SCB TFD ($C = 0.575$) and (g) PCB TFD ($\gamma = 2$).

TABLE 5.10 – Parameters of the Boashash-Sucic performance measure and P_i values of different TFDs of example 1 computed at the time instant $t_0 = 286$. The frequency region of interest is [0.2,0.5] Hz.

TFD (optimal parameters)	A_{M_1}	A_{M_2}	A_S	A_X	f_{i_1}	f_{i_2}	V_{i_1}	V_{i_2}	V_i	Δf_i	D	P_i
BJD	1.0000	0.2220	0.1104	0.0785	0.2250	0.2475	0.0150	0.0075	0.0112	0.0225	0.5000	0.7517
CWD ($\sigma = 0.62$)	1.0000	0.2039	0.1203	0.0879	0.2288	0.3312	0.0200	0.0050	0.0125	0.1025	0.8780	0.8684
ZAMD ($\alpha = 0.01$)	0.7809	1.0000	0.1284	0.0148	0.2238	0.2775	0.0150	0.0100	0.0125	0.0538	0.7674	0.8716
MBD ($\beta = 0.067$)	1.0000	0.3518	0.0572	0.0166	0.2266	0.3320	0.0130	0.0156	0.0143	0.1055	0.8641	0.9224
CB TFD ($C = 0.683$)	1.0000	0.3096	0.0320	0.0002	0.2143	0.3254	0.0159	0.0159	0.0159	0.1111	0.8571	0.9361
SCB TFD ($C = 0.575$)	1.0000	0.2885	0.0459	0.0066	0.2143	0.3254	0.0237	0.0158	0.0197	0.1111	0.8224	0.9153
PCB TFD ($\gamma = 2$)	1.0000	0.3251	0.0296	0.00002	0.2143	0.3254	0.0159	0.0159	0.0159	0.1111	0.8571	0.9375

Hence, the related P value reported in Table 5.9 does not reflect the right order of increasing performance of TFDs since it considers that the ZAMD performs better than the BJD and the CWD. This observation constitutes another drawback of the Boashash-Sucic methodology and can be explained by the fact that the crossterm, as depicted for example in Fig. 5.6-(c), is more dominant than the second autoterm whereas the true A_{M_2} is considered as a sidelobe component. Thus, the parameters' calculations using (4.11) and (4.12) become completely wrong (see Table 5.10). The same drawback is observed for the BJD. This results also on false estimation of the IF laws especially, in this case, for the second component.

Secondly, the MBD and the KCS-based TFDs are found to best estimate the true practical characteristics of the real-life bat echolocation signal in terms of the IF laws as well as the number of components and their relative energies and bandwidths. In this context, Table 5.10 indicates that the PCB TFD with a smoothing parameter $\gamma = 2$, is the optimal TFD of the signal $s_1(t)$ at the time instant $t_0 = 286$ and it performs almost

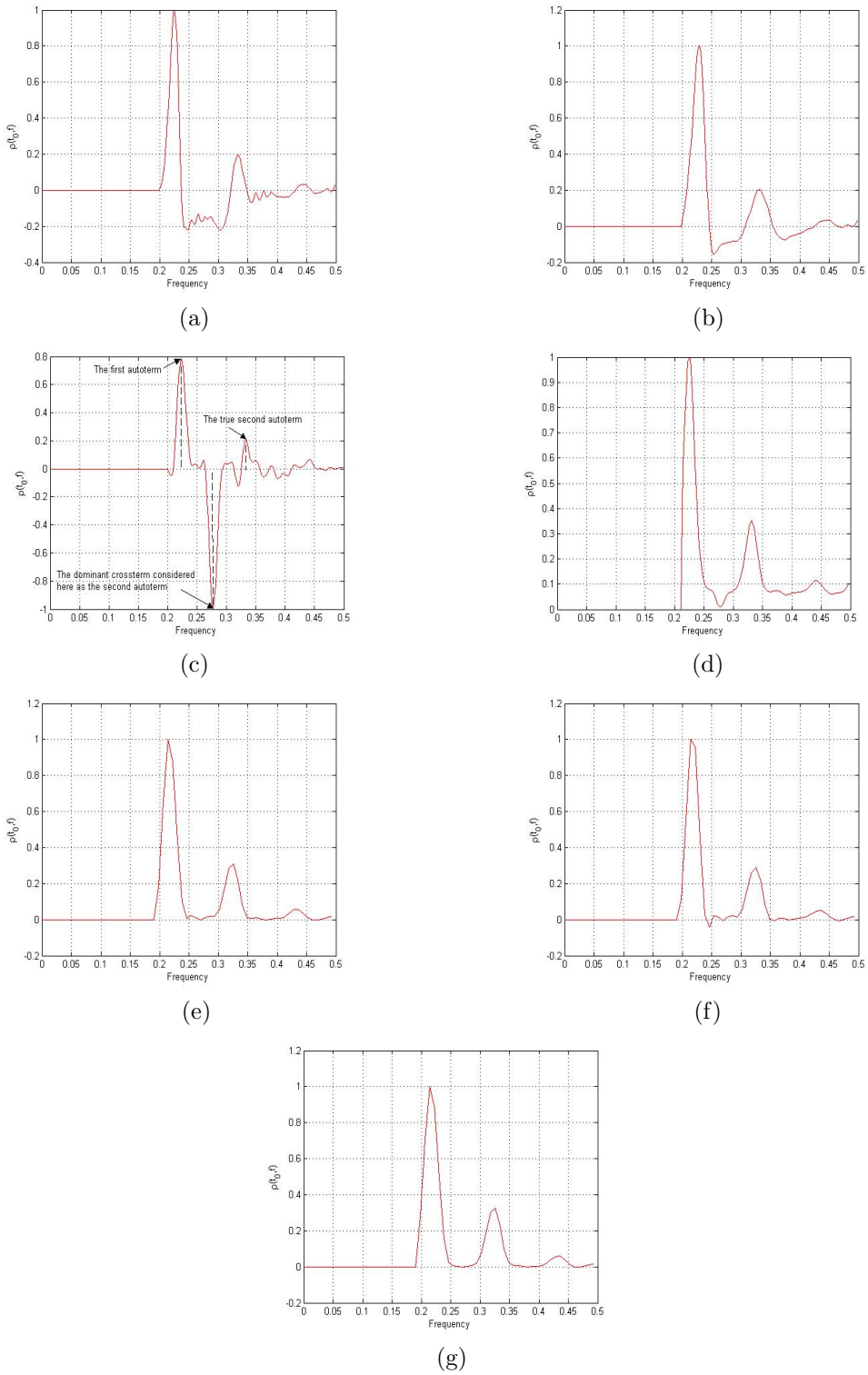

(a) (b) (c) (d) (e) (f) (g)

FIGURE 5.6 – Normalized slices of TFDs over a frequency range of about [0.2,0.5] Hz plotted at the time instant $t_0 = 286$ sec of the two overall closed components of the signal $s_1(t)$. (a) BJD, (b) CWD ($\sigma = 0.62$), (c) ZAMD ($\alpha = 0.01$), (d) MBD ($\beta = 0.067$), (e) CB TFD ($C = 0.683$), (f) SCB TFD ($C = 0.575$) and (g) PCB TFD ($\gamma = 2$).

the same as the CB TFD with $C = 0.683$.

Concerning the numerical complexity, the BJ kernel is the least costly and uses 4.15% only of the computing resources required by the CW kernel which is the most costly in this case. The computational cost of the SCB TFD is about 1.2 times the CB TFD'CC whereas the MBD and PCB TFD are of the same order of complexity and they are the second least costly distributions followed by the ZAMD and the CB TFD.

Let P_m be the mean value of the achieved P by the seven investigated distributions. If we select only the TFDs that ensure performance measures that exceed $P_m = 0.8620$; the optimal TFD of the signal $s_1(t)$ is then the MBD with a parameter $\beta = 0.067$ since it possesses the greatest value of $P = 0.8958$ and a required computational load that presents 41.82% and 50.25% of that required by the CB TFD and the SCB TFD, respectively. The second best performing TFD is the PCB TFD with a difference of only 0.0077 in P.

5.3.2 Example 2 : Sum of two crossing nonlinear FM components

Here, we deal with a two-component signal $s_2(t)$ of duration $T = 256$ sec composed of two crossing nonlinear FMs such that $f(t = 15) = 0.05$ Hz and $f(t = 128) = 0.3$ Hz for the hyperbolic frequency modulated component and $f(t = 1) = f(t = 256) = 0.3$ Hz for the increasing sinusoidal FM component with smallest and highest frequencies equal to 0.2 Hz and 0.4 Hz, respectively. Out of seven TFDs represented in Fig. 5.7, we want to select the TFD which is the best-performing for the given signal so that the computational cost CC is minimized. The kernel's length is firstly set to 32. The nonzero sets of the CB, SCB and PCB kernels are equal to 86, 100 and 86, respectively whereas $N_{rc}^{BJ} = N_{rc}^{ZAM} = 72$.

Table 5.11 records the resulting P's values by application of the optimization process over the time interval $[50, 250]$ sec and it reveals that the MBD with a control parameter $\beta = 0.1$ provides the greatest value of the Boashash-Sucic performance measure as expected from the visual inspection of its $t - f$ domain plot that shows a high concentration of the autoterms. The best resolution of the signal components is provided by the BJD, the ZAMD and the CWD but the inner and outer artifacts reduce the overall performance of these distributions. The KCS-based TFDs result in this case on poor concentration and resolution performances even if their computational costs are lower. The ZAMD TFD contains again high negative crossterms which explains its classification as the worst representing TFD of the signal $s_2(t)$.

Next, we consider the optimization of the fourth best representations of the signal $s_2(t)$ using a kernel length $L = 64$. The new optimized time-frequency representations are depicted in Fig. 5.8 and their relative performances are shown in Table 5.12 together with the kernels' computational costs.

We observe that the signal components are better concentrated around their respective bandwidths using the MBD ; the crossterms amplitudes, however, increase in the regions where the two components are close to each other. These interference terms are much better eliminated by application of the KCS kernels resulting on very high resolution performance. Moreover, the KCS TFDs present the largest values of P. Since the MBD and the SCB TFD have performance measure values that are less than the mean value

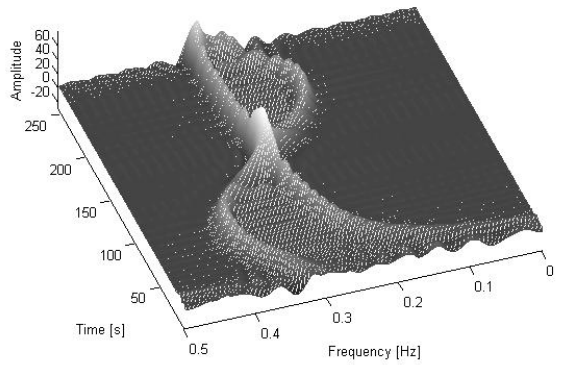
Amplitude
60
40
20
0
-20
250
200
150
100
50
Time [s]
0.5
0.4
0.3
0.2
0.1
0
Frequency [Hz]

(a)

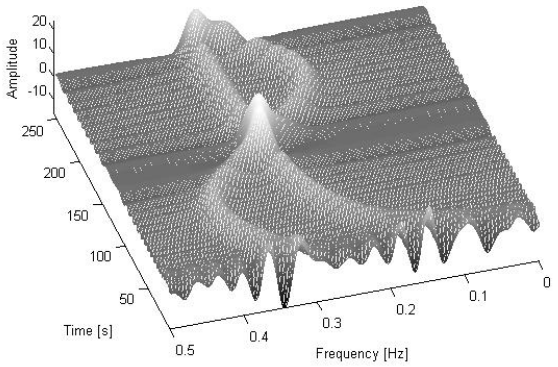
Amplitude
20
10
0
-10
250
200
150
100
50
Time [s]
0.5
0.4
0.3
0.2
0.1
0
Frequency [Hz]

(b)

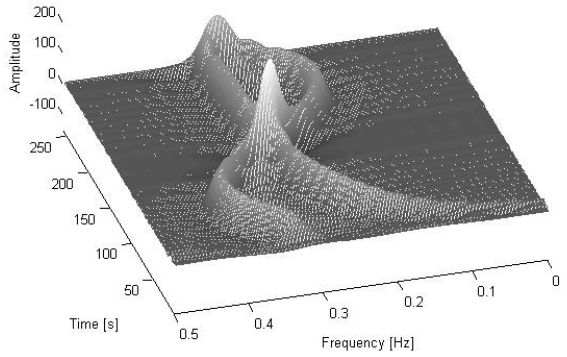
Amplitude
200
100
0
-100
250
200
150
100
50
Time [s]
0.5
0.4
0.3
0.2
0.1
0
Frequency [Hz]

(c)

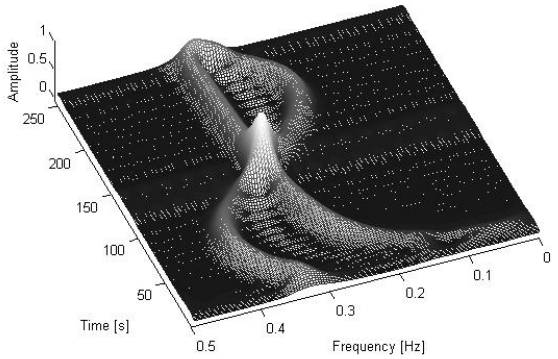
Amplitude
1
0.5
0
250
200
150
100
50
Time [s]
0.5
0.4
0.3
0.2
0.1
0
Frequency [Hz]

(d)

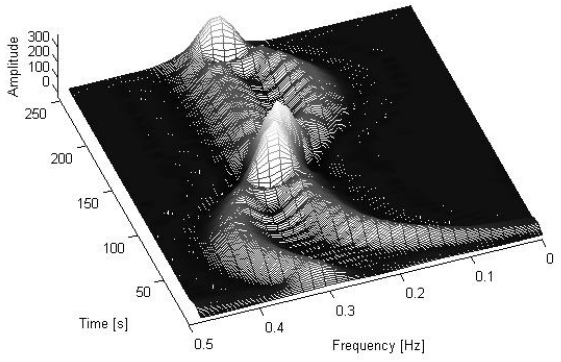
Amplitude
300
200
100
0
250
200
150
100
50
Time [s]
0.5
0.4
0.3
0.2
0.1
0
Frequency [Hz]

(e)

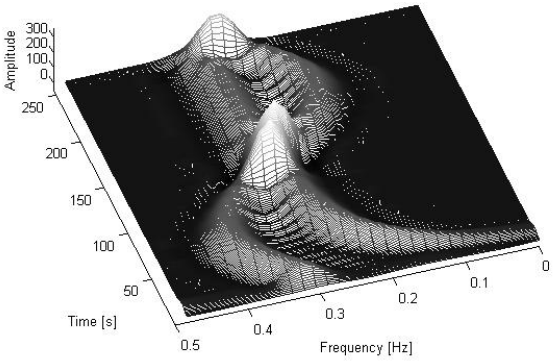
Amplitude
300
200
100
0
250
200
150
100
50
Time [s]
0.5
0.4
0.3
0.2
0.1
0
Frequency [Hz]

(f)

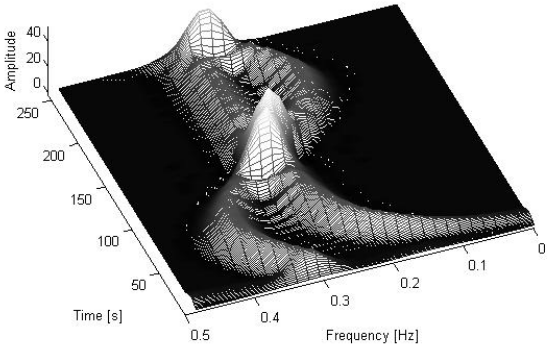

(g)

FIGURE 5.7 – Optimized TFDs over the time interval $t \in [50, 250]$ of the signal of example 2 composed of two crossing nonlinear FMs. (a) BJD, (b) CWD ($\sigma = 0.42$), (c) ZAMD ($\alpha = 0.18$), (d) MBD ($\beta = 0.1$), (e) CB TFD ($C = 1.19$), (f) SCB TFD ($C = 1.49$) and (g) PCB TFD ($\gamma = 2$).

TABLE 5.11 – Optimization results for a selection of TFDs of the signal of example 2 (two crossing nonlinear FMs) over the time interval $t \in [50, 250]$ with $L = 32$.

TFD	Optimal kernel parameters	P	CC
BJD	N/A	0.7860	$M_r = 648;\ \ A_r = 0$
CWD	$\sigma = 0.42$	0.7939	$M_r = 11625;\quad A_r = 2250$
ZAMD	$\alpha = 0.18$	0.7450	$M_r = 1988;\ \ A_r = 710$
MBD	$\beta = 0.1$	0.8328	$M_r = 4393;\quad A_r = 1799$
CB TFD	$C = 1.19$	0.8165	$M_r = 2720;\quad A_r = 1105$
SCB TFD	$C = 1.49$	0.8059	$M_r = 3168;\quad A_r = 1188$
PCB TFD	$\gamma = 2$	0.8156	$M_r = 1720;\quad A_r = 258$

$P_m = 0.8703$, the PCB TFD with optimal control parameter $\gamma = 4$ gives the best result for the two objective criteria and hence is selected as the best performing TFD of the signal $s_2(t)$ and the CB TFD with a parameter $C = 5$ is classified as the second best TFD.

TABLE 5.12 – Optimization results for a selection of kernel-based TFDs of the signal of example 2 over the time interval $t \in [50, 250]$ using $L = 64$.

TFD	Optimal kernel parameters	P	CC
MBD	$\beta = 0.09$	0.8497	$M_r = 5785;\ \ A_r = 2311$
CB TFD	$C = 5$	0.8778	$M_r = 11456;\ \ A_r = 4654$
SCB TFD	$C = 3.65$	0.8683	$M_r = 14080;\ \ A_r = 5280$
PCB TFD	$\gamma = 4$	0.8854	$M_r = 9334;\quad A_r = 1077$

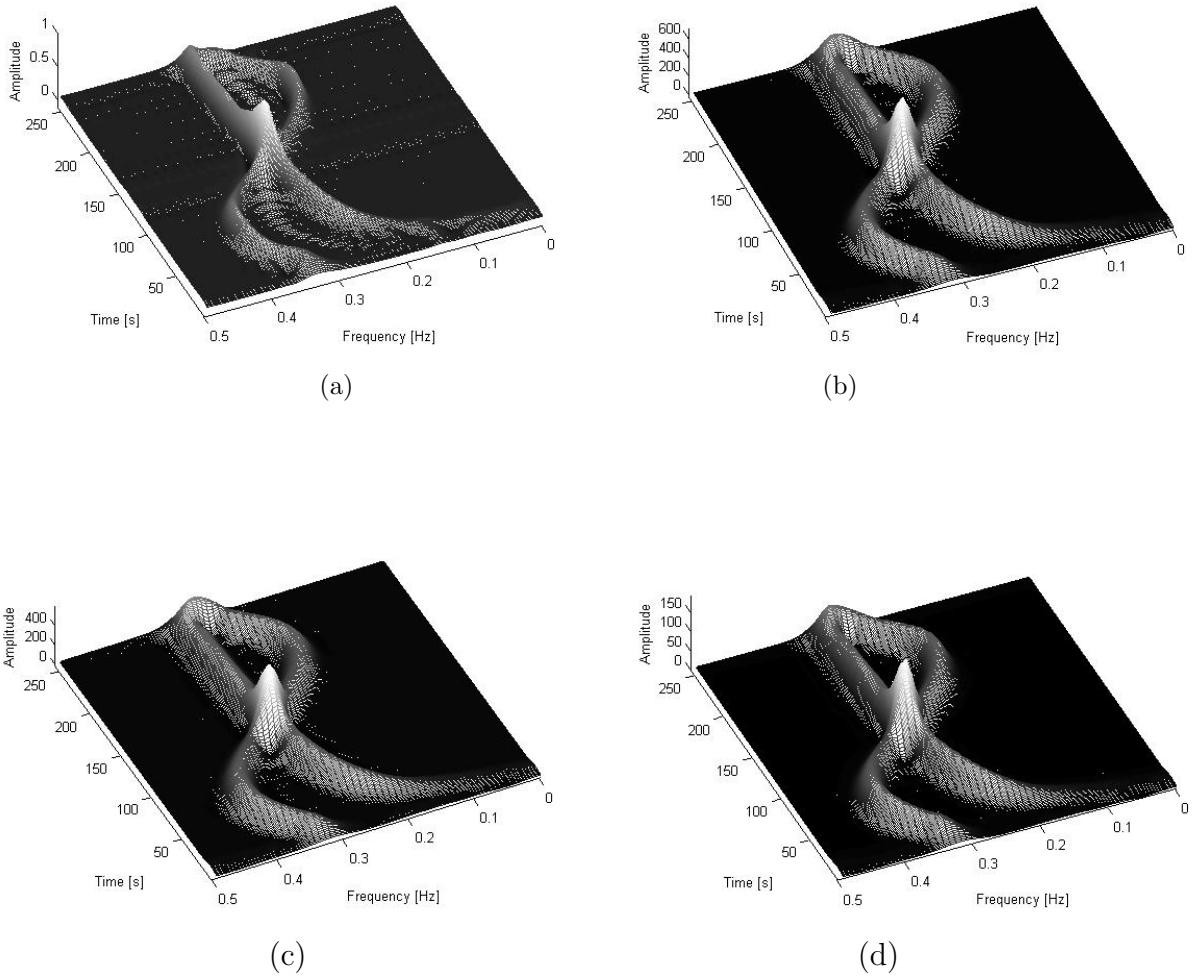

FIGURE 5.8 – Optimized MBD and KCS-based TFDs over the time interval $t \in [50, 250]$ of the signal of example 2 composed of two crossing nonlinear FMs ($L = 64$). (a) MBD ($\beta = 0.09$), (b) CB TFD ($C = 5$), (c) SCB TFD ($C = 3.65$) and (d) PCB TFD ($\gamma = 4$).

5.3.3 Example 3 : Signal with two parallel FM components embedded in noise

The optimization procedure is illustrated on a multicomponent signal $s_3(t)$ consisting of two closely spaced parallel linear chirps over the time interval $T \in [1, 256]$ with frequencies decreasing from 0.28 Hz to 0.18 Hz and from 0.33 Hz to 0.23 Hz, respectively. Next, we embed the signal $s_3(t)$ in additive white Gaussian noise with SNR= 10 dB in order to check the noise effects on the overall performance of kernel-based TFDs under the constraint of the lowest required computational load.

The signal $s_3(t)$ is analyzed in the $t - f$ domain using the same selection of TFDs as in examples 1 and 2. First, we set the kernel's length to 64. The time-frequency plots

of the optimized TFDs according to Boashash-Sucic's performance measure are shown in Fig. 5.9.

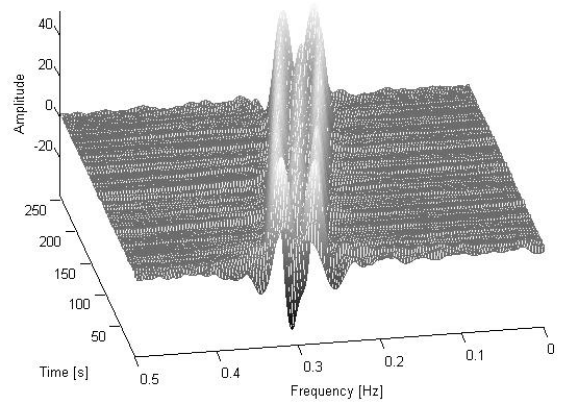

(a)

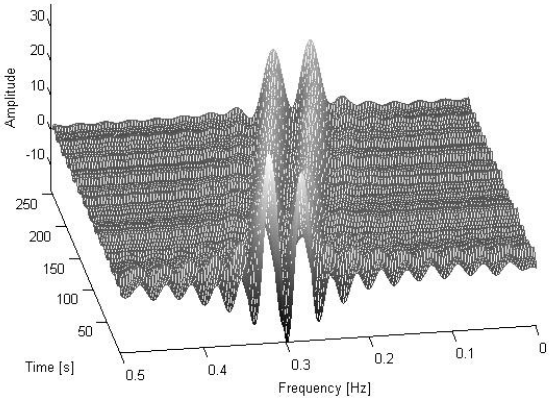

(b)

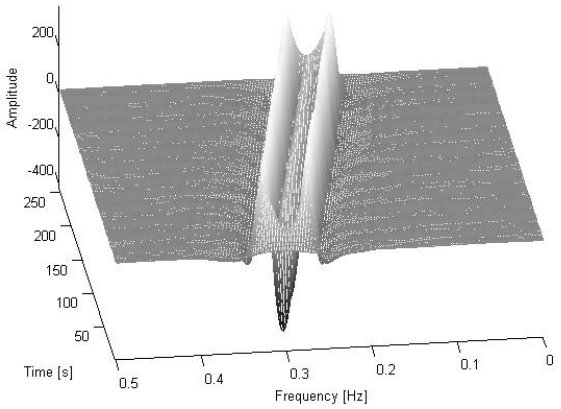

(c)

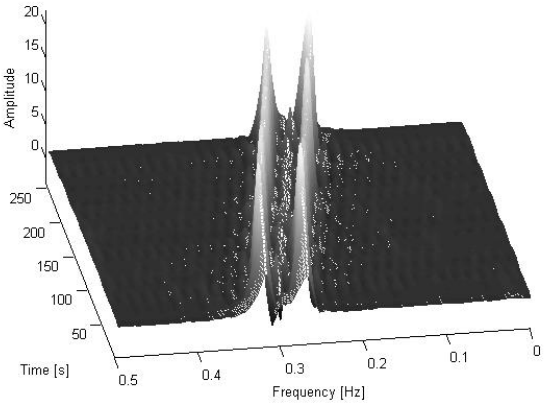

(d)

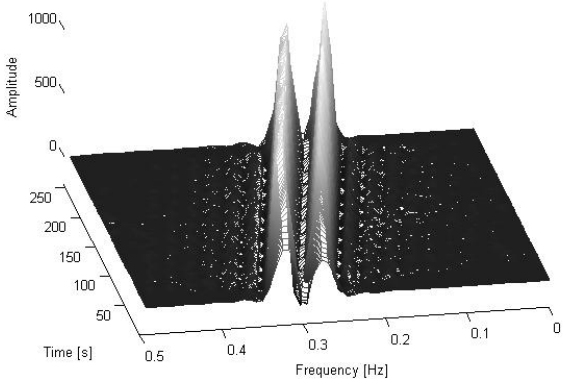

(e)

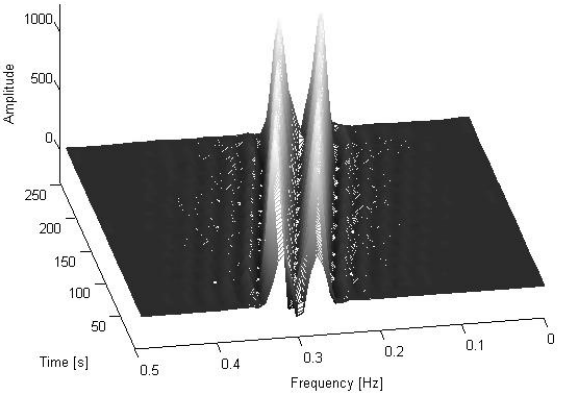

(f)

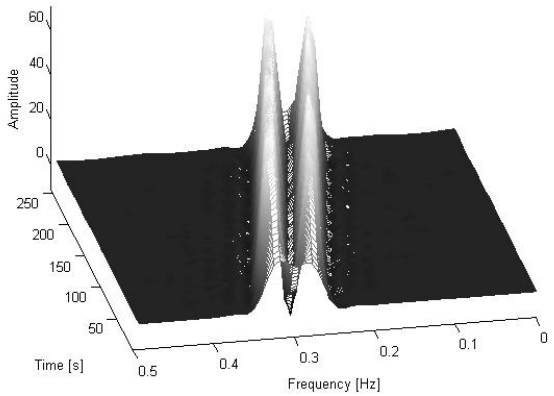

(g)

FIGURE 5.9 – Optimized TFDs over the full duration $T = 256$ of the signal of example 3 composed of two parallel LFMs with frequency ranges decreasing from 0.28 Hz to 0.18 Hz and from 0.33 Hz to 0.23 Hz, respectively ; embedded in 10 dB AWGN. (a) BJD,(b) CWD ($\sigma = 1.21$), (c) ZAMD ($\alpha = 0.19$), (d) MBD ($\beta = 0.037$), (e) CB TFD ($C = 0.046$), (f) SCB TFD ($C = 0.091$) and (g) PCB TFD ($\gamma = 1$).

Here again, from visual inspection, we can see that the KCS-based TFDs and the MBD perform much better that the other considered TFDs since they generate the sharpest plots. Moreover, the figure shows that the autoterms are better concentrated around their respective IFs using the Modified BD kernel whereas the crossterms are better suppressed by the KCS kernels resulting on high P values. This can be seen more clearly by inspecting the time slices at the instant $t_0 = 200$ sec plotted in Fig. 5.10 and their relative P_i values reported in Table 5.13. Furthermore, the CB TFD with control parameter $C = 0.046$ is selected as the best performing TFD of the signal $s_3(t)$ at $t_0 = 200$ since it achieves the greatest instantaneous Boashash-Sucic performance measure ($P_i = 0.9127$).

TABLE 5.13 – Parameters and the instantaneous Boashash-Sucic performance measure P_i of different TFDs of example 3 computed at the time instant $t_0 = 200$ ($L = 64$).

TFD (optimal parameters)	A_{M_1}	A_{M_2}	A_S	A_X	f_{i_1}	f_{i_2}	V_{i_1}	V_{i_2}	V_i	Δf_i	D	P_i
BJD	1.0000	0.9884	0.5293	0.9475	0.1914	0.2422	0.0078	0.0117	0.0098	0.0508	0.8077	0.5996
CWD ($\sigma = 1.21$)	0.9698	1.0000	0.3040	0.5741	0.1934	0.2422	0.0195	0.0117	0.0156	0.0488	0.6800	0.6933
ZAMD ($\alpha = 0.19$)	1.0000	0.9923	0.5760	0.9413	0.1914	0.2422	0.0078	0.0098	0.0088	0.0508	0.8265	0.5919
MBD ($\beta = 0.037$)	0.8371	1.0000	0.0941	0.0749	0.2031	0.2539	0.0156	0.0078	0.0117	0.0508	0.7692	0.8753
CB TFD ($C = 0.046$)	1.0000	0.9600	0.0670	0.0185	0.1984	0.2540	0.0088	0.0116	0.0102	0.0556	0.8158	0.9127
SCB TFD ($C = 0.091$)	0.8347	0.9096	0.1156	0.0412	0.2063	0.2540	0.0146	0.0099	0.0122	0.0476	0.7428	0.8622
PCB TFD ($\gamma = 1$)	1.0000	0.9641	0.0613	0.0327	0.2063	0.2540	0.0258	0.0159	0.0208	0.0476	0.5624	0.8278

Table 5.14 contains the optimization process over the full range of time instants and indicates that the KCS-based TFDs and the MBD outperform the other quadratic time-frequency distributions with a significant difference in the achieved P of about 0.1077 to 0.1249 compared to $P_{max} = 0.8473$. Furthermore, if we include the numerical complexity of the Hamming window used by the MBD to improve the frequency resolution ;

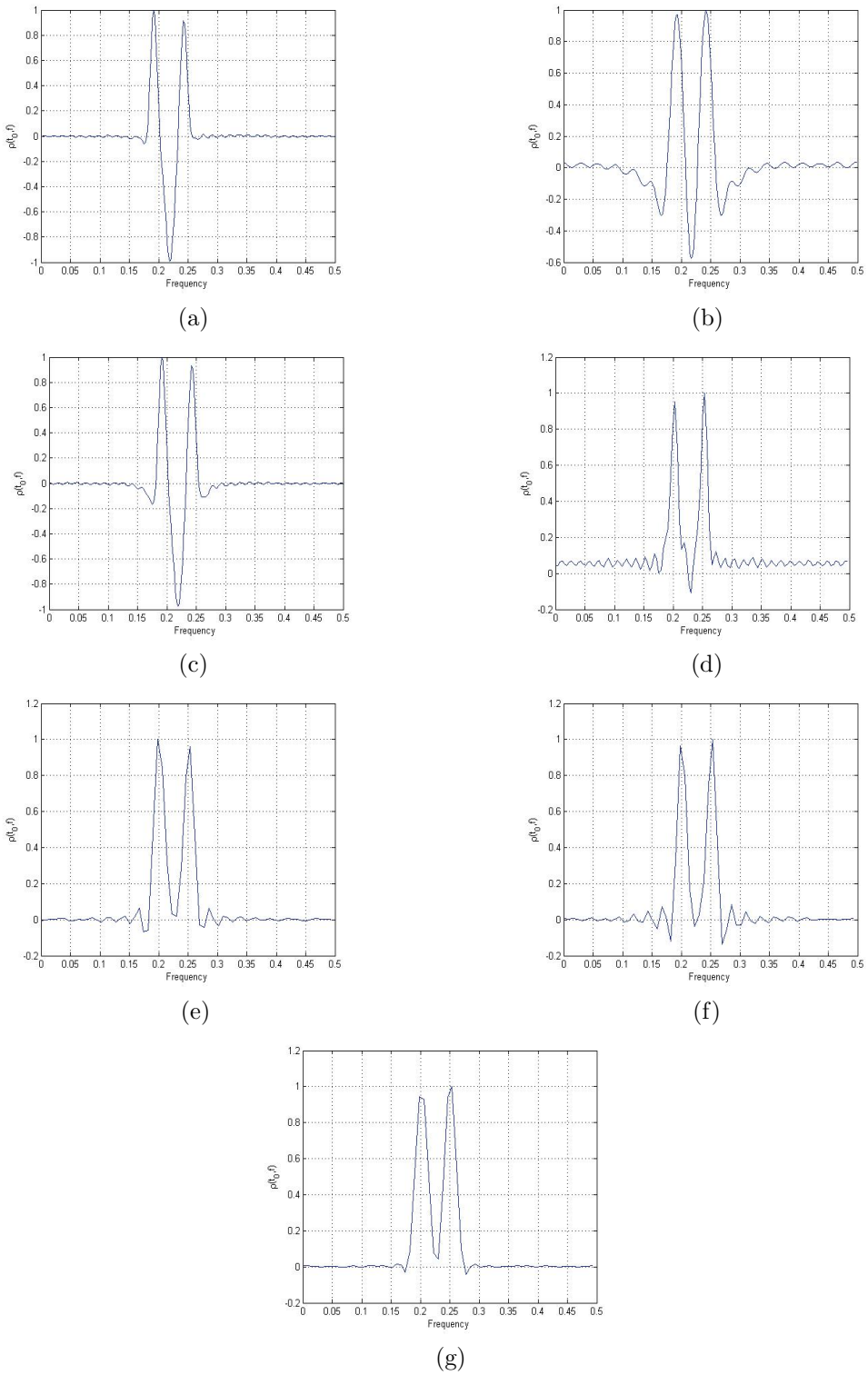

FIGURE 5.10 – Normalized slices of TFDs at the time instant $t_0 = 200$ sec of the signal $s_3(t)$ with $L = 64$. (a) BJD, (b) CWD ($\sigma = 1.21$), (c) ZAMD ($\alpha = 0.19$), (d) MBD ($\beta = 0.037$), (e) CB TFD ($C = 0.046$), (f) SCB TFD ($C = 0.091$) and (g) PCB TFD ($\gamma = 1$).

the signal $s_3(t)$ is then best represented in the $t-f$ plane using the PCB TFD with optimized parameter $\gamma = 1$ since it provides a P value that is very close to the optimal one achieved by the CB TFD and has the lowest numerical complexity corresponding to 64.62% and 53.77% of the computational loads required by the CB TFD and the SCB TFD, respectively.

TABLE 5.14 – Optimization results for a selection of TFDs of the signal of example 3 (two noisy parallel linear FMs) over the full range of time instants $T = 256$ with $L = 64$.

TFD	Optimal kernel parameters	P	CC
BJD	N/A	0.7224	$M_r = 2448$; $A_r = 0$
CWD	$\sigma = 1.21$	0.7396	$M_r = 49321$; $A_r = 9610$
ZAMD	$\alpha = 0.19$	0.7253	$M_r = 7588$; $A_r = 2710$
MBD	$\beta = 0.037$	0.8472	$M_r = 5785$; $A_r = 2311$
CB TFD	$C = 0.046$	0.8473	$M_r = 11456$; $A_r = 4654$
SCB TFD	$C = 0.091$	0.8442	$M_r = 14080$; $A_r = 5280$
PCB TFD	$\gamma = 1$	0.8412	$M_r = 6103$; $A_r = 1077$

Let us now check the effect of increasing the kernel length to 128 on the quality of the TF representations and the accurate estimation of the IF laws in particular for the KCS kernels. For this purpose, we optimize the sixth best performing TFDs. The compact support kernels are characterized by $N_{nz}^{CB} = 1422$, $N_{nz}^{SCB} = 1764$ and $N_{nz}^{PCB} = 1422$ while $N_{nz}^{ZAM} = 1056$. The resulting representations are shown in Fig. 5.11 and the overall Boashash-Sucic performance measures are recorded in Table 5.15 together with the kernels' computational loads. From visual inspection and the achieved P values, it is seen that the KCS-based TFDs give the best concentration/resolution performance and attenuate the crossterms clearly much better than the other distributions which allows an easy distinction of the two FM components.

TABLE 5.15 – Optimization results for a selection of TFDs of the signal of example 3 over the time interval $t \in [1, 256]$ with $L = 128$.

TFD	Optimal kernel parameters	P	CC
CWD	$\sigma = 1.32$	0.7308	$M_r = 203049$; $A_r = 39690$
ZAMD	$\alpha = 0.15$	0.7273	$M_r = 29540$; $A_r = 10550$
MBD	$\beta = 0.038$	0.8348	$M_r = 8569$; $A_r = 3335$
CB TFD	$C = 1.03$	0.9066	$M_r = 45472$; $A_r = 18473$
SCB TFD	$C = 1.96$	0.8979	$M_r = 56416$; $A_r = 21156$
PCB TFD	$\gamma = 2$	0.9026	$M_r = 28440$; $A_r = 4266$

Another objective inspection is obtained at $t_0 = 200$ sec from the time slices plotted in Fig. 5.12 and their relative parameters recorded in Table 5.16. Compared to the results obtained using a kernel length $L = 64$, we see a significant improvement of the IF laws' estimation, the crossterms' reduction and the achieved concentration and resolution measures. However, if real-time implementation is entended, the MBD with an optimized parameter $\beta = 0.038$ is selected as the optimal representation of the signal $s_3(t)$ since it results on a P value that is greater than the mean value of the achived performance

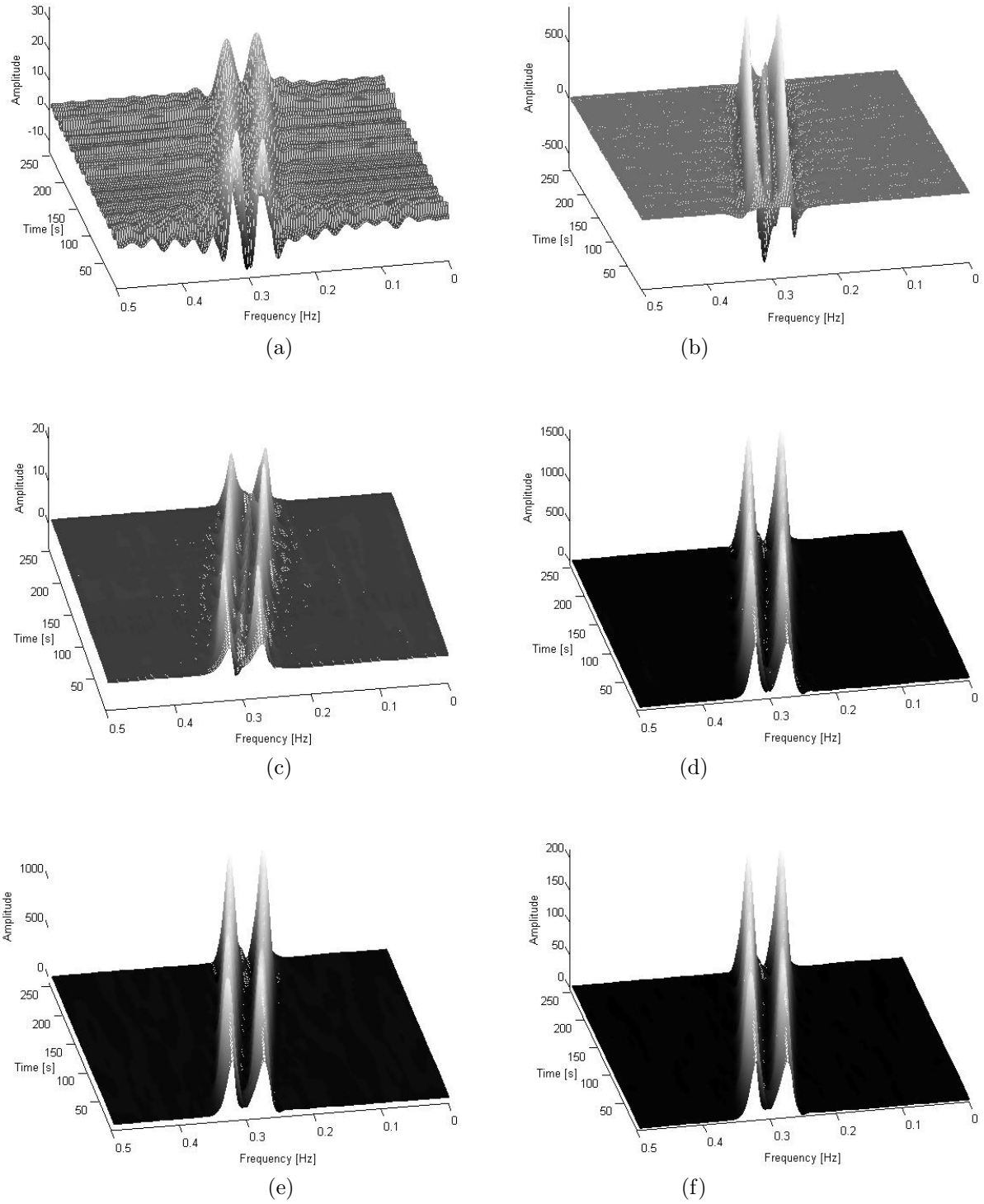

FIGURE 5.11 – Optimized TFDs over the full duration $T = 256$ of the signal of example 3 using a kernel length $L = 128$. (a) CWD ($\sigma = 1.32$), (b) ZAMD ($\alpha = 0.15$), (c) MBD ($\beta = 0.038$), (d) CB TFD ($C = 1.03$), (e) SCB TFD ($C = 1.96$) and (f) PCB TFD ($\gamma = 2$).

measures $P_m = 0.8333$ with a considerably low numerical complexity compared to the other kernel-based TFDs that is about 6.51 times smaller than the SCB TFD's *CC*, 5.37 times smaller than the CB TFD's *CC* and 2.74 times smaller than the PCB TFD's *CC*.

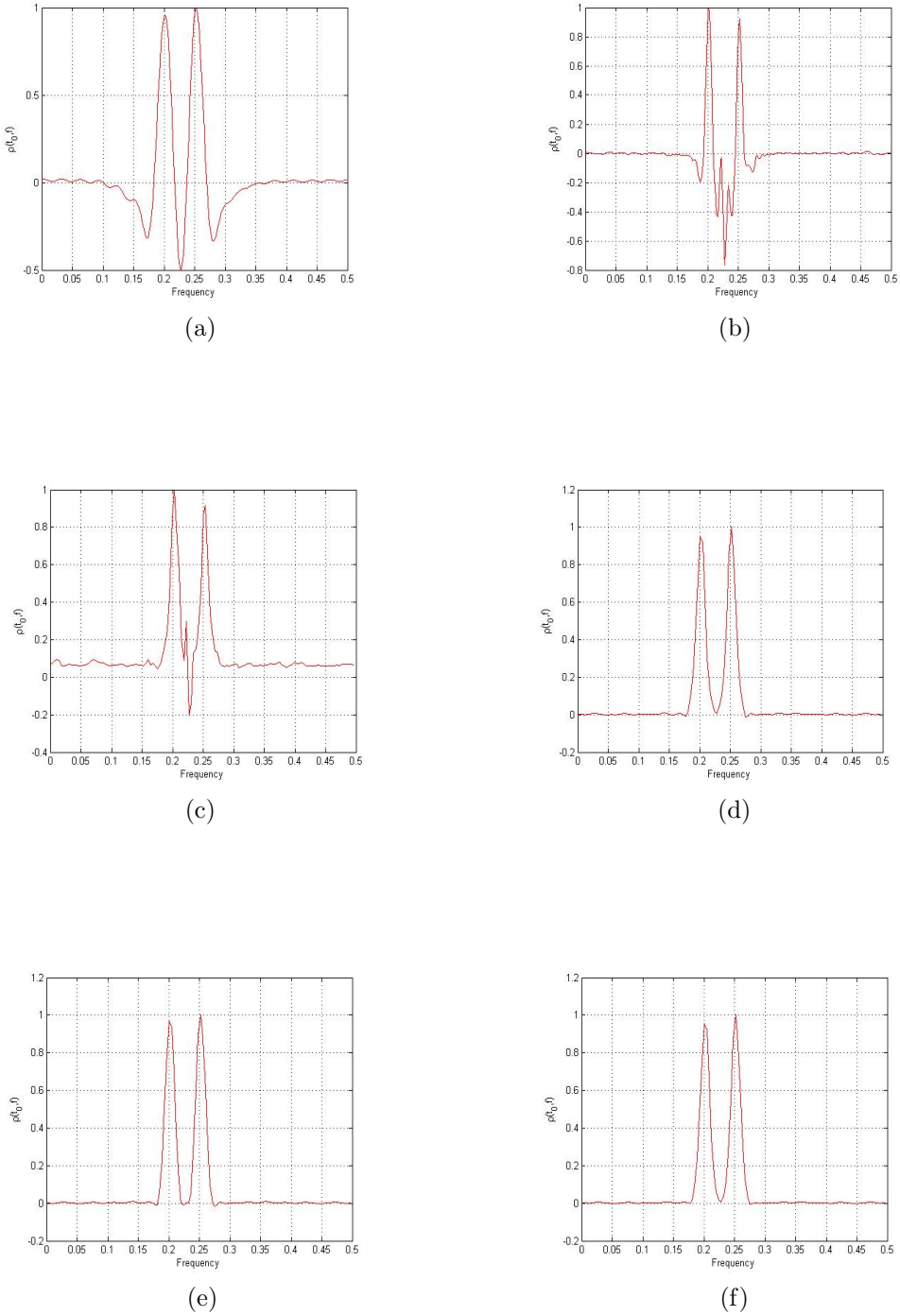

(a) (b) (c) (d) (e) (f)

FIGURE 5.12 – Normalized slices of TFDs at the time instant $t_0 = 200$ sec of the signal $s_3(t)$ with $L = 128$. (a) CWD ($\sigma = 1.32$), (b) ZAMD ($\alpha = 0.15$), (c) MBD ($\beta = 0.038$), (d) CB TFD ($C = 1.03$), (e) SCB TFD ($C = 1.96$) and (f) PCB TFD ($\gamma = 2$).

TABLE 5.16 – Parameters and the instantaneous Boashash-Sucic performance measure P_i of different TFDs of example 3 computed at the time instant $t_0 = 200$ ($L = 128$).

TFD (optimal parameters)	A_{M_1}	A_{M_2}	A_S	A_X	f_{i_1}	f_{i_2}	V_{i_1}	V_{i_2}	V_i	Δf_i	D	P_i
CWD ($\sigma = 1.32$)	0.9604	1.0000	0.3253	0.4971	0.2012	0.2520	0.0195	0.0156	0.0176	0.0508	0.6538	0.6895
ZAMD ($\alpha = 0.15$)	0.9686	0.8275	0.4296	0.7659	0.2031	0.2539	0.0117	0.0039	0.0078	0.0508	0.8462	0.6471
MBD ($\beta = 0.038$)	0.9605	1.0000	0.1203	0.1374	0.2031	0.2539	0.0104	0.0078	0.0091	0.0508	0.8203	0.8760
CB TFD ($C = 1.03$)	0.9507	1.0000	0.0143	0.0065	0.2008	0.2520	0.0090	0.0105	0.0048	0.0512	0.8089	0.9303
SCB TFD ($C = 1.96$)	0.9700	1.0000	0.0149	0.0044	0.2008	0.2520	0.0157	0.0157	0.0157	0.0512	0.6923	0.8916
PCB TFD ($\gamma = 2$)	0.9758	1.0000	0.0110	0.0062	0.2008	0.2520	0.0101	0.0115	0.0108	0.0512	0.7891	0.9249

In the same context, we check for the same test signal and selection of TFDs the effect of increasing the noise power to 0 dB on their performance in resolving the two components and estimating the IF laws. For the MBD, we use a Kaiser window of width 127 to enhance the frequency resolution. Fig. 5.13 displays the obtained time-frequency diagrams while Table 5.17 presents the overall P values. The time slices at $t_0 = 200$ are depicted in Fig. 5.14 and their relative parameters are recorded in Table 5.18.

It is clearly seen that the KCS-based TFDs give the best resolution and concentration results and still distinguish between the two linear components thanks to the efficient low-pass filtering performed by the Doppler-lag compact support kernels that attenuates the noise level too. The numerical values of Table 5.18 show that, at $t_0 = 200$ sec, the average crossterm amplitude of the KCS TFDs is ten times smaller than the CWD crossterm amplitude and approximately five times smaller than the artifacts generated by the ZAMD and the MBD. The average sidelobe amplitude of the KCS-based TFDs presents 17.41%, 38.13% and 42.88% of the generated sidelobes using the ZAM, the CW and the MBD kernels, respectively. On the other hand, Fig. 5.15 shows that the actual IF laws are still been best estimated from the KCS-TFDs' peaks even if signal and noise have the same power much better than the other investigated distributions. In this case, the PCB TFD with smoothing parameter $\gamma = 4$ is selected as the best performing distribution since it provides the greatest value of P followed by the CB TFD even if its computational cost is about 1.3 times the one required by the MBD because there is a difference of 0.1061 (10.61%) in the achieved P which is in fact a big value from overall performance point of view.

TABLE 5.17 – Optimization results for a selection of TFDs of the signal of example 3 with SNR= 0 dB and $L = 128$ over the time interval $t \in [1, 256]$.

TFD	Optimal kernel parameters	P	CC
CWD	$\sigma = 1.42$	0.7189	$M_r = 203049$; $A_r = 39690$
ZAMD	$\alpha = 0.11$	0.7087	$M_r = 29540$; $A_r = 10550$
MBD	$\beta = 0.06$	0.7617	$M_r = 8569$; $A_r = 3335$
CB TFD	$C = 3.2$	0.8678	$M_r = 45472$; $A_r = 18473$
SCB TFD	$C = 4.2$	0.8585	$M_r = 56416$; $A_r = 21156$
PCB TFD	$\gamma = 4$	0.8637	$M_r = 28440$; $A_r = 4266$

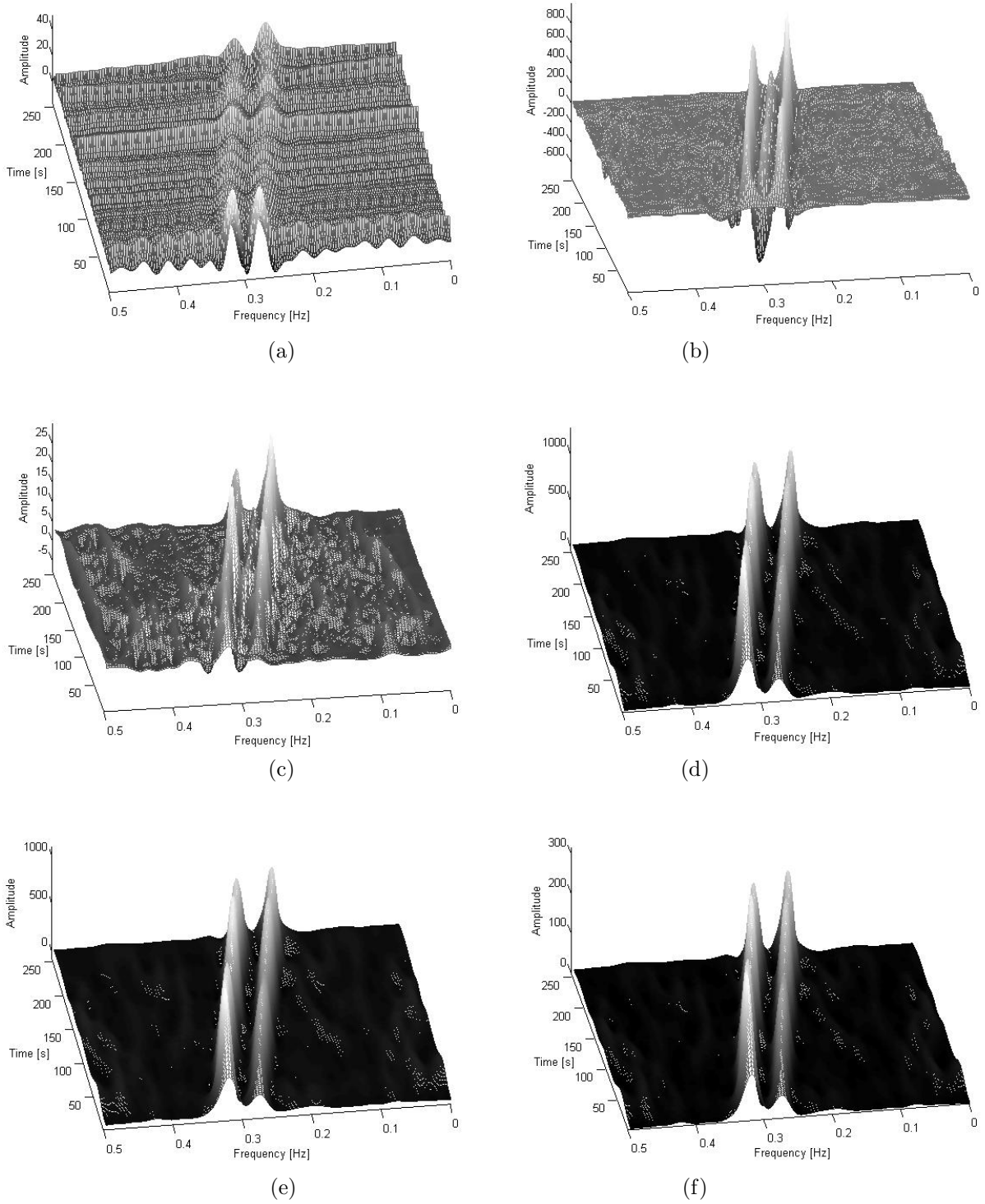

FIGURE 5.13 – Optimized TFDs over the full duration $T = 256$ of the signal of example 3 with SNR = 0 dB and a kernel length $L = 128$. (a) CWD ($\sigma = 1.42$), (b) ZAMD ($\alpha = 0.11$), (c) MBD ($\beta = 0.06$), (d) CB TFD ($C = 3.2$), (e) SCB TFD ($C = 4.2$) and (f) PCB TFD ($\gamma = 4$).

TABLE 5.18 – Parameters and the instantaneous Boashash-Sucic performance measure P_i of different TFDs of example 3 with SNR= 0 dB and $L = 128$ computed at the time instant $t_0 = 200$.

TFD (optimal parameters)	A_{M_1}	A_{M_2}	A_S	A_X	f_{i_1}	f_{i_2}	V_{i_1}	V_{i_2}	V_i	Δf_i	D	P_i
CWD ($\sigma = 1.42$)	0.9987	0.7332	0.2266	0.3221	0.2031	0.2539	0.0195	0.0156	0.0176	0.0508	0.6538	0.7354
ZAMD ($\alpha = 0.11$)	1	0.7560	0.4850	0.1627	0.2031	0.2285	0.0078	0.0078	0.0078	0.0254	0.6923	0.6824
MBD ($\beta = 0.06$)	1.0000	0.6774	0.2015	0.1612	0.2031	0.2539	0.0104	0.0156	0.0130	0.0508	0.7441	0.8026
CB TFD ($C = 3.2$)	0.9508	1.0000	0.0848	0.0323	0.2008	0.2520	0.0157	0.0126	0.0142	0.0512	0.7235	0.8733
SCB TFD ($C = 4.2$)	0.9436	1.0000	0.0887	0.0336	0.2008	0.2520	0.0157	0.0157	0.0157	0.0512	0.6923	0.8612
PCB TFD ($\gamma = 4$)	0.9357	1.0000	0.0858	0.0330	0.2008	0.2520	0.0157	0.0124	0.0141	0.0512	0.7247	0.8730

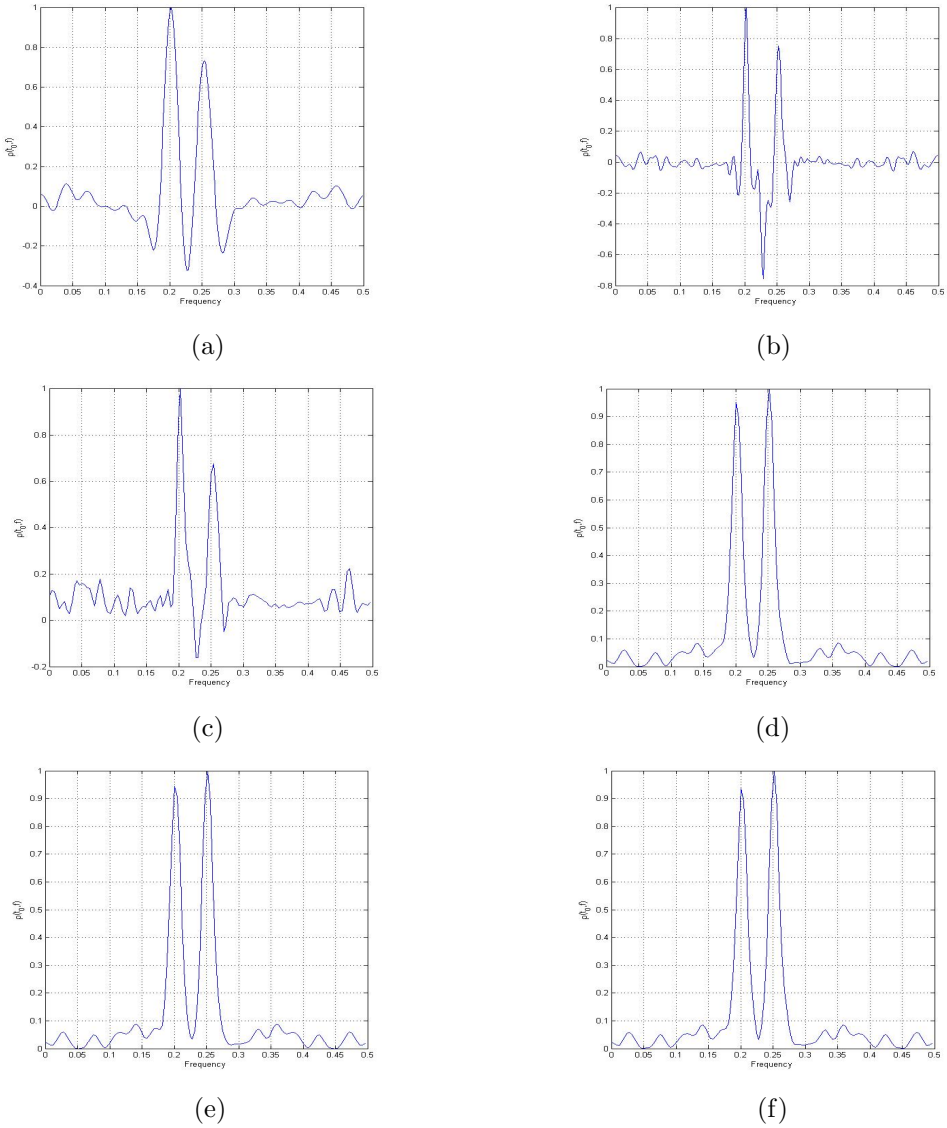

FIGURE 5.14 – Normalized slices of TFDs at the time instant $t_0 = 200$ sec of the signal $s_3(t)$ with SNR= 0 dB and $L = 128$. (a) CWD ($\sigma = 1.42$), (b) ZAMD ($\alpha = 0.11$), (c) MBD ($\beta = 0.06$), (d) CB TFD ($C = 3.2$), (e) SCB TFD ($C = 4.2$) and (f) PCB TFD ($\gamma = 4$).

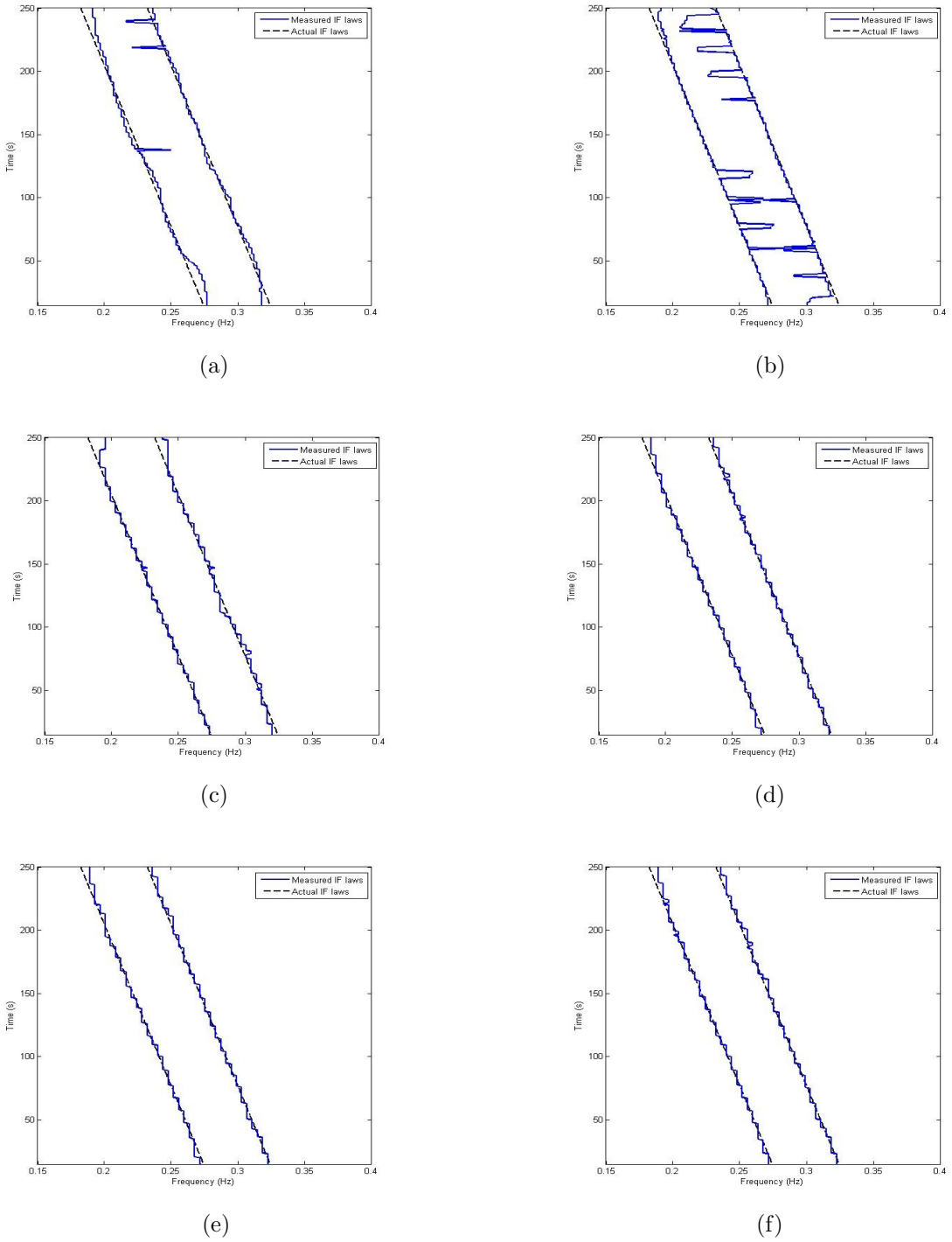

FIGURE 5.15 – Comparison of the measured and actual IF laws of the signal $s_3(t)$ composed of two parallel LFMs with frequency ranges decreasing from 0.28 Hz to 0.18 Hz and from 0.33 Hz to 0.23 Hz, respectively ; embedded in 0 dB AWGN ($L = 128$). (a) CWD ($\sigma = 1.42$), (b) ZAMD ($\alpha = 0.11$), (c) MBD ($\beta = 0.06$), (d) CB TFD ($C = 3.2$), (e) SCB TFD ($C = 4.2$) and (f) PCB TFD ($\gamma = 4$).

5.3.4 Example 4 : Sum of two quadratic FMs and two constant frequency signals.

In this example, the signal $s_4(t)$, of duration $T = 256$, consists of two very close constant frequency (CF) components of frequencies $f = 0.3$ Hz and $f = 0.35$ Hz, respectively and two noiseless crossing quadratic FMs such that $f(t = 1) = f(t = 256) = 0.25$ Hz for the convex component and $f(t = 1) = f(t = 256) = 0.1$ Hz for the concave one. The kernel length is set to 128.

Fig. 5.16 shows the superiority of the KCS-based TFDs and the MBD over the other quadratic time-frequency distributions in resolving the four closely spaced components as well as in reducing the crossterms. This visual result is confirmed by the time slices' plots depicted in Figs. 5.17-5.18 and the Boashash-Sucic instantaneous performance measures and parameters recorded in Tables 5.19-5.20 corresponding to the two intersecting quadratic FMs and the two CF components, respectively, observed at $t_0 = 138$ sec.

TABLE 5.19 – Parameters and the instantaneous Boashash-Sucic performance measure P_i of several TFDs of the two quadratic FM components of example 4 computed at the time instant $t_0 = 138$.

TFD (optimal parameters)	A_{M_1}	A_{M_2}	A_S	A_X	f_{i_1}	f_{i_2}	V_{i_1}	V_{i_2}	V_i	Δf_i	D	P_i
BJD	0.9249	1.0000	0.3666	0.2136	0.1523	0.2480	0.0117	0.0117	0.0117	0.0957	0.8776	0.7952
CWD ($\sigma = 0.9$)	0.9905	1.0000	0.2278	0.2612	0.1523	0.2480	0.0195	0.0156	0.0176	0.0176	0.8163	0.8187
ZAMD ($\alpha = 0.15$)	1.0000	0.9055	0.5508	0.0007	0.1543	0.2461	0.0078	0.0078	0.0078	0.0918	0.9149	0.7788
MBD ($\beta = 0.04$)	1.0000	0.9368	0.1829	0.0891	0.1523	0.2461	0.0078	0.0078	0.0078	0.0938	0.9167	0.8939
CB TFD ($C = 4$)	0.9955	1.0000	0.0229	0.0015	0.1496	0.2441	0.0157	0.0110	0.0134	0.0945	0.8583	0.9449
SCB TFD ($C = 4$)	1.0000	0.9864	0.0430	0.0017	0.1496	0.2441	0.0157	0.0102	0.0130	0.0945	0.8624	0.9394
PCB TFD ($\gamma = 4$)	1.0000	0.9820	0.0099	0.0004	0.1496	0.2441	0.0157	0.0097	0.0127	0.0945	0.8653	0.9517

TABLE 5.20 – Parameters and the instantaneous Boashash-Sucic performance measure P_i of several TFDs of the two constant frequency components of example 4 computed at the time instant $t_0 = 138$.

TFD (optimal parameters)	A_{M_1}	A_{M_2}	A_S	A_X	f_{i_1}	f_{i_2}	V_{i_1}	V_{i_2}	V_i	Δf_i	D	P_i
BJD	0.6811	1.0000	0.5693	0.1780	0.2539	0.3242	0.0011	0.0195	0.0103	0.0703	0.8530	0.6900
CWD ($\sigma = 0.9$)	1.0000	0.8667	0.4471	0.3211	0.3008	0.3477	0.0234	0.0156	0.0195	0.0469	0.5833	0.6441
ZAMD ($\alpha = 0.15$)	0.9896	0.8816	0.3840	0.2936	0.3008	0.3516	0.0078	0.0022	0.0050	0.0508	0.9012	0.7780
MBD ($\beta = 0.04$)	1.0000	0.9261	0.1026	0.0207	0.3008	0.3516	0.0078	0.0030	0.0054	0.0508	0.8932	0.9253
CB TFD ($C = 4$)	0.9957	1.0000	0.0200	0.0033	0.2953	0.3465	0.0102	0.0109	0.0106	0.0512	0.7934	0.9239
SCB TFD ($C = 4$)	0.9950	1.0000	0.0280	0.0042	0.2953	0.3465	0.0079	0.0103	0.0091	0.0512	0.8228	0.9309
PCB TFD ($\gamma = 4$)	0.9945	1.0000	0.0101	0.0018	0.2953	0.3465	0.0079	0.0099	0.0089	0.0512	0.8265	0.9385

It is seen that the KCS TFDs provide the highest resolution/concentration performances thanks to their compact support nature that best eliminates the crossterms. From Table 5.20, we see that the BJD provides wrong computation of the time slice parameters which results on wrong estimation of the IF laws that are best approximated using the ZAMD, the MBD, the KCS TFDs and the CWD even if it possesses the lowest value of P_i. We conclude that a better estimation of the true instantaneous frequency laws from the TFDs' peaks does not always implies suitable performances in terms of concentration,

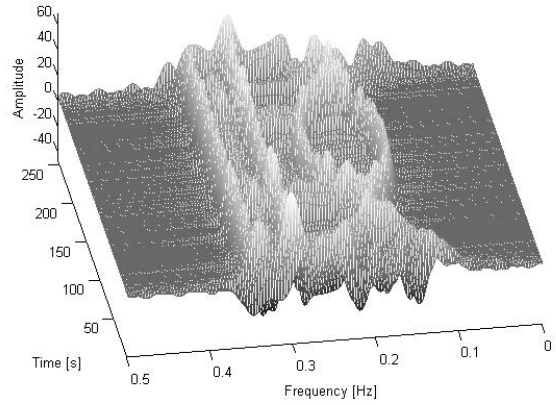
Amplitude
Time [s]
Frequency [Hz]

(a)

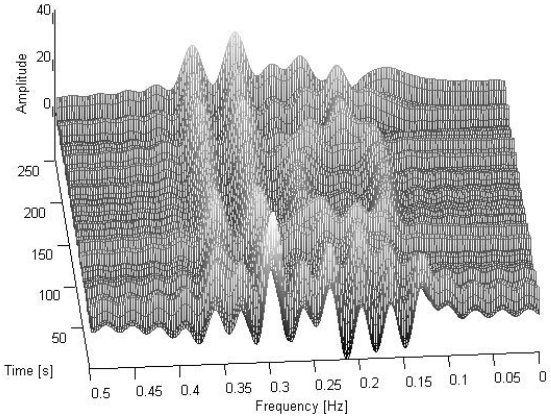
Amplitude
Time [s]
Frequency [Hz]

(b)

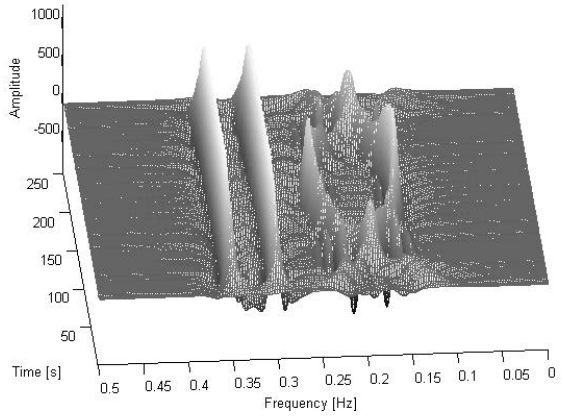
Amplitude
Time [s]
Frequency [Hz]

(c)

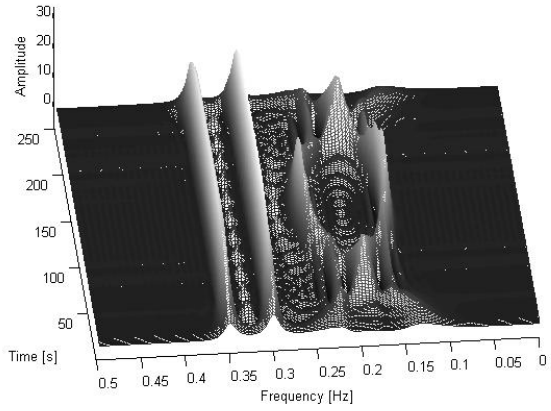
Amplitude
Time [s]
Frequency [Hz]

(d)

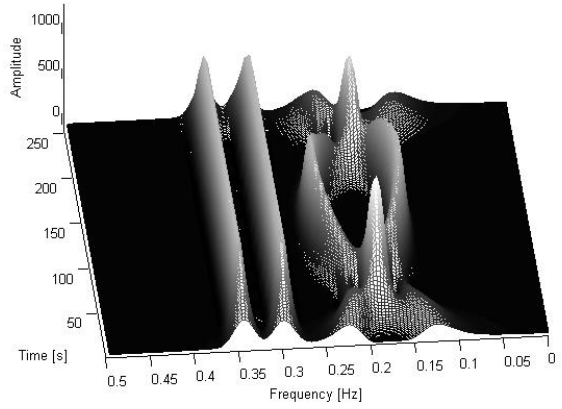
Amplitude
Time [s]
Frequency [Hz]

(e)

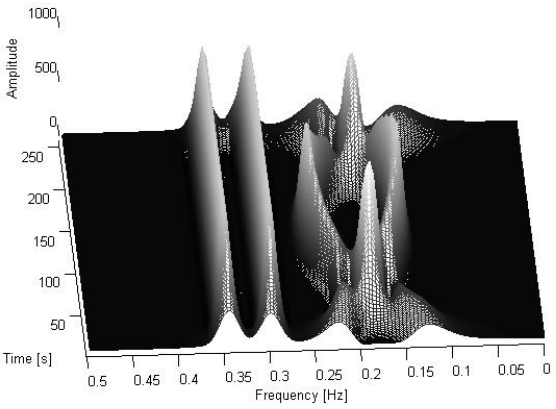
Amplitude
Time [s]
Frequency [Hz]

(f)

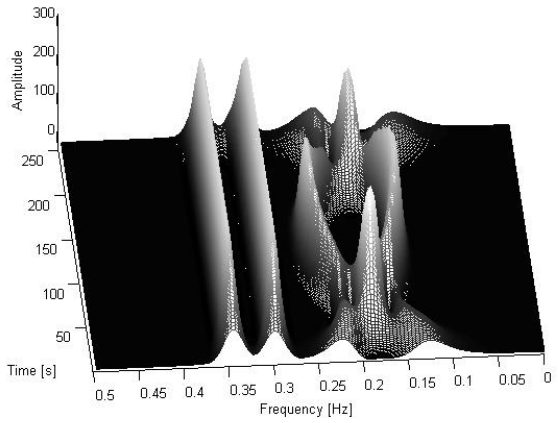

(g)

FIGURE 5.16 – Optimized TFDs over the time interval $t \in [70, 190]$ of the signal of example 4. (a) BJD, (b) CWD ($\sigma = 0.9$), (c) ZAMD ($\alpha = 0.15$), (d) MBD ($\beta = 0.04$), (e) CB TFD ($C = 4$), (f) SCB TFD ($C = 4$) and (g) PCB TFD ($\gamma = 4$).

resolution and crossterm reduction. Moreover, the obtained results indicate that the PCB TFD with bandwidth control parameter $\gamma = 4$ is the signal best representation at $t_0 = 138$ since it produces the largest average instantaneous performance measure ($P_{i_{av}} = 0.9451$) whereas the SCB TFD with a kernel parameter $C = 4$ is the second best performing TFD at this time instant ($P_{i_{av}} = 0.9351$).

Since the signal $s_4(t)$ is composed of $M = 4$ components, the Boashash-Sucic's procedure is then applied twice in order to measure the parameters for each of the pairs of consecutive components with dominant amplitudes of each TFD time slice. The time of interest is within the interval $[70, 190]$ sec. The optimizing TFDs' parameters are chosen so that they produce the largest value of the Boashash-Sucic's overall performance measure for both the two quadratic FMs ($P^{(1)}$) and the two CF components ($P^{(2)}$); the resulting P to maximize is equal to the average $(P^{(1)} + P^{(2)})/2$. Table 5.21 presents the numerical results of the optimization procedure including the P performance measure and the computational cost criterion.

TABLE 5.21 – Optimization results for a selection of quadratic TFDs of the signal of example 4 over the time interval $t \in [70, 190]$.

TFD	Optimal kernel parameters	$P^{(1)}$	$P^{(2)}$	P	CC
BJD	N/A	0.7592	0.7345	0.7469	$M_r = 9504;\ A_r = 0$
CWD	$\sigma = 0.9$	0.7754	0.7226	0.7490	$M_r = 203049;\ A_r = 39690$
ZAMD	$\alpha = 0.15$	0.8007	0.8552	0.8279	$M_r = 29540;\ A_r = 10550$
MBD	$\beta = 0.04$	0.8462	0.9253	0.8858	$M_r = 8569;\ A_r = 3335$
CB TFD	$C = 4$	0.8948	0.9229	0.9089	$M_r = 45472;\ A_r = 18473$
SCB TFD	$C = 4$	0.9059	0.9316	0.9187	$M_r = 56416;\ A_r = 21156$
PCB TFD	$\gamma = 4$	0.9041	0.9297	0.9169	$M_r = 36972;\ A_r = 4266$

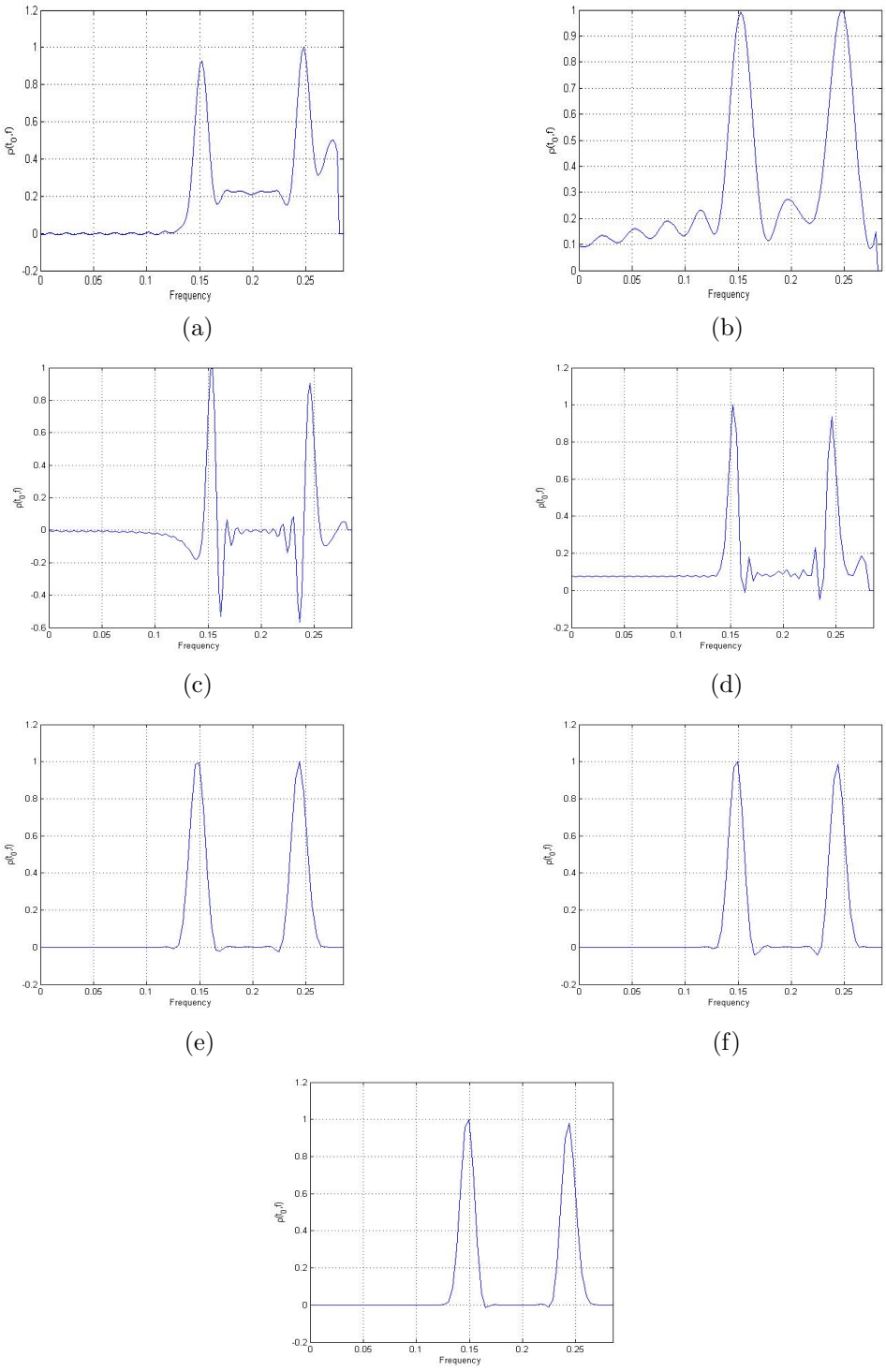

FIGURE 5.17 – Normalized slices of TFDs at the time instant $t_0 = 138$ sec of the two quadratic FMs of the signal $s_4(t)$. (a) BJD, (b) CWD ($\sigma = 0.9$), (c) ZAMD ($\alpha = 0.15$), (d) MBD ($\beta = 0.04$), (e) CB TFD ($C = 4$), (f) SCB TFD ($C = 4$) and (g) PCB TFD ($\gamma = 4$).

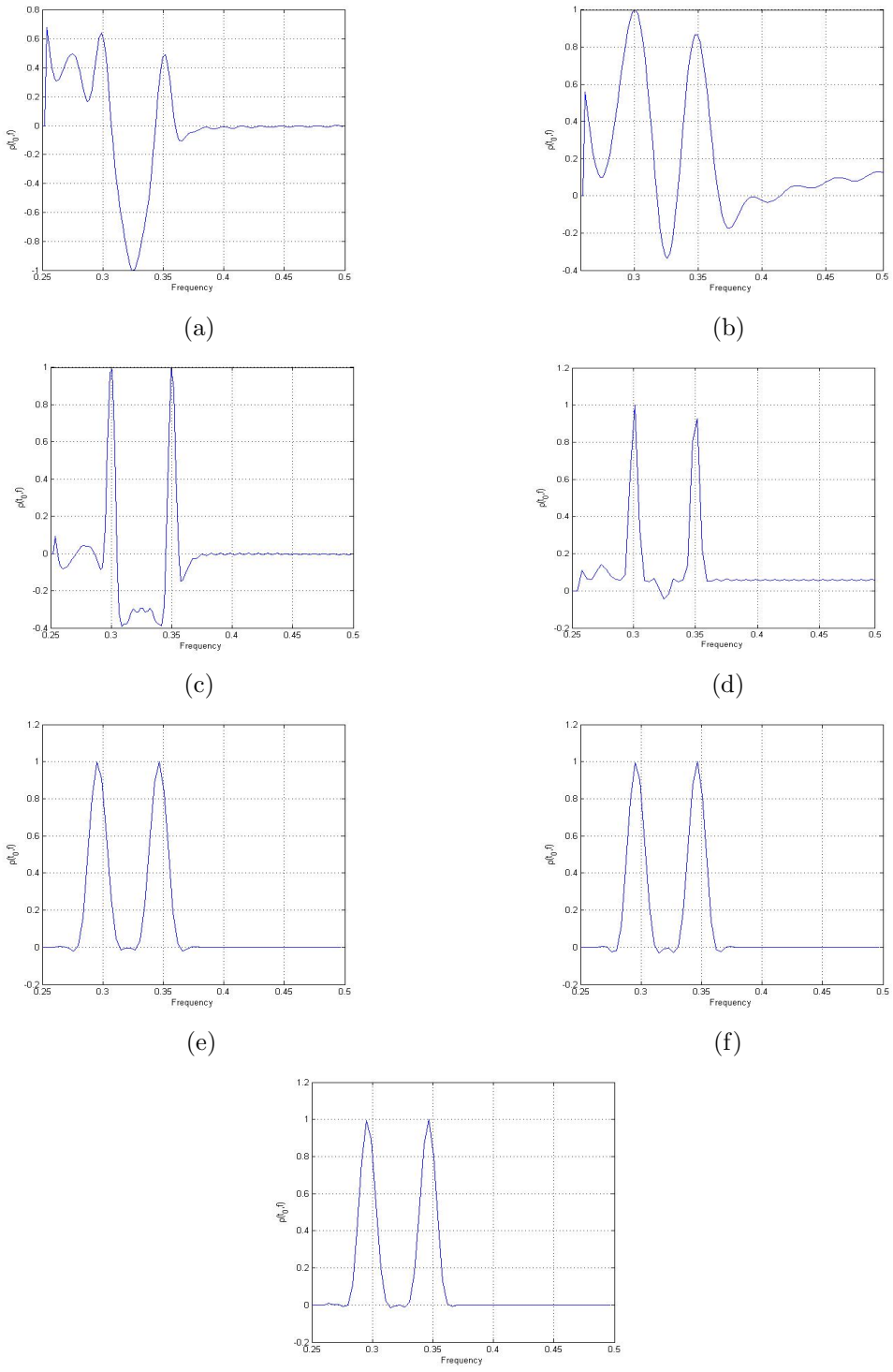

FIGURE 5.18 – Normalized slices of TFDs at the time instant $t_0 = 138$ sec of the two CF components of the signal $s_4(t)$. (a) BJD, (b) CWD ($\sigma = 0.9$), (c) ZAMD ($\alpha = 0.15$), (d) MBD ($\beta = 0.04$), (e) CB TFD ($C = 4$), (f) SCB TFD ($C = 4$) and (g) PCB TFD ($\gamma = 4$).

We observe that the KCS TFDs' family presents the highest values of P whereas the BJD and the MBD provide the lowest numbers of required real multiplications and additions. Moreover, the MB-distribution with optimized parameter $\beta = 0.04$ is selected as the optimal TFD for representing $s_4(t)$ since it produces the best compromise between a P value that is very close to the largest one achieved by the SCB TFD and a numerical complexity that is significantly lesser than the ones required by the other high performing kernels namely the compact support and the ZAM kernels.

5.4 Conclusion

The experimental results show that, even for real-life signals and closely spaced noisy components, the KCS TFDs, followed by the MBD, provide the best performance compared to the other well-known kernel-based distributions in terms of artifacts elimination, high time-frequency resolution of the signal components, accurate extraction of the instantaneous frequency laws from the TFD's peaks even with 0 dB noise power in addition to conservation of the autoterms' concentration while still requiring in general moderate numerical complexity thanks to their compact support nature that reduces considerably the number of points that need computation. Furthermore, the KCS-based TFDs provide two additional important advantages concerning optimization and hardware implementation : 1) No external smoothing windows are needed to achieve high resolution in time or frequency and 2) the induced distributions are computed and their performance are optimized through the tuning of a single parameter that controls the kernel's bandwidth. In particular, the PCB kernel gives in all studied cases one of the largest performance measures of the KCS family with the lowest required computational cost, and at the same time, its optimization procedure is the faster since the smoothing parameter γ of the kernel is an integer.

However, from various experimental tests, the compact support kernels are found to suffer from a considerable degradation of their overall performances, especially concentration, when the kernel's length is less than $L = 64$ while the performance is greatly improved when L is set to 128 yielding to a notable superiority of the KCS-based TFDs over the other powerful distributions even in the extreme case of very closely spaced linear chirps embedded in 0 dB white Gaussian noise.

The obtained results make the KCS TFDs the best candidates for real-time implementation of high-performing DSP and/or FPGA embedded systems for concrete estimation of nonstationary signals' energy due particularly to their high robustness to interference and noise, easy tuning and fast optimization. Their practical use can be made more interesting if some modifications are introduced on their basic formulation so that to allow lower numerical complexity. This subject constitutes one of the axes of our future research.

Chapter 6

Conclusions and Suggestions for Future Work

Signal-independent class of quadratic time-frequency distributions, and the Cohen's class in particular, constitutes the most powerful and efficient family of TFDs in representing and analyzing nonstationary multicomponent signals. The offered freedom in the kernels' design, provided that they are invariant by time and frequency shifts, motivated us to propose new high-resolution quadratic distributions based on a specific type of parametrization functions referred to as kernels with compact support [64] that are derived from the Gaussian kernel but vanish themselves outside a specific set.

The main objective of the research for new time-frequency tools is to enhance the readability of the TF diagrams so that the signal analyst is able to obtain the most precise description of the time-varying signals in terms of identification of the components' number, accurate estimation of the IF laws and thus the best localization of the start and the end of each time and frequency event. We have showed that the problem is reduced to the kernel design whose main task is to smooth the interference terms generated by the Wigner-Ville distribution in compromise with the preservation of a sufficient time-frequency resolution.

Since separable kernels are recognized to outperform many other popular TFDs in resolving closely spaced components and reducing the inner and outer artifacts ; the first main result is to build a high performing quadratic distribution referred to as the SCB TFD based on a separable version of the CB compact support kernel [42], allowing an efficient independent smoothing in time and in frequency. This distribution is implemented following the general time-lag expression given by (2.26).

The second main result consists of building a second kernel with compact support for time-frequency signal analysis having a polynomial form referred to as the PCB KCS. The latter is of great practical value, especially when hardware implementation and fast optimization are intended. The derived quadratic time-frequency distribution referred to as the PCB TFD is also implemented following the same general procedure as for the CB TFD and the SCB TFD.

The third result consists of comparing between the most known quadratic kernel-based distributions and the KCS TFDs from mathematical properties point of view. For each property, the relative requirement that must be satisfied by the kernel in different domains is derived. It is proved again that there is a tradeoff between the best interference suppression/components concentration compromise and the number of good properties. The KCS TFDs and the spectrogram, for example, satisfy three properties only : realness, energy conservation and translation covariance ; the MBD does not verify time marginal, instantanuous frequency and time support conservations and dilation covariance, however, it was shown that they are the best performing and valuable TFDs. Hence, the classical mathematical properties are not important if the main objective is practical time-frequency signal analysis.

The fourth principal result is objective assessment of the new proposed KCS TFDs together with the CB TFD and a selection of the well-known classical distributions of Cohen's class. Our biggest concern was to ensure that the use of a given quantitative measure reflects certainly the performance quality of the TFD of interest and hence provides the right order of the best performing quadratic distributions in representing the considered test signal. After a deep survey on the existing evaluation methods, we have established the following important guidelines

– We have showed through extensive illustrative examples that neither the subjective visual inspection of the time-frequency plots, nor the concentration-based theoretical performance measures [80]-[83] can provide in most cases an accurate objective quantification of the goodness of a given TFD,

– The objective evaluation of the TFD's performance requires the consideration of three important criteria namely autoterms' concentration, time-frequency resolution of the individual signal's components and crossterms' suppression,

– Compared to the concentration-based measures, the Boashash-Sucic's normalized instantaneous resolution performance measure [2, 4, 76] takes into account the three objective criteria cited above and shows the greatest discrimination capabilities of the best performing representation. Consequently, it was adopted to objectively evaluate the investigated time-frequency distributions,

– In addition to its use as a quantitative performance measure of quadratic TFDs, the Boashash-Sucic methodology [1, 26] provides a practical selection procedure of the best performing distribution so that the optimized TFD that maximizes the average of the instantaneous performance measures is selected as the best,

– Since the Boashash-Sucic methodology requires a deep analysis of each time slice, many important information can be deduced accordingly namely time durations and frequency bands of the autoterms, sidelobes and crossterms magnitudes, energy concentration of the signal components and mainlobes amplitudes that serve also to extract the instantaneous frequencies,

– The Boashash-Sucic's methodology, however, suffers from several practical drawbacks : Firstly, for each time instant, the related parameters of each time slice are computationally expensive and since they correspond to a unique pair of components ; they need to be computed $(M+1)/2$ times for a signal containing an odd number M of distinct components and $M/2$ times for M even. This produces two technical problems : 1) High numerical complexity and processing time, and 2) wrong determination of the signal autoterms, especially due to the superior extra energies generated by the interference terms, causes an incorrect estimation of the number of components and also completely wrongs the parameters' calculation of the Boashash-Sucic performance measure and so the optimization results. Secondly, for real-life signals in particular ; the regions of interest, i.e. the intervals of time instants and frequencies over which the distributions are optimized, cannot be determined only after visual inspection of the TFDs' diagrams.

The results from the optimization procedure proved in most studied cases the superiority of the KCS-based TFDs over the other best-known quadratic distributions in representing the analyzed signals even in the hard case of very closely spaced multicomponent signals embedded in noise. The proposed kernels provide the best reduction of the artifacts and the highest autoterms' concentration yielding to the best time-frequency localization of the signal components and the most accurate estimation of the IF laws from the peaks of the KCS TFDs.

The fifth and final main result is the introduction of a fourth optimization criterion of quadratic distributions which is the computational cost of the representation so that the TFD that maximizes the average of the Boashash-Sucic's instantaneous performance measures P and possesses the lowest required numerical complexity is selected as the best. In this context, the compact support kernels with lengths greater than or equal to 64 are found to require in general moderate computational costs and achieve at the same time the highest resolution, concentration and interference rejection. In particular, the PCB TFD gives for most of the considered signals the largest values of P with a numerical complexity that is smaller compared to the other best performing distributions.

The following research axes are highly recommended and may be followed based on the work presented in the thesis

• The real-time implementation of the proposed KCS TFDs as embedded TF signal analyzers using high-performing DSP and/or FPGA boards,

• The derivation of new compact support smooth kernels that provide higher time-frequency resolution with lower numerical complexity,

- The implementation of real-time embedded systems for automatic selection of the optimized signal TFD based on evaluation of some performance measures in order to make the quadratic distributions more appropriate and valuable in practical time-frequency signal analysis,

- The objective assessment and automatic optimization of other energy-based time-frequency distributions that are not elements of the Cohen's class, i.e. are not covariant by shifts in time or in frequency like for example the affine class, which is the class of time-frequency energy distributions covariant by translation in time and dilation and other groups of distributions that are not quadratic like the signal-dependent TFDs.

Appendix A

Toolbox for Time-Frequency Distributions' OPtimization (TFDOP) : A User Manual

A.1 General view of the realized toolbox

Fig. A.1 shows the graphical user interface (GUI) structure of the TFDOP toolbox.

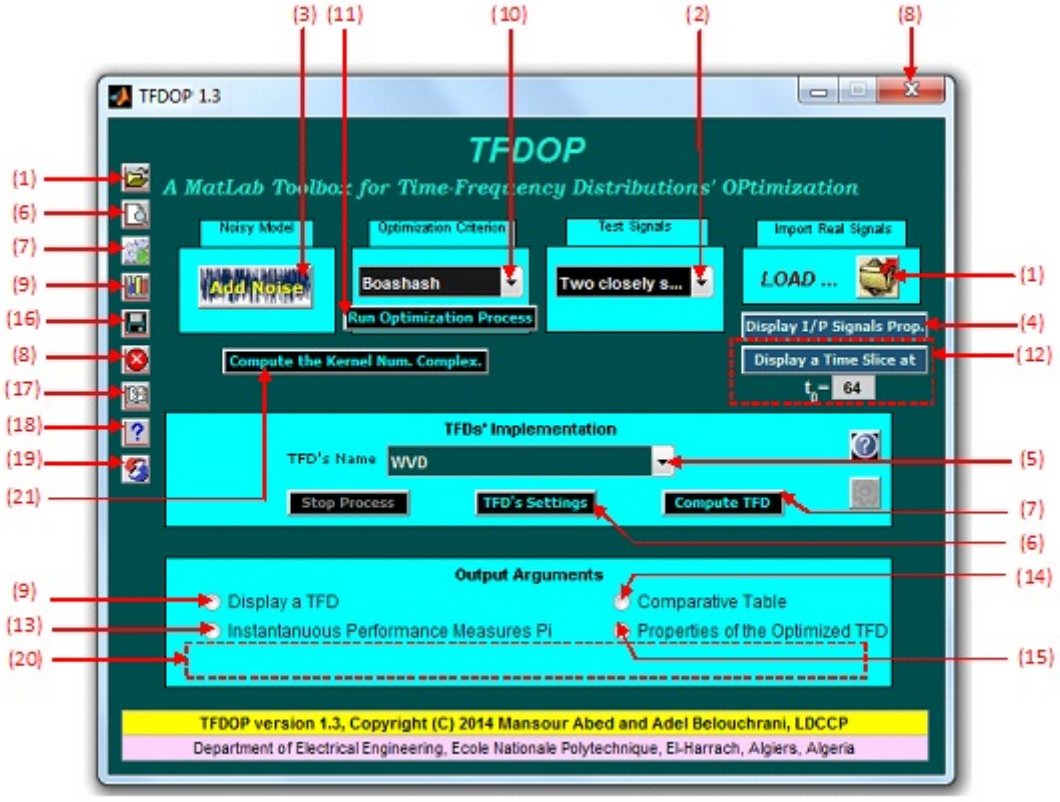

FIGURE A.1 – GUI structure of the TFDOP toolbox.

A.2 Actions of the different user interface control objects

Table A.1 summarizes the different callback routines executed by activating a specific user interface control object numbered from (1) to (21) as they appear in Fig. A.1.

TABLE A.1 – Callback actions of the different user interface control objects reported in Fig. A.1.

N°	Object type	Action
1	Push button	Load real-life signals from prepared *.mat* files
2	Popup menu	Select a synthetic test signal from a large variety of choices
3	Push button	Activate the GUI of Fig. A.2 that serves to set the noise parameters
4	Push button	Display time and frequency characteristics of the input test signal
5	Popup menu	Select the TFD to compute from the following : WVD, BJD, CWD, ZAMD, Spectrogram, MBD, CB TFD, SCB TFD and PCB TFD
6	Push button	Activate the GUI that permits to fix the selected TFD's smoothing parameters (if they exist). An example is shown in Fig. A.3. For the spectrogram, the window type includes the following : Hamming, Hanning, Rectangular, Triangular, Bartlett, Blackman, Gauss and Kaiser.
7	Push button	Compute the selected TFD of the test signal loaded by activating the push button (1) or selected from the popup menu (3)
8	Push button	Display the question dialog box of Fig. A.4 that allows to the user to either quit or keep working with TFDOP toolbox
9	Radio button	Display the computed TFD and the view menu of Fig. A.5 that serves to customize the TFD plot (display mode (contour, surf, mesh,...), display layout (display signal, display spectrum, add a grid,...), colors, ...)
10	Popup menu	Select the objective assessment measure of TFDs from the following : Boashash-Sucic performance measure, Rényi entropy normalized by signal energy concentration measure, Rényi entropy normalized by distribution volume concentration measure, Ratio of norms concentration measure and Stankovic concentration measure
11	Push button	Compute the value of the selected concentration measure and for the Boashash-Sucic method activate the GUI of Fig. A.6 in order to set the time interval of interest over which the TFD is optimized
12	Push button and editable text field	Display the time slice corresponding to the time instant specified by the user through the editable text field. The default value is $t_0 = 64$.
13	Radio button	Display a table a containing the entire Boashash-Sucic's normalized instantaneous resolution performance measures P_i over the optimization interval of time instants, the parameters of each P_i given by (4.11) and (4.12) and also the value of P ; the overall measure (see the example of Fig. A.7)
14	Radio button	Display a comparative table containing the optimization results for a selection of TFDs of the test signal as reported in the example of Fig. A.8
15	Radio button	Show the properties of the optimized TFD (general description of the test signal, optimization region of interest, optimized smoothing parameters of the kernel and performance measure value)
16	Push button	Save input and output parameters of the current simulation (test signal, smoothing parameters of the kernel, noise level, computed TFD, computed performance measure, computed computational cost of the kernel,...)
17	Push button	Display a brief history about the last obtained optimization results

18	Push button	Display a general help about the toolbox
19	Push button	When activated, this push button permits to clear all selected input variables and generated output variables from Matlab workspace and close all figures. The TFDOP setting parameters and graphical objects are reset to their default values and states
20	Static text label	Display indicative messages when needed and eventually error alarms when the user chooses wrong parameters' values. For example, when the TFD is computed, the following message is displayed : "Computation done"; the user can then display and objectively evaluate the selected TFD. If most of the main components of the analyzed signal are not resolved in frequency, the user is asked to change the current TFD's setting. The computed Boashash-Sucic P value is not retained and the following warning message is displayed in this field : " W A R N I N G ! Most of the main components are not resolved in frequency. Change your setting ! "
21	Push button	Evaluate the computational cost of the time-lag kernel according to the formulas of Chapter 5

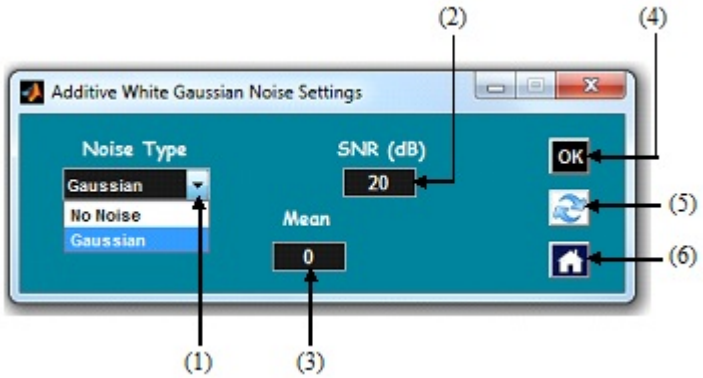

FIGURE A.2 – AWGN parameters setting window.

TABLE A.2 – Callback actions of the user interface control objects reported in Fig. A.2.

N°	Object type	Action
1	Popup menu	Choose either to add noise to the test signal or consider the noiseless case
2	Editable text field	Edit the signal to noise ratio in dB (default value : SNR=20 dB)
3	Editable text field	Edit the mean value of the Gaussian noise (default value : mean=0)
4	Push button	Validate the current noise setting
5	Push button	Restore default values
6	Push button	Return to TFDOP

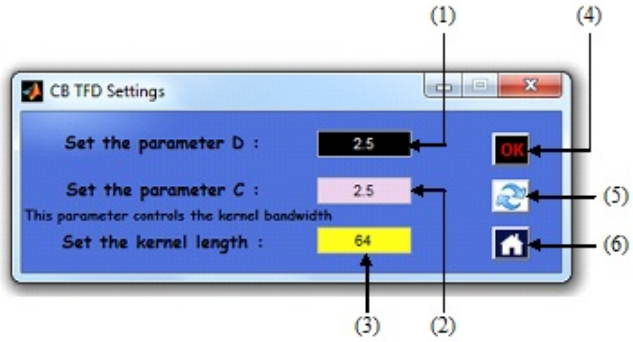

FIGURE A.3 – CB TFD setting window.

TABLE A.3 – Callback actions of the user interface control objects reported in Fig. A.3.

N°	Object type	Action
1	Editable text field	Edit the parameter D of the CB kernel (default value : $D = 2.5$)
2	Editable text field	Edit the control parameter C of the CB kernel (default value : $C = 2.5$)
3	Editable text field	Edit the kernel length L (default value : $L = 64$)
4	Push button	Validate the current CB kernel setting
5	Push button	Restore default values
6	Push button	Return to TFDOP

FIGURE A.4 – Question dialog box permetting to quit or keep working with the toolbox.

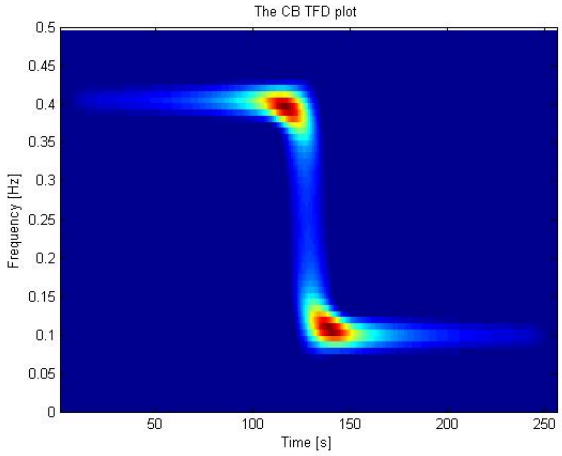

(a)

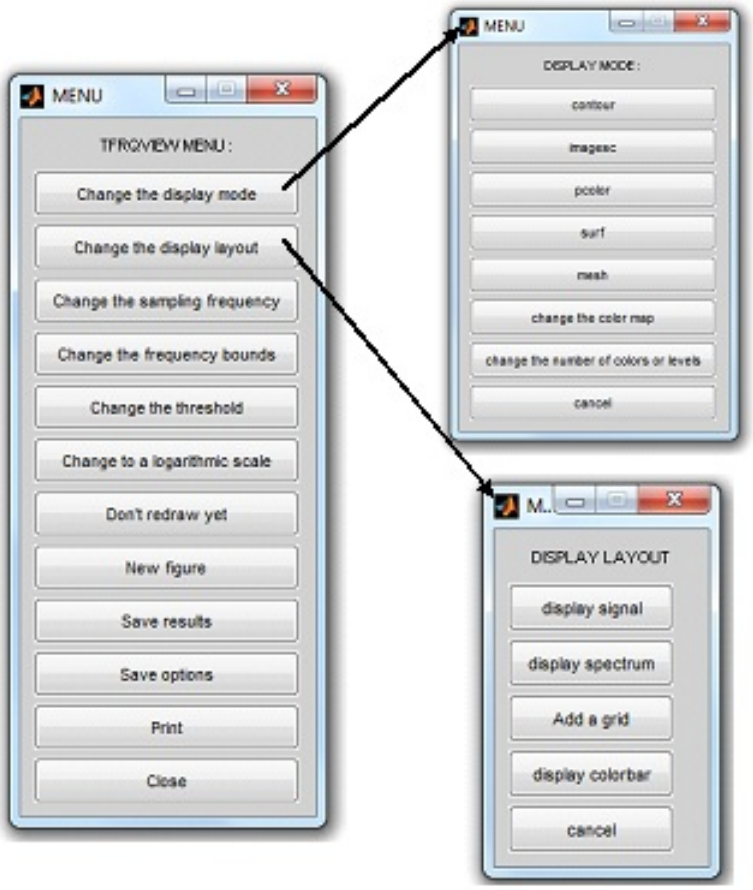
MENU
TFR/VIEW MENU :
Change the display mode
Change the display layout
Change the sampling frequency
Change the frequency bounds
Change the threshold
Change to a logarithmic scale
Don't redraw yet
New figure
Save results
Save options
Print
Close
MENU
DISPLAY MODE :
contour
imagesc
pcolor
surf
mesh
change the color map
change the number of colors or levels
cancel
M..
DISPLAY LAYOUT
display signal
display spectrum
Add a grid
display colorbar
cancel

(b)

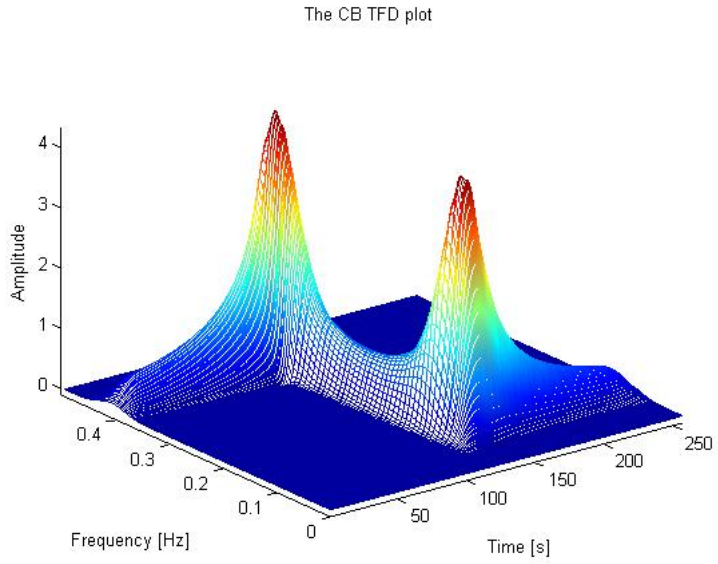
The CB TFD plot
Amplitude
Frequency [Hz]
Time [s]

(c)

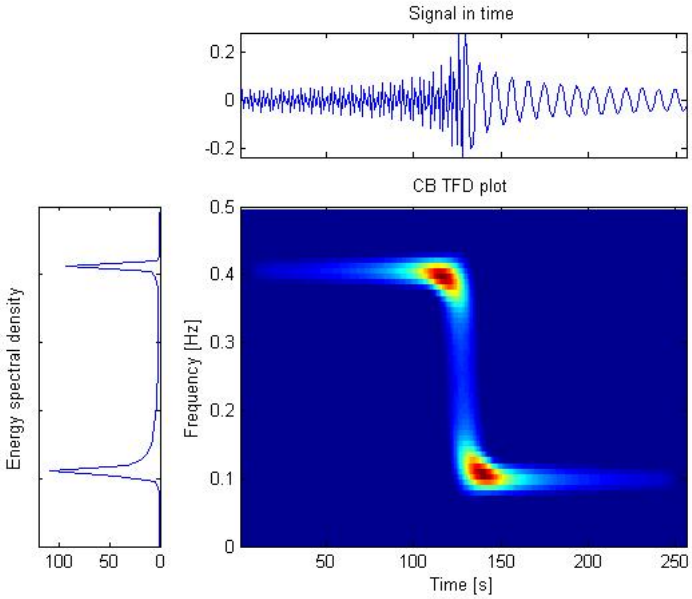

(d)

FIGURE A.5 – Display of a TFD plot and the view menu when the radio button (9) is enabled : (a) Default plot of a TFD, (b) view menu controling the display options, (c) TFD plot after changing the display mode to mesh and (d) TFD plot after changing the diaplay layout so that the signal and the spectrum are plotted together with the TFD diagram.

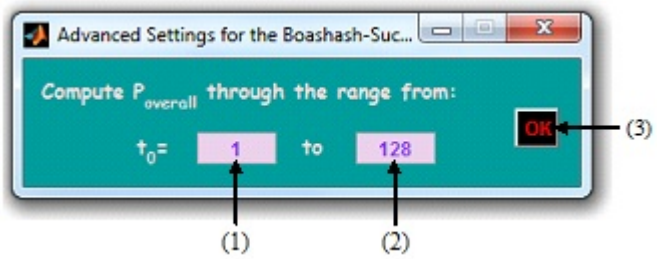

FIGURE A.6 – Setting window of the time interval (region of interest) over which the TFD is optimized using the Boashash-Sucic methodology.

TABLE A.4 – Callback actions of the user interface control objects reported in Fig. A.6.

N°	Object type	Action
1	Editable text field	Edit the initial time instant (default value : $t_0 = 1$)
2	Editable text field	Edit the final time instant (default value : the full range of time instants, i.e. the length of the test signal)
3	Push button	Validate the current optimization interval setting

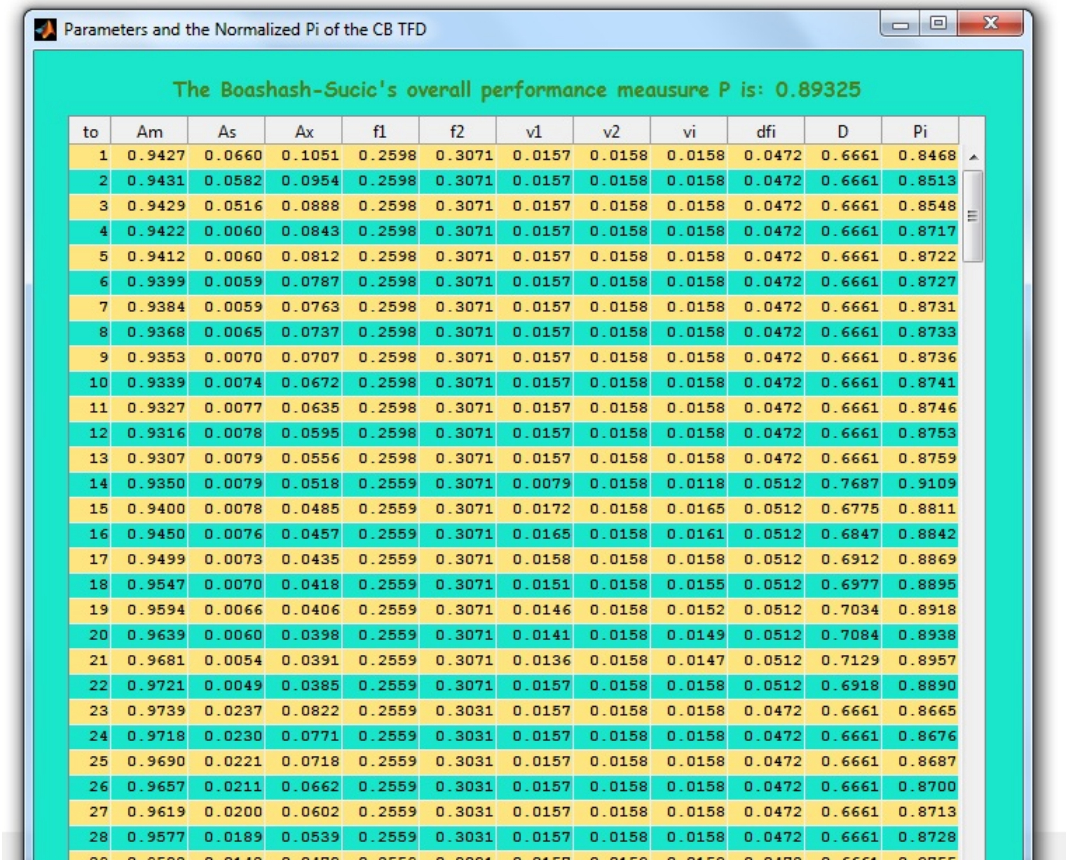

to	Am	As	Ax	f1	f2	v1	v2	vi	dfi	D	Pi
1	0.9427	0.0660	0.1051	0.2598	0.3071	0.0157	0.0158	0.0158	0.0472	0.6661	0.8468
2	0.9431	0.0582	0.0954	0.2598	0.3071	0.0157	0.0158	0.0158	0.0472	0.6661	0.8513
3	0.9429	0.0516	0.0888	0.2598	0.3071	0.0157	0.0158	0.0158	0.0472	0.6661	0.8548
4	0.9422	0.0060	0.0843	0.2598	0.3071	0.0157	0.0158	0.0158	0.0472	0.6661	0.8717
5	0.9412	0.0060	0.0812	0.2598	0.3071	0.0157	0.0158	0.0158	0.0472	0.6661	0.8722
6	0.9399	0.0059	0.0787	0.2598	0.3071	0.0157	0.0158	0.0158	0.0472	0.6661	0.8727
7	0.9384	0.0059	0.0763	0.2598	0.3071	0.0157	0.0158	0.0158	0.0472	0.6661	0.8731
8	0.9368	0.0065	0.0737	0.2598	0.3071	0.0157	0.0158	0.0158	0.0472	0.6661	0.8733
9	0.9353	0.0070	0.0707	0.2598	0.3071	0.0157	0.0158	0.0158	0.0472	0.6661	0.8736
10	0.9339	0.0074	0.0672	0.2598	0.3071	0.0157	0.0158	0.0158	0.0472	0.6661	0.8741
11	0.9327	0.0077	0.0635	0.2598	0.3071	0.0157	0.0158	0.0158	0.0472	0.6661	0.8746
12	0.9316	0.0078	0.0595	0.2598	0.3071	0.0157	0.0158	0.0158	0.0472	0.6661	0.8753
13	0.9307	0.0079	0.0556	0.2598	0.3071	0.0157	0.0158	0.0158	0.0472	0.6661	0.8759
14	0.9350	0.0079	0.0518	0.2559	0.3071	0.0079	0.0158	0.0118	0.0512	0.7687	0.9109
15	0.9400	0.0078	0.0485	0.2559	0.3071	0.0172	0.0158	0.0165	0.0512	0.6775	0.8811
16	0.9450	0.0076	0.0457	0.2559	0.3071	0.0165	0.0158	0.0161	0.0512	0.6847	0.8842
17	0.9499	0.0073	0.0435	0.2559	0.3071	0.0158	0.0158	0.0158	0.0512	0.6912	0.8869
18	0.9547	0.0070	0.0418	0.2559	0.3071	0.0151	0.0158	0.0155	0.0512	0.6977	0.8895
19	0.9594	0.0066	0.0406	0.2559	0.3071	0.0146	0.0158	0.0152	0.0512	0.7034	0.8918
20	0.9639	0.0060	0.0398	0.2559	0.3071	0.0141	0.0158	0.0149	0.0512	0.7084	0.8938
21	0.9681	0.0054	0.0391	0.2559	0.3071	0.0136	0.0158	0.0147	0.0512	0.7129	0.8957
22	0.9721	0.0049	0.0385	0.2559	0.3071	0.0157	0.0158	0.0158	0.0512	0.6918	0.8890
23	0.9739	0.0237	0.0822	0.2559	0.3031	0.0157	0.0158	0.0158	0.0472	0.6661	0.8665
24	0.9718	0.0230	0.0771	0.2559	0.3031	0.0157	0.0158	0.0158	0.0472	0.6661	0.8676
25	0.9690	0.0221	0.0718	0.2559	0.3031	0.0157	0.0158	0.0158	0.0472	0.6661	0.8687
26	0.9657	0.0211	0.0662	0.2559	0.3031	0.0157	0.0158	0.0158	0.0472	0.6661	0.8700
27	0.9619	0.0200	0.0602	0.2559	0.3031	0.0157	0.0158	0.0158	0.0472	0.6661	0.8713
28	0.9577	0.0189	0.0539	0.2559	0.3031	0.0157	0.0158	0.0158	0.0472	0.6661	0.8728

FIGURE A.7 – An example showing the parameters, the normalized P_i and the overall value of P related to the Boashash-Sucic performance measure after enabling the radio button (13).

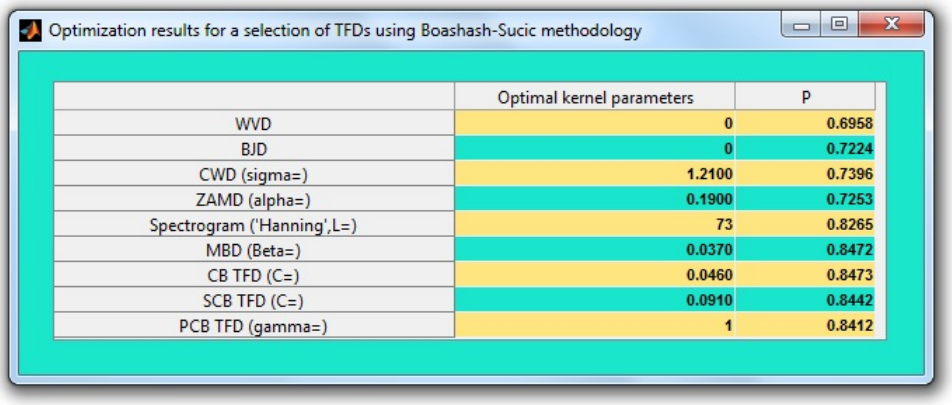

	Optimal kernel parameters	P
WVD	0	0.6958
BJD	0	0.7224
CWD (sigma=)	1.2100	0.7396
ZAMD (alpha=)	0.1900	0.7253
Spectrogram ('Hanning',L=)	73	0.8265
MBD (Beta=)	0.0370	0.8472
CB TFD (C=)	0.0460	0.8473
SCB TFD (C=)	0.0910	0.8442
PCB TFD (gamma=)	1	0.8412

FIGURE A.8 – An example of a comparative table obtained by enabling the radio button (14) and containing the optimization results for a selection of TFDs using Boashash-Sucic methodology.

Appendix B

List of publications

[1] M. Abed, A. Belouchrani, M. Cheriet and B. Boashash, "Time-frequency distributions based on compact support kernels : Properties and performance evaluation," *IEEE Trans. Signal Process.*, vol. 60, no. 6, pp. 2814-2827, Jun. 2012.

[2] M. Abed, A. Belouchrani, M. Cheriet and B. Boashash, "Compact support kernels based time-frequency distributions : Performance evaluation," in *Proc. 36th IEEE International Conference on Acoustic, Speech and Signal Processing (ICASSP 2011)*, pp. 4180-4183, Prague, Czech Republic, May 22-27, 2011.

References

[1] V. Sucic and B. Boashash, "Parameter selection for optimising time-frequency distributions and measurements of time-frequency characteristics of nonstationay signals," in *Proc. IEEE Int. Conf. Acoust., Speech Signal Process.*, Salt Lake City, UT, May 2001, vol. 6, pp. 3557-3560.

[2] B. Boashash and V. Sucic, "Resolution measure criteria for the objective assessment of the performance of quadratic time-frequency distributions," *IEEE Trans. Signal Process.*, vol. 51, no. 5, pp. 1253-1263, May 2003.

[3] B. Boashash, "Time-frequency signal analysis," in *Advances in Spectrum Analysis and Array Processing*, S. Haykin, ed. Englewood Cliffs, NJ :Prentice-Hall, 1991, vol. 1, ch. 9, pp. 418-517.

[4] B. Boashash, (Ed.), *Time-Frequency Signal Analysis and Processing : A Comprehensive Reference.* Elsevier : Amsterdam, 2003.

[5] R. L. Allen and D. W. Mills, *Signal Analysis : Time, Frequency, Scale and Structure.* New York : IEEE-Wiley, 2004.

[6] E. Wigner, "On the quantum correction for thermodynamic equilibrium," *Physical Review*, vol. 40, pp. 749-759, 1932.

[7] J. Ville, "Théorie et applications de la notion de signal analytique," *Cables et Transmission*, vol. 2A, pp. 61-74, 1948.

[8] B. Barkat and B. Boashash, "Adaptive window in the PWVD for IF estimation of FM signals in additive Gaussian noise," in *Proc. IEEE Int. Conf. Acoust., Speech Signal Process.*, Phoenix, AZ, Mar. 1999, vol. 3, pp. 1317-1320.

[9] B. Barkat and B. Boashash, "Instantaneous frequency estimation of polynomial FM signals using the peak of the PWVD : Statistical performance in the presence of additive Gaussian noise," *IEEE Trans. Signal Process.*, vol. 47, no. 9, pp. 2480-2490, Sep. 1999.

[10] B. Boashash, "Time-Frequency Analysis." Englewood Cliffs, NJ :Prentice-Hall, 1995.

[11] P. Flandrin, "Some features of time-frequency representations of multicomponent signals," in *Proc. IEEE Int. Conf. Acoust., Speech Signal Process.*, San Diego, CA, Mar. 1984, vol. 9, pp. 266-269.

[12] B. Boashash and P. O'Shea, "Adaptive window in the PWVD for IF estimation of FM signals in additive Gaussian noise," in *Proc. SPIE, Advanced Signal Processing Algorithms, Architectures, and Implementations II*, San Diego, CA, USA, Jul. 1991.

[13] B. Boashash and P. O'Shea, "Polynomial Wigner-Ville distributions and their relationship to time-varying higher order spectra," *IEEE Trans. Signal Process.*, vol. 42, no. 1, pp. 216-220, Jan. 1994.

[14] L. Cohen, "Generalized phase-space distribution functions," in *Journal of Mathematical Physics*, vol. 7, pp. 781-786, Jan. 1966.

[15] T. A. C. M. Claasen and W. F. G. Mecklenbrauker, "The Wigner distribution- A tool for time-frequency signal analysis, Part I : Continuous-time signals," *Philips Journal of Research*, vol. 35, pp. 217-250, 1980.

[16] T. A. C. M. Claasen and W. F. G. Mecklenbrauker, "The Wigner distribution- A tool for time-frequency signal analysis, Part II : Discrete-time signals," *Philips Journal of Research*, vol. 35, pp. 276-300, 1980.

[17] T. A. C. M. Claasen and W. F. G. Mecklenbrauker, "The Wigner distribution- A tool for time-frequency signal analysis, Part III : Relations with other time-frequency signal transformations," *Philips Journal of Research*, vol. 35, pp. 372-389, 1980.

[18] B. Boashash, "Représentation temps-fréquence," Tech. Rep. 373/78, Soc. Nat. ELF-Aquitaine, Pau, France, 1978.

[19] I. Shafi, "Time-frequency analysis using neural networks : De-Âblurred time-frequency distributions using neural networks" PhD thesis, Department of Computer Engineering, Centre for Advance Studies in Engineering, Islamabad, University of Engineering and Technology (UET), Taxila, Pakistan, Sep. 2009.

[20] C. P. Janse and A. J. M. Kaizer, "Time-frequency distributions of loudspeakers : The application of the Wigner distribution," *Journal of Audio Eng. Soc.*, vol. 31, no. 4, pp. 198-223, Apr. 1983.

[21] D. Gabor, "Acoustical quanta and the theory of hearing," *Nature*, vol. 159, no. 4044, pp. 591-594, May 1947.

[22] D. Gabor, "Theory of communication," *J. IEE*, vol. 93, no. 26, pp. 429-457, Nov. 1946.

[23] A. V. Oppenheim, " Speech spectrograms using the fast Fourier transform," *J. IEEE Spectrum*, vol. 7, no. 8, pp. 57-62, Aug. 1970.

[24] A. L. Levshin, V. F. Pisarenko and G. A. Pogrebinsky, "On a frequency-time analysis of oscillations," in *Ann. Geophys.*, vol. 28, pp. 211-218, 1972.

[25] M. R. Portnoff, "Time-frequency representation of digital signals and systems based on short-time Fourier analysis," *IEEE Trans. Acoust., Speech Signal Process.*, vol. 28, no. 1, pp. 55-69, Feb. 1980.

[26] V. Sucic, "Parameters selection for optimizing time-frequency distributions and measurements of time-frequency characteristics of nonstationary signals," PhD thesis, School of Electrical and Electronic Systems Engineering, Queensland University of Technology, Brisbane, Australia, Mar. 2004.

[27] H. Choi and W. J. Williams, " Improved time-frequency representation of multicomponent signals using exponential kernels," *IEEE Trans. Acoust., Speech Signal Process.*, vol. 37, no. 6, pp. 862-871, June 1989.

[28] L. Cohen, " Time-frequency distributions- A review," in *Proc. IEEE*, vol. 77, no. 7, pp. 941-981, Jul. 1989.

[29] M. Born and P. Jordan, " Zur quantenmechanic," *Zeitschrift fur Physik*, vol. 34, pp. 858-888, 1925.

[30] L. Cohen, " Introduction : A primer on time-frequency analysis," in *Time-Frequency Signal Analysis : Methods and Applications*, B. Boashash, Ed. Melbourne/N.Y. : Longman-Cheshire/Wiley, 1992, ch. 1, pp. 3-42.

[31] Y. Zhao, L. E. Atlas, and R. J. Marks, " The use of cone-shaped kernels for generalized time-frequency representations of nonstationary signals," *IEEE Trans. Acoust., Speech Signal Process.*, vol. 38, no. 7, pp. 1084-1091, Jul. 1990.

[32] A. Papandreou and G. F. Boudreaux-Bartels, "Generalization of the Choi-Williams distribution and the Butterworth distribution for time-frequency analysis," *IEEE Trans. Signal Process.*, vol. 41, no. 1, pp. 463-472, 1993.

[33] A. Papandreou, F. Hlawatsch, and G. F. Boudreaux-Bartels, "The hyperbolic class of quadratic time-frequency representations. I. Constant-Q warping, the hyperbolic paradigm, properties, and members," *IEEE Trans. Signal Process.*, vol. 41, no. 12, pp. 3425-3444, Dec. 1993.

[34] LJ. Stankovic, "Highly concentrated time-frequency distributions : Pseudo quantum signal representation," *IEEE Trans. Signal Process.*, vol. 45, no. 3, pp. 543-551, Mar. 1997.

[35] A. Papandreou, F. Hlawatsch, and G. F. Boudreaux-Bartels, "Quadratic time-frequency representations with scale covariance and generalized time-shift covariance : A unified framework for the affine, hyperbolic, and power classes," *Digital Signal Process. : A Review Journal*, vol. 8, no. 1, pp. 3-48, 1998.

[36] A. Papandreou-Suppappola, R. L. Murray, B. G. Iem, and G. F. Boudreaux-Bartels, "Group delay shift covariant quadratic time-frequency representations," *IEEE Trans. Signal Process.*, vol. 49, pp. 2549-2564, Nov. 2001.

[37] M. G. Amin, "Recursive kernels for time-frequency signal representations," *IEEE Signal Process. Letters*, vol. 3, no. 1, pp. 16-18, Jan. 1996.

[38] M. G. Amin, "Minimum variance time-frequency distribution kernels for signals in additive noise," *IEEE Trans. Signal Process.*, vol. 44, no. 9, pp. 2352-2356, Sep. 1996.

[39] M. G. Amin and W. J. Williams, "High spectral resolution time-frequency distribution kernels," *IEEE Trans. Signal Process.*, vol. 46, no. 10, pp. 2796-2804, Oct. 1998.

[40] V. Sucic, B. Barkat, and B. Boashash, "Performance evaluation of the B-distribution," in *Proc. 5th Int. Symp. on Signal Process. and its Applications (ISSPA'99)*, Brisbane, Australia, 22-25 Aug. 1999, vol. 1, pp. 267-270.

[41] Z. M. Hussain and B. Boashash, "Multi-component IF Estimation," in *Proc. 10th IEEE Workshop on Statist. Signal Array Process.*, Pocono Manor, PA, Aug. 2000, pp. 559-563.

[42] B. Barkat and B. Boashash, "High-resolution quadratic time-frequency distribution for multicomponent signal analysis," *IEEE Trans. Signal Process.*, vol. 49, no. 10, pp. 2232-2238, Oct. 2001.

[43] Z. M. Hussain and B. Boashash, "Some features of time-frequency representations of multicomponent signals," in *Proc. IEEE Int. Conf. Acoust., Speech Signal Process.*, Istanbul, 5-9 June 2000, vol. 2, pp. 657-660.

[44] A. Belouchrani and M. Cheriet, "On the use of a new compact support kernel in time-frequency analysis," in *Proc. 11th IEEE Workshop on Statist. Signal Process.*, Singapore, May 2001, pp. 333-336.

[45] M. Cheriet and A. Belouchrani, "Method and system for measuring the energy of a signal," *World Intellectual Property Organization*, Patent number WO02088760 A2, Nov. 2002.

[46] A. Belouchrani and M. G. Amin, "New approach for blind source separation using time-frequency distributions," in *Proc. SPIE, Advanced Signal Processing Algorithms, Architectures, and Implementations VI*, 22-Oct. 1996, vol. 2846, doi :10.1117/12.255434.

[47] A. Belouchrani and M. G. Amin, "Blind source separation using time-frequency distributions : algorithm and asymptotic performance," in *Proc. IEEE Int. Conf. Acoust., Speech Signal Process.*, Munich, 21-24 Apr. 1997, vol. 5, pp. 3469-3472.

[48] A. Belouchrani and M. G. Amin, "Blind source separation based on time-frequency signal representations," *IEEE Trans. Signal Process.*, vol. 46, no. 11, pp. 2888-2897, Nov. 1998.

[49] Y. Zhang and M. G. Amin, "Blind separation of nonstationary sources based on spatial time-frequency distributions," *EURASIP Journal on Applied Signal Process.*, pp. 198-198 , Jan. 2006.

[50] M. G. Amin, "Interference mitigation in spread spectrum communication systems using time-frequency distributions," *IEEE Trans. Signal Process.*, vol. 45, no. 1, pp. 90-101, Jan. 1997.

[51] A. Belouchrani and M. G. Amin, "Time-frequency MUSIC," *IEEE Signal Process. Letters*, vol. 6, no. 5, pp. 109-110, May 1999.

[52] M. G. Amin, "Direction finding based on spatial time-frequency distribution matrices," *Digital Signal Process.*, vol. 10, no. 4, pp. 325-339, Oct. 2000.

[53] Ming Li, X. K. Gu, and W. Zhao, "Experimental analysis of pattern similarity between Bessel kernel and Born-Jordan kernel," *Int. Journal of Circuits, Systems and Signal Process.*, vol. 1, no. 2, pp. 150-154, 2007.

[54] P. Flandrin, *Time-Frequency/Time-Scale Analysis.* San Diego : Academic Press, 1999, original French edition : Temps-fréquence (Paris :Hermès, 1993), pp. 104-132.

[55] F. Auger, O. Lemoine, P. Gonçalvès and P. Flandrin, "Time-Frequency toolbox for use with Matlab," Tutorial, Centre National de la Recherche Scientifique CNRC (France) and Rice University (USA), Oct. 26, 2005.

[56] W. Heisenberg, *Physical Properties of the Quantum Theory.* New York : Dover, 1949.

[57] L. Cohen, "Time-Frequency Analysis." Englewood Cliffs, NJ : Prentice-Hall, 1995.

[58] F. Hlawatsch, "Time-frequency methods for signal processing," Technical Report 1291-0001, Department of Electrical Engineering, University of Rhode Island, 1991.

[59] B. Barkat and B. Boashash, "Higher order PWVD and Legendre based time-frequency distribution," in *Sixth IEEE Internat. Workshop on Intelligent Signal Process. and Communication Systems (ISPACS'98)*, Melbourne, Australia, Nov. 5-6, 1998, vol. 2, pp. 532â536.

[60] P. Flandrin and W. Martin, *A general class of estimators for the Wigner-Ville spectrum of non-stationary processes.* Analysis and Optimization of Systems, Lecture Notes in Control and Information Sciences, A. Bensoussan and J. L. Lions, ed., Berlin :Springer-Verlag, 1984, vol. 62, pp. 15-23.

[61] W. Willams and J. Jeong, *Reduced interference time-frequency distributions.* Time-Frequency Signal Analysis- Methods and Applications, B. Boashash, ed., Melbourne :Longman-Cheshire, 1992, pp. 74-97.

[62] I. Weiss, "High-order differentiation filters that work," *IEEE Trans. Pattern Anal. Mach. Intell.*, vol. 16, no. 7, pp. 734-739, Jul. 1994.

[63] S. Saryazdi and M. Cheriet, "PKCS : A polynomial kernel family with compact support for scale-space image processing," *IEEE Trans. on Image Processing*, vol. 16, no. 9, pp. 2299-2307, Sep. 2007.

[64] L. Remaki and M. Cheriet, "KCS- New kernel family with compact support in scale space : Formulation and impact," *IEEE Trans. on Image Processing*, vol. 9, no. 6, pp. 970-981, June 2000.

[65] E. B. Braiek, A. Meghoufel, and M. Cheriet, "SKCS-New kernel family with compact support," in *Proc. IEEE Int. Conf. Image Process. (ICIP 2004)*, Oct. 24-27, 2004, vol. 2, pp. 1181-1184.

[66] R. Horaud and O. Monga, *Vision par Ordinateur, Outils Fondamentaux.* Paris, France : Hermes, 1995, p. 425.

[67] T. Lindeberg, *Scale-Space Theory in Computer Vision.* Norwell, MA : Kluwer, 1994, p. 423.

[68] K. O. Friedrichs, "The identity of weak and strong extensions of differential operators," *Trans. of the American Mathematical Society*, vol. 55, no. 1, pp. 132-151, Jan. 1944.

[69] R. E. Showalter, *Hilbert Space Methods in Partial Differential Equations.* Pitman Publishing Ltd., 1979.

[70] Z. Denkowski, S. Migorski and N. S. Papageorgiou, *An Introduction to Nonlinear Analysis : Theory.* Kluwer Academic/Plenum Publishers, 2003.

[71] V. Sucic and B. Boashash, "The optimal smoothing of the Wigner-Ville distribution for real-life signals time-frequency analysis," in *Proc. 10th Asia-Pacific Vibration Conf. (APVC'03)*, Gold Coast, Australia, Nov. 2003, vol. 2, pp. 652-656.

[72] Z. M. Hussain and B. Boashash, "The T-class of time-frequency distributions : Time-only kernels with amplitude estimation," *J. Franklin Inst.*, vol. 343, no. 7, pp. 661-675, 2006.

[73] V. Sucic, "Estimation of components frequency separation from the signal Wigner-Ville distribution," in *Proc. 5th Int. Workshop on Signal Process. Appl. (WoSPA'08)*, Sharjah, U.A.E, Mar. 2008.

[74] A. Mertins, *Signal Analysis : Wavelets, Filter Banks, Time-Frequency Transforms and Applications.* Chichester, U.K. : Wiley, 1999.

[75] F. Hlawatsh, T. G. Manickam, R. L. Urbanke, and W. Jones, "Smoothed pseudo-Wigner distribution, Choi-Williams distribution, and cone-kernel representation : Ambiguity-domain analysis and experimental comparison," *Signal Process.*, vol. 43, pp. 149-168, 1995.

[76] LJ. Stankovic, "An analysis of some time-frequency and time-scale distributions," *Ann. Telecommun.*, vol. 49, no. 9-10, pp. 505-517, Sept./Oct. 1994.

[77] LJ. Stankovic, "Auto-term representation by the reduced interference distributions : A procedure for kernel design," *IEEE Trans. on Signal Process.*, vol. 44, pp. 1557-1563, June 1996.

[78] "Bat echolocation chirp," DSP group, Rice University, Houston, Texas, USA. Available : http ://dsp.rice.edu/software/bat-echolocation-chirp, 2009.

[79] F. Auger, O. Lemoine, P. Gonçalvès and P. Flandrin, "The Time-Frequency Toolbox (TFTB)," Available : http ://tftb.nongnu.org, last update Oct. 2008.

[80] W. J. Williams, M. Brown and A. Hero, "Uncertainty, information and time-frequency distributions," in *SPIE- Advanced Signal Processing Algorithms, Architectures and implementations II*, vol. 1556, pp. 144-156, 1991.

[81] D. L. Jones and T. W. Parks, "A resolution comparison of several time-frequency representations ," in *Proc. IEEE International Conference on Acoustic, Speech and Signal Processing (ICASSP 1989)*, vol. 4, pp. 2222 - 2225, Glasgow, 23-26 May 1989.

[82] T. -H. Sang and W. J. Williams, "Rényi information and signal-dependent kernel design," in *Proc. IEEE International Conference on Acoustic, Speech and Signal Processing (ICASSP 1995)*, vol. 2, pp. 997-1000, Detroit, 9-12 May 1995.

[83] R. G. Baraniuk, P. Flandrin, A. J. E. M. Janssen and O. J. J. Michel, "Measuring time-frequency information content using the Rényi entropies," *IEEE Trans. Information Theory*, vol. 47, no. 4, pp. 1391-1409, May 2001.

[84] D. L. Jones and T. W. Parks, "A high resolution data-adaptive time-frequency representation," in *Proc. IEEE International Conference on Acoustic, Speech and Signal Processing (ICASSP 1990)*, vol.38, pp. 2127-2135, Detroit, Dec. 1990.

[85] L. Stankovic, "A measure of some time-frequency distributions concentration," *Signal Processing*, vol. 81, no. 3, pp. 621-631, Mar. 2001.

[86] B. Boashash and V. Sucic, "High performance time-frequency distributions for practical applications ," *Wavelets and Signal Processing*, L. Debnath, Ed. Boston : Birkhäuser, ch. 6, pp. 135-175, 2003.

[87] M. Abed, A. Belouchrani, M. Cheriet and B. Boashash, "Compact support kernels based time-frequency distributions : Performance evaluation," in *Proc. 36th IEEE International Conference on Acoustic, Speech and Signal Processing (ICASSP 2011)*, pp. 4180-4183, Prague, Czech Republic, May 22-27, 2011.

[88] M. Abed, A. Belouchrani, M. Cheriet and B. Boashash, "Time-frequency distributions based on compact support kernels : Properties and performance evaluation," *IEEE Trans. Signal Process.*, vol. 60, no. 6, pp. 2814-2827, Jun. 2012.